2012

# Small-Scale MDCT-Based Measures of Ventilation and Perfusion: the Development and Evaluation of New Tools for Examining the Etiology of Regional Lung Disease

Matthew Kyle Fuld
*University of Iowa*

# SMALL-SCALE MDCT-BASED MEASURES OF VENTILATION AND PERFUSION: THE DEVELOPMENT AND EVALUATION OF NEW TOOLS FOR EXAMINING THE ETIOLOGY OF REGIONAL LUNG DISEASE

by

Matthew Kyle Fuld

An Abstract

Of a thesis submitted in partial fulfillment
of the requirements for the Doctor of
Philosophy degree in Biomedical Engineering
in the Graduate College of
The University of Iowa

July 2012

Thesis Supervisor: Professor Eric A. Hoffman

ABSTRACT

Pulmonary diseases are characterized by small-scale and large-scale alterations in structure and function of the lung. Multidetector-row computed tomography (MDCT) is a powerful tool for quantitatively assessing small-scale lung structure including parenchymal destruction, air trapping and airway remodeling. When combined with novel imaging techniques and contrast agents, measuring small-scale regional ventilation ($r\dot{V}_A$) and perfusion ($r\dot{Q}$) also becomes possible. This thesis focuses on developing and evaluating MDCT-based tools for measuring regional lung function in animal models and transitioning them to studying humans.

Wash-in xenon-CT $r\dot{V}_A$ measurements acquired in an animal model were validated with inhaled fluorescent microspheres (FMS), an invasive but recognized gold standard. Xenon-CT correlated well with FMS, demonstrating similar gradients in prone and supine postures. Small-scale $r\dot{V}_A$ measurements from xenon-CT were less susceptible to partial voluming and resulted in reduced scatter.

To facilitate the measurement of regional structure and function on awake-free-breathing humans, we developed systems for lung volume standardization during scanning for both static and dynamic breathing. Anesthetic properties dictated using 30% rather than 55% xenon-gas, reducing signal-to-noise ratio. This reduction, in addition to the influence of free breathing, made xenon-CT more susceptible to noise and required additional post-processing to bolster confidence in $r\dot{V}_A$ measurements acquired in humans. Improvements to the available curve-fit algorithms were made and 4D image registration was developed to align time-series datasets.

Applying these techniques, we compared $r\dot{V}_A$ between normal never-smokers (NS), normal smokers (SNI), normal smokers with early signs of centrilobular emphysema not evident by PFTs (SCE) and smokers with COPD. There was increased heterogeneity in SNI versus NS and time constants were lengthened in COPD and in SCE. This is consistent with our earlier hypothesis that while patchy inflammation will

occur in all smokers, only a subset of the population with decreased $r\dot{Q}$ in regions of inflammation stemming from a failure to block HPV will be susceptible to emphysema.

In order to facilitate translation into the clinical research environment, we established dual-energy-CT (DECT) methods to replace more elaborate time-series laboratory-centered techniques. Xe-DECT $r\dot{V}_A$ measures were optimized through a series of phantom and animal studies to determine the proper three-material decomposition parameters, imaging parameters, gas mixture and delivery protocol. DECT perfused blood volume was validated as a surrogate for $r\dot{Q}$ in animal studies in which blood flow patterns were altered by increasing lung inflation or occluding a portion of the pulmonary vasculature.

To examine the intricacy of lung function, the effects of disease, and provide insight into their etiology we must study gas-exchange on a small-scale. MDCT-based techniques provide the spatial resolution necessary to examine $r\dot{V}_A$ and $r\dot{Q}$ on a small-scale offering an avenue to identify novel phenotypes that may not only yield insights into disease processes but also may provide tools leading to drug and device developments, outcomes assessment and ultimately to the selection of subpopulations suitable for a particular intervention.

Abstract Approved: _____
Thesis Supervisor

_____
Title and Department

_____
Date

# SMALL-SCALE MDCT-BASED MEASURES OF VENTILATION AND PERFUSION: THE DEVELOPMENT AND EVALUATION OF NEW TOOLS FOR EXAMINING THE ETIOLOGY OF REGIONAL LUNG DISEASE

by

Matthew Kyle Fuld

A thesis submitted in partial fulfillment
of the requirements for the Doctor of
Philosophy degree in Biomedical Engineering
in the Graduate College of
The University of Iowa

July 2012

Thesis Supervisor: Professor Eric A. Hoffman

Graduate College
The University of Iowa
Iowa City, Iowa

CERTIFICATE OF APPROVAL

---

PH.D. THESIS

---

This is to certify that the Ph.D. thesis of

Matthew Kyle Fuld

has been approved by the Examining Committee
for the thesis requirement for the Doctor of Philosophy
degree in Biomedical Engineering at the July 2012 graduation.

Thesis Committee: _____
Eric A. Hoffman, Thesis Supervisor

_____
Joseph M. Reinhardt

_____
Brett A. Simon

_____
John D. Newell

_____
Edwin L. Dove

To my mother and father Eileen Claire and Garry Allen Fuld, my sister Dr. Kimberly Beth Fuld, my maternal grandparents Ruth and Richard Gross, and my paternal grandparents Carol and Kurt Fuld…

Almost everything–all external expectations, all pride, all fear of embarrassment or failure–these things just fall away in the face of death, leaving only what is truly important. Remembering that you are going to die is the best way I know to avoid the trap of thinking you have something to lose. You are already naked. There is no reason not to follow your heart.

Stay hungry, stay foolish.

*Stephen Paul Jobs*

There are no mistakes in Lindy Hop (or in life), but variations.

*Frankie Manning*

Here's to the crazy ones. The misfits. The rebels. The troublemakers. The round pegs in the square holes. The ones who see things differently. They're not fond of rules. And they have no respect for the status quo. You can quote them, disagree with them, glorify or vilify them. About the only thing you can't do is ignore them. Because they change things. They push the human race forward. While some may see them as the crazy ones, we see genius. Because the people who are crazy enough to think they can change the world, are the ones who do.

*Apple Inc.*

ACKNOWLEDGMENTS

The road to completing my Ph.D. has been a long and fruitful one, however I never could have completed this journey on my own. I am grateful for all the support and assistance I have received over the years, and have numerous people to thank. I apologize in advance if I forget to mention anyone.

I would like to thank Dr. Eric A. Hoffman, my thesis supervisor, for recognizing my potential and warmly welcoming me into his laboratory. He has been a consistent source of encouragement and guidance over the years, and has even given me a swift kick or two when I have gotten off track and needed to refocus on the problem at hand. With his help I have matured significantly as a researcher and have gained considerable insight into the planning and implementation of scientific research. It has been a privilege working with him and I hope to continue to collaborate with him in the future.

I likely would not be completing a thesis focused on pulmonary physiology if it had not been for Dr. Brett A. Simon, my mentor during my time at Johns Hopkins. I am fortunate that the day I was walking out of an interview with one of his colleagues he pulled me into to his office to chat. When I walked out after about 30 minutes I knew that I wanted to work with him, and that decision paid off. He was a great teacher and an inspiration, and it was through his research that I eventually ended up at the University of Iowa. We had a fantastic group in Brett's lab at JHU including Daniel G. Mulreany, Tim Burman, Drs. R. Blaine Easley, David A. Kaczka, Ana Fernandez-Bustamante, Bryan J. McVerry and David N. Hager. They all played an important role in my early development as a researcher.

I would like to thank Dr. Joseph M. Reinhardt who taught me the ins and outs of medical imaging and image registration in addition to serving as an excellent source of academic guidance during my Ph.D. Also, I would like to thank the remainder of my committee members Dr. Edwin L. Dove and Dr. John D. Newell for their encouragement

and guidance throughout this journey. Thank you to the late Dr. Geoffrey Mclennan, for his guidance during the beginning of my PhD career at Iowa. I will always remember his considerable insight into the clinical/translational perspective of lung imaging as well as his impeccable humor.

I want to like to thank several other faculty and clinical collaborators including Dr. Abhay A. Divekar – Pediatric Cardiology, Dr. Susan E. Hanes – Pediatric Cardiology, Dr. William Lynch – Cardio-Thoracic Surgery, Dr. David Stoltz – Internal Medicine (Pulmonary) and Dr. Jessica C. Sieren – Radiology for all their technical expertise and assistance in many of our projects. I would also like to thank Dr. H. Tom Robertson and Wayne J. E. Lamm for their assistance with the fluorescent microsphere mapping method as well as J. H. Song and Dr. Gary E. Christensen for their assistance performing image registration. I would also like to thank Drs. Kung-Sik Chan and Gideon J. Zamba for their keen insight into statistical analyses. I would like to thank Dr. Merryn Tawhai for our collaboration with her group at the Auckland Bioengineering Institute including her colleagues Dr. Alys Clark, Dr. Jennine Mitchell and Yik Ching Lee. Thank you Dr. Edwin J.R. van Beek your support during your time at Iowa.

My colleagues and co-workers in the Department of Radiology's Iowa Comprehensive Lung Imaging Center (I-CLIC) were significant in many ways, in particular for their friendship, hard work, and understanding throughout the past few years. I would like to specifically thank: Ann M. Thompson for all her behind the scenes work, in particular hunting down Dr. Hoffman when we all needed him; Joanie M. Wilson for her role human subject recruitment, I will miss hearing that enormous laugh; Dr. Junfeng Guo has patiently worked with me over the years, allowing me to request many new features to his software gem (PASS); Keith Brautigam, Nathan E. Burnette and Brian K. Walton for their generous support and always helping me get the latest and greatest computer toys, Heather Baumhauer was crucial in organizing our clinical trials work, dealing with all the IND and FDA paperwork, and was always ready to listen when

I needed to talk to someone; Janice Cook-Granroth meticulously organized all our animal protocols without which I would never have gotten my experiments completed, John H. Morgan for helping with experiments and always being ready to pull out the soldering iron, Liz Minard and Jered P. Sieren for operating the scanners and cooperating with our lengthy experiments; Drs. Youbing Yin (CFD & Image Registration), Ahmed F. Halaweish (MRI), Sara K. Alford (Blood Flow), and Dragos M. Vasilescu (Micro-CT); graduate students Randall W. Grout, Krishna S. Iyer, Olga A Kravchuck, Sean D. Mobberley and Samantha Hansen.

I would also like to thank Siemens Medical Solutions for their continuous support that enabled projects like external lung volume control and optimization of dual-energy CT protocols; specifically I would like to mention Christoph Panknin, Drs. Osama I. Saba, Andrew N. Primak and Bernhard Krauss. Thank you to the staff at VIDA Diagnostics for their work and support of Pulmonary Workstation & Apollo.

I would also like to thank my friends Michael & Eve Brafford, Kate Jochum, Erin Taylor, Laurie Mathena and the rest of my swing dancing friends from Baltimore, Iowa City and beyond. You were all a wonderful outlet for me during my Ph.D. providing much needed distractions from life as a graduate student and were always a source of much needed encouragement.

Special thanks to my partner in crime Ashley Dau for being such a good friend to me these past few years, opening up her heart and treating me as part of her family. I have loved our time together and genuinely look forward to our future.

I am sincerely grateful for the love and support of my parents Eileen and Garry, my sister Kimberly and all of extended family. You were constantly encouraging me and I feel honored to have received so much praise. Thanks to my mom and dad for always making sure I remembered to try and learn at least one thing new everyday. Thanks to my sister for being a consistent nudge in my side reminding me to always work hard and push to get things done.

ABSTRACT

Pulmonary diseases are characterized by small-scale and large-scale alterations in structure and function of the lung. Multidetector-row computed tomography (MDCT) is a powerful tool for quantitatively assessing small-scale lung structure including parenchymal destruction, air trapping and airway remodeling. When combined with novel imaging techniques and contrast agents, measuring small-scale regional ventilation ($r\dot{V}_A$) and perfusion ($r\dot{Q}$) also becomes possible. This thesis focuses on developing and evaluating MDCT-based tools for measuring regional lung function in animal models and transitioning them to studying humans.

Wash-in xenon-CT $r\dot{V}_A$ measurements acquired in an animal model were validated with inhaled fluorescent microspheres (FMS), an invasive but recognized gold standard. Xenon-CT correlated well with FMS, demonstrating similar gradients in prone and supine postures. Small-scale $r\dot{V}_A$ measurements from xenon-CT were less susceptible to partial voluming and resulted in reduced scatter.

To facilitate the measurement of regional structure and function on awake-free-breathing humans, we developed systems for lung volume standardization during scanning for both static and dynamic breathing. Anesthetic properties dictated using 30% rather than 55% xenon-gas, reducing signal-to-noise ratio. This reduction, in addition to the influence of free breathing, made xenon-CT more susceptible to noise and required additional post-processing to bolster confidence in $r\dot{V}_A$ measurements acquired in humans. Improvements to the available curve-fit algorithms were made and 4D image registration was developed to align time-series datasets.

Applying these techniques, we compared $r\dot{V}_A$ between normal never-smokers (NS), normal smokers (SNI), normal smokers with early signs of centrilobular emphysema not evident by PFTs (SCE) and smokers with COPD. There was increased heterogeneity in SNI versus NS and time constants were lengthened in COPD and in

SCE. This is consistent with our earlier hypothesis that while patchy inflammation will occur in all smokers, only a subset of the population with decreased $r\dot{Q}$ in regions of inflammation stemming from a failure to block HPV will be susceptible to emphysema.

In order to facilitate translation into the clinical research environment, we established dual-energy-CT (DECT) methods to replace more elaborate time-series laboratory-centered techniques. Xe-DECT $r\dot{V}_A$ measures were optimized through a series of phantom and animal studies to determine the proper three-material decomposition parameters, imaging parameters, gas mixture and delivery protocol. DECT perfused blood volume was validated as a surrogate for $r\dot{Q}$ in animal studies in which blood flow patterns were altered by increasing lung inflation or occluding a portion of the pulmonary vasculature.

To examine the intricacy of lung function, the effects of disease, and provide insight into their etiology we must study gas-exchange on a small-scale. MDCT-based techniques provide the spatial resolution necessary to examine $r\dot{V}_A$ and $r\dot{Q}$ on a small-scale offering an avenue to identify novel phenotypes that may not only yield insights into disease processes but also may provide tools leading to drug and device developments, outcomes assessment and ultimately to the selection of subpopulations suitable for a particular intervention.

TABLE OF CONTENTS

LIST OF TABLES

LIST OF FIGURES

LIST OF EQUATIONS

# CHAPTER 1: MOTIVATION AND AIMS

It is basic human nature to seek out knowledge and understanding of the world around us. According to Frank Herbert, "The beginning of knowledge is the discovery of something we do not understand." When it comes to understanding the human body, despite decades of modern science alongside hundreds of years of early investigation, there is much we do not understand and we are left with just as many questions as we have answers. In particular, the lung is an astonishingly complex organ with a range of functions including the critically important function of respiration; capturing oxygen from ambient air and removing carbon dioxide waste generated by the body.

The process of physiologic respiration is composed of two major components; ventilation ($\dot{V}_A$), the bulk flow movement of gases through the conducting air spaces to the alveoli and back out again, and perfusion ($\dot{Q}$), the movement of blood through the lungs enabling the exchange of oxygen and carbon dioxide. The study of pulmonary physiology is a field with a long history of research and discovery. Work in the modern era includes the groundbreaking work by Ewald Weibel studying the morphometry of the human lung (1,2) as John B. West lead the charge to understand the mechanisms of lung function (3) including the relationship between ventilation and perfusion. To better understand normal function and the effects that disease processes have on the lungs, the examination of small-scale regional function becomes essential. Many techniques have been developed to assess ventilation and perfusion, however most have either been limited to global whole lung measurements (4-9) or are exceedingly invasive (10-13). Therefore the primary goals of this work are to engineer a minimally invasive approach for the assessment of the basic regional function of the lung: ventilation-perfusion matching. A motivation for this engineering effort is to gain a better understanding of the etiology of parenchymal destruction (centrilobular emphysema) associated with smoking-derived COPD.

The ability to image small-scale regional function has finally become a reality with the advent of modern thin-slice multidetector-row computed tomography (MDCT) scanners. Not only can these new scanners show impressive structural detail, in ~1 $mm^3$ isotropic voxels, but when they are combined with contrast agents they can also elucidate function in fine detail. Spatial resolution is critical when investigating subtle changes in lung structure and function related to the initial stages of the disease process. Prior techniques have poor spatial resolution limiting their ability to provide new insights into pathological processes occurring at the interface to gas-exchange (4-9). New MDCT-based techniques offer a potential avenue to identify novel phenotypes that may not only yield insights into disease processes but also may provide the tools leading to drug and device developments, outcomes assessment and ultimately to the selection of subpopulations suitable for a particular intervention.

In our laboratory, it has been hypothesized that smoking-associated centrilobular emphysema, a disease characterized by regional alveolar destruction, is caused by an inability to regulate hypoxic pulmonary vasoconstriction (HPV) on a local level resulting in the inability to resolve inflammation (14,15). A core premise to this hypothesis is that there is an initial heterogeneous pattern of ventilation due to very regionalized alveolar flooding resulting from patchy inflammation. While we believe that patchy inflammation will occur in all smoking subjects, there is a subset of the population in which perfusion will be decreased because of a failure to block HPV. While we have demonstrated the increased heterogeneity of perfusion in normal smokers susceptible to emphysema this thesis is aimed at the development and validation of imaging methods to assess regional ventilation and to test the hypothesis that ventilation in normal smokers is more heterogeneous than normal never-smokers.

In order to examine this idea, it is necessary to systematically develop tools to adequately control the conditions under which subjects are scanned so that we can acquire measures of regional structure and function on awake-free-breathing humans.

Post-processing methods facilitating image analysis must then be developed to optimize the images to allow for the quantification of regional lung structure accompanied by functional measures of regional ventilation and perfusion. We will use these imaging methods to compare differences in regional ventilation between disease-free never-smokers with those from smokers with "normal" pulmonary function tests, in order to understand subtle physiological differences that potentially precede noticeable disease.

Unfortunately, some groundbreaking techniques offer solid ground truth measurements at the price of being overly complex-to-perform. This has the potential of preventing them from ever leaving a laboratory setting. Our goal is to establish some of these more ground truth methods, such as wash-in xenon-MDCT (xenon-CT), for use with human subjects so that they can then serve as a comparator for less complicated methods. Multispectral CT assessment of regional ventilation and perfused blood volume (PBV) is such a method offering decreased complexity. In this thesis we adapt the wash-in xenon-CT method for human subjects, develop dual-energy imaging techniques for measuring regional ventilation and perfusion, and use these tools to perform some initial comparisons of regional ventilation measures in human subjects laying the groundwork for future multi-center studies.

In Chapter 2, we present relevant background material to provide a foundation in which this body of work can be understood in the proper context. We begin with background and current knowledge regarding pulmonary structure and function with a focus on ventilation ($r\dot{V}_A$), perfusion ($r\dot{Q}$) and $\dot{V}_A/\dot{Q}$ heterogeneity. This leads to a brief discussion regarding lung volume control and the role it plays in quantitative imaging, followed by a discussion of medical imaging methods, predominantly the development and limitations of X-ray computed tomography. This leads to the final topic in the background review, a discussion of functional MDCT including recent developments in multi-spectral imaging.

The first aim of this work is to validate the use of dynamic, respiratory-gated wash-in xenon-CT ventilation imaging and evaluate its suitability for the determination of regional pulmonary ventilation and ventilation parameters. These studies serve as a platform to evaluate tools and techniques intended for use with human subjects. The xenon-CT validation was accomplished through a comparison with fluorescent microsphere (FMS), a previously established gold standard, by correlating regional ventilation measurements from both techniques (Chapter 3). A series of experiments in a swine model were performed to obtain both FMS and MDCT ventilation measurements and demonstrated good correlation between methods. In order to compare the two techniques, image registration techniques were utilized to match MDCT-based regional ventilation measurements to FMS regional ventilation measurements at the FMS resolution level of 1.9 $cm^3$. Comparison of mean values, coefficients of variation, vertical gradients and correlations were obtained on regular and normalized data and serve to emphasize the effect that normalization can have on one's interpretation of lung physiology.

MDCT has emerged as a tool for quantitative assessment of parenchymal destruction, air trapping (density metrics) and airway remodeling (metrics relating airway wall and lumen geometry) in chronic obstructive pulmonary disease (COPD) and asthma (16-23). Critical to the accuracy and interpretability of these MDCT-derived metrics is the assurance that the lungs are scanned during a breath-hold at a standardized volume.

The dynamic wash-in xenon-CT method has proven to be a powerful tool in animal studies for a reliable assessment of regional ventilation (24-27). During these studies the animals were anesthetized and mechanically ventilated therefore the anesthetic properties of xenon did not hinder efforts to scan at a repeatable set of respiratory pauses as xenon gas was washed into and out of the lungs. The challenge for human subjects arose from the fact that subjects must be awake and freely breathing. This necessitates using a lower concentration of xenon gas and identifying repeatable

pause points in sequential respiratory cycles when axial scans can be acquired. Maintaining a consistent end-expiratory lung volume can be difficult even without the extra hurdle of anesthetic effects of xenon (28-30). Thus the xenon-CT technique requires considerable development to overcome the limitations essential to scanning human subjects, including increased safety requirements and adaptation of the method for use during spontaneous breathing. The first step in this process was to develop tools and techniques for reliably controlling the lung volume of awake, spontaneously breathing human subjects that are suitable for both static breath-hold imaging and the wash-in xenon-CT method (Chapter 4).

Lung volume control systems play a critical role in the accuracy of quantitative imaging especially in conjunction with methods based on time-series imaging. Unfortunately, no method for controlling the lung volume in awake, spontaneously breathing human subjects will be without limitations. The spirometric-based methods presented in this thesis are limited by the compliance of human subjects to maintain an adequate seal of the respiratory circuit such that all of their respiratory effort can be monitored. In order for the wash-in xenon-CT method to tolerate the resultant variations in end-expiratory lung volume from imperfections in lung volume control as well as subtle image movement due to subject movement and cardiogenic motion, a system for time-series image registration was developed. The Image Segmentation & Registration Tool Kit (ITK) provides a robust environment for prototyping and developing registration workflows (31). The thesis utilizes ITK to speed the development process of an image registration workflow aimed at properly registering the phases of a 4-dimensional wash-in xenon-CT dataset, thereby reducing misalignment artifacts caused by cardiac and subject motion as well as the subtle variations in lung volume between breaths (Chapter 5).

Once the technical challenges of lung volume control and time-series image registration have been solved, we further refine the practical procedures during imaging

and the analysis process. We use animal studies to determine the proper image acquisition timing, along with testing improvements to post-processing algorithms to allow for better quantitative discrimination between subject populations.

With the imaging and analysis protocols for wash-in xenon-CT method established, we can begin to test our hypothesis that ventilation is more heterogeneous in normal smokers compared with normal never-smokers, providing evidence for heterogeneously impaired gas delivery associated with the heterogeneously impaired blood flow observed in smokers susceptible to centrilobular emphysema (14). We use the wash-in xenon-CT method in a 44-subject subset (23 Males / 21 Females, 34 Normal Never-smokers, 7 Normal Smokers; 3 COPD; Age (years): min=20, max=73, median=31.5; BMI: min=17.9, max=32.7, median=25.1) of an ongoing effort to establish a normative lung atlas. We start by demonstrating the suitability of the wash-in xenon-CT for detecting variations in regional ventilation patterns not evident by pulmonary function, followed by demonstrating differences between normal never-smokers and normal smokers (Chapter 6).

Clinical feasibility is an essential component for any diagnostic technique. Dynamic time-series-based methodologies provide ground truth assessment of regional lung function comparable to previously established gold standards; however, the complexity in performing them in a clinical setting is a barrier to large-scale applications. Advances in multi-spectral imaging, particularly dual-energy CT (DECT), provide the opportunity for the development of new imaging-based metrics of lung function that are considerably less complex to obtain than their time-series measurements counterparts.

Utilizing dual-energy imaging simplifies the acquisition of regional ventilation in human subjects. The challenge is to understand how single breath measures of xenon distribution relate to more established ventilation measures, such as wash-in xenon-CT. In Chapter 7 we present and validate techniques for obtaining dual-energy-based metrics of regional pulmonary ventilation, we develop and test dual-energy xenon-CT three-

material decomposition calibration parameters, optimize DECT imaging protocols, and determine the optimum protocol and gas mixture for single breath xenon inhalation studies.

Similarly in Chapter 8, we compare dynamic time-series ECG-gated pulmonary blood flow measurements (CT-PBF) with dual-energy metric of pulmonary blood volume (CT-PBV). A series of experiments in two swine models of pulmonary perfusion heterogeneity were performed in which regional pulmonary blood flow was assessed with CT-PBF and CT-PBV. Anatomical regions were matched and the normalized mean values of CT-PBF and CT-PBV along with their associated coefficients of variation were compared demonstrating the suitability of dual-energy CT-PBV as a surrogate for dynamic CT-PBF.

The work represented in this thesis lays a foundation for functional CT imaging of the lung and comparison of small-scale regional lung function between normal and diseased populations. The importance of this work lies in the establishment of imaging tools for characterizing regional differences in lung function that can be readily translated into large multi-center clinical trials. In combination with the developmental aspects of the presented work, the differences in regional ventilation patterns between normal smokers and never-smokers showing a more heterogeneous pattern of regional ventilation time constants in normal smokers is step in the right direction, helping to confirm our hypothesis that an initial heterogeneous pattern of ventilation, due to very regionalized alveolar flooding resulting from patchy inflammation, does in fact occur. The combination of both ventilation and perfusion dual-energy techniques will allow for larger clinical studies related to obtaining a better understanding of the developmental process of COPD.

# CHAPTER 2: BACKGROUND

## 2.1 Pulmonary Structure and Function

The lung is a complex and versatile organ responsible for a variety of functions necessary for life including operating as a blood reservoir and filtration system, a cushioned insulator for the heart, as well as facilitating the pH balance of blood. However, the most crucial function of the lungs is extracting oxygen from inspired air and eliminating carbon dioxide waste generated by the body. This process, dubbed physiologic respiration, is composed of two major components: ventilation ($\dot{V}_A$), the bulk flow of gases through the conducting air spaces to the alveoli and back out again, and perfusion ($\dot{Q}$), the movement of blood through the lungs enabling the exchange of oxygen and carbon dioxide at the air-blood interfaces within the terminal, acinar, units of the lung. Both ventilation and perfusion are critical, and are linked to the imaging efforts that are the topic of this thesis.

The study and discussion of pulmonary ventilation requires an appreciation of some underlying concepts and terminology. The lung is comprised of approximately 300 million air-filled sacs known as alveoli. It is within the alveoli that the majority of the gas-exchange process occurs. Alveoli are grouped together at the end of a long bifurcating series of conducting tubes known as the bronchial tree. A simplified graphical representation of the bifurcating bronchial tree is shown in Figure 1. As we breathe, inspired air enters from the mouth and/or nose and continues through the trachea, the largest and upper-most section of the airway tree. Past the trachea, the conducting bronchial tree splits into the right and left main bronchi. Humans, for the most part, have a bifurcating airway branching pattern that results in a fairly equal splitting of a parent bronchial segment into two smaller child bronchial segments. While deviations do occur, especially in the presence of genetic abnormalities, this is the general airway branching pattern up until approximately the $16^{th}$ airway generation. As the airway generation

increases, the corresponding airway diameter decreases. These main conducting airway segments do not directly contribute to the process of gas-exchange, except to a minor extent whereby gas-exchange occurs within the bronchial circulation. Based on this distinction, the volume occupied by these airways is often referred to as the anatomic dead space. Beyond the conducting bronchioles, at approximately the 16th airway generation, alveoli start appearing within what is know as the respiratory bronchioles until, at the terminal respiratory bronchiole there is a large outcropping of alveoli along which is known as alveolar ducts. The unit beyond the terminal respiratory bronchiole is known as an acinus. Acinar structures typically arise at approximately the 23rd airway tree generation and beyond. Due to the intricate structure of the dividing tree, the space occupied in the volume of the lung is mainly comprised of alveoli rather that conducting airways, thus maximizing the area available for gas-exchange to occur. Furthermore, the human lungs are actually a pair of structures somewhat separated by the positioning of the heart between the lungs. Overall, they are sectioned into 5 distinct lobes by a series of fissures yielding three lobes on the right and two on the left.

### 2.1.1 Pulmonary Ventilation ($r\dot{V}_A$)

During inspiration, air is drawn into the lungs from the environment because of an expansion of the thoracic cavity that causes a negative surface pressure (pleural pressure) on the lung. Lung expansion is generated through a combination of diaphragmatic contraction, causing the diaphragm, and thus the lung, to descend caudally, and action of the intercostal muscles, which raise the ribs. A mixture of bulk flow through the conducting airways and diffusion in the peripheral airways combines to move gas into and out of the gas-exchange regions of the lungs. A common set of terminology is used to describe the various states of lung inflation. During normal dynamic steady-state breathing, the amount of air moved in and out per breath is referred to as tidal volume ($V_T$). Upon relaxation of the diaphragm and intercostal muscles at the end of a normal

breath, the lung is in a relatively relaxed state (outward recoil of the chest wall balances inward recoil of the lung). The volume of the lung in this state is dubbed functional residual capacity (FRC). At FRC, the lungs are not completely empty, and they can be forced to empty further through forced contraction of the chest wall and diaphragmatic muscles until no further volume change is possible because of airway closure. At this state, the remaining volume of gas in the lung is known as residual volume (RV). The amount of air required to bring the lung from RV to TLC is known as the vital capacity (VC). The level of lung inflation is an important factor that must be considered when performing measurements of pulmonary structure and function. This is especially important for imaging methods such as multidetector-row computed tomography that assesses the lung by linking X-ray attenuation with structure and function. Small changes in volume cause appreciable changes in lung parenchymal density thus altering X-ray attenuation and change the dimensions of the bronchial tree. Furthermore, a given volume of gas inhaled from RV versus some higher lung volume will result in differences in relative regional volume changes. When inhalation occurs from RV, the initial volume of gas preferentially is distributed to the non-dependent (upper most) lung regions which an inhalation of gas from a lung volume above FRC will result in greater regional ventilation in the dependent lung region. This is because at RV, there is a certain amount of surface force on the lung required simple to overcome airway closure while at higher lung volumes, the non-dependent lung has reached it's non-compliant limits and thus a greater change in regional volume is seen in the dependent lung. The inspiratory volume changes at which these differences in ventilation occur scale with lung size / vital capacity and thus significant care must be taken when examining a given subject such that data can be compared between subjects and within a subject across time. This topic will be discussed in depth in Chapter 4.

Traditional measures of lung volumes that require the inclusion of RV (gas left in the lung after a full expiration), such as FRC, are obtained by performing helium dilution,

or by using a body plethysmograph and utilizing Boyle's Law (32). Measurements of VC and $V_T$ can be directly measured using spirometry-based techniques. Once FRC is determined using one of the above methods, values for TLC and RV can be determined by connecting RV (or FRC) volume with additional spirometric results. The low solubility of helium in the body makes the dilution method possible. If respiratory gas is contained in a closed system, the overall amount of helium in the system will remain constant. Thus, a simple mass balance can be performed to provide a measurement of FRC after an equilibrium is reached after breathing helium contained in a reservoir as part of a closed circuit (32).

$$V_2 = V_1(C_1 - C_2)/C_2$$

Equation 1. It is possible to determine the volume of the lung at FRC using a mass balance with a helium reservoir while breathing in a closed circuit.

$V_1$: Reservoir Volume, $V_2$: FRC Volume

$C_1$: Original Concentration, $C_2$: Equilibrium Concentration

The body plethysmograph enables the determination of FRC lung volume by utilizing Boyle's Law, which states that pressure multiplied by volume is constant at constant temperature. By measuring the pressure in a subject's mouth, the box, and knowing the volume of the box before and after respiratory effort against a closed mouthpiece, the FRC lung volume can be determined. The rise in box pressure caused by an increase in the subject's lung volume translates into a change in volume of the box.

$$P_1V_1 = P_2V_2 \qquad P_3V_3 = P_4V_4$$
$$P_1V_1 = P_2(V_1 - \Delta V) \qquad P_3V_3 = P_4(V_3 + \Delta V)$$
$$\Delta V = V_1 - \frac{P_1V_1}{P_2} \qquad V_3 = \frac{P_3V_3}{P_4} - \Delta V$$
$$\therefore V_3 = FRC = \frac{P_3V_3}{P_4} - \frac{P_1V_1}{P_2}$$

Equation 2. Measurements of FRC lung volume are also possible by using Boyle's law in conjunction with a body plethysmograph.

Volumes: $V_1$: Box Before, $V_2$: Box After, $V_3$: Lung Before (FRC), $V_4$: Lung After

Pressures: $P_1$: Box Before, $P_2$: Box After, $P_3$: Mouth Before, $P_4$: Mouth Before

Since alveoli are only present beyond the ~16th generation in the respiratory zone, inspired gas residing within the conducting airways (generations 0 through ~15) does not contribute to gas-exchange. This volume can be measured using Fowler's method (Figure 2). Fowler's method includes measuring the concentration of nitrogen at the mouth in addition to exhaled breath volume following a single inspiration of 100% oxygen. By plotting the percent nitrogen against exhaled volume as the subject exhales, the volume of anatomic dead space can be determined. The nitrogen concentration in the exhaled gas is initially zero due to the exhalation of pure dead space gas filled with pure oxygen. The concentration then rises as exhaled gas is derived from alveoli. The rise in nitrogen concentration eventually reaches a plateau that represents the concentration of nitrogen contained in pure alveolar gas. The volume of the anatomic dead space is then determined by placing a vertical line on the plot such that the area below the curve on the left and above the curve on the right is equal. The anatomic dead space volume will then be the location of the vertical line on the abscissa.

In addition to dead space located in the conducting airways, there can be additional inspired gas within some alveoli that does not contribute to gas-exchange due to insufficient blood flow in their capillary beds. This wasted gas volume when combined with the anatomic dead space is known as physiologic dead space, and can also be measured. Bohr's method uses the partial pressure of $CO_2$ in both the expired gas and in arterial blood circulation for the calculation.

$$V_D = V_T \frac{P_{aCO_2} - P_{ECO_2}}{P_{aCO_2}}$$

Equation 3. Physiologic dead-space can be determined using Bohr's method.

$V_D$: Physiologic Dead Space Volume, $V_T$: Tidal Volume

$P_{aCO2}$: Arterial $CO_2$, $P_{ECO2}$: Expired $CO_2$

In addition to the volume of gas within the lung, the relative distribution fresh gas exchange relative to the elative distribution of perfusion is an obviously important question relevant to both normal and pathophysiological processes. As mentioned earlier, it is the matching of ventilation and perfusion that brings about the exchange of $O_2$ and $CO_2$. Multiple techniques exist for measuring ventilation including body plethysmography (assessing global lung function) and methods assessing increasingly more regional physiology including nitrogen washout tests (33-36), the multiple inert gas elimination technique (37-41) radiation scintigraphy (42-47), single emission computed tomography (48-51) and positive emission tomography (52,53), etc. It is important to recognize that the manner in which these techniques measure ventilation influences their results considerably. Each technique must be considered separately and interpreted with

respect to any limitations or assumptions inherent in the measurement. Regardless of whether a method measures global whole lung aspects of ventilation or examines it on a regional level, care must be taken to keep results in the proper context. We will discuss a variety of measurement methods for examining regional ventilation ($r\dot{V}_A$), the change in volume per unit resting volume of a region. All of the above mentioned methods global or regional ventilation at a scale much larger than an acinus.

Techniques for measuring regional ventilation have provided insight into the behavior of the lungs in health and disease. Past findings demonstrate that ventilation is posture and positional dependent due to the structure of the thoracic cavity and airway tree (54). Also, information regarding pleural pressure gradients, weight of the perfused lung, weight and positioning of the heart and the dynamics of gas flow in a bifurcating airway tree have been shown to affect the distribution of inspired gas in the lungs (55,56). Within a normal lung, ventilation has been shown to be higher in the basal and gravity dependent regions of the lung (8,43,57,58) (Figure 3). These regions generally have smaller resting lung volumes and require lower inspiratory pressures to cause expansion compared to regions in apical and non-dependent areas of the lung. This is the likely significant cause for their higher relative ventilation. In addition, it has been demonstrated that ventilation has an almost linear relationship with height (9,26,32,43,47,59-61). Further discussion of ventilation patterns will be included with the various techniques described in this thesis, but as a general rule the regional ventilation is highly heterogeneous likely to a point beyond has currently been measured with available techniques. We will use a variety of different techniques in this thesis to provide additional insight into regional ventilation.

### 2.1.2 Pulmonary Perfusion ($r\dot{Q}$)

Similar to the intricate structure of the airway tree, vessels in the lungs form a complex series of branching tubes that facilitate the movement of blood. Beginning with

the main pulmonary artery, blood travels down the arterial side of the pulmonary vasculature, closely following the branching patterns of the airways. Upon reaching the level of the alveoli, blood vessels diverge into large capillary beds situated within the alveolar walls. Capillaries are densely distributed along and juxtaposed with the alveolar walls such that they form an almost a continuous sheet of blood for gas-exchange with the alveolar space and the structure of the alveoli and capillary bed are designed so as to maximize surface area for gas-exchange. Weibel has likened the surface area for gas-exchange within the human lung to the approximate surface area of a standard tennis court (2). Upon exiting the capillary bed, blood converges more succinctly into the pulmonary veins and returns back to the heart for the distribution of oxygenated blood throughout the body (32).

Blood flow in the lung periphery, referred to as pulmonary or parenchymal perfusion, is governed by a variety of factors. Thus, similar to the process of understanding ventilation, general knowledge will aid the discussion of pulmonary perfusion as well as place the interpretation of their measurements in the proper context. Similar to the effects of lung volume on regional ventilation, relative distribution of blood volume and perfusion is altered with lung volumes and body postures, again making the standardization of lung volume at the time of imaging critical.

Similar to the global measures provided by the pulmonary function test, Fick's principle can be used to measure total pulmonary blood flow ($\dot{Q}$) by utilizing measures of expired oxygen concentration ($\dot{V}_{O_2}$) as well as the concentration of oxygen in arterial ($Ca_{O_2}$) and mixed venous blood ($C_{\bar{v}O_2}$). It can be an important tool in the global measurement of perfusion. Fick's principle states that the $O_2$ consumption per minute is equal to the amount of $O_2$ taken up by the blood in the lungs per minute (32). Functional imaging measures use a variety of techniques to measure blood flow some of which will be described in more detail below.

$$\dot{Q} = \frac{\dot{V}_{O_2}}{Ca_{O_2} - C_{\bar{v}O_2}}$$

Equation 4. Total pulmonary blood flow measure with Fick's principle.

Similar to ventilation, the distribution of blood flow throughout the lungs is a complex process that results in a significant amount of regional heterogeneity. It has been shown that blood flow in the lungs is greatly influenced by subject posture and vessel branching anatomy. Even more so than ventilation, gravitational forces have a considerable impact on blood flow. In a normal lung it causes strong vertical gradient from gravitationally non-dependent to dependent regions. When a human is positioned upright, blood flow becomes higher in the basal regions of the lung. However, if instead they are suspended inverted, blood flow will shift away from the base of the lung and shift towards the apex instead (Figure 4). Exercise has also been shown to have an impact blood flow distribution, usually by increasing flow throughout the lung (32).

A common way to describe the different regions of perfusion in the lungs is to use the "West" zones of the lung as shown in Figure 5 (32,60,62-64). Idea was originally described by Permutt (65) and later proven through experimentation by West (62). They yield a convenient way to discuss different ventilation perfusion relationships present throughout the lung.

In Zone 1, pulmonary artery pressure is less than alveolar pressure thus creating a scenario in which capillaries are squashed flat, resulting in no flow. This increases the amount of alveolar dead-space in the lung, by increasing the amount of lung with ventilation but no perfusion. These regions therefore do not contribute to gas-exchange. Zone 1 occurs when blood pressures are insufficient to drive blood to the top of the lung, and can occur in case of severe disease or as a result of hemorrhage. In addition, the

application of extreme pressures in the alveolar spaces from the use of extreme positive end-expiratory pressures ventilation (PEEP) can also result in Zone 1 effects further increasing dead-space. Zone 2 is characterized by venous pressure and alveolar pressures that are both less than pulmonary artery pressure. Blood flow in this scenario is governed by the difference between arterial and alveolar pressures as opposed to the normal arterial venous difference present in Zone 3. A Starling resistor can be used to model flow in Zone 2. If you place a flexible tube inside a rigid chamber, and apply pressure in the chamber (alveolar) that is greater than downstream pressure (venous), flow will become restricted. Zone 3 is the normal scenario in the lung in which alveolar pressures are less than venous pressures, which is also less than pulmonary artery pressures. Flow in Zone 3 is thus governed by the traditional arterial venous pressure difference. At low lung volumes, extra-alveolar vessels are less expanded causing their resistance to blood flow to increase. This increase in resistance causes a corresponding reduction in blood flow described as Zone 4. Finally, in some cases of dysfunction and disease, it is possible for blood to enter the arterial system without having first gone through adequately ventilated regions of the lung resulting in a phenomenon known as shunt (1,62).

### 2.1.3 Ventilation / Perfusion Ratio ($\dot{V}_A/\dot{Q}$)

Heterogeneity in the distributions of $\dot{V}_A$ and $\dot{Q}$ are quite complex when considered alone. Their distributions vary with posture, position, and in the face of disease. This complexity further increases when you couple $\dot{V}_A$ and $\dot{Q}$ together as the ventilation-perfusion ratio ($\dot{V}_A/\dot{Q}$), making it even more challenging to measure and interpret. The human body has developed a number of mechanisms to naturally maximize the exchange of $O_2$ and $CO_2$ in the lungs by matching the local rates of $\dot{V}_A$ and $\dot{Q}$. As the correlation of $\dot{V}_A$ and $\dot{Q}$ decreases, so does overall gas-exchange; this is especially evident in disease where normal flow patterns are greatly altered (Figure 6, right panel).

In normal subjects, ventilation and perfusion increase from top to bottom in the upright human lung. Compared to ventilation, the increase in perfusion follows a more rapid progression resulting in a gradient in $\dot{V}_A/\dot{Q}$ ratio that decreases down the length of the lung. In each alveolus, gas-exchange is determined by the relative amounts of $\dot{V}_A$ and $\dot{Q}$ present. Typical values for $\dot{V}_A/\dot{Q}$ in a normal lung fall into a relatively narrow range with a unimodal distribution centered around 1 (Figure 6, left panel). The lowest $\dot{V}_A/\dot{Q}$ is shunt represented by perfused but non-ventilated alveoli ($\dot{V}_A/\dot{Q} = 0$) while the highest $\dot{V}_A/\dot{Q}$ is pure dead-space, represented by ventilated but unperfused alveoli ($\dot{V}_A/\dot{Q} = \infty$). Assessing $\dot{V}_A/\dot{Q}$ is used to gain insight and understanding into the body's physiological response to stress and disease. The ability to measure $\dot{V}_A/\dot{Q}$ has been one of the primary driving forces in development of functional lung imaging. The ability to accurately and repeatedly measure $\dot{V}_A/\dot{Q}$ in a straightforward manner would be an important tool that would enable physicians to track disease progression, treatment and potentially emerge as a way to detect early indications of disease development.

Significant study of the patterns of $\dot{V}_A$, $\dot{Q}$ and $\dot{V}_A/\dot{Q}$ have been conducted over the years by examining of normal function and disease (9,38,66-68). The ability to detect alterations from established normal patterns is a key component in the diagnosis of disease and monitoring treatment regimens (Figure 6, right panel). This can only be accomplished through careful study, using tools and techniques designed to accurately measure function. Many techniques have been developed with the goal of assessing $\dot{V}_A$ and $\dot{Q}$. These techniques include radioactive gas scintigraphy and the Multiple Inert Gas Elimination Technique (MIGET). Unfortunately, these techniques yield either global whole lung (MIGET) or large-scale measurements derived from limited numbers of external detectors (scintigraphy). In addition, they are often too complex and invasive for routine clinical use. These limitations yield information predominantly based on large-scale function, and it is likely that small-scale patterns of heterogeneity in $\dot{V}_A$ and $\dot{Q}$ are missed. Though they are limited in resolution, radioactive gas scintigraphy and the

MIGET are considered gold standards for the measurement of $\dot{V}_A$, $\dot{Q}$ and $\dot{V}_A/\dot{Q}$ and have been used to provide much of our current understanding of function in the normal lung (9,38,66-68).

Newer nuclear medicine techniques using radioisotopes including Single Photon Emission Computed Tomography (SPECT) and Positron Emission Tomography (PET) have improved upon scintigraphy considerably, but still have relatively low spatial resolution (~1 $cm^3$) when compared to the size of the functional units being studied (69). Hyperpolarized Noble Gas Magnetic Resonance Imaging (HP MRI) has emerged as a non-ionizing alternative, and theoretically provides methods (Apparent Diffusion Coefficient: ADC) that interrogate the size of air spaces at the respiratory bronchiolar and acinar level (70-74). HP MRI is still in the early stages of true quantification and suffers from limited availability of noble gas supplies (75) and the need for specialized polarization equipment and MR equipment upgrades providing broad-band capabilities. A key limitation of MR is that the measures are in isolation of anatomic detail provided by modern MDCT imaging.

There are methods that have been developed to interrogate regional lung function which have no place in human research because of the invasiveness of the methods but have proven useful in animal studies. These include the delivery of radionuclide or fluorescently labeled microspheres (FMS) through inhalation or injection. This method requires the removal and regional dissection of the lungs to derive functional measurements. They also include a technique incorporating the implantation of rigid parenchymal markers to monitor tissue deformation. X-ray MDCT remains the most promising tool available for studying small-scale regional changes in $\dot{V}_A$ and $\dot{Q}$ due to its high spatial and temporal resolution and because of the tools that we have been involved in developing which allow for function as well a structural assessment of the lung (24). Techniques utilizing X-ray MDCT will be described in detail later in this chapter.

## 2.2 The Necessity of Lung Volume Control

MDCT has emerged as a tool for assessing parenchymal destruction, air trapping and airway remodeling in chronic obstructive pulmonary disease (COPD) and asthma (16-18). Critical to the accuracy and interpretability of these MDCT-derived measures is the assurance that the lungs are scanned during a breath-hold at a standardized volume. Large multi center trials have determined specific thresholds for emphysema-like tissue (< -950 HU) in an inspiratory scan and air trapping (< -856 HU) in an expiratory scan that can be used as potential imaging biomarkers (Figure 7) (16,19-23). The challenge is that these values can only be relied upon as a standard biomarker if they consistently represent the same phenomenon. Therefore the manner in which scans are acquired must also be consistent for their underlying measurements to be reliable. This is where using the appropriate lung volume control and coaching procedures becomes critically important. For example, if the disease progression of an asthma patient is to be followed by examining changes in the amount of air trapping over time, lung volume at the time of imaging becomes very important. If during an initial scan the subject only partially exhales to a lung volume somewhere in between FRC and TLC (Figure 8), the test would indicate a high amount of air trapping. However, if during their next scan they exhale more completely and accurately achieve FRC, the results from these scans would create the illusion that their treatment regimen was working due to an apparent decrease in the amount of measured air trapping. However, due to the difference in lung volume between scans, there is no reliable way to determine whether they are truly improving. The only way to be prevent this type of scenario is to accurately control lung volume during image acquisition (76).

## 2.3 Medical Imaging

In the discipline of biomedical engineering, one must decide specifically what measurements are required to answer a particular question, determine what one is

actually able to measure, and finally decide how this information will ultimately help improve our understanding of the question at hand. The purpose of developing new measurement tools to assess regional lung structure and function is to establish "normal" and to understand the etiology of the pathologic process which leads to specific smokers acquiring chronic obstructive lung disease (COPD) or specifically, centrilobular emphysema. The goal is to also develop a set of tools that will generalize to a much broader set of pulmonary diseases.

While complicated methodologies have important roles to play in limited environments, ideally tools should be designed so as to have only the amount of complexity as is necessary so as to be broadly deployable and outputs which are minimally complex to interpret. To that end, one must start by fully characterizing new tools when they are developed in order to properly understand what they measure. There is a need to first determine what is "normal" before one can describe changes that occur during disease. Imaging provides an indispensible tool for non-invasively assessing the underlying structure and function of the human body, which is comprised of a wide range of materials and tissue types including blood, fat, muscle, bone, and in the lungs, a significant amount of air. It can help us assess this diversity in composition and function, and can provide significant insight into the changes caused as a result of disease processes.

The keystone discovery leading to MDCT used in this thesis was the discovery of X-ray itself in 1895 by Wilhelm Conrad Röntgen (77). The first radiograph created using X-rays was of the hand of Röntgen's wife's (Figure 9). In 1901, Röntgen was awarded the first Nobel Prize in Physics for this important achievement. Devices that generated X-rays were widely available for recreational purposes and were used outside the realm of medicine before the dangers of ionizing radiation was identified. The technique of radiography works by using an X-ray tube containing an anode and cathode. The high-energy negatively cathode shoots a beam of electrons at very high speeds towards the

positively charged tungsten anode. When the electrons collide with the anode, there is an upward shift in the energy level of an electron within the tungsten atoms. When these electrons fall back to their natural state, high-energy photons are released. It is these photons that are filtered and directed towards a detector, often a film-based camera, that produce the X-ray images.

### 2.3.1 X-ray Computed Tomography

Conventional X-ray projection is somewhat limited by problems of superposition of tissue regions. By taking advantage of the computational power of computers, X-rays can be used to obtain three-dimensional images with a remarkable amount of detail.

The principles of X-ray computed tomography (CT) involve the measurement of X-ray attenuation at multiple projection angles through object utilizing attenuation differences to identify material types. Measuring attenuation from a single projection angle through an object would not yield sufficient information to distinguish the variable density of materials along the path of the single photon. However, by combining information from multiple projection angles and solving a system of simultaneous equations, attenuation coefficients through heterogeneous structures can be determined. Algorithms that can perform these types of image reconstructions are critical to the successful implementation of CT. The development of methods which lead to X-ray CT by Oldendorf (78) Cormick (79) and Hounsfield (80) lead to another Nobel Prize, this time in physiology and medicine in 1979.

CT scanners have gone through a number of design iterations over the last 40 years in order to obtain images more quickly while producing images with greater detail (Figure 10, Figure 11, Figure 12). Early first-generation scanners used a “pencil-like” beam of X-rays that traveled across to a single detector on the opposite side of the object. Through a combination of translation and rotation, the source and detector were moved around the object in order to obtain projection data. Second generation scanners also

employed translation and rotation methods, however instead of a "pencil-like" X-ray source, they projected a fan beam across multiple detectors to acquire data more quickly. Third generation scanners used wider-angle fan beams and a larger detector arrays in order to remove the need for translation. Fourth generation scanners employ a ring of stationary detectors and utilize an X-ray source that rotates around the object. Third generation scanners are currently the most common.

Early generation scanners required lengthy acquisition times to image large portions of the body, likely a barrier to more common usage. In an effort to shorten acquisition times, a variety of techniques were developed. The most significant was the development of spiral acquisition CT scanning modes. In spiral mode, the source is constantly spun around an object while the table moves through the detector ring. Initially, the number of times that an X-ray source could be rotated around an object had physical limitations that were related to the length of high-voltage cable providing power to the X-ray source. This limitation made it necessary to stop the rotation of the X-ray source and switch directions increasing scan times significantly. The advent of "slip-ring" technology in late 1980's allowed for unrestricted rotation of the X-ray source finally making spiral-scanning modes practical (81,82).

Beyond the traditional $1^{st}$ – $4^{th}$ generation CT scanners two other types have been developed, though their use has primarily been for scientific study rather than widespread clinical usage. These scanners are the Electron Beam CT (EBCT) scanner and the Dynamic Spatial Reconstructor (DSR) depicted in Figure 11 and Figure 12 respectively. Both scanners took new approaches to CT imaging diverging from the common idea of using a single X-ray source and associated detector setup. Both scanners were designed to increase temporal resolution in an effort to more accurately capture function.

The EBCT scanner incorporates a design based on sweeping an electron beam across a hemi-cylindrical anode target surrounding the patient. As electrons strike the tungsten anode, X-rays are produced and transmitted through the object. These X-rays

are then measured by a stationary array of solid-state detectors on the opposite side. Scan times were approximately 50 to 100 msec when the high temporal resolution mode was used. Short scan times enable the acquisition of stop action images of the heart minimizing artifacts from cardiac motion on the lung parenchyma. In addition, the short scan times can be sacrificed to provide a high spatial resolution mode. EBCT scanners produced images similarly to those of fourth generation scanners, differing mainly in how X-rays are generated and directed at the subject. These scanners are no longer in production.

The DSR was developed in the early mid to late 1970's with early prototypes pre-dating commercial CT. It was designed specifically for measuring function of the heart, lungs and the circulatory system (83-85). The DSR's unique design allowed it to capture a volume instead of just a singe slice with very high spatial and temporal resolution. It represented a unique milestone in technology for dynamic volumetric physiologic imaging. The DSR was able to capture images very quickly allowing for true stop action imaging of the heart and lungs. A key limitation of the DSR in the mid to late 1970's was the fact that computer technologies could not handle the computational requirements needed to reconstruct or analyze the image data fast enough to allow the system to be used for anything more than very basic physiologic research. The DSR's main distinction in terms of design was the use of multiple X-ray tubes; most modern generation CT systems use only one X-ray tube that spins around the subject. Recent MDCT scanners have now incorporated two X-ray tubes for dual-energy imaging and for imaging at faster speeds. Rotation speeds currently are on the order of one rotation per 0.25 sec. The DSR's rotatable gantry was lined with multiple cone beam X-ray tubes and was paired with low-light-level high-contrast video cameras on the opposite sides of the gantry. This allowed for the rapid acquisition of X-ray projection data from which multiple transverse cross sections could be reconstructed. The subject was placed within the bore of the gantry inside a stationary radiolucent tunnel composed of 2-mm carbon

filament and positioned on a radiolucent table. The system employed a number of then state-of-the-art technologies in order to handle the high data throughput created by so many X-ray tube-camera pairs (84).

By utilizing the high temporal resolution of the DSR, the concept of indicator dilution was taken to a whole new level. Instead of simply looking at pre- and post-images, 60 images-per-second could be acquired enabling the assessment of regional time-series density change. From this information, average flow in a vessel can be calculated and compared to its downstream branches. One of the most exciting advances from the DSR was the ability to observe the spatial distribution of the dynamics of blood flow distribution at high-speed. Even though 30 years have passed since the use of the DSR, today's fastest scanners can only obtain images every 75 to 100 msec, 1/6 of the speed of the DSR in 1980. In addition to blood flow, pulmonary ventilation was evaluated by examining the change in parenchymal density cause by lung expansion. High spatial-resolution density profiles were generated using the DSR in order to examine the of the distortion and redistribution of lung parenchyma at various states of inflation and postures (54).

A substantial amount of effort has been invested in increasing the speed of CT scanners, improving image quality and spatial resolution, while at the same time minimizing patient risk. As CT scanners have continued to evolve, advancements in volumetric coverage and temporal resolution have been achieved. The latest scanners are able to either cover the majority of the lung in either one rotation or can lower scan apertures to ~75 msec. Furthermore, new scanners are being developed that incorporate multiple X-ray tubes that can either be tuned to different photons energies to exploit attenuation differences between materials, or they can be set to the same energy level and further reduce acquisition times by reducing the degree of tube rotation necessary to acquire multiple angles of view.

MDCT scanners utilize the principles of X-ray attenuation to non-invasively determine the density of materials within the imaging field of view thereby allowing the characterization of the various material components that comprise the lung. As the density of a material increases, the amount of X-ray photons blocked or absorbed also increases. Using the Hounsfield unit (HU) scale for calibrating CT attenuation air becomes -1000 HU, water 0 HU, tissue ~60 HU and bone varies between 400 and 2000+ HU (80,86). The HU scale between air and water is linear, therefore an increase in the amount of air in the lungs (decrease in tissue density) can be observed in a straightforward manner (86). CT imaging is a widely available and routinely used imaging modality in the developed world for assessing lung structure in fine detail. Today's modern MDCT scanners have significantly shorter acquisition times and lower radiation doses than previous versions and are frequently improved through enhancements in spatial and temporal resolution. When these scanners are coupled with contrast agents, multiple X-ray sources and a variety of image gating techniques, MDCT scanners also become a powerful tool for assessing lung function in addition to its underlying structure.

## 2.4 Functional MDCT

### 2.4.1 Contrast Enhanced Imaging

While MDCT scanners have become advanced significantly since their original development, their underlying principle remains the same: measuring X-ray attenuation to identify material composition. Certain materials, known as contrast agents, can be used to temporarily alter the density of materials within the body and provide an avenue for of using density-based imaging techniques to measure function. Since X-ray attenuation is principally defined by material density, functional MDCT contrast agents are materials that alter regional density. One of the contrast agents currently available for examining ventilation is $^{131}$Xe gas (24,87,88). While the radioactive isotope $^{133}$Xe was

used extensively to measure ventilation and perfusion using external scintillation detectors by following the emissions from $^{133}$Xe as it traveled through the pulmonary system (43,45,62,62,89-93), $^{131}$Xe alters the air space density as it replaces lighter resident gases. In addition to xenon, there are a variety of other radio-dense contrast agents suitable for MDCT including krypton and iodine. Other medical imaging technologies incorporate a wide variety of contrast agents to measure function.

### 2.4.2 Wash-in xenon-CT

The advent of higher resolution CT technologies in the late 1970's / early 1980's allowed researchers to exploit the higher radiodensity of $^{131}$Xe gas as compared to room air and use it as a contrast agent for wash-in (WI) and wash-out (WO) ventilation studies (94,95). The density enhancement resulting from the inhalation of xenon gas depends on both the concentration of gas as well as the kilovolt (kVp) settings of the scanner. Lower kVp settings yielding greater CT attenuations (~2.24 HU ↑ / %Xe @ 80 kV) (96,97). According to Kety, "The kinetics of an inert, insoluble gas such as xenon can be approximated in the lung by a continuous model" (93). Therefore, if one assumes a constant input gas concentration and minimal diffusion of the gas through lung-blood barrier, the wash-in and clearance of alveoli can be exponentially characterized as shown in Figure 13. By performing these studies at a constant lung volume, the ventilation rate constant K is directly proportional to $\dot{V}/V$ (volume-normalized ventilation).

Using the WI-WO methods pioneered by Kety, Gur et al. performed a series of studies on anesthetized mechanically ventilated sheep using $^{131}$Xe-CT (95). Subjects breathed in an 80% $^{131}$Xe mixture from closed circuit system for 2 to 6 minutes with images being acquired at 30 to 60 second intervals during WI. Once equilibrated, the inspired gas source was changed to room air and scanning continued until the xenon gas completely washed out. Each scan acquisition required 10 seconds to complete and yielded a 512 x 512 image using 10 mm collimation. Care was taken to ensure that scan

acquisitions were performed during a consistent portion of the respiratory cycle in order to minimize lung inflation differences between scans. In addition to utilizing the lung contour, preselected anatomic markers were used to verify positioning between scans. Lung volume control continues to be a challenge when using this method to assess regional ventilation in both human and animal models. There have been substantial efforts to develop appropriate respiratory gating methods necessary to overcome this challenge (98-103). These efforts include work performed in the thesis described in Chapter 4 (98). Gur's study was a significant leap in the assessment of ventilation on a regional level and provided important insights related to volume control, contrast agents and tissue characterization.

Ideas presented by Gur created a strong foundation that has been built upon for the last 3 decades (24,26,27,97,104-110). Some of the additional studies performed since Gur's experiments include examining various details of the xenon-CT method including differences between WI and WO time constants as well as characterizing the effect of xenon absorption and reperfusion (105,111). An example time intensity curve that is achieved using the xenon-CT method is presented in Figure 14. Kreck et al. presented a variation to the Kety model that described four-compartment model for use in $^{131}$Xe-CT that attempted to address the inaccurate insolubility assumption in the single exponential model. This model also has the added benefit of measuring $\dot{V}_A$ and $\dot{Q}$ simultaneously with CT. By measuring the rise in density within a pulmonary artery resulting from the absorption of $^{131}$Xe gas, regional perfusion could be quantified (111). Kreck asserted that the absorbed $^{131}$Xe during WI would circulate and re-evolve back into airspace altering WI measurements. However, it has since been shown that a 4-compartment model is likely unnecessary since dissolved $^{131}$Xe does not readily escape back into airspaces and only minimally affects CT density in the lung (105). Simon et al. used a Monte Carlo approach to test the repeatability and accuracy of the xenon-CT measurements and determined how small variations in the measurement would impact the overall result

(108). Simon suggested that the WI-WO model would yield the most accurate results since coverage of the steep density change region would be the greatest (108). This assertion would likely be the best approach if $^{131}$Xe did not alter the dynamics of flow, however findings by Chon et al. regarding the differences between WI and WO time constants indicate that a combined model should be considered with caution WI and WO techniques both have unique advantages. WI studies require less xenon gas, which is very expensive and presents additional risks to the patient. However, using only a WI methodology will create the possibility of not achieving inspired gas equilibrium in poorly ventilated regions, resulting in inaccurate measurements. A WO approach is more sensitive at detecting regions with long time constants and also provides an index of gas volume through a comparison of equilibrium and baseline images. However, the WO approach requires considerably more exposure to xenon gas. Chon et al. demonstrated that $^{131}$Xe concentration was the most significant factor in the differences between WI and WO time constants, and is potentially explained by Raleigh-Taylor instabilities created by washing a heavier gas into a lighter gas and vice versa (25,112,113). Studies using lower concentrations of xenon gas (30%) had greater similarity between WI and WO time constant values, however they suffered from increased noise. Supplementation with 30% krypton yielded improved signal compared to 30% xenon alone and provides an alternative for situations when using >30% xenon is not feasible. Xenon is known to have anesthetic properties in concentrations above 30% that result in disorientation. This would be a considerable barrier when using the xenon-CT method to study spontaneously breathing human subjects (28,30,112,114).

### 2.4.3 Dynamic ECG-Gated Perfusion-CT

The measurement of pulmonary perfusion has been achieved to varying degrees of success using a variety of methods over the years; however, it has been limited to large-scale measurements typically on a lobar-basis or along rough axial gradients. CT-

based methodologies make it possible to observe of the distribution and heterogeneity of blood flow on a much finer scale, thus improving our understanding of blood flow changes on a local level in response to disease processes and medical interventions (115-123).

Hoffman et al. (124) utilized the high temporal and spatial resolution of the EBCT to create high resolutions maps of blood flow in the lung. Using a combination of respiratory control and ECG gating, the entire lung volume could be acquired with high spatial resolution. By making use of the fact that the volume of the lung is most easily and consistently held at FRC, they performed a series of image acquisitions during breath-hold maneuvers in order to capture the entire lung at the highest resolution possible. Subjects inhaled to TLC, exhaled to RV, and then inspired to 50% VC using volume control techniques. A portion of the lung volume would be scanned during each breath-hold. Subjects would be permitted to take a few intervening breaths between scans before imaging resumed following the next breath-hold maneuver to 50% VC. Perfusion measurements were then obtained during an additional breath-hold in which iodinated contrast material was injected into the right ventricular outflow tract in a sharp 2-second bolus. Due to the rapid acquisition necessary to capture the first pass kinetics of the injection, the entire lung could not be simultaneously sampled. Instead images were acquired in pairs as the electron beam swept across the tungsten anodes as a series of six 8 mm cross sections spaced 4 mm apart. ECG gating was used to ensure each image location was acquired during the same portion of the cardiac cycle. Due to image storage limitations at the time, only 13 time points were sampled including 1 obtained pre-injection to establish a baseline. The region of lung scanned was required to include a cross section of the right and left main pulmonary arteries that were necessary to perform blood flow calculations described below.

By adapting methods used for microsphere blood flow analysis and insights from Wolfkiel regarding the movement of a contrast bolus, a series of equations were

developed relating the flow from a feeding pulmonary artery into and out of a region of parenchymal tissue (118).

$$F_i C_i(t) = \frac{dA}{dt} + F_o C_o(t)$$

$$A = C_i * V$$

$$\frac{F_i}{V_p} = \frac{CT_{peak} - CT_{base}}{\int_0^{\infty} CT_{pa}(t)dt}$$

Equation 5. Method for calculating regional blood flow by relating to a reference pulmonary artery.

A = accumulated amount of indicator, C = concentration of indicator in and out

F = flow in and out of the tissue, V = volume of parenchyma

CT = Hounsfield units at the peak, base, and in the feeding artery

Additionally, by utilizing the linear relationship between image intensity and material density they were able to determine the amount of contrast material present from the magnitude of the regional "time-intensity" curve. Using these equations, parenchymal blood flow measurements can be determined by relating the results of a non-linear curve fit of the gamma-variate model applied to a series of time-intensity measurement taken in an area of lung parenchymal to a time-intensity curve derived from the feeding pulmonary artery (120). In order to then express blood flow per gram of

parenchyma, they again utilized the linear nature of the Hounsfield unit scale to separate the "water" component into blood and parenchyma.

Using those equations it was then possible to automate the process to create maps of blood flow for the entire imaged region. In addition to raw blood flow and blood flow normalized to air and tissue, their technique enables them to measure regional tissue, blood and air contents, regional mean transit and arrival times, time to peak, peak opacification, area under the regional time-intensity curve and the associated chi square error value of the non-linear curve fit (120).

During the analysis of data obtained using this technique, Won and Tajik observed a bimodal shape present within the regional time-intensity curves for regions of interest within lung parenchyma. They hypothesized that instead of a bimodal flow profile within the capillary beds themselves, that flow within small arteries and veins in proximity to the capillary beds was also being measured resulting in partial volume artifacts due to the short acquisition times of the EBCT. These partial volume effects influenced the shape of the time-intensity curves giving the false impression of a bimodal distribution within the capillary beds.

$$R(t) = F^{-1}\{R(\omega)\} = F^{-1}\{\frac{Y_{ROI}(\omega)}{X_{PA}(\omega)}\}$$

Equation 6. Using the temporal and spatial resolution of EBCT it is possible to calculate residue curves of capillary bed blood flow using deconvolution.

R = residue intensity, $F^{-1}$ = inverse FFT

Y = parenchymal curve, $X_{PA}$ = feeding pulmonary artery curve

To remove these artifacts, they implemented a refinement in their post-processing methods that utilized frequency domain information within the time-intensity curves to allow for the separation of the two curves. Therefore MTTs could then be calculated for both small arteries and capillary beds separately (121,122). Residue functions were obtained by using a series of deconvolution, algebraic manipulations, and reconvolution resulting in the following equation.

After separation (Figure 15), a decrease in peak amplitude of the arterial residue curves was observed from dependent to nondependent lung regions of animals scanned in the supine posture. However, residue peaks remained consistent across lung regions in the prone posture. This finding is consistent with known lung physiology regarding fewer arterial regions present in the nondependent lung, which becomes less dense and more fully expanded in the supine posture (122). Monte Carlo simulations were performed to determine the robustness of this method considering the inherent noise in CT imaging. Simulation results support the conclusion that image noise does not factor heavily in the measurement of MTT using this method. With the improved spatial resolution of CT-based methodologies these results have not been confirmed due to a lack of an appropriate gold standard in which to measure them against. Experiments utilizing this technique in animals yielded measurements of MTTs on the same magnitude of those previously published using in-vivo microscopy. Vertical gradients were observed in the supine posture, while measurements in the prone posture were flat (Figure 16).

Similar studies conducted in both humans and dogs in the supine posture by Dakin et al. using EBCT highlighted differences in blood flow between the species (123). When normalized to water content, dogs demonstrated a characteristic linear vertical gradient in perfusion, while human subjects showed a relatively uniform flow profile. However, a modest vertical gradient was present in raw blood flow values, highlighting the importance that normalization methods play in our interpretation of physiology.

Additionally, while human subjects demonstrated a drop in blood flow in the most dependent lung regions (Zone 4), dogs did not despite additional compression of the dependent lung due to imaging at FRC in the dogs rather than TLC in humans. These findings indicate that differences in pulmonary branching patterns likely play an important role in the distribution of blood flow.

Until very recently MDCT scanners have been considerably slower than the DSR or EBCT scanners despite their higher spatial resolution. The slower scan speeds prevent using the deconvolution methods for measuring capillary bed MTTs. However, newer scanners, especially those with multiple X-ray tubes, are rapidly decreasing scan times and will soon reach the speeds necessary to reintroduce these methodologies using MDCT.

### 2.4.4 Multi-spectral Imaging

Recent developments in multi-spectral imaging, particularly dual-source dual-energy MDCT, enhance the ability of contrast agents in the pursuit of measuring function (125-130). Second-generation dual-source CT scanners (Somatom Definition Flash: Siemens Medical Systems, Erlangen, Germany) contain two X-ray guns within the rotating gantry; primarily designed to increase temporal resolution by decreasing the extent of X-ray source rotation required to acquire a complete image acquisition (131-133). Fortunately, by having two X-ray guns with adjustable photon energy levels coupled with two sets of detector rows, the possibility of dual-energy scanning becomes feasible. When set at different kVp, two reconstructed images are acquired, one from each X-ray tube, making it possible to perform image-based material decomposition; the process of identifying materials which have an X-ray attenuation shift from one photon energy to another (126,127,131,134). The lungs consist primarily of air, blood and tissue, all of which have very consistent attenuation values over the range kVps available on commercial CT scanners. However, certain contrast agents like xenon, krypton and

iodine have large attenuation shifts that can be exploited to enhance structural measures as well as measure function (112,135,136). If a dual-energy CT (DECT) scan of the lungs is acquired following the administration of a contrast agent that reflects physiologic function, we will be able to extract the signal from that contrast agent using three-material decomposition methods thus enabling the study of regional function.

For example, the distribution of inhaled xenon or krypton gas can be measured, and depending on the method of delivery, it becomes possible to obtain information regarding regional ventilation or structure through DECT imaging (98,135,135,137-142). Similarly, when injected into the pulmonary vasculature, iodine can be extracted using DECT three-material decomposition to provide a measure of perfused blood volume, a potential surrogate for regional perfusion (127,143-150).

## 2.5 Summary

While we would all likely agree that Thomas Jefferson was correct in his assertion that "all men are created equal", when one gets down to the details of the pulmonary vascular and airway trees, the branching structure, while similar, is possibly as individualized as the fingerprint. As discussed in Chapter 1, it has recently been hypothesized that genetic differences in regional vascular response to, for instance inflammation, may serve as the basis for disease etiologies such as smoking associated susceptibility to emphysema in a subset of the population (14,24). Pulmonary arteries have much thinner walls and are exposed to considerably lower perfusion pressures than their systemic counterparts. Because of this, gravitational effects are fairly profound, with vessels considerably more dilated in the dependent vs. non-dependent lung (151-153). Under states of low oxygenation, pulmonary arteries constrict (hypoxic pulmonary vasoconstriction: HPV), thus shunting perfusion to better-ventilated lung regions. In the systemic circulation, if a tissue region is irritated, part of the natural inflammatory response is to dilate the vessels regionally to enhance perfusion so as to promote

resolution of whatever is causing irritation. In the case of the lung, when there is a regional irritation, such as that caused by smoking, regional irritation can cause regional alveolar flooding, regional hypoxia and thus HPV unless a mechanism is in place to block that HPV response. If HPV is not blocked and is in the non-dependent lung region (apex in the upright human) then gravity effects serving to reduce perfusion to the non-dependent lung region and compounded by regional vascular constriction and the inflammatory processes serving to limit the effect of regional tissue irritation and subsequent reparative processes are confounded. If a portion of the population were missing the ability to block HPV in the face of inflammation, this would provide an explanation for why smokers with emphysema show a predilection for the emphysema to concentrate in the apical lung regions. Despite similarities amongst the normal never-smoking population, there is expected to be heterogeneity of regional function. It is thus important to define normal bounds of these newly developed imaging methodologies. Furthermore, if one is to track individuals between interventions or across time, one must establish methods to assure that the desired intervention is the principle driving force leading to the observed temporal changes, thus lung volume at the time of scanning is critical. Finally, if one is to implement these imaging methods at multiple centers and within the context of a clinical imaging environment, the methods must be relatively simple to implement. Thus, more rigorously correct imaging must serve as a gold standard against which to establish the suitability of simplified imaging approaches, such as is done by comparing methodologies using first pass kinetics for perfusion and wash-in methods for ventilation to understand the simplified dual-energy approaches to assessing regional ventilation and perfusion based upon single volume scans.

Thus, the remainder of this thesis is dedicated to the validation of tools for standardizing lung volumes, validating wash-in methods for assessing regional ventilation, translating the xenon-CT method for assessing regional ventilation to humans, establishing alternative single breath dual-energy methods for assessing regional

ventilation and identifying and validating single volume dual-energy methodologies for assessing regional perfusion.

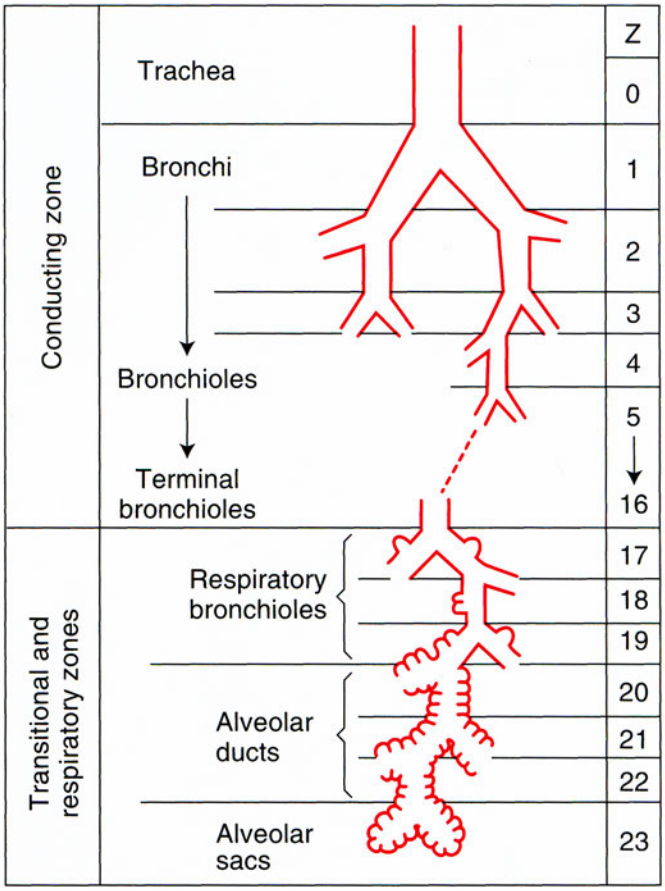


Figure 1. The human airway tree begins with the trachea and splits following a bifurcating pattern down to the level of the alveoli. Gas-exchange occurs from the 17th airway generation and beyond.

Reproduced with permission Figure 1-4 from (32)

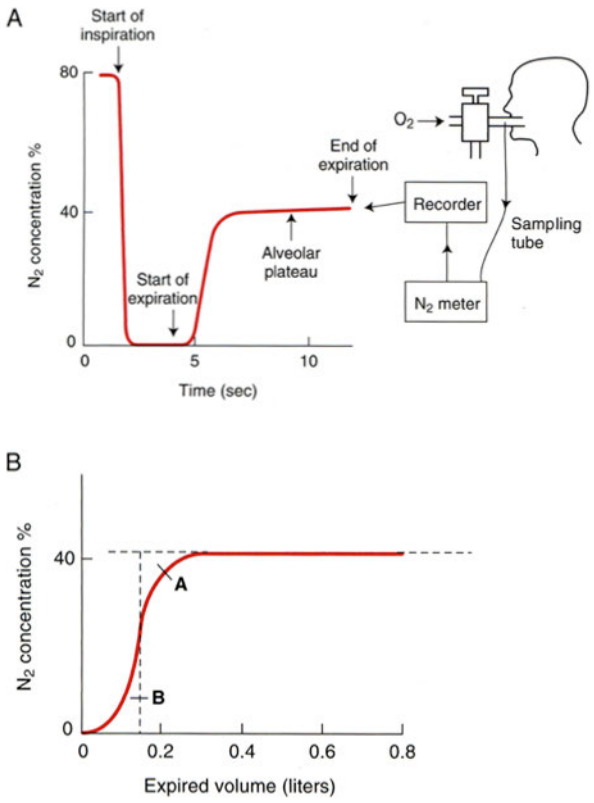


Figure 2. Fowler's method of measuring anatomical dead space by identifying the volume at which the area above the curve is equal to the area below the curve on a plot of exhaled $N_2$ versus expired volume, following a deep inspiration of 100% $O_2$.

Reproduced with permission Figure 2-6 from (32)

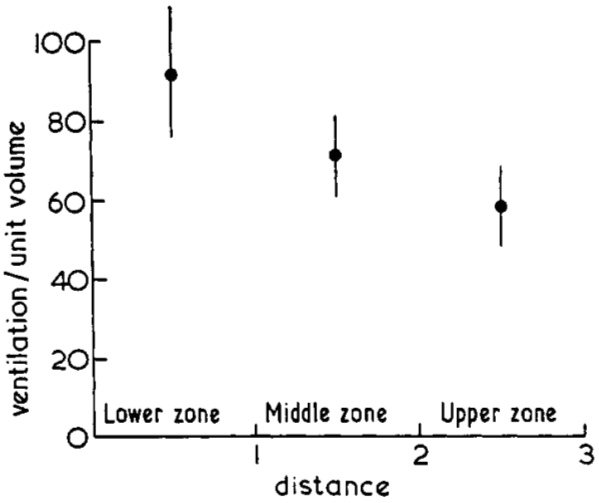


Figure 3. Typical vertical gradients in ventilation in normal subjects measured with radioactive gas scintigraphy.

Reproduced Figure 5 from (60)

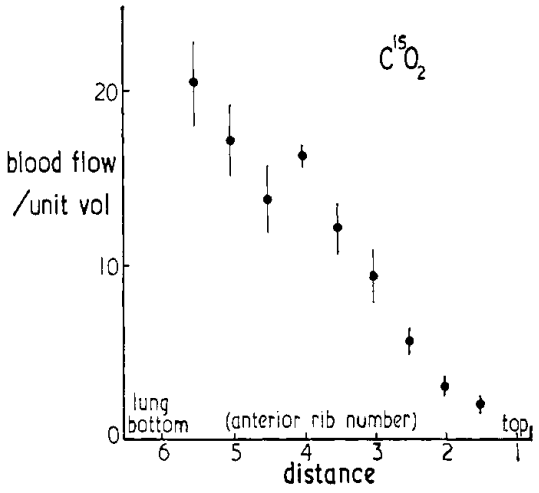


Figure 4. Vertical gradients in blood flow as measured with radioactive gas scintigraphy.

Reproduced Figure 4 from (60)

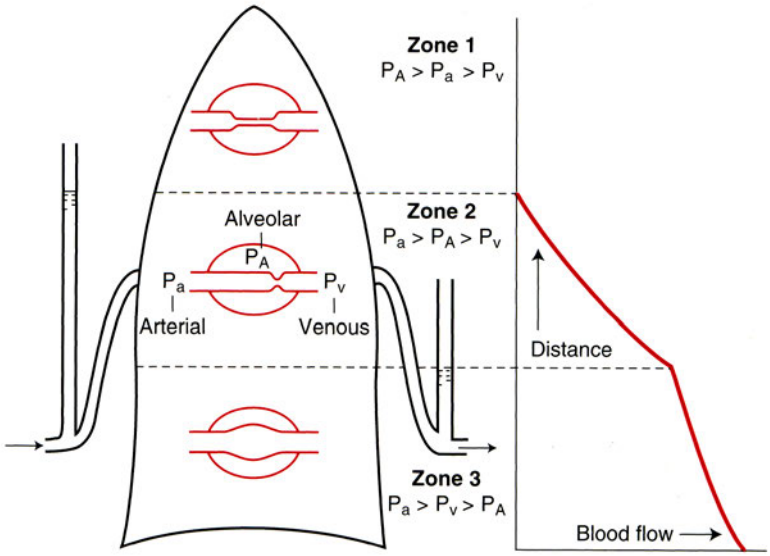


Figure 5. West zones of the lung based on alveolar and pulmonary pressures.

Reproduced with permission from (32,62)

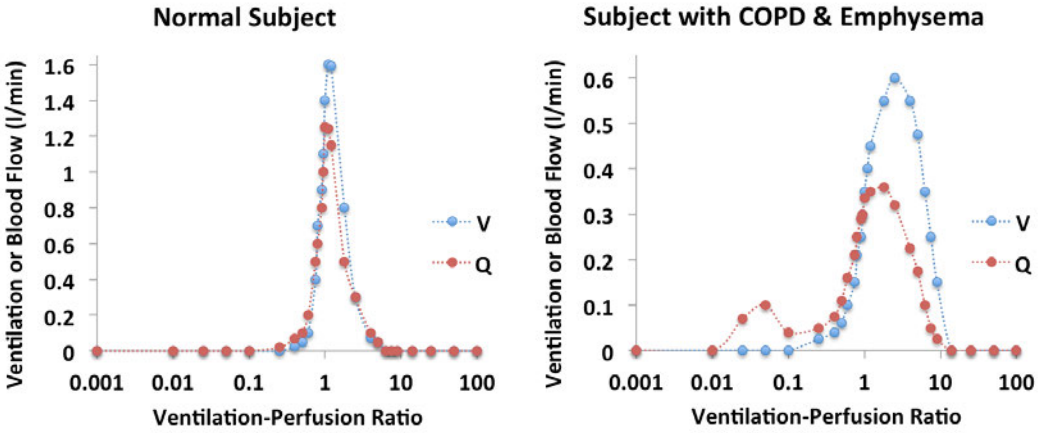


Figure 6. Mock-up example distributions of $\dot{V}_A$, $\dot{Q}$, and $\dot{V}_A/\dot{Q}$ in a normal subject and one with COPD and emphysema.

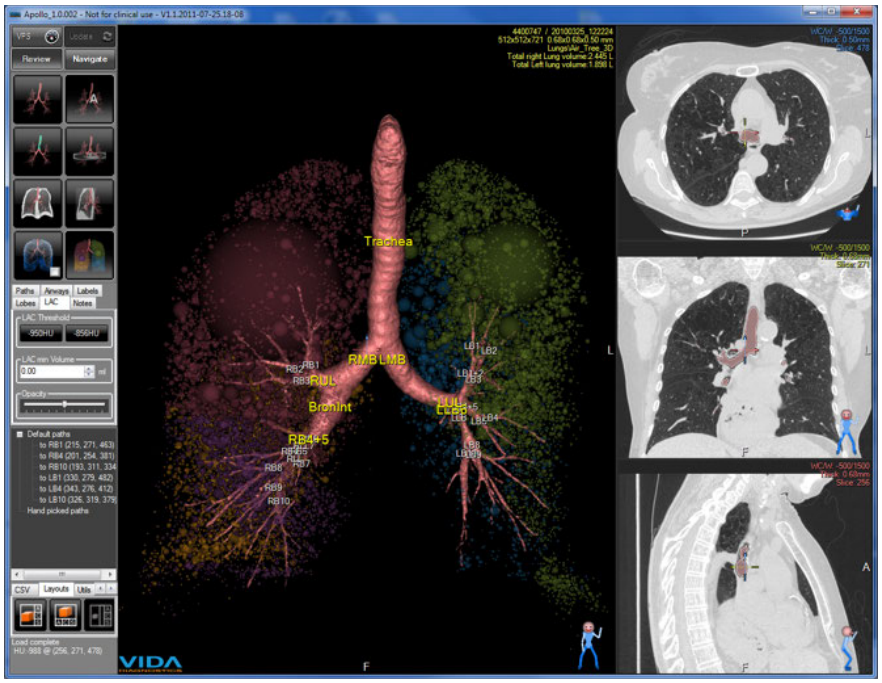


Figure 7. Apollo (VIDA Diagnostics, Coralville, IA) is a pulmonary analysis software tool for assessing the airways and lung parenchymal in a MDCT scan.

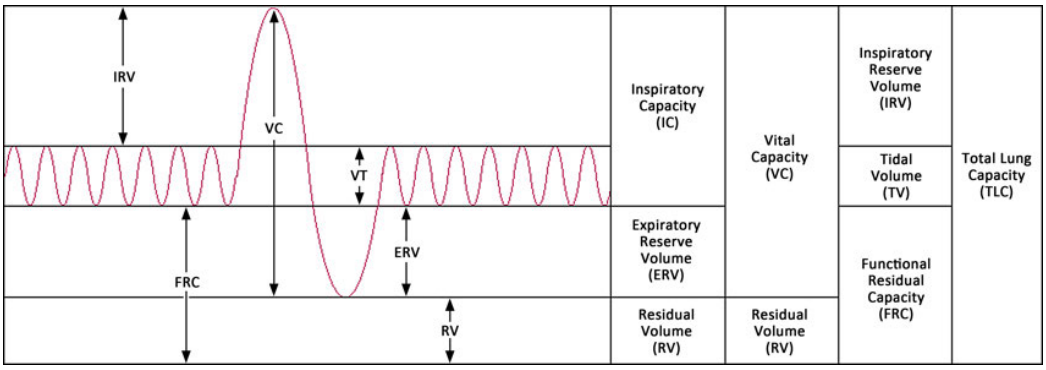


Figure 8. Illustration of lung volume terminology as typically used in discussions of lung physiology and medical imaging.

Figure 9. Radiograph of Röntgen's wife's hand in 1895

Reproduced with permission from (77)

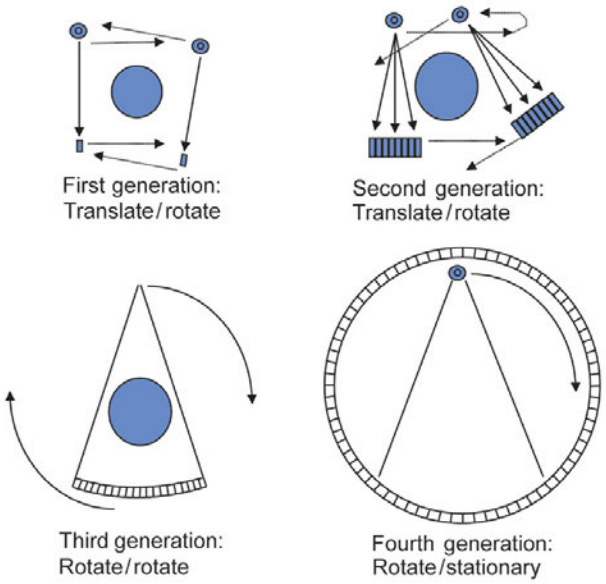


Figure 10. General schematic diagrams of CT scanner generations 1-4.

http://www.medcyclopaedia.com/library/topics/volume_i/c/ct_generation/ct_generation_fig1.aspx

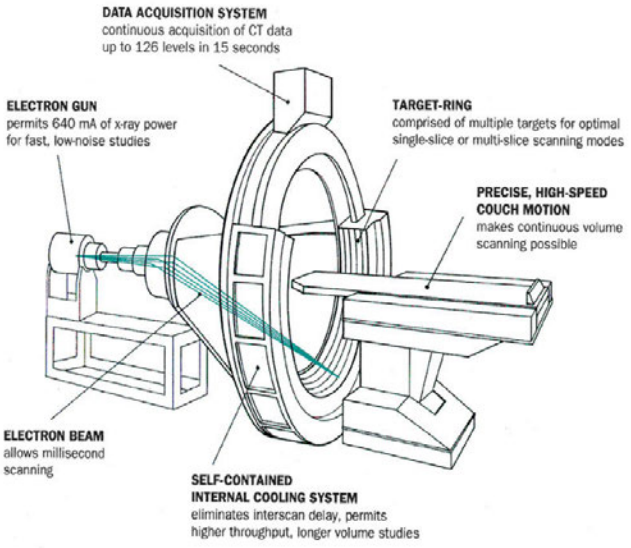


Figure 11. Diagram of the EBCT.

http://www.medcyclopaedia.com/library/topics/volume_i/c/ct_generation/ct_generation_fig1.aspx

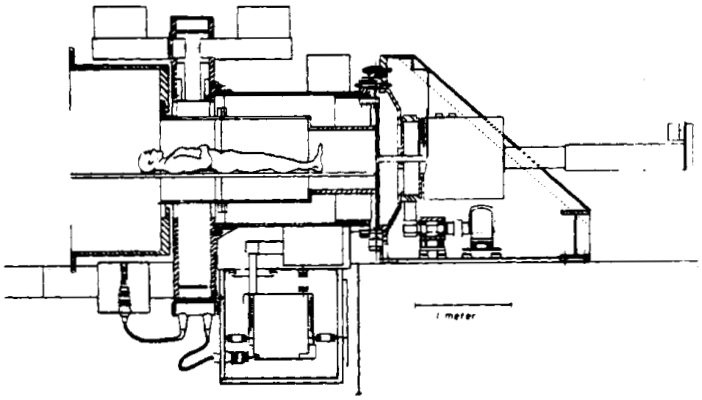


Figure 12. Diagram of the Dynamic Spatial Reconstructor.

Reproduced Figure 6 from (83)

$$C(t) = C_x\left(1 - e^{-Kt}\right)$$

$$K = \frac{1}{T_{mean}}$$

Figure 13. Characteristic equation of an exponential wash-in. $C_x$ = concentration of xenon in lungs at equilibrium; K = ventilation rate constant; $T_{mean}$ = mean transit time

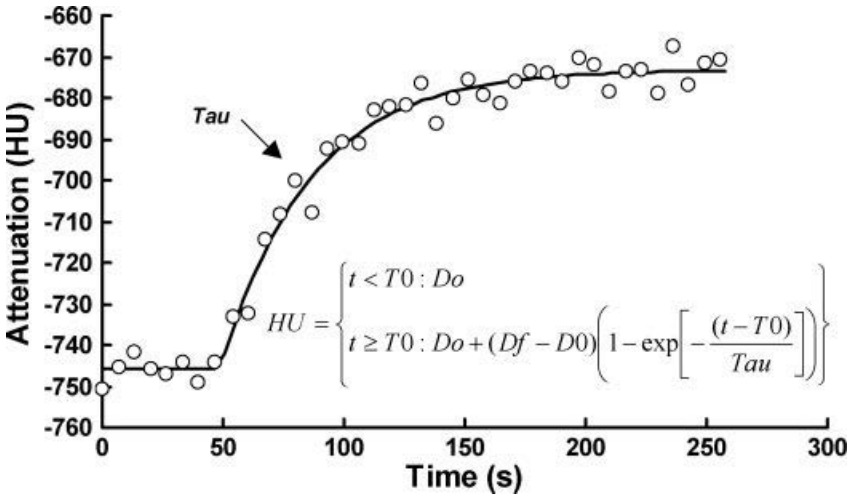


Figure 14. An example time intensity curve from a xenon wash-in. $D_0$ = baseline density; $D_f$ = equilibration density; Tau = time constant

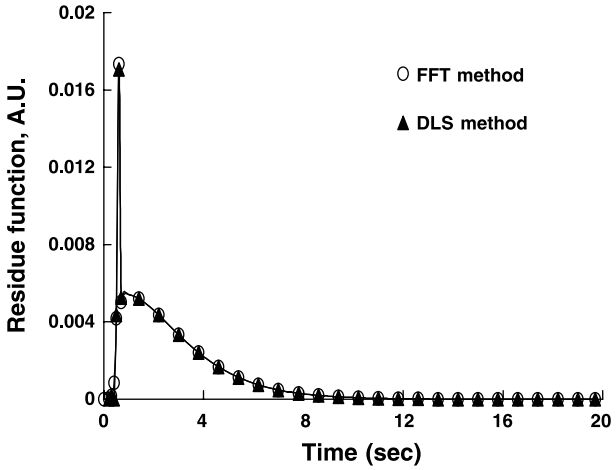


Figure 15. Separation of the capillary blood flow from neighboring arteries and veins.

Reproduced figure 2 from (122)

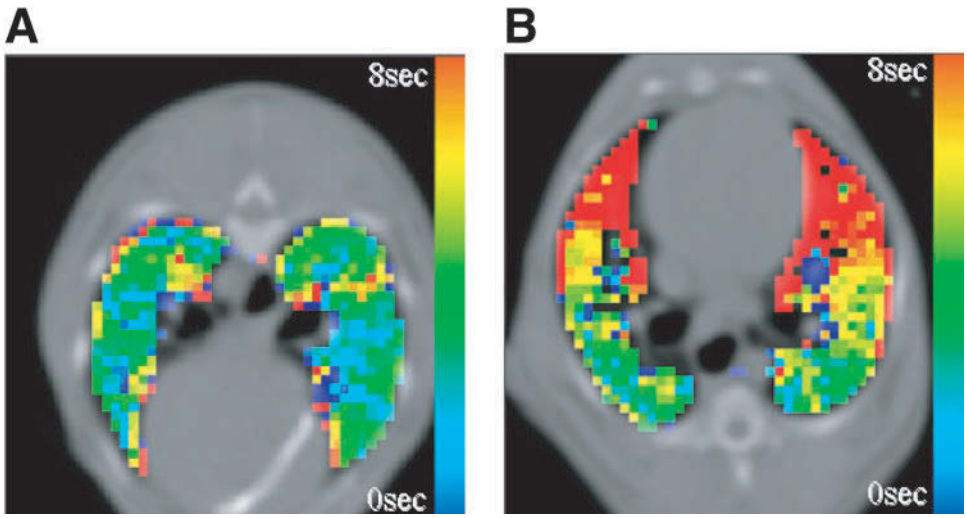


Figure 16. Color maps of MTT in Prone (A) and Supine (B) postures. A vertical gradient is clearly evident supine, while Prone values are highly uniform.

Reproduced figure 7 from (122)

# CHAPTER 3: WASH-IN XENON-CT VALIDATION WITH FLUORESCENT MICROSPHERES

## 3.1 Rationale

A significant advantage of wash-in xenon-CT, and MDCT in general, is the ability to acquire information at a high-resolution enabling greater insight into small-scale structure and function. To validate wash-in xenon-CT measures of regional ventilation ($r\dot{V}_A$) the measures are compared, through a series of physiological manipulations, to inhaled fluorescent-labeled microspheres (FMS). Injectable and aerosolized FMS have been used previously for the measurement of $r\dot{V}_A$ and regional perfusion ($r\dot{Q}$) (10,154,155) to investigate small scale heterogeneities, not detectable through the use of scintillation counting methods (43,46,60,156-158). Functional maps created using FMS have a resolution on the order of ~1.9 $cm^3$ which is a scale larger than that which we think is achievable via xenon-CT, but is the closest to a 'gold-standard" as we have been able to identify. The FMS mapping method measures $r\dot{V}_A$ thru aerosolizing and inhaling microspheres of ~1.0-μm in diameter or injecting microspheres ~15-μm in diameter intravenously to measure $r\dot{Q}$. Following microsphere delivery, the lung is extracted and fixed, systematically cut into pieces, and dissolved to measure the microsphere concentration within each piece. Because xenon-CT assesses the lung in-vivo while FMS methodology estimates in-vivo lung function through lung excision and air drying, an immediate difficulty comes both in the matching of in-vivo to ex-vivo anatomy and in selecting suitable normalization procedures since the lung, ex-vivo is exsanguinated and cleared of tissue fluids. Accounting for these differences when cross-correlating $r\dot{V}_A$ measurements between the methods are addressed in the current work.

To accomplish these comparisons, we match $r\dot{V}_A$ measurements obtained in-vivo using wash-in xenon-CT with inhaled 1-μm fluorescent microsphere (FMS) $r\dot{V}_A$

measurements in swine. By imaging the in-vivo lung and the ex-vivo states of the lung via CT, we are able to link the lung across the experimental protocol.

## 3.2 Methods

### 3.2.1 Animal Preparation

The University of Iowa Animal Care and Use Committee approved all animal studies reported here. Seven anesthetized, intubated, mechanically ventilated farm-raised swine were studied in the prone and supine postures using both inhaled FMS and wash-in xenon-CT. Half of the animals were studied first supine and then prone and the other half were studied in the reverse order. Animals were of either gender and had a mean weight of 19.8 ± 1.0 kg (weight range, 18.6 to 21.8 kg). Animals were pre-medicated with Ketamine (20 mg/kg) and Xylazine (2 mg/kg) intramuscularly, and anesthetized with 3-5% isoflurane in oxygen by nose cone inhalation. Once surgical depth of anesthesia was achieved, an 8.0-mm inner diameter cuffed endotracheal tube was placed through a tracheostomy and the animal was mechanically ventilated with the following ventilation settings: tidal volume of 10-14 mL/kg, rate of 10-20/min adjusted to achieve an end-tidal $PCO_2$ of 30–40 mm Hg, and positive end-expiratory pressure (PEEP) of 7.5-cm $H_20$. Carotid arterial and external jugular venous introducers were placed. A 7-French pigtail catheter (Cook Inc, Bloomington, IN) was advanced into the right ventricle under hemodynamic and fluoroscopic control to enable MDCT $r\dot{Q}$ measurements also performed during this study. Following surgery, the animal was moved to the MDCT scanner suite. Surgical plane of anesthesia was maintained with a continuous infusion of thiopental (20 mg/kg bolus followed by 20 mg/kg/hr) sufficient to prevent spontaneous respiratory effort was utilized for the duration of MDCT scanning and FMS administration. Minute ventilation, rectal temperature, heart rate, ECG signal, arterial pressure, oxygen saturation, and airway pressures were monitored throughout the study.

### 3.2.2 MDCT and FMS Data Acquisition

Imaging was performed on a Siemens Sensation 64 MDCT scanner (Siemens, Erlangen, Germany). For each body posture (prone and supine), measurements occurred in the following sequence: 1) spiral non-contrast volumetric MDCT scans were obtained at two fixed lung volumes, TLC and FRC; 2) axial time-series end-expiratory gated wash-in xenon-CT scans were performed at two contiguous locations along the z-axis (cranial-caudal); 3) aerosolized FMS were administered. The TLC and FRC volumetric scans were obtained during breath-holds at 25 and 7.5 cm $H_20$ respectively. Volumetric scans were performed with the following settings: 100 mA; 120 kV; 1mm pitch; 0.5 sec rotation time; 0.75mm slice thickness; 0.5 mm slice increment; 512 x 512 matrix; 240mm FOV; B31f reconstruction kernel. Voxel dimensions were 0.47 x 0.47 x 0.50 mm. Using the FRC volumetric scan as a guide, the two adjacent cranial-caudal 2.8-cm transverse axial slice stacks were selected such that the first slice of the first stack began just distal to the carina. While not discussed further here, an additional series of images were acquired to assess regional perfusion via CT, and an additional set of fluorescent microspheres (of colors which did not overlap the colors used in the ventilation studies) were delivered to the pulmonary vasculature to tag regional perfusion.

Respiratory end-expiratory-gated axial MDCT images were acquired prior to and during the delivery of radiodense xenon gas. Radiodense xenon gas was introduced into the breathing circuit from a concentration-controlled reservoir (Enhancer 3000, Diversified Diagnostic Products, Houston, TX). The reservoir was attached to a custom dual-Harvard piston-ventilator setup (Harvard Apparatus, Holliston, MA) that was specifically designed for external computer control, allowing for remote switching between room air and an oxygen-xenon mixture. Delivered tidal volumes were matched between both ventilators using a calibrated pneumotachograph (model 3700A, Hans Rudolph, Kansas City, MO). Each series included 10-baseline (room air) and 35-xenon wash-in (55% Xe, 45% $O_2$) breaths. Ventilation imaging parameters were as follows: 150

mA; 80 kV; 0.33 sec rotation time; 512 x 512 matrix; 240mm FOV; and B30f reconstruction kernel. Each imaged volume consisted of 12 slices, with a slice thickness of 2.4mm. Voxel dimensions were 0.47 x 0.47 x 2.4 mm. There was a 5-minute waiting period between scans of the two adjacent regions to allow clearance of xenon gas from the lungs.

Immediately following imaging, 1.0-μm FMS (FluoSpheres, Molecular Probes, Eugene OR) were delivered over a period of 5 minutes via a bag-in-a-box ventilator with an aerosol generation system (155). FMS color pairings for each animal were rotated among six possible color labels. In one animal, in the supine posture, two FMS colors were delivered simultaneously to allow assessment of the repeatability of the microsphere counting used to assess $r\dot{V}_A$. This was performed in the supine posture since there is a greater ventral-dorsal oriented ventilation difference and thus a greater range of $r\dot{V}_A$ is present. We have previously demonstrated repeatability of the wash-in xenon-CT measures (108,112) and thus did not repeat the measures here because of time and expense. Once MDCT images and FMS delivery were completed, the animal's body posture was changed (prone to supine or supine to prone) and MDCT imaging and FMS administration was repeated.

Following the administration of the final pair of FMS labels and MDCT imaging, 5,000 units of heparin, 45 mg of papaverine, and an additional bolus of 25 mg/kg of thiopental were injected intravenously to further anesthetize the animals, allowing the animal to be exsanguinated and flushed with a 2% Dextran solution prior to removal from the thorax and separation from the heart. After excision, the lungs were inflated to 25 cm $H_2O$ airway pressure while Super Glue (Super Glue Corp, Rancho Cucamonga, CA) was used to fix the lobes in their approximate in-vivo anatomic positions. Once positioned, 20-30 punctures of the pleura were made with a 20-gauge needle, and the lungs were air-dried with heated air at 25 cm $H_2O$ pressure for 3 days. The dried lungs were then coated with a ~1-cm thick layer of Kwik Foam (DAP Inc, Dayton OH), and encased in a block

of rapid setting urethane foam (2 lb. polyol and isocyanate, International Sales Corp., Seattle, WA). Spiral non-contrast volumetric images with the same parameters as outlined for the in-vivo scans were performed on the dried lung specimens encased in foam blocks (Figure 17). Keeping the foam block stationery on the table, the resultant MDCT-derived image data was used to identify the table location associated with the carina, and the scanner-positioning laser was used to mark a line around the foam block at this location.

### 3.2.3 FMS Data Analysis

Beginning at the level of the carina, identified from the MDCT-derived images, the lung block was cut into 1.2 cm x 1.2 cm x 1.2 cm (volume: 1.8-$cm^3$) cubes using a rectilinear grid (Figure 18). The spatial coordinates, weight, and lobe of each cut lung piece were recorded. For any cube encompassing two different lobes, the smaller lobe portion was discarded. Pieces were placed in a fixed volume of 2-ethoxyethyl acetate (Cellosolve, Aldrich Chemical, Milwaukee, WI) to extract the fluorescent labels. Once extracted, the fluorescence signals were measured with a fluorescence spectrophotometer (Perkin-Elmer LS50B, Boston, MA), as described previously (12,159) with correction for spillover from adjacent colors in the emission spectrum using a matrix inversion program (160).

### 3.2.4 MDCT Imaging Analysis

Semi-automatic lung segmentation was performed using Pulmonary Analysis Software Suite (PASS) (161). TLC and FRC volumetric scans were analyzed to obtain measures of total lung volume, air volume, non-air volume, mean and standard deviation of HU. The Time Series Image Analysis (TSIA) software (112) incorporated into a module of PASS (161) was used to analyze wash-in xenon-CT datasets to determine $r\dot{V}_A$ by fitting the data points to an exponential model (described in Chapter 2). Voxels from the xenon-CT dataset were binned into 3 x 3 regions of interest (1.4 mm x 1.4 mm x 2.4

mm) resulting in regional data for a 4.7 $mm^3$ volume of lung parenchyma. Data were filtered to remove major airways and vessels using the following criteria: 40 – 90 percent air; mean squared residual < 500; specific ventilation < 7.5. Data were also excluded if the non-linear curve-fitting algorithm could not achieve an appropriate fit. Magnitude of xenon wash-in, percent air (%), time constant of the exponential fit (sec), regional ventilation (ml/min) and specific ventilation (1/sec) were determined for each ROI.

### 3.2.5 Normalization Methods

FMS $r\dot{V}_A$ measurements were normalized by two methods. First, the FMS per-piece fluorescence is divided by the mean fluorescence to provide mean normalized measurements (FMS $r\dot{V}_A$ MEAN). In the second method, $r\dot{V}_A$ was normalized by the product of the mean and weight of the lung piece. This provided weight-normalized $r\dot{V}_A$ measurements (FMS $r\dot{V}_A$ WTNORM). Pieces that predominantly included large conducting airway were excluded. MDCT $r\dot{V}_A$ measurements were normalized in a similar manner to the first FMS normalization method thus yielding mean normalized measurements (MDCT $r\dot{V}_A$ MEAN).

### 3.2.6 MDCT and FMS Data Registration

To compare the datasets at the FMS piece size resolution, MDCT and FMS $r\dot{V}_A$ datasets were registered to obtain coordinate-matched datasets (Figure 19) according the schematic shown in Figure 20. Rigid alignment (translation and rotation only) of the in-vivo xenon-CT datasets with the in-vivo FRC volume scans was performed using the normalized mutual information-based rigid registration algorithm in the Analyze™ software package (Mayo Clinic, Rochester, MN) for the supine and prone postures. The initial phase of the time-series was extracted as the reference slab to be matched against the FRC volume. Thresholding of the image intensities was performed to improve contrast, and the sampling region was limited to the lung boundaries. To properly register the $r\dot{V}_A$ FMS data to the in-vivo FRC coordinate system, a hybrid registration

involving rigid alignment using normalized mutual information and small-deformation inverse consistent linear elastic (SICLE) image registration (162) was performed on the air-dried ex-vivo and the in-vivo volume scans in the prone and supine postures. The SICLE image registration method jointly estimates forward and reverse transformations between two images while minimizing the inverse consistency error (ICE). ICE is defined as the difference between the starting and ending position of a point that is mapped through the forward transformation followed by the reverse transformation. Registration accuracy was quantified by comparing the positions of 10-12 user-selected landmark points placed at branch points of the airway tree in both the ex-vivo and in-vivo FRC volume scans and comparing their locations after registration of the ex-vivo landmarks to the in-vivo coordinate system. Average registration error was calculated for each registration (prone and supine for each animal) by comparing the registration-predicted positions to the user-determined positions.

### 3.2.7 Statistical Analysis

Statistical analyses were performed using SPSS (Windows 17.0, SPSS, Inc; Chicago, IL) and Excel (Microsoft, Redmond, WA). MDCT $r\dot{V}_A$ values within each registered FMS block were averaged to obtain similar resolution levels (~1.9 $cm^3$). Vertical gradients were assessed for each method utilizing data from supine and prone postures via a linear regression with $r\dot{V}_A$ as a function of height (cm) of the in-vivo lung from the dependent to non-dependent lung border. Slope and correlation coefficients were calculated. Paired t-tests were performed to determine if significant differences in vertical gradient exist between the supine versus prone postures. A p-value less than 0.05 were considered significant. Pearson correlation coefficients were calculated between the FMS and MDCT $r\dot{V}_A$ measurements to quantify the similarity of the two methods at the scale of FMC piece size (~1.9 $cm^3$) and by 0.25 cm vertical height sections.

## 3.3 Results

$r\dot{V}_A$ measurements determined using wash-in xenon-CT correlate well with the $r\dot{V}_A$ FMS measurements. Similar spatial and gravitational patterns are observed using both methods in the supine and prone postures (Figure 22, Figure 23, Figure 24). Preliminary analysis of the data showed much better correlation of MDCT $r\dot{V}_A$ measurements with mean + weight normalized FMS data compared to mean normalized FMS data. As shown in Figure 25, FMS data utilizing mean + weight normalization yielded a statistically significant ($p<0.05$, paired samples student t-test) reduction in measurement noise when compared to mean normalized data as measured by the CV (Prone: FMS CV=0.54, FMS-WTNORM CV=0.41; Supine: FMS CV=0.64, FMS-WTNORM CV=0.44) in the first three swine. Because this agrees with previous findings that weight correlated measures correlate with other methods as well (10,119,155,163), the results presented here only include $r\dot{V}_A$ comparisons between MDCT and weight-normalized FMS data. In one animal in the supine posture, FMS measurements were repeated to demonstrate reproducibility of the FMS technique for measuring $r\dot{V}_A$. As seen in Figure 26, there is a strong agreement between the repeated FMS measurements ($R^2$=0.996).

FMS and MDCT $r\dot{V}_A$ measurements were acquired in 6 of the 7 swine, due to a xenon delivery problem in 1 animal. For 2 of the xenon-CT datasets only 1 location was scanned due to a scanner input error (animal 4 prone; animal 2 supine). In addition, 1 set of measurements was excluded because problems with the air-drying process resulted in a poorly inflated and a non-uniformly dried lung (likely due to the presence of pre-existent pneumonia) that was not suitable for image registration or FMS analysis. The remaining 5 animals successfully underwent wash-in xenon-CT, FMS administration, and data processing. Registration was performed for both prone and supine postures; $r\dot{V}_A$ measurements were normalized and compared at FMS resolution (1.9 $cm^3$) and by vertical height (0.25 cm). This resulted in an average of 407 ± 93 FMS-sized ROIs per

data set along with 43 ± 4 vertical height sections. Figure 19 shows representative transverse and coronal slices for wash-in xenon-CT and FMS $r\dot{V}_A$ measurements at their native resolution.

### 3.3.1 Registration Accuracy

Image registration matched in-vivo MDCT $r\dot{V}_A$ measurements to ex-vivo FMS $r\dot{V}_A$ measurements with a fair amount of success in all five animals in both prone and supine postures. As seen in Figure 21, the transverse slice in the ex-vivo lung column, demonstrates that there were some bullae formed during the air drying process. These cause some mismatches in the image registration process. Visually, the registered lung regions seemed better matched the in-vivo scan closer the central airway tree distal the carina and degraded in quality as one moved outward towards the periphery or basal sections of the lung. The image registration utilized a segmentation mask of the right and left main bronchi that improved the results near the lung core. 3D surface renderings of the central airway tree pre (*top row*) and post (*bottom row*) image registration are shown in Figure 27 demonstrating good correspondence between airway tree segmentation masks from the in-vivo FRC (*left column*) and registered ex-vivo lung scans (*right column*). Difference images pre and post registration are also shown (*middle column*). The effectiveness of image registration is further demonstrated by the values for landmark error from each registration summarized in Table 1. The average landmark error was 2.6 ± 0.8 mm and 3.1 ± 1.0 mm for prone and supine position respectively.

### 3.3.2 Volumetric Analysis

The total lung volume and densitometry measurements were obtained for in-vivo FRC, in-vivo TLC, and ex-vivo dried lung data sets are summarized in Table 2. The air-dried lung was less dense (decreased mean lung density HU) and more homogenous (smaller SD) compared to the in-vivo lung volumes. Figure 31 illustrates the similarity of the in-vivo and ex-vivo lungs by comparing a photograph of the ex-vivo air-dried

lungs (*upper-left panel*), a 3D volume rendering (*upper-right panel*), a rendering of vasculature tree and airway trees (*lower-left panel*), and 3D volume rendering with overlay of regional specific ventilation (*bottom-right panel*) obtained from the MDCT in-vivo image data sets at FRC (PEEP of 7.5 cm $H_20$) in the prone position. Volumes of the air-dried lungs corresponded most closely to in-vivo lung volume measurements obtained from lungs at FRC levels of lung inflation rather than TLC as expected. Lung volume measurements from the in-vivo and ex-vivo scans are compared further in Table 1. Mean ex-vivo air-dried lung volumes were 112 ± 8% (range: 102 - 123%) and 107 ± 4% (range: 101 - 112%) of the in-vivo FRC lung volumes in the prone and supine postures respectively. Ex-vivo lung volumes were greater than in-vivo FRC lung volumes for all scans in both postures. Lung volumes in 4 of the 5 lungs in the supine posture were greater than similar measurements prone, and matched more closely with ex-vivo lung volume measurements.

### 3.3.3 CV of MDCT $r\dot{V}_A$ and FMS $r\dot{V}_A$ Measurements

Mean CV measurements with SD error bars for supine and prone postures for each method are shown in Figure 30. Coefficient of variation of $r\dot{V}_A$ was higher in the FMS measurements and in the supine versus prone posture. There were statistically significant differences between CV in the prone and supine postures in both methods (FMS p=0.22; MDCT p=0.009) as well as between FMS and MDCT in the prone and supine postures (Prone p=0.003; Supine p=0.001). There is clear $r\dot{V}_A$ heterogeneity present throughout the lung parenchyma; however, $r\dot{V}_A$ was more homogenous when the pigs were placed in the prone posture.

### 3.3.4 Correlation of MDCT and FMS $r\dot{V}_A$ Measurements

Mean and standard deviation of regional correlations at FMS piece size (1.9 $cm^3$) and by lung height (per 0.25 cm) were obtained to compare the associations between FMS and MDCT $r\dot{V}_A$ measurements and are summarized in Table 3. For the

measurements by lung height, data was grouped the y coordinates into slabs 0.25 cm thick to 40-50 data points per position. Individual correlations from the 5 animals are shown in Figure 28. Correlations strengthened when the analyzed volume was increased from FMS piece size to the vertical slabs, likely because, despite our registration attempts, registration was not perfect and reduction to slabs minimizes mis-registration. The prone data from animal 3 did not correlate well between the two methods well and, if considered an outlier and removed from analysis, mean correlations improve and standard deviations decrease. We present data both ways. Correlations were stronger in the supine position compared with the prone position, as is expected. It is well recognized that there is a stronger ventral-dorsal gradient in the supine posture and thus the wider range of $r\dot{V}_A$'s in the supine posture provide for a stronger correlation between the two methods.

### 3.3.5 Comparison of Vertical Gradients

A simple linear regression model was used to determine the functional gradient with lung height for each method. The slope was determined for the lung region straddling the most non-dependent edge to maximal flow point, with a negative slope indicating a gradient or decrease in ventilation from dependent to non-dependent regions of the lung (Figure 23). The most dependent region of the lung ("zone 4" or atelectasis) was excluded from the linear regression calculations. Mean slope with error bars representing standard deviation of the vertical gradients are shown in Figure 29. Vertical gradients were higher in all cases in the supine versus prone posture. The difference in vertical gradient between prone and supine postures using FMS was visually different but not statistically significant ($p=0.06$). When MDCT was used, this difference was both visually different and statistically significant ($p=0.03$). Vertical gradients accounted for 21.3% and 25.1% of the variability in $r\dot{V}_A$ measurements in the prone posture measured by FMS and MDCT respectively. Similarly, vertical gradients accounted for 67.2% and

60.3% of the variability in $r\dot{V}_A$ measurements in the supine posture measured by FMS and MDCT respectively.

## 3.4 Discussion

FMS and MDCT measurements of $r\dot{V}_A$ correlated well at the scale of FMS piece size (~1.9-$cm^3$) and further improve when lumped into vertical height sections. FMS data is typically presented as a weight normalized number representing $r\dot{V}_A$ as "ventilation per alveolus". Since FMS are delivered in-vivo, they should directly correspond to the in-vivo MDCT measurements. Some variation and measurement error is expected as the FMS are measured ex-vivo and suffer from variability in air-dried inflation level, surface bleb (which can more-or-less be ignored) or internal bullae formation (less easy to ignore), and distortion of the lung positioning during the drying process and subsequent image registration (10,164). Because our goal was to validate small-scale xenon-CT measurements of $r\dot{V}_A$, the higher spatial resolution of FMS over other methods made it the best method for use in smaller-scale comparisons with MDCT.

The FMS weight-normalization method yielded stronger correlations to all MDCT-based $r\dot{V}_A$ measurements. Weight-normalization takes into account the weight of the lung piece in order to account for piece size that should and does improve the correlation with in-vivo measurements. The importance of weight-normalization becomes clear when examining FMS pieces on the edge of the lung. While the high-resolution of MDCT-based measurements limits partial volume effects, without accounting for FMS piece size at the edge of the lung, these regions might appear as low flow regions when in reality $r\dot{V}_A$ is normal however the piece represents a much smaller chunk of lung parenchyma. Published literature regarding FMS states that FMS measurements are obtained with alveoli uniformly expanded and the number of alveoli for a given piece of lung is proportional to the weight of the piece since the lungs were air-dried fully expanded at TLC (165,166). When we compared our measurements of

lung volume from the ex-vivo dried lungs to the in-vivo FRC and TLC volumes, we observe that the volume of the ex-vivo lung more closely resembles an inflation level slightly larger than FRC, not TLC. This is not surprising since, to promote drying, a series of holes were placed in the surface of the ex-vivo lung. At FRC, alveoli are not uniformly expanded. Hoffman et al. demonstrated increasing gradients in lung density at lower lung volumes, with the greatest effect in the dependent lung regions (54). If FMS $r\dot{V}_A$ measurements are obtained at FRC, alveoli will not be uniformly expanded, resulting in lung expansion effects on $r\dot{V}_A$ FMS measurements. This may explain some of the incongruity of FMS and MDCT $r\dot{V}_A$ measurements.

Clear $r\dot{V}_A$ heterogeneity was evident using both FMS and MDCT techniques, with ventilation being consistently more homogenous when the animals were in the prone posture. CV of $r\dot{V}_A$ was statistically significantly higher in the supine posture compared to the prone posture for both methods as well as statistically significantly higher using the FMS technique compared to MDCT. CV measured by xenon-CT is lower than FMS in disagreement of previous studies that used lower resolution CT measurements without image registration techniques (163). Increased CV in the FMS technique likely represents a reduced resolution of the FMS method at small-scales because of the large piece sizes. This could also represent differences between the normalization factors used in-vivo vs. ex-vivo. It has been presented that CV will predictably increase as the scale of measurements decreases; a fractal-based hypothesis suggests that heterogeneity will increase progressively as measurement resolution improves (167).

Our comparison of FMS and wash-in xenon-CT $r\dot{V}_A$ measurements demonstrated good agreement between the techniques. However, there are a number of factors that likely played a role in weakening the correlation. First, technical reasons necessitated that FMS and MDCT-based measurements be sequential instead of simultaneous. This resulted in a 10-minute window in which both sets of measurements were collected. While animals were hemodynamically stable during this window, subtle changes in $r\dot{V}_A$

were possible that would not be reflected by global measurements. The higher-resolution MDCT measurements would be more adept at detecting these changes and might result in subtle variation when lumped together at FMS piece-size resolution. Secondly, swine examined in this study were healthy and had a relatively narrow range of ventilation values. Within such a small range, measurement errors would have a greater impact on the correlation. This becomes evident when comparing the differences in correlation between the prone and supine postures. Correlations were statistically significantly higher in the supine posture likely due to a wider range of values caused by the vertical gradient in lung expansion. In the prone posture, lungs become more uniformly expanded and $r\dot{V}_A$ heterogeneity decreases further narrowing the range of $r\dot{V}_A$ values in which the two techniques were compared. The correlation between FMS and MDCT-based $r\dot{V}_A$ measurements would likely improve if the range of $r\dot{V}_A$ values were expanded by utilizing extreme tidal volumes or by inducing additional heterogeneity through a lung injury model. The most critical factor weakening the correlation between FMS and MDCT was the improper alignment of examined lung regions. Both methods are performed in-vivo, however FMS measurements are obtained from the ex-vivo lung after their excision from the body and air-drying. While image registration improved our ability to compare the methods on a regional basis, shortcomings within the registration process still prevent an exact region-to-region comparison.

The registration process incorporated information regarding lung shape and the positioning of the central airway trees in order to match the in-vivo and ex-vivo images. Unfortunately, the air-drying process sometimes alters the anatomical shape, density and overall composition of the lungs compared to the in-vivo state. Prior to air-drying, blood was removed from the lungs by flushing with a Dextran solution that evaporates during the air-drying process. This results in an air-dried lung without any representation for the missing blood, thus yielding a less dense (lower HU value) and more homogenous (decreased SD) lung parenchyma compared to in-vivo. This difference considerably

impairs the use of intensity-based registration metrics for image matching. In addition, without the constraints provided by the thorax and the heart, differences in the overall shape of the lung during air-drying occurred despite our efforts to glue lobes together during air-drying to maximize the similarity between in-vivo to ex-vivo lobar relationships. Mismatched geometries between in-vivo and ex-vivo lungs at the apical regions of the lung seemed to be greatest. Lungs were hung vertically from the trachea causing an elongation compared to the recumbent, in-vivo posture. Additionally, blebs formed in 3 out of the 5 lungs further distorting the lung shape at the major fissures. The more that the ex-vivo lung shape and density differed from the in-vivo state the more difficult it was for image registration to achieve an exact transformation between the scans. Even with all of the information incorporated into this sophisticated image registration algorithm, user-placed landmarks at airway-tree branch points demonstrated a mismatch on the order of 2-3 mm. Registration results worsened the closer a region was to the periphery or the base of the lungs. Even with the limitations with this registration scheme, we were able to demonstrate good correlation on a FMS piece size resolution of 1.9 $cm^3$ and by 0.25 cm vertical height between FMS weight-normalized and MDCT mean-normalized $r\dot{V}_A$ measurements.

With the wash-in xenon-CT method established and validated with FMS in Chapter 3 we can now shift our focus to translating this method from the animal laboratory to a clinical research setting. For this translation to be successful we will need to tackle a number of issues related to scanning humans. We address these issues in Chapters 4 through 6.

In Chapter 4 we address the need to develop lung volume control techniques that will allow the wash-in xenon-CT method to be performed on awake spontaneously breathing human subjects rather that on anesthetized mechanically ventilated animals. Chapter 5 deals with image registration and image processing tools that were needed to handle variations that could not be solved with lung volume control alone. Finally, in

Chapter 6, we begin to use the wash-in xenon-CT method in a cohort of normal never-smokers and smokers. We also address the confounding factor of increased noise compared to animal datasets and needed to implement improvements to generate more accurate non-linear curve fits. We then compare normal never-smokers and smokers to gain insight in the difference in regional ventilation distribution and heterogeneity between the groups.

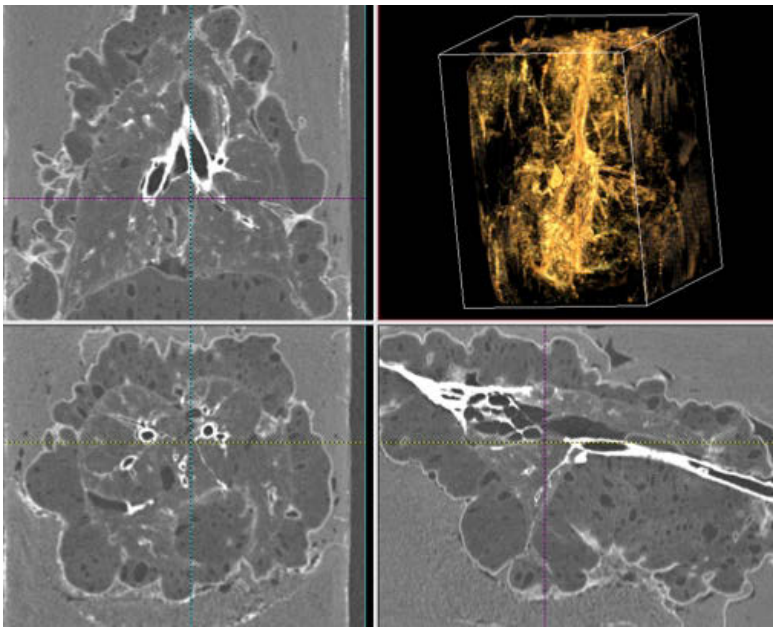

Figure 17. Cross-section and 3D rendered views generated from MDCT scans of an example set of ex-vivo lungs encased in foam.

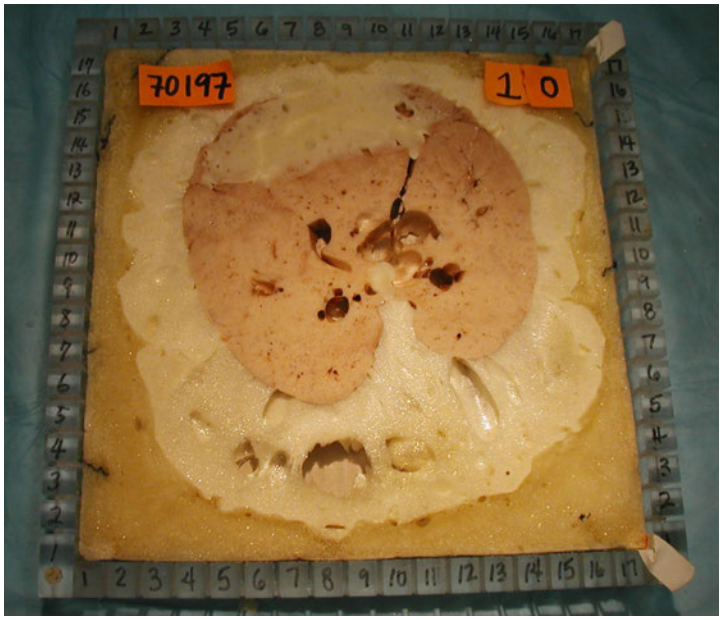


Figure 18. Photograph of the ex-vivo lung prior to being cut into 1.2x1.2x1.2 cubes for FMS count measurements.

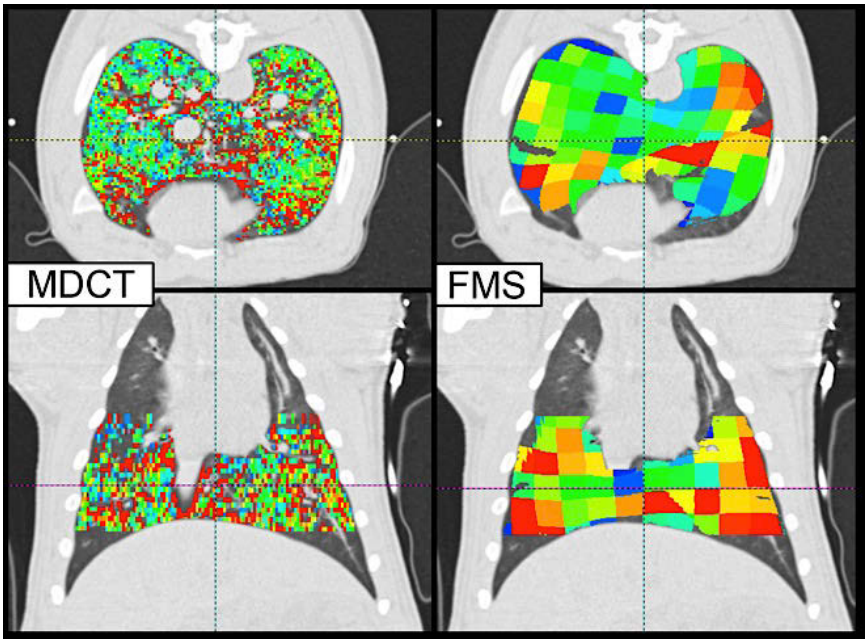


Figure 19. Resolution comparison of MDCT (*left*) and FMS (*right*) $r\dot{V}_A$ measurements after image registration.

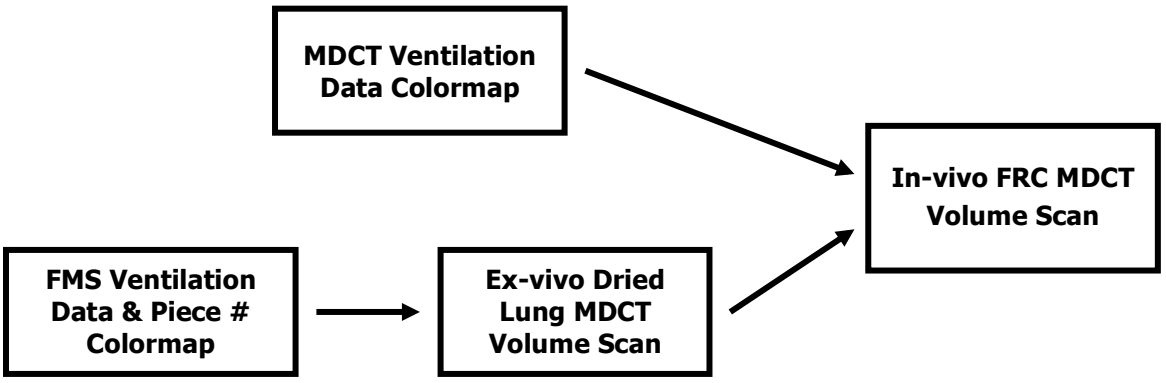


Figure 20. Schematic diagram of the ex-vivo to in-vivo image registration process.

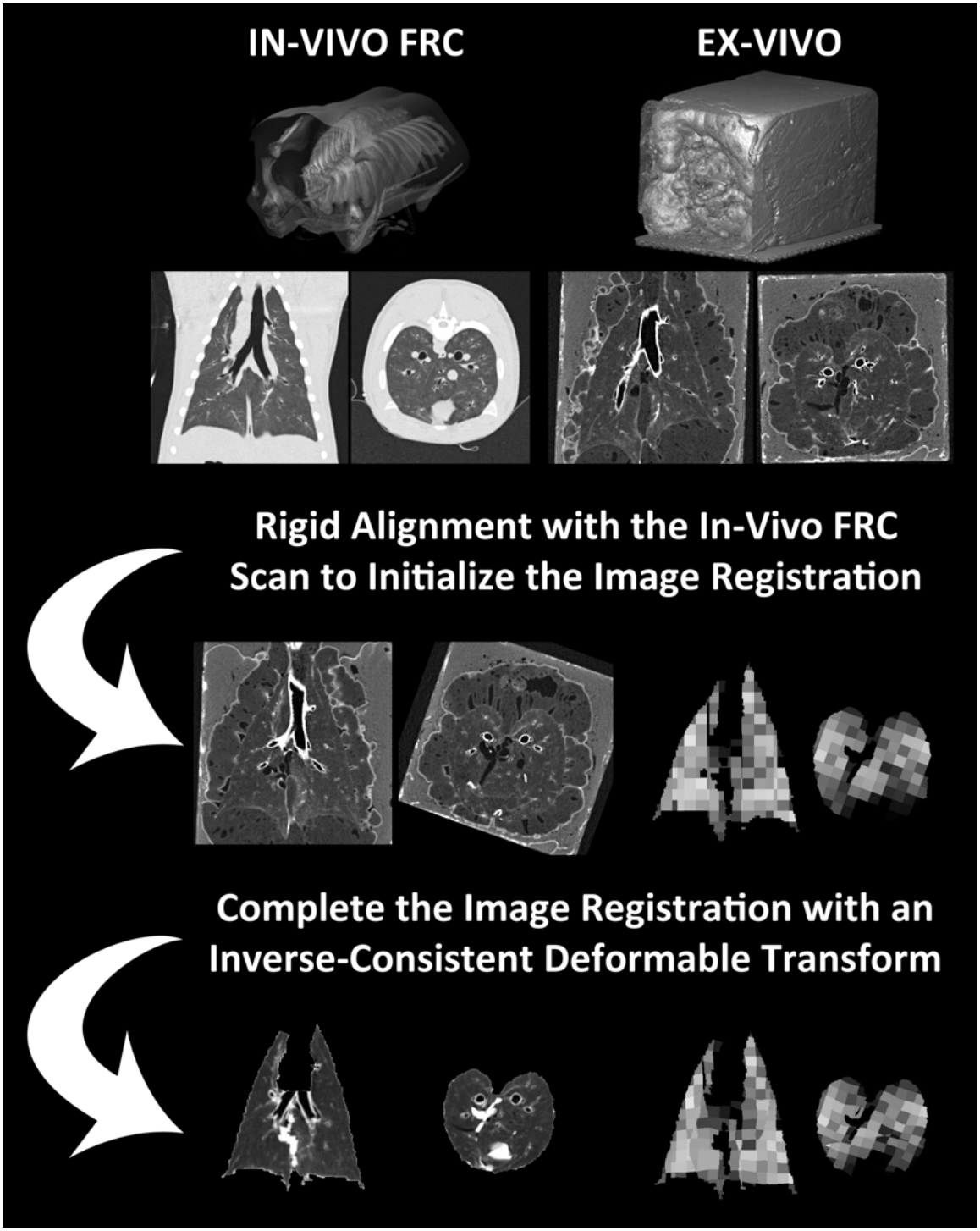


Figure 21. Schematic diagram of the image registration process.

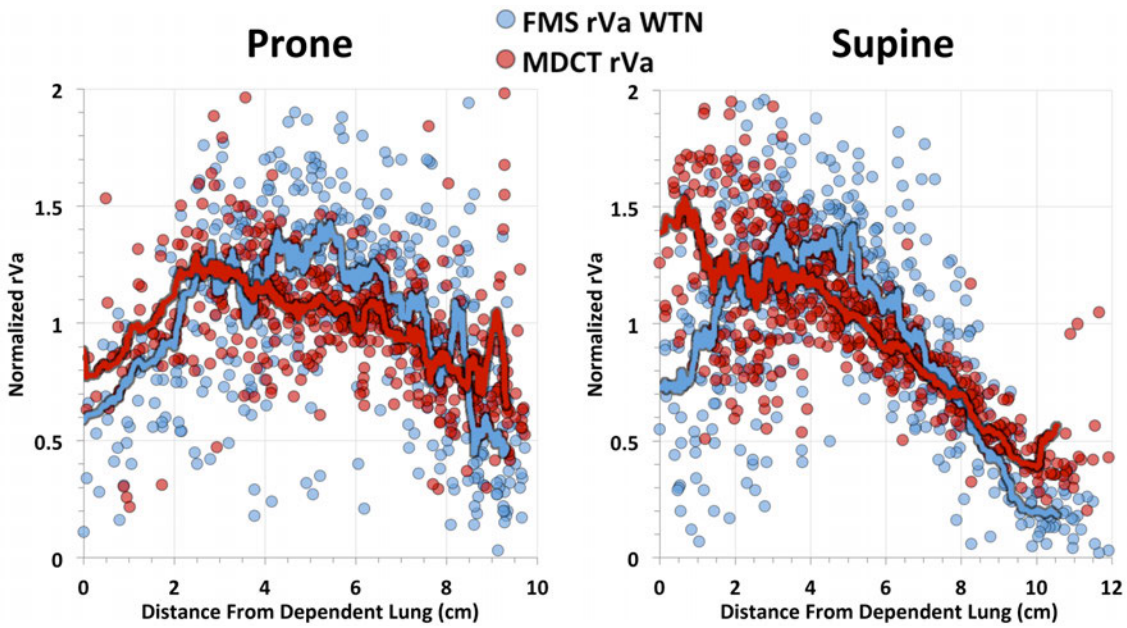


Figure 22. Plots of normalized ventilation as a function of distance from the dependent edge of the lung from a representative animal in the prone and supine postures.

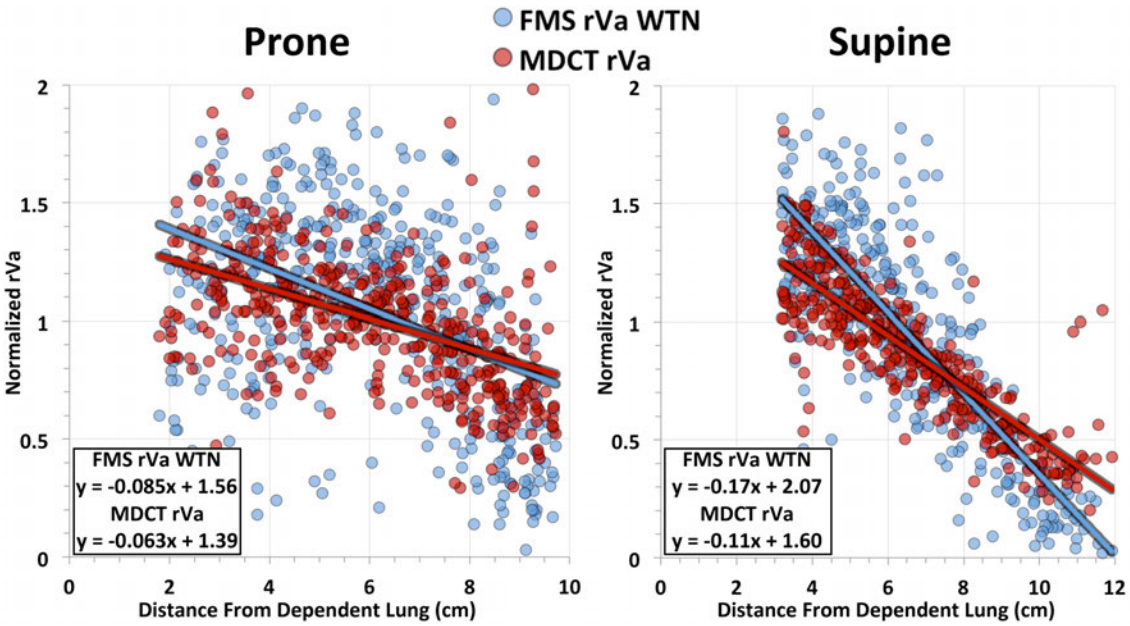


Figure 23. As expected, there is greater vertical gradient in regional ventilation present in the supine (*right panel*) versus prone (*left panel*) posture. Plots from a representative animal in the prone and supine postures are shown above.

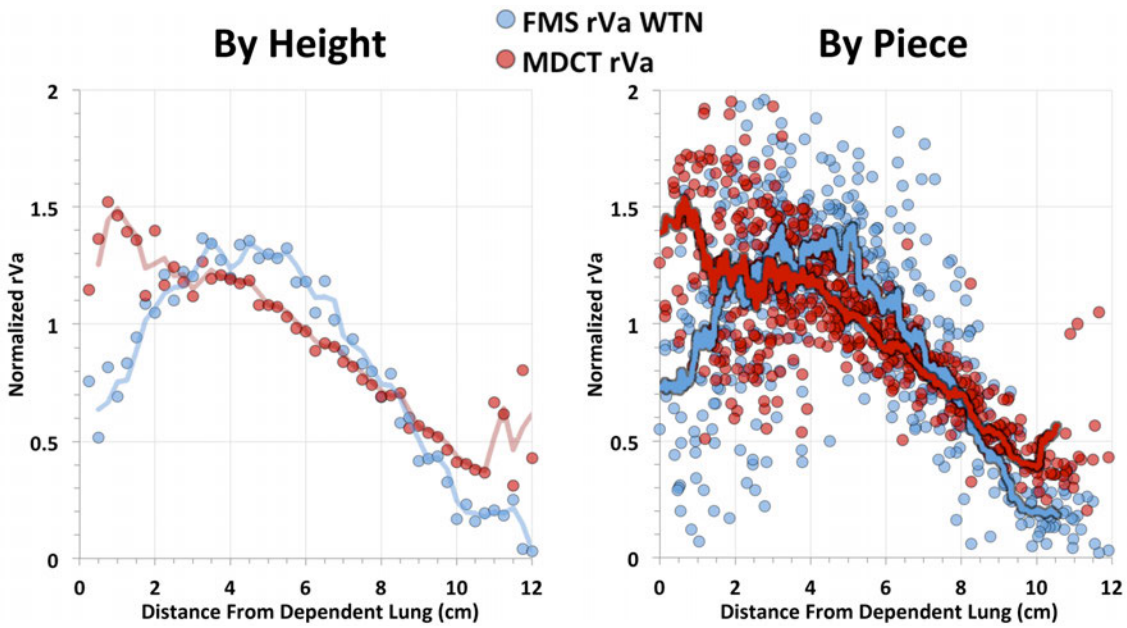


Figure 24. To further match the data after image registration, the FMS piece size data was grouped by vertical height. The above plots are from a representative animal in the supine posture showing the FMS piece size data (*right panel*) and the aggregated by height data (*left panel*).

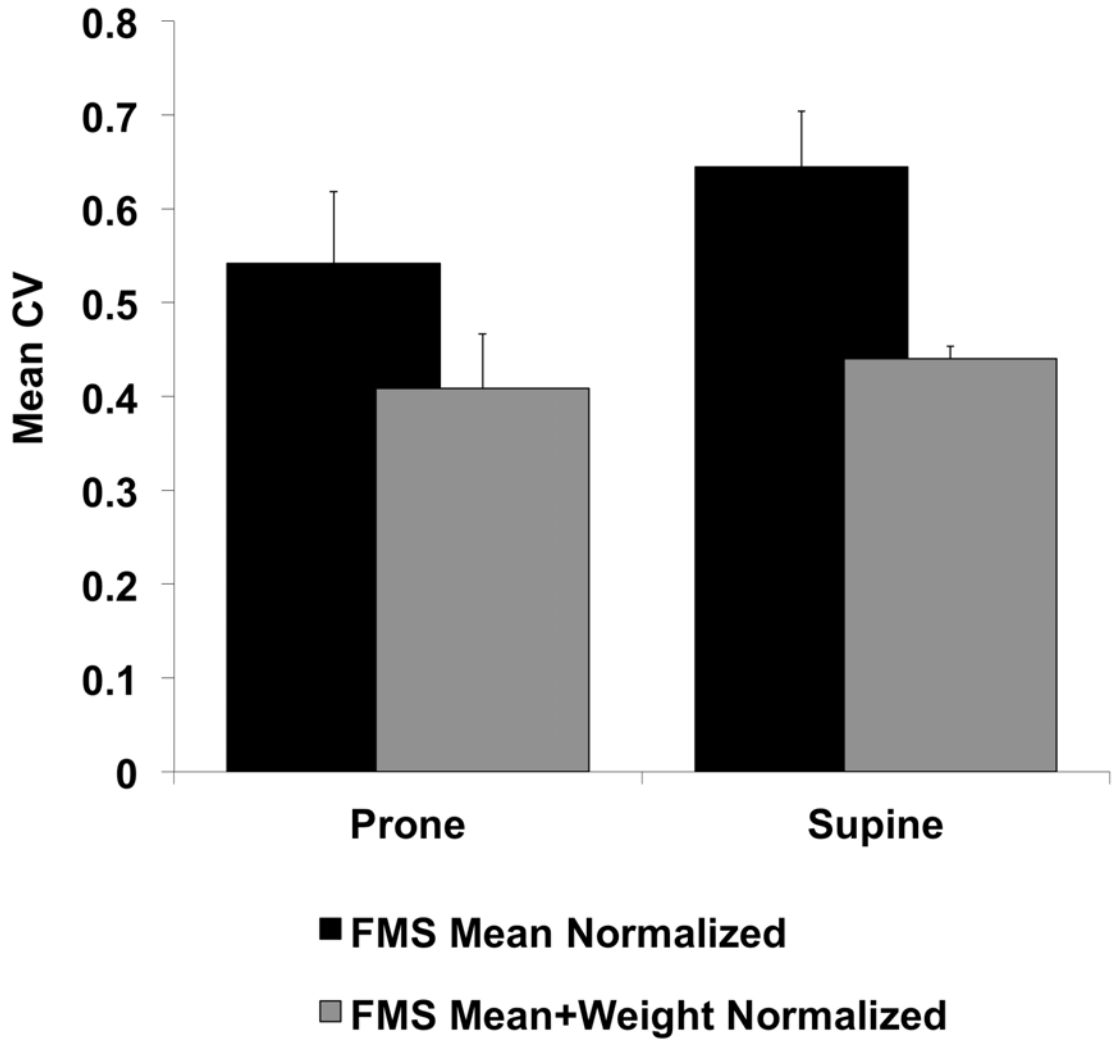


Figure 25. Preliminary analysis of our data demonstrated a considerable reduction in FMS measurement noise when mean + weight normalization was utilized.

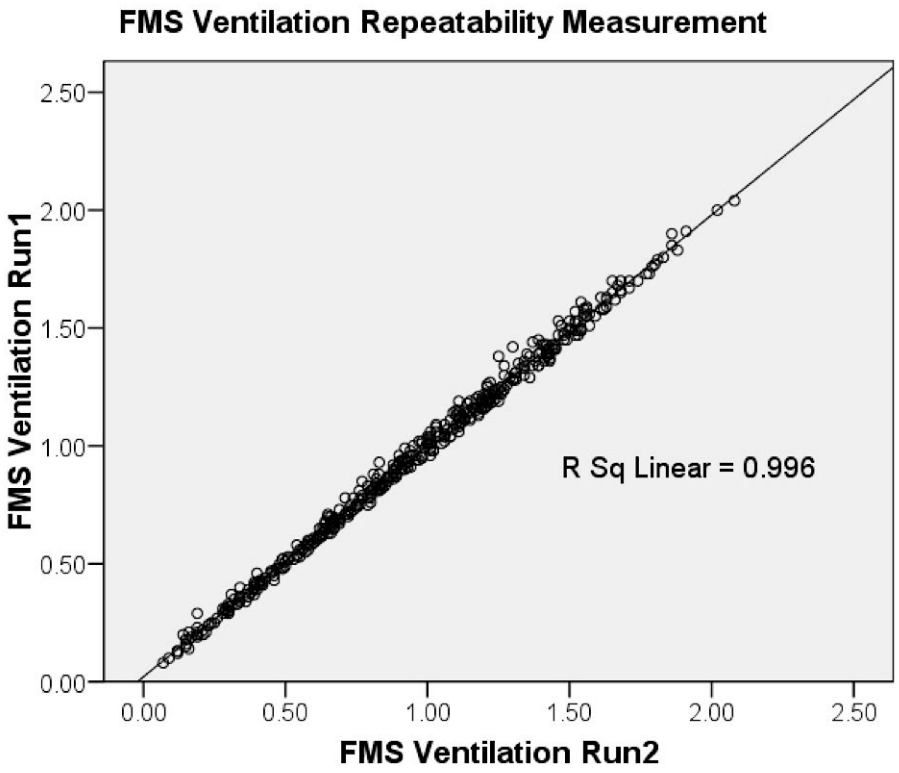


Figure 26. FMS measurements of $r\dot{V}_A$ are highly repeatable, $R^2$=0.996.

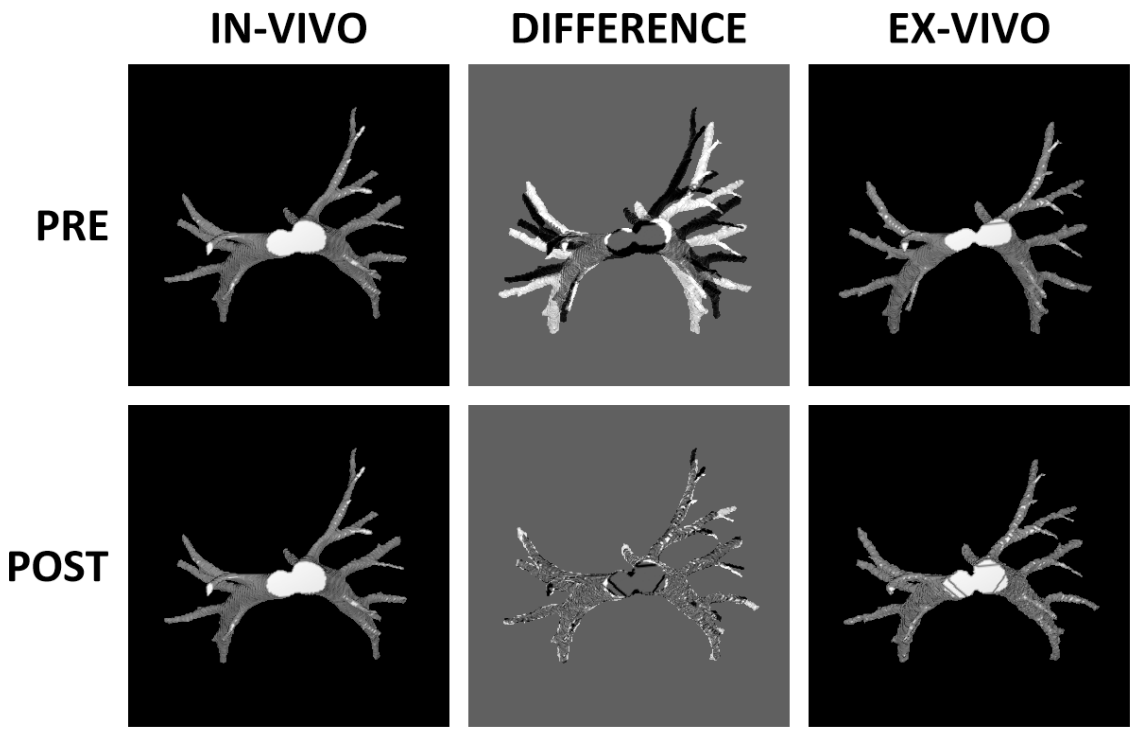


Figure 27. An airway segmentation mask of the right and left main bronchi was used to improve registration results especially in the lung core. A 3D surface rendering of the central airway tree from the in-vivo FRC scan (*left column*), the ex-vivo scan (*right column*), and a subtraction image (*middle column*) are shown pre (*upper row*) and post (*bottom row*) image registration.

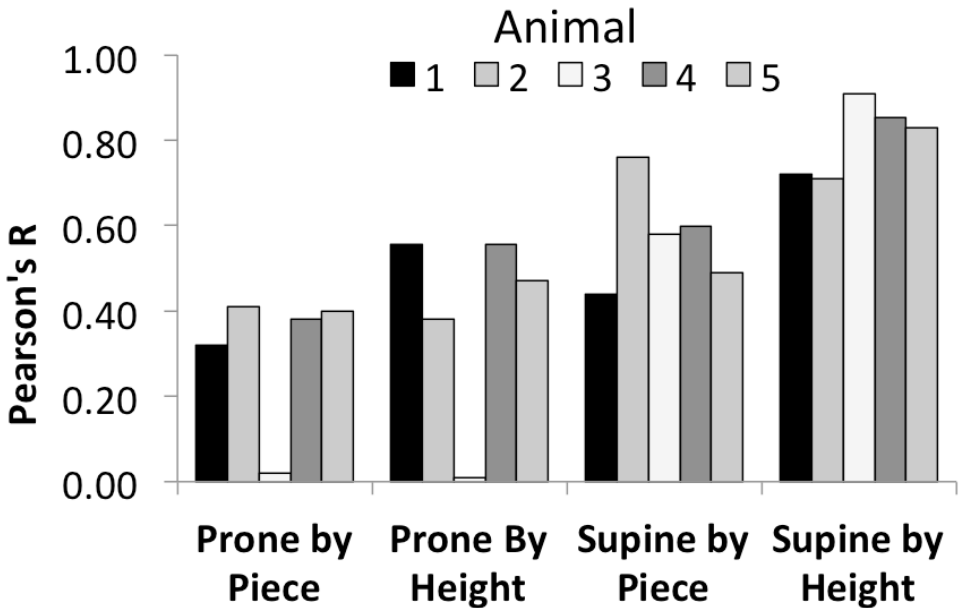


Figure 28. The plot shows Pearson's correlation coefficients for the comparison between FMS and MDCT in the five animals in the prone and supine postures by FMS piece size and by vertical height. Aggregating the data considerably improves the correlation between the methods.

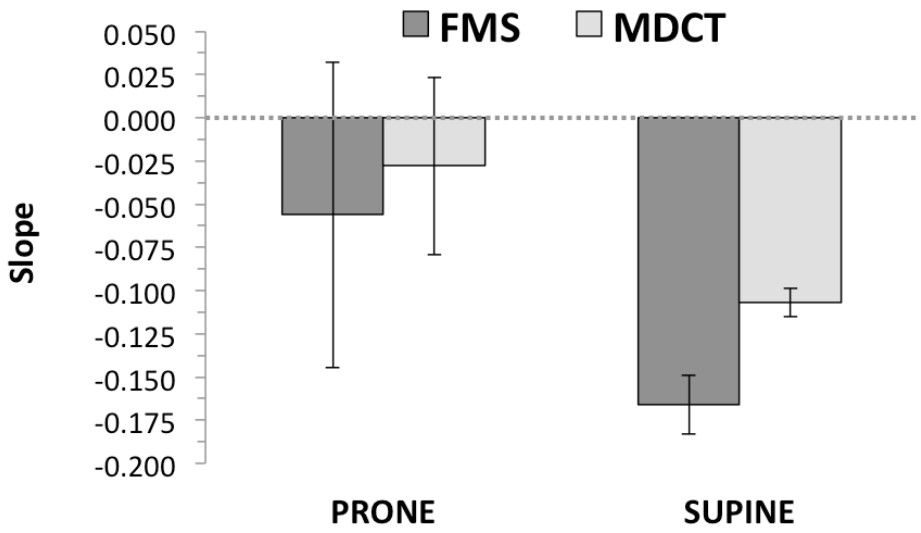


Figure 29. The slopes of the vertical gradient in $r\dot{V}_A$ are comparable between the methods in both the prone and supine postures. The vertical gradient is more extreme in the supine versus prone posture as expected with the gradient prone being close to zero. Values are the mean value from the 5 animals with the error bars indication ± SD.

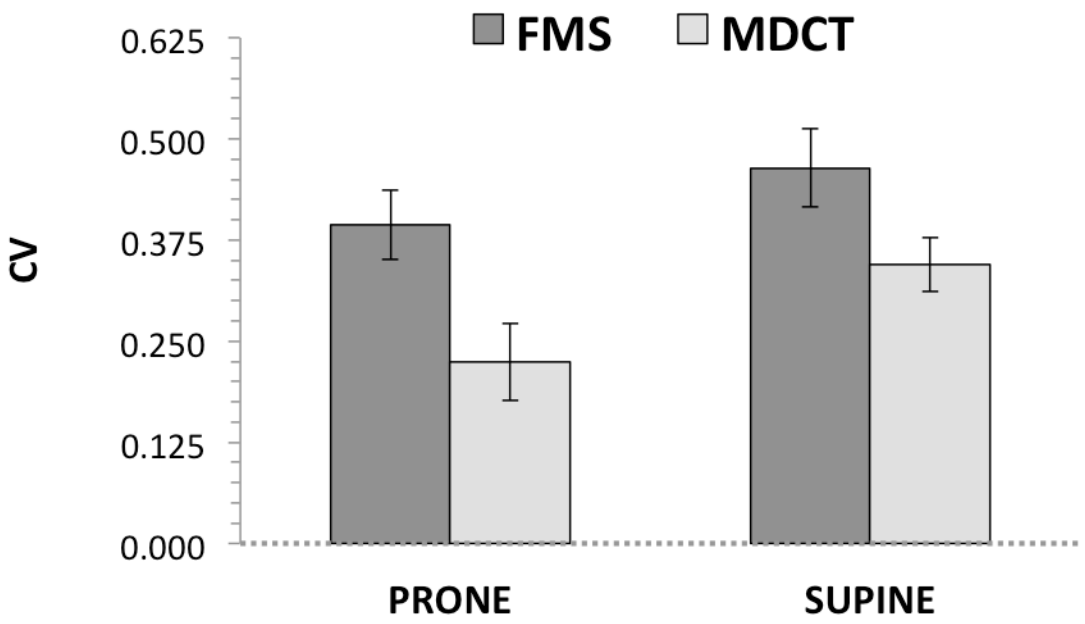


Figure 30. The coefficient of variation (CV) of $r\dot{V}_A$ is higher in the FMS measurements and higher in the supine versus prone posture. Values are the mean value from the 5 animals with the error bars indication ± SD.

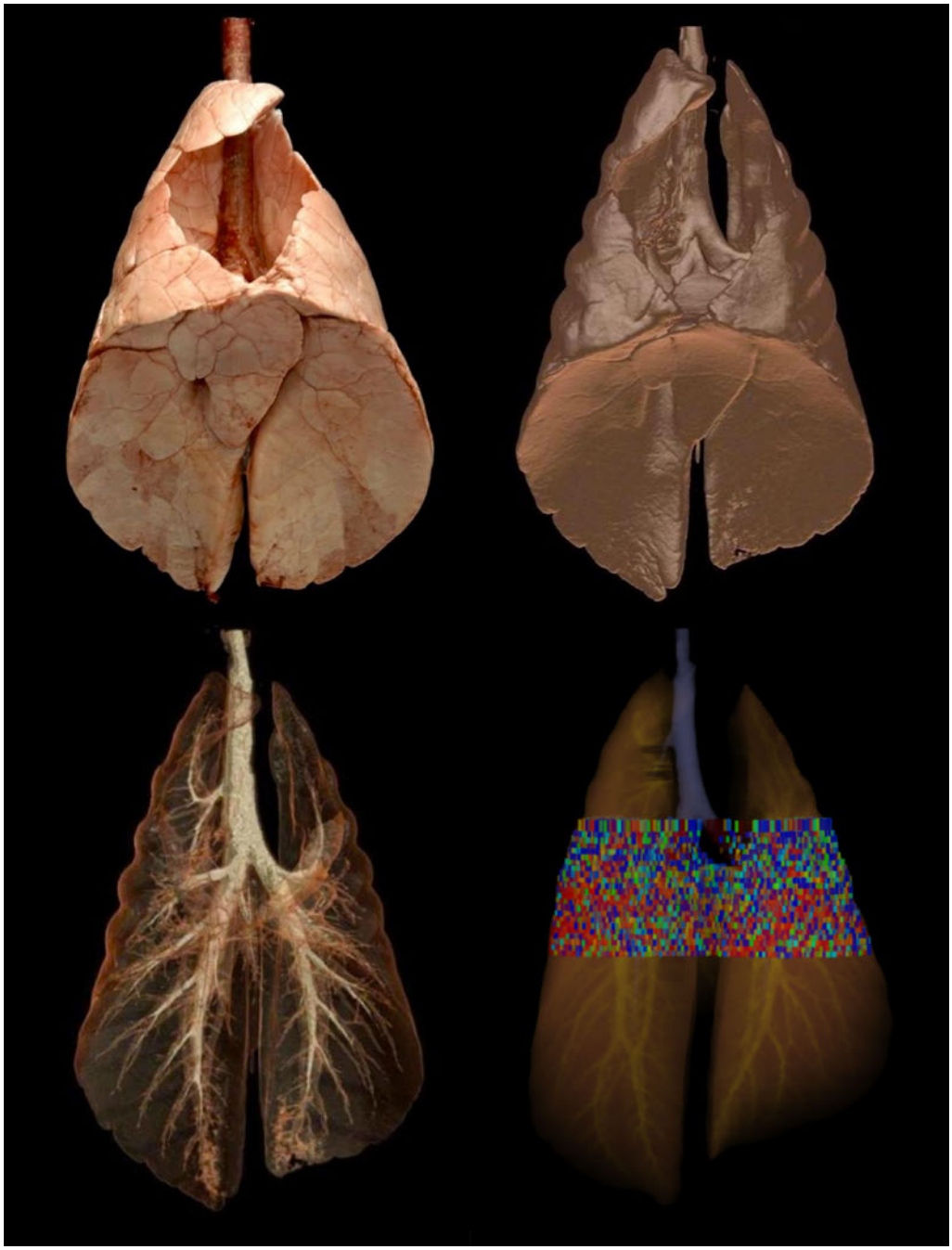

Figure 31. Digital photo of air-dried lungs (*upper-left panel*), 3D volume rendering of the lungs (*upper-right panel*), vasculature tree and airway tree obtained from the volumetric spiral MDCT in-vivo image data set at FRC (PEEP of 7.5 cm $H_20$) in the prone position (*lower-left panel*), and 3D volume rendering of the lungs with overlay of regional specific ventilation (*bottom-right panel*).

| | | *Supine* | | | *Prone* | | |
|---|---|---|---|---|---|---|---|
| | **Ex-Vivo Lung Volume** | **FRC Lung Volume** | **Ex-Vivo / FRC Supine** | **Landmark Error, mm** | **FRC Lung Volume** | **Ex-Vivo / FRC Prone** | **Landmark Error, mm** |
| **Animal 1** | 1061 | 946 | 112% | 1.8 ± 1.3 | 865 | 123% | 2.2 ± 2.8 |
| **Animal 2** | 1072 | 1011 | 106% | 2.4 ± 1.2 | 1047 | 102% | 1.8 ± 0.9 |
| **Animal 3** | 1051 | 1044 | 110% | 3.0 ± 1.5 | 933 | 113% | 2.2 ± 1.1 |
| **Animal 4** | 1033 | 938 | 101% | 3.7 ± 5.2 | 890 | 116% | 3.9 ± 3.4 |
| **Animal 5** | 943 | 876 | 108% | 4.5 ± 6.3 | 864 | 109% | 2.7 ± 3.9 |
| **Mean** | 1032 ± 52 | 963 ± 66 | 107 ± 4% | 3.1 ± 1.0 | 920 ± 77 | 112 ± 8% | 2.6 ± 0.8 |

Table 1. An analysis of lung volume comparing the registered ex-vivo dataset with the in-vivo dataset accompanied by a quantification of registration accuracy from 10-12 landmark points in both the supine and prone postures. Error measurements from user-determined landmark points are reported as mean ± SD. Lung volume measurements are reported in units of $cm^3$.

| | PEEP (cm $H_20$) | Mean Lung Density (HU) | SD Lung Density (HU) | Total Volume ($cm^3$) |
|---|---|---|---|---|
| **In-Vivo FRC** | 7.5 | -639.6 ± 18.8 | 148.3 ± 15.0 | 919.7 ± 76.7 |
| **In-Vivo TLC** | 25.0 | -754.9 ± 21.0 | 146.0 ± 7.2 | 1312.7 ± 108.3 |
| **Ex-Vivo Air-Dried** | n/a | -956.6 ± 6.6 | 46.3 ± 15.3 | 1032.3 ± 51.9 |

Table 2. Lung volume and densitometry measurements from the in-vivo prone FRC, in-vivo prone TLC and ex-vivo air-dried lungs.

| | Prone by Piece | Prone By Height | Supine by Piece | Supine by Height |
|---|---|---|---|---|
| **All Animals** | 0.31 ± 0.16 | 0.39 ± 0.23 | 0.57 ± 0.12 | 0.80 ± 0.09 |
| **Excluding Animal 3** | 0.38 ± 0.04 | 0.49 ± 0.08 | 0.57 ± 0.14 | 0.78 ± 0.07 |

Table 3. Mean ± SD of Pearson correlation coefficients for the comparison between FMS and MDCT $r\dot{V}_A$ measurements at FMS piece size and by vertical height in the prone and supine postures.

# CHAPTER 4: SYSTEMS FOR LUNG VOLUME STANDARDIZATION DURING STATIC AND DYNAMIC MDCT-BASED QUANTITATIVE ASSESSMENT OF PULMONARY STRUCTURE AND FUNCTION

## 4.1 Introduction

Multidetector-row Computed Tomography (MDCT) has emerged as a tool for quantitation of parenchymal destruction, air trapping and airway remodeling in chronic obstructive pulmonary disease (COPD) and asthma (16-23). Critical to the accuracy and interpretability of these metrics is the assurance that the lungs are scanned during a breath-hold at a standardized volume (168). Methods have been reported in which correction factors are proposed for inconsistent lung volumes (169,170). However, there is no replacement for accurate control of lung volume at the time of scanning.

In addition to structural-based measurements, wash-in xenon-CT enables the measurement of regional ventilation by utilizing the increase in measured density of a region of interest caused by the wash-in of radiodense xenon gas. This method has proved reliable in animal studies (24-27), and because the animals were anesthetized the anesthetic properties of xenon were not a problem (29,30). Animals were mechanically ventilated thus it was very straightforward to scan at a repeatable set of respiratory pauses as xenon gas was washed into and out of the lungs. The goal for measuring ventilation in humans is to capture the dynamic nature of ventilation in awake, free-breathing subjects. This therefore necessitates the use of a lower concentration of xenon gas and identifying repeatable pause points in sequential respiratory cycles when axial scans can be acquired. Currently a 30% xenon / 70% oxygen mixture is used for safety purposes, though a mixture which also includes krypton would be preferred (109). However, the introduction of gases of varying densities complicates the tracking of gas flow at the mouth with standard respiratory gas flow meters. With the emergence of dual-energy computed tomography methods for single breath xenon-based assessment of regional

lung function have been reported (138,139). However, there have been no reports validating these single breath techniques against a method that assesses true regional ventilation. The dynamic volume control approach we present here provides for such a comparator.

To yield an accurate measure of regional ventilation the dynamic wash-in xenon-CT method requires subjects to precisely achieve the same end-expiratory lung volume repeatedly over multiple breaths. When asked to maintain a consistent end-expiratory lung volume most subjects have modest difficulty even when they are being monitored and coached. Additionally, the slight anesthetic effect of xenon, even at 30%, represents an extra hurdle to overcome.

Many methods for lung volume control have been tried including belt systems and pressure drop pneumotachometers (76,103,171-173), each with varying degrees of success. When monitoring changes in the rib cage to estimate changes in lung volume, it has been shown that one must take into account shifts between rib cage and diaphragm breathing (174,175).

Devices for measuring in-line air movement suitable for use in conjunction with CT scanning include pressure-drop pneumotachometers, hot-wire anemometers, ultrasonic transducers, and turbine-based flow meters (176). Pressure-drop pneumotachometers are widely used (Figure 32), however they suffer from a number of drawbacks stemming from difficulties in calibration. A volumetric flow rate signal is generated from the pressure drop across the permeable screen; this signal is then integrated to determine volume. Minor errors in zeroing may cause volume creep over time. The devices are linear under a specific set of calibrated conditions; changes in humidity, temperature, or gas composition will cause invalid measurements. Since the eventual goal is to create a system suitable for lung volume control during both static breath-hold imaging and dynamic wash-in multi-breath xenon-CT scans, it was decided that an alternative to a pressure-drop pneumotachometer was required.

We present here solutions for lung volume control to facilitate: 1) static breath-holds and 2) intermittent breath-holds within a multi-breath imaging sequence in which gas density varies on expiration.

## 4.2 Materials and Methods

*In order to achieve both types of lung volume control two systems were developed and tested.*

### 4.2.1 Breath-hold Lung Volume Control

*Turbine-Based Breath-hold System Design*

The lung volume control system, comprised of a mouthpiece, filter, turbine-based airflow measurement device, balloon occlusion valve and integrated software control, is calibrated via a slow vital capacity (SVC) maneuver with a display visible to the system operator for coaching and control purposes (Figure 33-A). The primary component in the system is the VMM-400, a turbine-based flow meter (Interface USA, Laguna Niguel, CA) (Figure 33-B). The turbine relies on the rotation of an extremely low friction impeller spinning due to air movement. One rotation of the impeller indicates a specific volume passing through the circuit. This volume depends on the size of the chosen insert used; in this case the small turbine was used to obtain the highest volume resolution (0.5 mL increments). To assist subjects during breath-hold procedures, an inflatable balloon-type 2-way shutoff valve (9430 series, Hans Rudolph, Shawnee, KS) is placed between the turbine and the system's end; the valve is controlled remotely (Figure 33-C). It can be set to automatically inflate as the subject approaches a particular lung volume or can be manually inflated by the operator in the control room with a click of a button. The balloon is inflated with helium rather than compressed room air to achieve the minimum response time. As this is a pressure-inflated balloon valve, it is meant as an assist to timing and comfort of the patient, but in the case of an emergency the balloon can be

overwhelmed by a forceful effort from the patient. Reusable, sterilizable mouthpieces are connected to single use bacterial viral filters, placed between the patient and the turbine. To comfortably position the breathing circuit during the scan, a clamp holds the circuit above the patient using an articulating locking arm (CIVCO, Kalona, IA).

To combine the components into an easy to use device, a custom computer control system was developed in the LabVIEW 8.0 platform (National Instruments, Austin, TX) **(**Figure 34**)**. The system utilizes a data acquisition board to capture the digital counter signal from the turbine and an on/off signal signifying X-ray on while also outputting a signal to trigger the solenoid valve controlling balloon inflation. The procedure for acquiring a volume controlled scan involves a series of system calibrations and breathing maneuvers directed by the system operator (Figure 35).

*Turbine-Based Breath-hold System Calibration and Testing*

Initially, the system was calibrated with and validated by use of a 3-L calibration syringe (Model 5530: Hans Rudolf, Kansas City, MO). A wide range of volumes and flow rates were delivered through the system using the super syringe to check accuracy and reliability over the typical respiratory range.

A large animal piston ventilator (Harvard Apparatus, Holliston, Massachusetts) was used to test the system for cyclical repeatability. The large animal piston ventilator is a fixed volume delivery system, which delivers the same stroke volume every time. This consistency makes it more suitable for testing purposes rather than more modern pressure-based ventilators that have a wide tolerance in delivered volume per breath. The inlet and outlets of the ventilator were connected to the system to simulate inhalation and exhalation in a complete circuit mimicking typical tidal breathing.

Following system validation tests, the volume controller was tested as part of an ongoing MDCT repeatability study using a 37-subject subset (16 Males / 21 Females, 21 Normal Never-smokers, 16 Normal Smokers; Age (years): min=20, max=64, median=27;

BMI: min=18.5, max=32.0, median=23.4). The Institutional Review Board approved this study, and written informed consent was obtained from all subjects before they entered the study. Study inclusion criteria were "never smokers" (with a total smoking history of less than 1 pack-year, NS) and smokers currently smoking one pack per day. Exclusion criteria were known heart disease, kidney disease, diabetes, presence of metal in the lung field, pregnancy, an X-ray/CT scan in the past 12 months, and a body mass index over 32. NS with clinically important pathology detected on MDCT were excluded, as were smokers with significant lung disease other than emphysema. The baseline dyspnea index was determined (177). Prebronchodilator spirometry including DLCO measurements were performed via a V6200 Body Box (Sensor Medics) or an OWL body plethysmograph (Ferraris Respiratory), verified for equivalency. Spirometry quality followed the American Thoracic Society and European Respiratory Society guidelines (178).

Subjects received three volume-controlled spiral lung scans acquired during breath-holds at either total lung capacity (TLC) or functional residual capacity (FRC: designated as 20% vital capacity) measured by the volume controller. All subjects received at least one TLC and FRC scan after which they were assisted off the scanner table and permitted to walk around the room before being repositioned on the scanner for the third scan randomized to either TLC or FRC. Volumetric MDCT scan times were less than 10 seconds with a z-coverage of 22–30 cm, adjusted to capture the full apical-basal extent of the lung. Voxels were near isotropic at 0.61 mm × 0.61 mm × 0.5 mm. The following imaging protocol was used with our 64-slice MDCT scanner: 100 mAs, 120 kV, 1 mm pitch, 512 × 512 matrix, and B35f reconstruction kernel. Lung segmentation was performed on the scans using the software program PW2 (VIDA Diagnostics, Iowa City, Iowa) to assess the total CT-measured air volume within the lungs in each of the three scans. CT-measured air volumes from the repeated scans were compared using linear regression and Bland-Altman plots. The CT-measured air volume

difference (CTVD) between repeated scans (i.e. CT-measured air volume from TLC scan 2 minus TLC scan 1) was calculated and compared to the analogous air volume difference recorded from the volume controller (VCVD) using linear regression, Bland-Altman plots, and Pearson correlation (statistical significance assessed for $P < 0.05$). Additional dependent variables of height, weight, age, sex, inflation level (FRC or TLC), smoker status, CT technician and volume controller operator were included in the linear regression model. Statistical analysis was performed using SPSS (IBM SPSS Version 19: IBM, Armonk, New York).

### 4.2.2 Dynamic Lung Volume Control

To achieve dynamic lung volume control that permits intermittent breath-holds for image acquisition, an enhanced version of the turbine-based breath-hold system was developed and tested. As seen in the results, this solution was inadequate and necessitated the development of an additional system better suited to dynamic lung volume control that incorporated a dual rolling-seal piston design.

#### *Turbine-based Dynamic System Design*

The turbine-based system for lung volume control during static breath-hold was enhanced to facilitate lung volume control during dynamic imaging (Figure 36). A pneumatic 3-way valve (8500 series: Hans Rudolph, Shawnee, KS) with a pre-filled bag of 30% Xe / 70% $O_2$ attached to one side was positioned at the end of the circuit to control the inspired gas composition. Additionally two giant one-way valves (5800 series: Hans Rudolph, Shawnee, KS) were added to control the direction of gas movement and prevent rebreathing from the circuit aiming to achieve a consistent inspired gas composition between breaths. Finally, an LCD screen with readout of respiratory rate and lung volume was positioned above the subject's head to allow them to monitor and adjust their depth of breathing. The principle of the system was that

subjects could monitor their lung volume on a breath-by-breath basis and adjust as needed.

*Dual Piston-Based Dynamic System Design*

To lessen the responsibility of the subjects to synchronize respiration and depth of breathing to a feedback system, a second type of system was designed specifically to control the volume of air inspired and expired on a breath-by-breath basis (Figure 37).

The main idea of the system was to employ a dual-piston reservoir design that would separate the control of inspiration from expiration. To rapidly test the design concept for feasibility, two commercial rolling-seal spirometers (S700: SensorMedics / Viasys / CareFusion, Yorba Linda, CA) were acquired and adapted for use as fixed volume reservoirs. External solenoid valves (*bottom-left panel*, Figure 37) and micro-switches placed on the end of the piston's shaft (*middle panel*, Figure 37) to facilitate system operation and allow for the detection of full and empty states using a custom designed LabVIEW control VI. The positioning of the micro-switches could be adjusted to change the volume of the spirometers. The spirometers were designed to facilitate pulmonary function testing which required the measurement of large changes in volume in a short period of time. In order to perform that function efficiently, the spirometers were designed with a large cross-sectional area piston. As we were using them to control tidal breathing, the large piston cross-sectional area necessary for PFTs became a drawback as a small change in the positioning of the micro-switches led to large changes in reservoir volume. Initial testing of this design concept gave us confidence in this approach for dynamic lung volume control therefore we moved the process forward in order to develop a fully custom solution that would alleviate the limitations in this initial design (Figure 38).

The pistons in the final design, fabricated from Plexiglas, each employ a dual rolling-seal design to ensure a smooth low-resistance chamber. Each piston has a linear

variable differential transformer (LD620 Series: Omega, Stamford, CT) attached to the piston to measure piston displacement. A system of solenoid valves controls input gas and vacuum sources. Pneumatic shutter and three-way valves (4200 series & 8500 series: Hans Rudolph, Shawnee, KS) coupled with giant one-way valves (5800 series: Hans Rudolph, Shawnee, KS) coordinate the breathing cycle through a LabVIEW based computer control system. Initial tidal volume settings are estimated based on patient size and prior pulmonary function tests and can be easily adjusted by the system operator during a brief training session with each subject. Subjects begin with a series of deep inspirations used for lung recruitment followed by coaching to their FRC lung volume at which point they are asked to place the mouthpiece in their mouth so the system can assert control over their breathing cycle. As the subject begins to inhale, the expiratory reservoir is evacuated by the vacuum source. Once the pre-set tidal volume is fully inhaled the system closes the mouth shutter and switches the 3-way value to permit exhalation while beginning to refill the inhalation reservoir from the appropriate gas source. Typically, the initial three breaths consist of room air followed by 17 breaths of a xenon-oxygen mixture (30% Xe, 70% $O_2$). Once exhalation is complete the three-way valve switches back to the inspiratory reservoir closing the respiratory circuit. At this point the scanner is triggered and images are acquired. Once complete the mouth shutter opens to allow the inspiration process to begin again.

*Dynamic Systems Calibration and Testing*

Both dynamic systems were validated with the 3-L calibration syringe (Model 5530: Hans Rudolf, Kansas City, MO) using a variety of tidal volumes and respiratory rates.

Following calibration and testing, the dynamic lung volume controllers were utilized to facilitate the wash-in xenon-CT method to obtain regional ventilation measurements as part of an ongoing effort to establish a normative lung atlas. This effort

included a 6-subject subset (1 Male / 5 Females, 4 Normal Never-Smokers, 2 Normal Smokers; Age (years): min=21, max=44, median=24; BMI: min=18.8, max=31.4, median=26.7) using the turbine-based dynamic system, and a 41-subject subset (20 Males / 21 Females, 34 Normal Never-smokers, 7 Normal Smokers; Age (years): min=20, max=73, median=30; BMI: min=19.6, max=32.7, median=25.3) using the dual piston-based system. The Institutional Review Board approved this study, and written informed consent was obtained from all subjects before they entered the study. Study inclusion criteria were the same as the described earlier for the MDCT repeatability study.

Subjects received a dynamic volume-controlled axial lung scan consisting of 20 time points scanned during brief end-expiratory breath-holds at FRC. Scan times varied between 1 to 3 minutes, dependent on subject specific respiratory rates, with a z-coverage of 3 cm positioned between the carina and the diaphragm. Voxel sizes were around 0.61 mm × 0.61 mm × 1.2 mm depending on field of view. The following imaging protocol was used with our 64-slice MDCT scanner: 150 mAs, 80 kV, 0.375 sec rotation time, 512 × 512 matrix, and B35f reconstruction kernel. The density change over time in each lung parenchymal voxel in the series was determined and fit to an exponential model, the time constant of which is equal to the inverse of the voxel-specific ventilation, as previously described (179). Lung segmentation and regional ventilation analysis was performed on the scans using Pulmonary Analysis Software Suite (PASS) (161). The Institutional Review Board approved all studies reported here.

## 4.3 Results

### 4.3.1 Turbine-Based Breath-hold System

The system accurately controlled lung volume for 32 out of 37 subjects that complied with coaching procedures. 5 subjects were excluded from evaluation because of protocol deviations including an inadequate seal around the mouthpiece, or not following coaching procedures. The difference of VCVD subtracted from CTVD

normalized to represent a percentage of CT measured air volume was 0.7 ± 2.85%. The difference between VCVD from CTVD likely represents non-compliance of the subject in one form or another, including loss of air around the mouthpiece. This measure of "non-compliance" was not explained by height, weight, age, gender, smoking status, lung capacity, CT technician or volume controller operator as demonstrated in Error! Reference source not found.. As shown in Figure 39, the relationship of CT measured air volume between repeated scans was examined; for all scans together (*top panel*) there was a linear relationship with a slope=0.9953, R-squared=0.99797; for TLC alone (*middle panel*), a slope=1.0252, R-squared=0.99391; for FRC alone (*bottom panel*), a slope=0.9664, R-squared=0.97156. The middle and right columns of Figure 39 show corresponding Bland-Altman and difference value histogram plots for each group. As shown in Figure 40, the relationship between CTVD and VCVD was examined; there was a linear relationship with a slope=0.7037, R-squared=0.4589. Similar to Figure 39, the middle and right columns of Figure 40 show Bland-Altman and difference value histogram plots the CTVD versus VCVD comparison. The Pearson correlation coefficient showed moderate positive relationship between CTVD and VCVD ($r = 0.677$, $P < 0.0001$) between differences in repeat scan volumes using the volume controller versus MDCT.

### 4.3.2 Turbine-Based Dynamic System

As demonstrated in the top panel of Figure 41, failures of the turbine system were more common. When end-expiratory lung volumes fluctuated they often trended in a particular direction. As seen in this example, a downward shift in lung density is noticeable in the time vs. density curve from the turbine-based system. Once the subject began inhaling xenon gas, they became distracted and no longer maintained an adequate seal around the mouthpiece resulting in a greater volume of inspired versus expired gas causing the end-expiratory lung volume to increase resulting in a decrease in lung density over time;

contrary to the expected increase in density over time expected with the buildup of xenon gas.

While testing of the enhancements to the turbine-based system to enable dynamic lung volume control indicated that a trained operator could maintain a consistent lung volume over time, the majority of recruited subjects had moderate difficulty. None of the resulting images from the six subjects utilizing the turbine-based system for dynamic lung volume control were suitable for wash-in xenon-CT analysis.

### 4.3.3 Dual-Piston-Based Dynamic System

The dual-piston system has been better tolerated and has successfully facilitated dynamic wash-in xenon-CT studies in 31 out of 41 human subjects. Failures were due, most commonly, to subjects not following verbal instructions or proper procedures, predominantly resulting in an inadequate seal around the mouthpiece preventing the system from accurately controlling lung volume.

When the system worked, a repeatable end-expiratory lung volume was achieved and can be verified by examining the improved time versus density curves from these subjects. An example set of curves from a subject using the dual-piston system are displayed in the lower row / middle panel of Figure 41. With the improved regional curve fits, one can also observe a greatly improved color-map reflecting regional sensitivity to local lung function differences (*right panel*). Gravitational gradients in lung density are evident by the incremental shift of baseline density demonstrated by the early time points of the regional time-density curves displayed in the middle column of Figure 41 whereby the non-dependent lung region is more expanded than the dependent region at FRC. Additionally, the wash-in rate seen the lower middle panel is considerably slower (ventilation is reduced) in the non-dependent lung region, consistent with known physiology (43). The color-map in the lower-right panel of Figure 41 also reflects the vertically oriented differences in ventilation.

## 4.4 Discussion

Our static volume control system presented here utilizes a turbine-based flow meter that was determined to be the best balance between the strengths and weaknesses of previously described methods. The turbine is based on the principle of impeller rotation, and is therefore only affected by the volume of gas that moves across it while unaffected by temperature, humidity, or gas composition. While suitable for static breath-hold volume control, the system was ultimately not suitable for dynamic imaging. We thus presented a second system suitable for dynamic imaging consisting of a dual set of custom rolling seal pistons. The primary purpose of the lung volume controllers, maintaining a consistent lung volume during imaging, was successfully demonstrated using both the turbine-based breath-hold system and the dual piston-based dynamic system.

The newly designed turbine-based system performed well under mechanical testing and during the in-vivo breath-hold imaging (Figure 39). As shown in **Error! Reference source not found.**, study failure (with the turbine-based static breath-hold system) was not related to a particular subject characteristic or a particular technologist, but rather was influenced by individual subject compliance with instructions. With increased technologist familiarity with the system and with instructing the subjects, success of volume control improved.

To increase subject comfort, and thus compliance, the systems were designed to incorporate a mouthpiece for subject interaction. Subjects must themselves ensure a complete seal around the mouthpiece by biting down on the bite guards and firmly closing their lips around the mouthpiece. The system can only measure the volume of air that actually moves through the circuit. Thus, if subjects do not completely seal the circuit, the system will not accurately control lung volume. Detecting this type of leak is difficult; currently there is no way for a technician to easily identify the problem other than noticing a consistent increase or decrease in the subject's overall volume during

steady-state tidal breathing. This could potentially be resolved through the use of a facemask in the future, which provides an improved seal for the circuit. However, facemasks give an increased sense of confinement and can fail to seal if subjects have facial hair. It is clearly a given that compliance in the presence of significant disease will be less. It is our belief that such a system of volume control is more appropriate for subject populations in which quantitation of early disease and disease progression is sought.

The VMM-400 manufacturer specifications indicate optimal linearity of measurements in the 0.2 – 2.0 L/s flow rate range (±1.5% of reading) and an accuracy of ±1.5%. Above and below this range the system becomes increasingly unreliable. Therefore, specific care is required to ensure patients breathe in the appropriate flow range. This will sometimes require more than one attempt at achieving a desired volume as to ensure accuracy. The VMM-400 was designed primarily for respiratory cyclic flow, but can also be used to measure uni-directional flow. The turbine was designed to minimize friction on the impeller to allow for the measurement very low flow rates, however this creates an artifact during uni-directional flow when the rate goes to zero; the impeller continues to spin for short time causing a volume overshoot. This overshoot is flow rate dependent and is more significant at higher flow rates. Calibration and coaching can help minimize this issue by re-zeroing before each scan and limiting starts and stops and maintaining as smooth a respiratory cycle as possible.

We have observed that a flow rate indicator / warning light, letting the subject and technician know when inspiration or expiration is occurring too slowly or quickly (out of bounds for the turbine's linear range) would be useful. Additionally, a system to detect leaks around the subject's mouthpiece would likely reduce failure rates. It has been demonstrated in earlier studies that TLC is a more reproducible lung volume compared to FRC (102,103,180-182). Our studies show that, with the use of the turbine volume

controller (Figure 39), the difference between TLC and FRC repeatability is negligible (0.99391 vs. 0.97156).

The dual-piston dynamic lung volume control system successfully controlled lung volume in 31 out of 41 subjects, a considerable improvement over the success rate experienced with the turbine-based dynamic system or cases in which lung volume control was not used. The failure to control lung volume from breath-to-breath was not due to any technical or mechanical problems inherent in the system design but rather was a function of subject non-compliance in following instructions or proper procedures. Again, maintaining an adequate seal around a mouthpiece requires subjects to sustain proper focus on their breathing, a task that can be difficult for extended periods. The slight anesthetic effects of xenon make focusing and following instructions more difficult. This often resulted in proper lung volume control during the baseline breaths and initial xenon wash-in phase but loss of compliance as the levels of systemic absorption of xenon increased. Empirically, we have found that the number of scans can be significantly reduced by eliminating some of the later time points that were often excluded because of subject non-compliance. The wash-in xenon-CT scanning protocol for the 41 subjects in this study was comprised of 3 baseline and 17 xenon wash-in breaths. By reducing the number of baseline scans from 3 to 2 and reducing the wash-in phase from 17 scans to 12, we have been able to reduce the radiation dose by 30%.

We recognized that the wash-in xenon-CT method presented here is likely too complicated for routine clinical use. However, when performed properly it provides considerable information about regional lung function, including influences of heterogeneous resistance of various forms that may not be obvious from a single inspiratory maneuver. The strength of the method presented lies in the fact that it provides a dynamic protocol against which newer, more clinically feasible, single breath dual-energy xenon-CT, can be compared.

This study demonstrated that if care is taken, one is able to coach patients to a standardized lung volume. Because lung density and airway metrics are lung volume dependent, the standardization of lung volumes during imaging is required for both cross sectional as well as longitudinally designed studies.

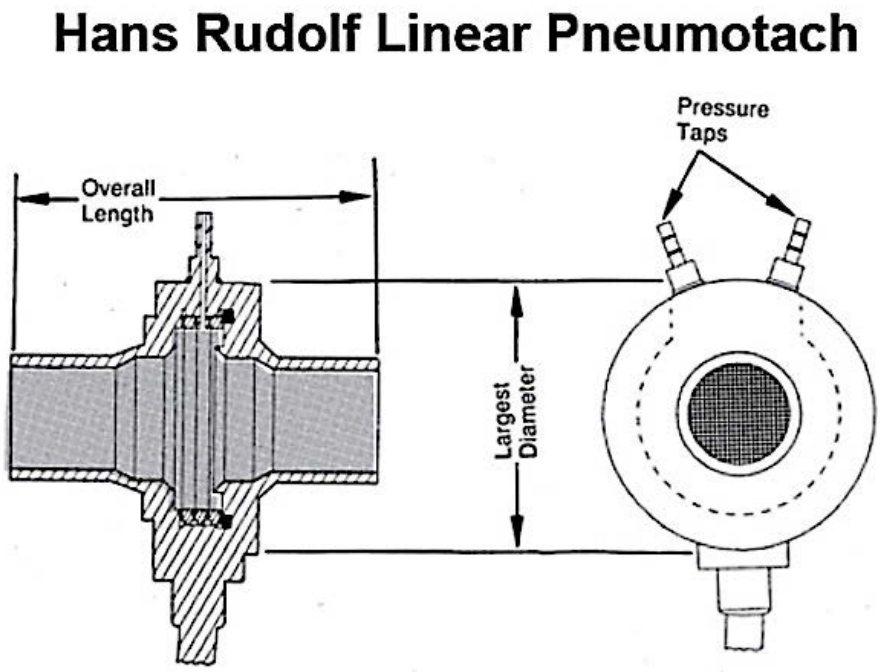


Figure 32. Manufacturer's diagram of the Hans Rudolf Linear Pneumotach that is commonly used in systems for monitoring inspired gas flow and lung volume.


Figure 33. Components of the turbine-based breath-hold lung volume controller: overall system (*top panel*); Interface USA, VMM-400 turbine-based flow meter (*bottom-left panel*); Hans Rudolph two-way balloon occlusion valve (*bottom-right panel*).

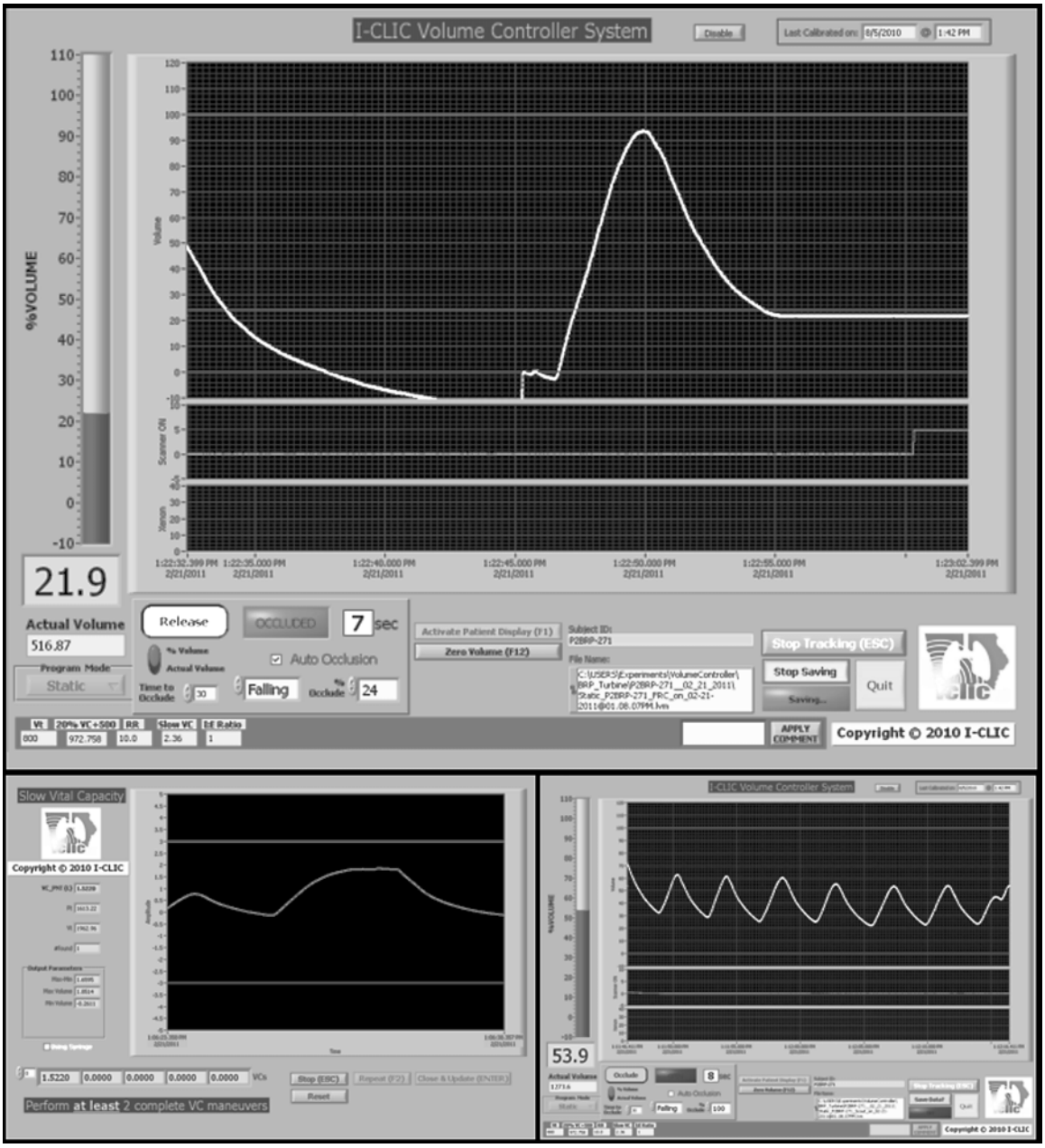


Figure 34. Screenshots of the LabVIEW control interface, during an FRC scan *(top panel)*, during SVC calibration *(bottom-left panel),* and during tidal breathing *(bottom-right panel)*.

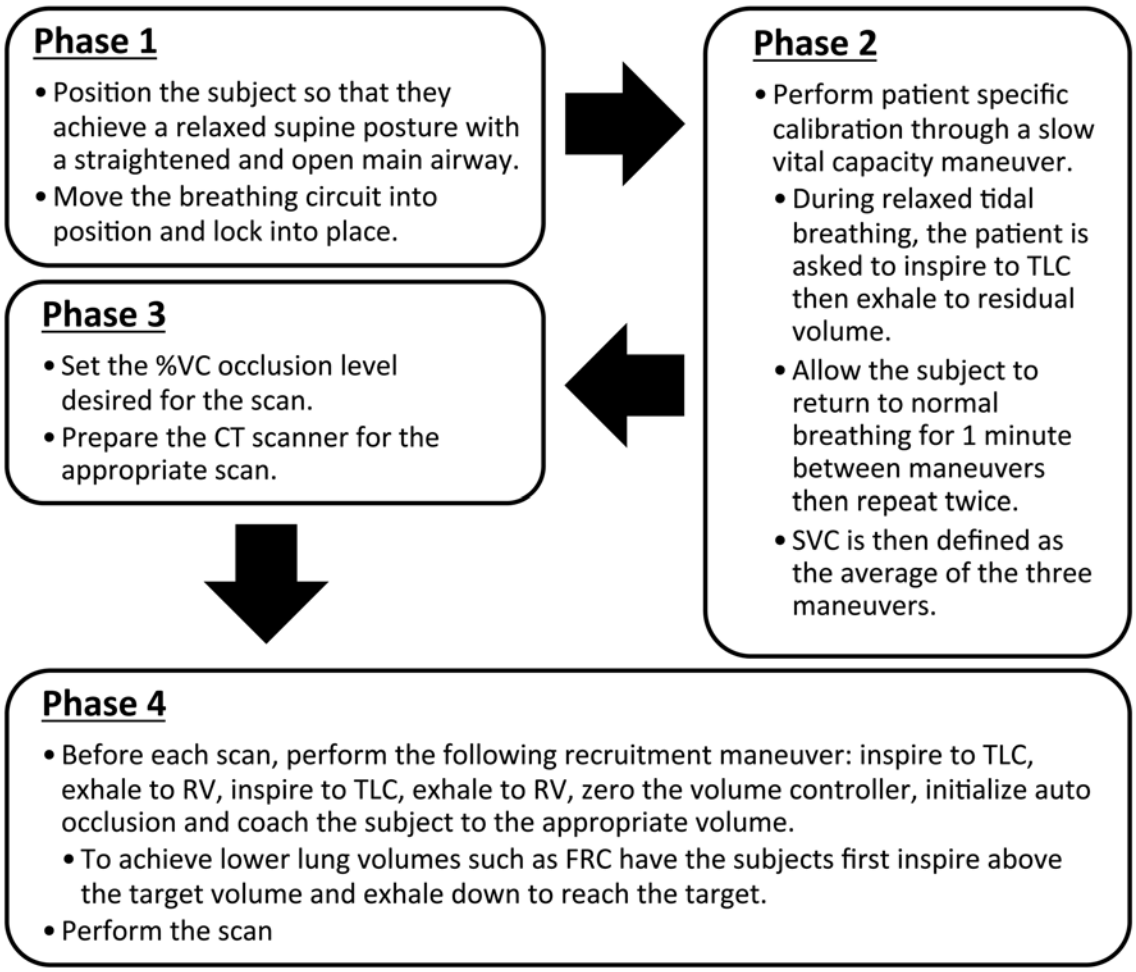


Figure 35. Flow diagram of turbine-based breath-hold volume controller usage.

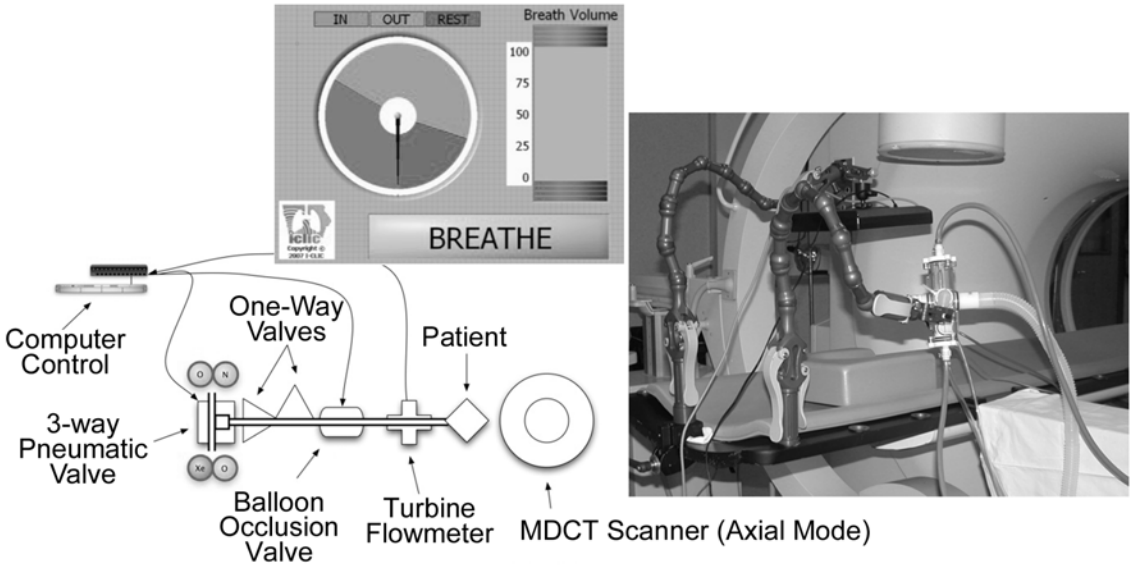


Figure 36. Adaptation of the turbine-based breath-hold volume controller for dynamic xenon-CT. CIVCO's "Imaging Overlay" which is made of carbon fiber with a foam core is positioned onto the scanner table which in turn allows for the attachment of CIVCO multi-articulated arms to custom fit the volume control's patient interface so that the subject can comfortably bite down on the system mouthpiece (*right panel*). A second multi-articulated arm is used to hold the display screen used to help guide the subject regarding inspiratory timing and depth of breathing (*left panel*).

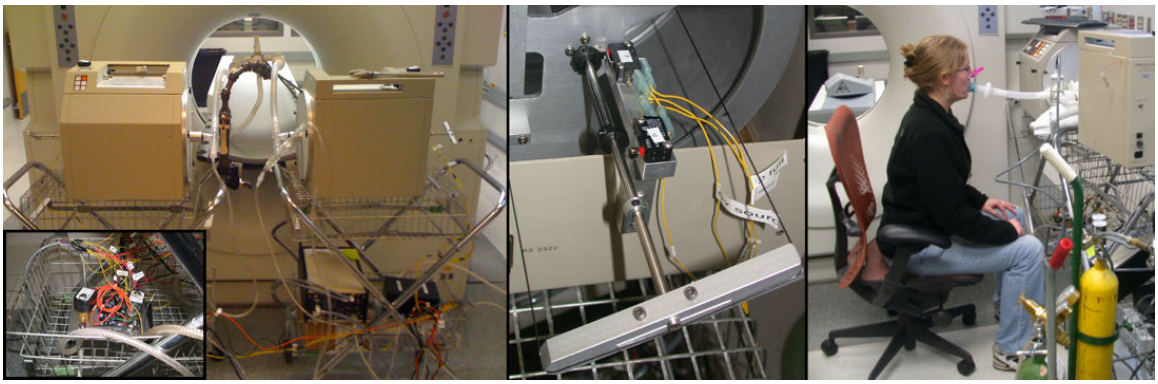

Figure 37. Initial prototype design of the dual-piston dynamic lung volume controller. The system was assembled using commercially available rolling-seal spirometers (S700: SensorMedics / Viasys / CareFusion, Yorba Linda, CA) that allowed us to test the design concept without spending considerable time manufacturing custom hardware. A series of external solenoid valves (*bottom-left panel*) and micro-switches (*middle panel*) were added to facilitate system operation.

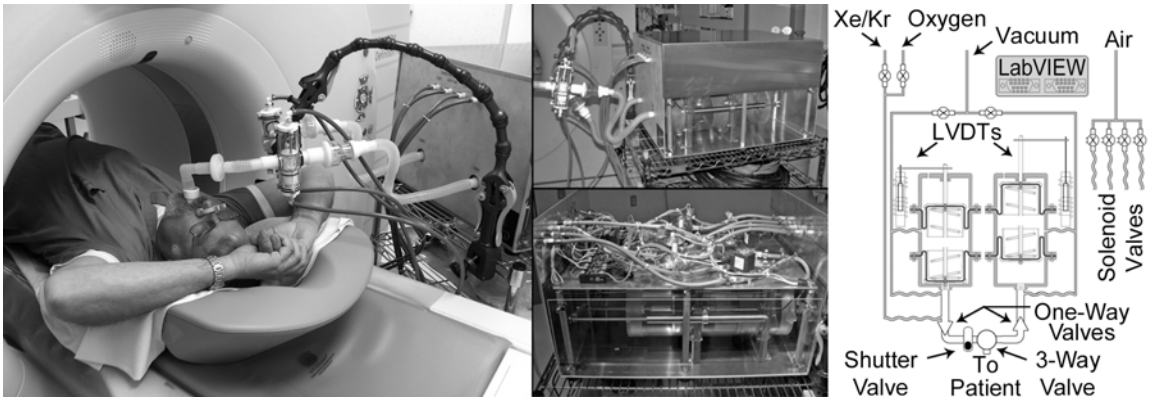


Figure 38. Photograph and schematic diagram of the dual-piston rolling seal volume controller. During a wash-in xenon-CT study, the system is situated next the to scanner table with the subject positioned inside the gantry for axial image acquisition (*left panel)*. The lower portion of the system casing *(middle-top panel)* is composed of Plexiglas to allow visualization of piston motion by the system operator. Through the Plexiglas casing, the separate Plexiglas rolling seal pistons can been seen with their LVDTs positioned along the side. The upper casing has been removed (*middle-bottom panel*) to reveal the system's internal components including electronics and solenoid valves. A simplified schematic diagram illustrates individual component connectivity (*right panel*).

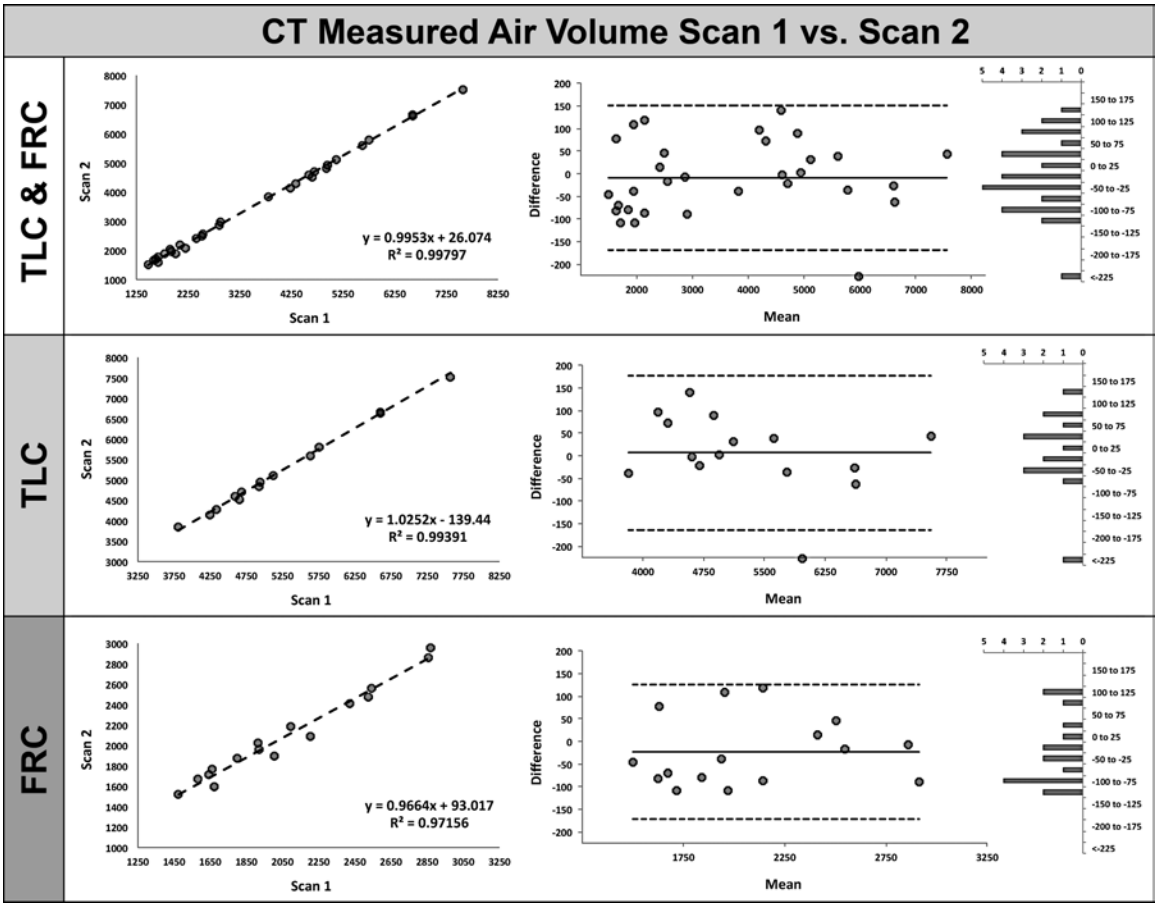


Figure 39. MDCT measured air volume correlates well between repeated scans utilizing the turbine-based breath-hold lung volume controller. Plots of CT-measured air volume comparing scan 1 vs. scan 2 for TLC & FRC combined (*left-top panel*), TLC (*left-middle panel*), and FRC (*left-bottom panel*). The middle and right columns show corresponding Bland-Altman and difference value histogram plots for each group.

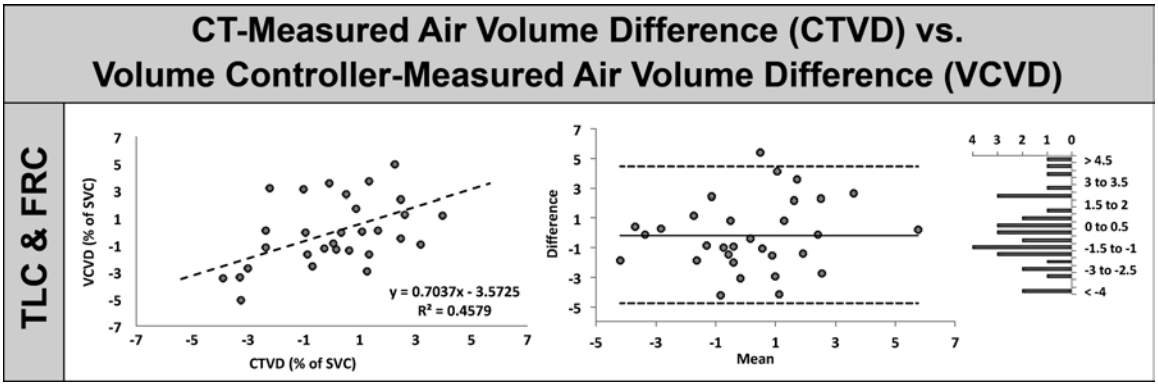


Figure 40. The CT-measured air volume difference (CTVD) between repeated scans correlates well with the analogous turbine-based breath-hold volume controller-measured air volume difference (VCVD). Plots of CTVD vs. VCVD for TLC & FRC combined (*left panel*), Bland-Altman (*middle panel*), and difference value histogram (*right panel*).

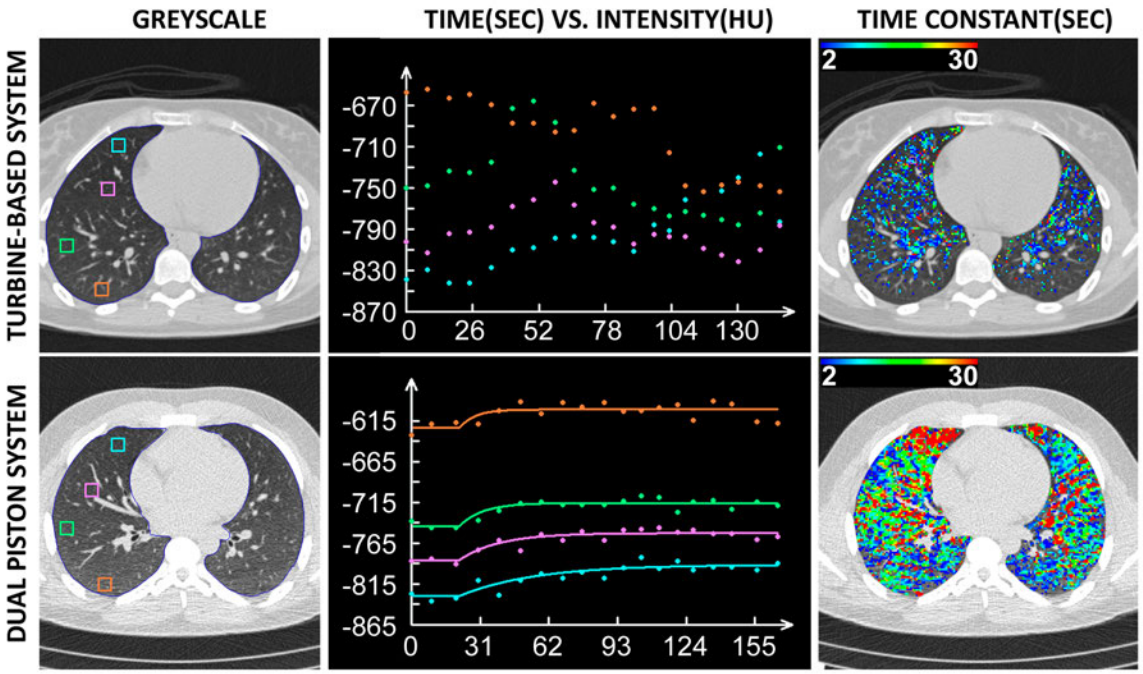


Figure 41. Wash-in xenon-CT results: The turbine-based dynamic system fails to maintain a consistent end-expiratory lung volume yielding noisy time vs. density curves (*top-middle panel*) and incorrect and incomplete color-map data (*top-right panel*). The dual-piston system more reliably controls end-expiratory lung volume yielding cleaner time vs. density curves (*bottom-middle panel*) and accurate and complete color-map data (*bottom-right panel*). Note the lower density and slower wash-in time constants (*blue curve, bottom-middle panel*) in the non-dependent vs. dependent (*orange curve, bottom-middle panel*) representing a greater lung expansion at FRC and reduced ventilation to this same region in the non-dependent lung region. This is in agreement with well-recognized heterogeneity of lung function. Despite the inconsistent lung volumes at FRC achieved by the turbine-based system, the same vertically oriented relationship in lung density is observed within the early time points.

| Parameter | p-value |
|---|---|
| Height | 0.876 |
| Weight | 0.336 |
| Age | 0.398 |
| Lung Capacity | 0.807 |
| Smoking Status | 0.925 |
| Gender | 0.590 |
| CT Technician | 0.351 |
| VC Operator | 0.771 |

Table 4. Results from a linear model indicate that none of the listed parameters statistically influence the difference between VCVD and CTVD.

# CHAPTER 5: IMAGE REGISTRATION AND POST-PROCESSING

As seen throughout this thesis, medical imaging is a powerful tool for studying the regional structure and function of the lungs. However, as the technology behind MDCT image acquisition has evolved to increase spatial and temporal resolution, the burden of data management and analysis has become more challenging. Thus it is necessary to design and implement tools that can simplify the image analysis process, while at the same time use caution and remember to evaluate how these tools shape our understanding and interpretation of the results.

The image processing content of this thesis has been divided into two sections: 1) time-series image registration in order to adjust for subtle inflation or motion based artifacts that occur during the acquisition of time-series image datasets and 2) a regional, parenchymal signal analysis tool that can be used to filter functional imaging results as well as characterize their results by performing statistics on an entire dataset or on a series of sub-divided regions. These tools have been widely utilized throughout this thesis and throughout our laboratory in general for a variety of projects.

To implement these tools, a series of programs were written in C++ using an ITK-based application framework (31). The code is structured to easily allow for further enhancements in the future and contains the appropriate level of commenting throughout in order to simplify this process for future users. To create a simple execution workflow as well as provide a consistent way of documenting input parameters for each program, a common Windows batch (.bat) file is used. While not currently developed, a similar-style batch execution script could also be easily implemented in a Linux environment. Where appropriate, it is possible to input an additional *.txt* parameters file to provide flexibility in the program's input. For example, the user can adjust the number of filters or registration levels by altering the number of parameters in the corresponding parameter input file. This approach allows for easy manipulation of the available input parameters

(Table 5, Table 6, Table 7) without requiring the user to manually input a large number of flags during the execution process or necessitating a recompile of the applications due to hard coded parameters. This flexible input parameter process is facilitated through the use of the MetaCommand (Kitware) option available in ITK, which parses command line options to execute the each program with the desired parameters. This including images, masks, labels and other input parameters.

The medical imaging community utilizes numerous image data formats that are currently available including Analyze, Nifti and Nrrd. Based on the current tools used in our laboratory, the Analyze 7.5 (originally developed in conjunction with the DSR project discussed in Chapter 2) was chosen as the default file format. Our in-house software solution, Pulmonary Analysis Software Suite (PASS), is used to import DICOM image series generated by reconstruction algorithms on the MDCT scanner and convert them into the Analyze 7.5 file format (161). PASS utilizes a modified Analyze 7.5 file format that retains the 4D timing information normally stripped from the DICOM image headers when creating and Analyze file. By retaining this information, PASS is able to properly perform times-series based calculations. In addition, PASS includes previously described semi-automated lung segmentation tools that are used in this thesis to generate initial lung segmentation masks. PASS also provides an environment for manual editing these masks when necessary.

## 5.1 Time-Series Image Registration

Time-series imaging enables the measurement of functional information from MDCT, a technology designed primarily to measure structure, by examining how the densities of structures change over time. If you use a series of equations to define a model of physiological function and fit time-series density data to that model, you can extract information that characterizes the physiological function. MDCT measures the density of an object in three dimensions. Thus if that object stays in a consistent location

within the image over time while its density is changing, MDCT can be used to measure those changes. Conversely, if the object being observed changes size or location, it becomes likely that MDCT would measure intensity changes due to movement, partial volume effects and misalignment instead of the physiological process itself. This would cause considerable error in intensity-based time-series measurements and would severely diminish their usefulness. A significant advantage of MDCT over other imaging techniques is its higher relative spatial resolution. While this is an advantage when structures do not move, if structures shift between voxels at the level of image resolution during time-series imaging, high levels of noise would be caused as result and require the use of larger regions of interest (ROI) to average out the effects of motion.

In order to alleviate the concern of motion artifacts, two techniques are used to control the positioning of objects within the imaging field of view. First, as described in Chapter 4, the stability of subject positioning and lung volume between time points can be achieved through the use of various systems for lung volume control coupled with specific subject coaching techniques. While these methods considerably reduce positioning artifacts caused by free breathing, they do not completely eliminate all subject and cardiac motion artifacts nor do they always precisely control lung volume, as some subjects will fail to comply with breathing protocols and coaching instructions. Therefore, we have also incorporated an image registration workflow to further align time-series datasets that alleviates additional motion artifacts and allows ROI size to be reduced improving spatial resolution of time-series functional imaging measurements.

The development of novel image registration techniques is a complex and diverse field of study, and would likely require a body of work equivalent to a PhD thesis. As the aims of this thesis are focused on deriving small-scale functional measurements and not image registration algorithms, we utilize pre-existing methods to generate a robust workflow suitable for improving the results from time-series imaging. The Insight Segmentation and Registration Toolkit (ITK) was chosen as the platform for the

development of this registration workflow (31). ITK provides a flexible framework for the testing and development of image processing techniques and enables the exploration of multiple strategies without the need for "reinventing the wheel."

### 5.1.1 Methods

The primary aim for the development of an image registration workflow is to align time-series image datasets to allow accurate time-series intensity-based MDCT measurements of lung function. Image registration requires at least two images to function. First, a fixed image with the coordinate system of interest and second, a moving image that needs to be transformed into the fixed image coordinate system. When using time-series image data that was acquired while contrast material was added and observed over time, the initial phase of the dataset is typically used as the fixed image for time-series image registration. It usually represents the baseline-unenhanced state of the system, and all the other phases from the time-series can be individually considered as moving images and registered back to the initial phase.

Once you have identified two images to register, the image registration process consists of four parts: 1) a similarity metric that gives a measure of correspondence between the two images, 2) a transformation model that defines the path by which a moving image is deformed to match the fixed image, 3) an optimizer to maximize the value of the similarity metric and 4) an interpolation algorithm to apply the resultant deformation on the moving image (162,183-185).

In order to drive image registration, some measure of image similarity or difference must be employed to systematically compare the two images being registered. A similarity metric is usually based on a set of geometric or intensity-based features sometimes including both. Geometric features consist of identifiable anatomical landmarks, which can be easily identified in both images. Within the lungs these tend to consist of transition points such as airway or vessel walls, structural bifurcation points or

other such reasonably static structures. Intensity-based features are similarly strong in areas of transition within the images and define mathematical patterns that can be identified by the computer. The fundamental premise of using a similarity metric is that the pair of images will be most similar when they are properly registered. A number of different techniques were explored in the initial phases of testing during this project and the techniques with the most promise utilized the notion of mutual information. Mutual information maximizes intensity-based information common to the two images. In MDCT, image intensity is the primary piece of information available within an image. Since we are attempting to register images in which the intensity of a structure can change over time, simple metrics such as sum of square intensity differences would suffer from artifacts in the most contrast enhanced phases of the time-series dataset. Mutual information, on the other hand, uses density distribution information in the form of joint probability density distributions and can better match images of differing density (183,184).

Initially, we employed a simple workflow based on an example provided with the ITK code base that utilized rigid and affine transforms for the transformation model and were driven by a mutual information similarity metric using a gradient descent optimizer. A rigid transform allows for the translation and rotation of an object, but does not distort an image; preserving the distance between pairs of points, maintaining the size and shape of the object. This is often applied as an initialization process for more advanced registration methods. An affine transform, a very basic non-rigid transform, permits shear and stretch to be added to the transformation process. After some initial testing with this simple workflow, it quickly became apparent that while it provided and an improvement to image alignment, this workflow would not appropriately account for non-uniform expansion of the thoracic structures and we would need to use more complex methods to completely align our time-series image datasets. Therefore a b-spline transform, another type of deformable transform, was added to the image

registration workflow. A b-spline deformable transform overlays a grid of control points on the image that can be individually adjusted to allow for more complex non-linear deformations (183-186). This three-step workflow delivered adequate results in some cases, however suffered from slow run-times and was inadequate to properly align all datasets tested. While not completely successful, this initial workflow provided a way to obtain useful time-series imaging results until a more complex registration workflow could be developed (Figure 42).

Finally, a more flexible and sophisticated workflow was developed that incorporated multi-threading using the previous workflow as a template. This final workflow is customizable using both batch and parameter files. It allows for the optional use of rigid and affine transforms, and contains the framework for using multi-level multi-resolution b-splines transforms. It also has the options for specifying a mask file as well as defining of specific region boundaries, both of which can be used to reduce memory and CPU costs by limiting the size of the image regions used for registration. There is an option to perform density truncation, which limits the maximal density enhancement in order to more reasonably constrain intensity histogram values typically present in time-series blood flow data. Several options for image interpolation have been implemented including linear, b-spline and windowed-sync. Additionally, a few pre-processing steps are available options that can be used to improve registration accuracy. The steps include image smoothing (curvature anisotropic diffusion) and image sharpening (unsharp masking). Finally, the need for placing constraints on b-spline node displacement became apparent and was added to the workflow to ensure more realistic registration results. The full set of available parameters for the *TSreg* time-series image registration program is listed in Table 5 and the final workflow is presented in Figure 43.

### 5.1.2 Results

Image registration is a non-trivial task that can often produce unexpected results. As seen in an example case presented in Figure 44, the usage of a segmentation mask or b-spline node displacement can severely affect the results. The original greyscale image (phase 0, slice 12) (Figure 44, *top row & 2nd image column*) is subtracted to obtain difference images from each case and is presented in the *3rd image column* of Figure 44. The moving image (phase 18, slice 12) and the slice most visually similar to fixed image within that phase (phase 18, slice 6) are shown in Figure 44 in the 2nd row and 3rd row respectively. Registration results in the *4th row* were forced to only use voxels within the segmentation boundaries and resulted in an explosion of the lung boundaries (Figure 44, *4th row, 1st column*). In addition, this case did not incorporate b-spline node displacement constraints and resulted in extreme jacobian values (Figure 44, *4th row, 4th column*). Values for the jacobian in this physiological system should always remain positive and be reasonably constrained. Jacobian values in this case ranged from -8 to 20. When the image masking condition was substituted with a method that set the background voxels to a single intensity value, and b-spline node displacement constraints are added, the registration results became considerably improved (Figure 44, 5th row, 1st column). The values for the jacobian in this case are much more realistic and range from 0.25 to 1.6.

Identifying poor registration results from a simple visual inspection of the resultant deformed images is not always feasible. If you compare the greyscale images in the *top row* of Figure 45, visually you see highly similar images and would presume similarly accurate registration results. However, a closer inspection of the associated jacobian images in the *bottom row* shows a distinctly different story. When b-spline node displacement constraints were added in addition to permitting spatial sampling outside of the segmentation mask, the registration results improve dramatically (Figure 45, *bottom-right panel*).

Another way to examine the benefits of image registration connected with time-series image data is to examine the results of their analysis with and without registration. Figure 46 shows the wash-in xenon-CT results from an example human subject (Male 21yrs never-smoker) with and without registration. It includes a series of colormaps from each case that represent various parameters from the xenon-CT method including the magnitude of xenon wash-in, percent air based on initial ROI intensity, regional time constant of ventilation, and a measure of curve fit error - normalized RMS. While the colormaps for percent air match well, their similarity ends here. After registration, the colormap of ROI curve fit error is dramatically different. The effect of airway and vasculature motion between time-points affected the results for both wash-in magnitude and time constant as well. Image registration was clearly necessary to provide accurate time-series wash-in xenon-CT regional ventilation measurements from this subject.

### 5.1.3 Discussion

A robust image registration workflow has been developed and utilized to successfully align time-series wash-in xenon-CT and ECG-gated bolus iodine datasets to improve the accuracy of time-series measurements of regional ventilation and perfusion. It was designed to be flexible such that a user could easily vary input parameters to provide either a quick test of the registration outcome or comprehensive image registration that generates extremely well matched images needed for final image analysis. The workflow incorporates optional rigid and affine transforms, a multi-scale multi-resolution b-spline transform using node displacement constraints, and is driven by a mutual information metric optimized by the Limited-Memory Broyden–Fletcher–Goldfarb–Shannon (LBFGSB) optimizer. While this solution is adequate for our needs in a research environment, the lengthy time of execution per case (approximately 6 hours) would be an obstacle for more common clinical deployment. While ITK offers a proven method for developing image registration tools, its flexibility sometimes results in

decreased performance compared to custom designed image processing tools. Therefore the methodologies presented here can be rewritten on another platform if improved performance becomes necessary in the future.

## 5.2 Quick Compare: A Region-Based Image Analysis Tool

As discussed in Chapter 2, the lung is a heterogeneous structure comprised of a variety of elements with different structural and physiological properties. It is sometimes beneficial to separate these elements from one another to gain a clearer picture of how the individual elements contribute to function. Within the scope of this work, it was prudent to examine regional ventilation and perfusion solely in the lung parenchyma by removing the influence from detectable airway and vasculature structures. After the parenchyma was isolated, we also needed to develop a straightforward way of presenting the functional results that could be use to compare the results from different subjects or functional methodologies.

### 5.2.1 Methods

The region-based analysis is comprised mainly of two software programs. The first program, *Vesselness*, is designed to import 3D or 4D greyscale MDCT scans of the lungs and a previously created lung segmentation mask to generate a new lung mask with the airways and vessels removed. The second program, *QuickCompare*, takes the results of a functional MDCT scan as the input, and outputs the results of a region-based statistical analysis in the form of a *.csv* file or as additional Analyze 7.5 images.

#### *Vesselness Segmentation Program*

Several approaches for removing airway and vessel structures from the lung segmentation were attempted, beginning with simple thresholding-based approaches. After our initial testing, it became clear that a simple thresholding approach would not be sufficient to extract the vessels. We therefore have implemented a solution that combines

double thresholding to segment large airways, while using a vesselness measure to segment the vasculature.

Measured densities within large airways generally lie in a predicable range relative to lung inflation. This would suggest that a single threshold might be capable of performing a proper segmentation. However, a single threshold can sometimes be unreliable in the presence of image noise and partial volume artifacts that cause neighboring structures to blur together giving the impression of speckled airways in the presence of noise. The *DoubleThresholdFilter* addresses the difficulty of selecting a single threshold that will select the objects of interest without selecting extraneous voxels by instead considering two threshold ranges: a narrow range and a wide range (where the wide range encompasses the narrow range). When used in a traditional single thresholding process, the wide range would often include many extraneous voxels that would survive the threshold operation. While at the same time, if only the narrow range was used, then too few of the voxels would survive the thresholding process. Instead, the *DoubleThresholdFilter* uses the narrow threshold image as a marker image and the wide threshold image as a mask image for geodesic dilation. Essentially, the marker image (narrow threshold) is dilated but constrained to lie within the mask image (wide threshold). Thus, only the objects of interest (those pixels that survived the narrow threshold) are extracted, but they appear in the final image as if they had the wide threshold instead. This filter implements requires an input of four greyscale values (wide range min, narrow range min, narrow range max, wide range max) and the coordinates of a seed point placed in the central airway tree. These values are obtained from the user input in the batch file.

When segmenting bright structures like blood vessels, thresholding can be confounded by inflammation and atelectasis. Therefore an approach that incorporates not only the intensity of a structure but its shape as well can be beneficial. The *Hessian3DToVesselnessMeasureImageFilter* takes into account that the Eigen values

play a crucial role in discriminating shape and orientation of structures. Bright tubular structures will have low $|\lambda_1|$ and large negative values of $|\lambda_2|$ and $|\lambda_3|$. Conversely dark tubular structures will have a low value of $|\lambda_1|$ and large positive values of $|\lambda_2|$ and $|\lambda_3|$. The *Hessian3DToVesselnessMeasureImageFilter* uses a line filter to provide a vesselness measure for tubular objects from the hessian matrix. The filter takes as input an image of hessian pixels and preserves pixels that have Eigen values $|\lambda_3|$ close to 0 and $|\lambda_2|$ and $|\lambda_1|$ as large negative values (for bright tubular structures). The *MultiScaleHessianBasedMeasureImageFilter* evaluates a Hessian-based enhancement measure, such as vesselness, at multiple scale levels. The Hessian-based measure is computed from the Hessian image at each scale level and the best overall response is selected. The user specifies the minimum and maximum sigma values as options in the batch file along with the number of scale levels to perform. Exponentially distributed scale levels are computed within the bound set by the minimum and maximum sigma values. A higher number of scale levels can provide greater accuracy, but requires additional computation time.

Prior to performing either the greyscale airway or vessel segmentation the user has the option of performing a few pre-processing steps to either increase accuracy or decrease processing time. The *CurvatureAnisotropicDiffusionImageFilter* has been implemented to reduce the effect of image scatter and should be used in most cases. Similar to the implementation within the time-series image registration workflow presented above, user specified values for time step, number of iterations, and filter conductance can be provided in the batch file. Additionally, the option to downsample the image by a factor of 2 or crop the dataset to the mask boundaries are available to the user to decrease execution time. The use of the image cropping option is suggested by default, however, downsampling should only be used when absolutely necessary, as it will degrade the final results due to a loss of spatial resolution.

In addition, a number of morphologic operators are implemented as options to further improve the final segmentation results. These options include pruning and closing operators in addition to basic dilation and erosion. The overall workflow for the *Vesselness* program is depicted in Figure 47.

*Regional Analysis Program (QuickCompare)*

With the vessels and large airways removed from the lung segmentation mask we then needed to determine a consistent way to characterize and compare the results from functional scans between interventions and methodologies. A flexible workflow was developed that allowed the user to divide the lung into as many regions as needed (up to the voxel resolution of the dataset). The user simply specifies the number of regions in the X, Y and Z-axis directions and the program divides the scan accordingly. In addition, the user has the option of either specifying specific analysis boundaries can opt to let the program to automatically limit the analysis solely to the area within the lung segmentation mask. The ability to define specific analysis boundaries can be necessary to facilitate comparisons with other methods that have limited spatial resolution and lack anatomical markers needed for alignment other than the outline of the thorax. For example, in our laboratory, we have performed an experiment utilizing xenon-CT as the gold standard to test the effectiveness of electrical impedance tomography (EIT) measurements of regional ventilation and perfusion. Besides dividing the analysis region, the program was allows the user to filter the functional image data input by placing limits and defining acceptable values for the main functional parameter. In addition, the program permits the user to specify additional filter criteria, as desired, each with their own acceptable value limits.

After the analysis region is divided into sections and filtered, statistics are performed on each section in order to determine the number of valid voxels, the sum of the functional parameter, the mean value, its standard deviation and coefficient of

variation. A similar set of parameters is determined considering the entire lung region as a single unit. Finally, the program incorporates two normalization schemes, allowing the user to normalized the data by either the mean value or sum. Similar region and whole lung statistical analyses are then repeated for the normalized dataset.

The *QuickCompare* program can outputs two types of results: 1) Analyze 7.5 images that reflect the calculated results including the filtered, normalized and region-based datasets, and 2) a *.csv* file that includes the data from both the standard and normalized datasets (if normalization is selected). Additional statistical analysis can be performed on the output of *QuickCompare* by importing the *.csv* files into Microsoft Excel or other statistical processing programs such as CRAN (*v2.9.2*) or PASW (*v19, SPSS Inc., Chicago, IL*). These programs contain powerful tools for statistical analysis and did not need to be duplicated in a custom ITK-based program.

### 5.2.2 Results

#### *Vesselness Segmentation Program*

The use of a double threshold filter allows for better segmentation of the airway tree than single thresholding alone. When using single threshold range of -1024 to -830 on an example human subject (Figure 48, *top row*) significant extraneous voxels are selected predominantly in the greater expanded non-dependent lung. Conversely, when double thresholding is used with a wide range of -1024 to -830 and a narrow range of -1024 to -905 (Figure 48, *bottom row*) only the desired voxels are selected. When segmenting the vasculature, the use of a multi-scale approach allows for the segmentation of both small and larger caliber vessels. This is accomplished by varying the sigma value over a number of steps. Using 2 steps (Figure 49, *top row*) yields results with a high number of small sized vessels, but also more errors from noise. Using 6 steps (Figure 49, *bottom row*) yields a cleaner vessel tree that is able to handle both small and large

vessels. Vessels in the 6-step process are solid while vessels using from the 2-step process sometimes contain gaps (Figure 49, *top row*).

Multi-scale vesselness requires a considerable amount of available computer memory and depending on dataset size, downsampling can be necessary to allow the vesselness program to properly execute using the amount of system memory available. While downsampling would allow the program to execute on a computer with limited memory, it would also result in a loss of spatial resolution producing a staircase effect on the edges of vessel borders. For example, a full lung human dataset (512x512x575 voxels, with voxel dimensions 0.6x0.6x0.5 mm) takes 3 minutes and 40 seconds to execute after downsampling while the full resolution dataset requires 6 minutes and 30 seconds.

With the airways and vessels removed the parenchyma can be analyzed without contamination. An example of the final result of the *vesselness* program, a lung mask with the airways and vessels removed, is shown in Figure 51.

*Regional Analysis Program (QuickCompare)*

The ability to filter our data and analyze it on a regional basis is crucial to furthering our understanding of lung function and facilitates the comparison of function on a regional level between interventions or methodologies. Figure 52 depicts the output of *QuickCompare* using a variety of example settings performed on DECT perfused blood volume (CT-PBV) dataset from an animal subject that had a portion of its pulmonary vasculature occluded with a balloon. The panels in Figure 52 show from left to right then top to bottom the original greyscale image, the original DECT functional CT-PBV image, a normalized and filtered CT-PBV image, then the results of using 2-X 10-Y 1-Z, 2-X 10-Y 5-Z, 40-X 40-Y 20-Z, 10-X 2-Y 1-Z or 10-X 2-Y 5-Z regions.

## 5.3 Time-Series Algorithm Improvements

### 5.3.1 Improvements in Non-Linear Curve Fitting

The ability to derive functional data from time-series imaging is contingent on finding an appropriate mathematical model for each physiological process. As explained in Chapter 2, the wash-in xenon-CT method employs Kety's model of inert gas wash-in to describe regional ventilation through a single compartment exponential model. Similarly, dynamic ECG-gated perfusion-CT (CT-PBF) uses a gamma-variate model to describe the first pass kinetics of a bolus iodine tracer injection. Critically important to the success of using either mathematical model to describe a set of time-series data points is the ability of non-linear curve fitting procedures to accurately portray the underlying data. Several enhancements to the non-linear curve fitting algorithms developed for animal use were necessary to apply these methods on human subject data due to increases in artifacts and noise.

Time-series analysis in our laboratory is accomplished using the TSIA module of Pulmonary Analysis Software Suite (PASS)(161). PASS utilizes the Numerical Recipes (NR) library for a variety of core mathematical functions including solving systems of non-linear equations with the Levenberg-Marquardt method (187). The implementation in NR is widely used throughout the scientific community, however is subject to some limitations. The most serious limitation of the implementation of the Levenberg-Marquardt method in NR is the ability to apply constraints to individual parameters. Without parameter constraints, it is possible for the optimal solution to contain impossible or non-physiologically values for individual parameters. This limitation could then result in incorrect functional parameters derived from the improper curve fit and thus yield incorrect conclusions based on their results. As the number of ROIs in a single dataset can number in the millions it would be a daunting task to check every curve fit by hand. Therefore the newest versions of both the wash-in xenon-CT algorithm (*KCB5*)

and the dynamic perfusion CT-PBF algorithm (*Wolfkiel7*) contain modifications to the NR library to implement boundary constraints. Additionally, both algorithms include quality control checks to evaluate whether or not the final curve fit results are possible based on known physical parameters at the time of scanning. For example, as human wash-in xenon-CT scans are performed using a tube voltage of 80 kVp before and during the inhalation of 30% xenon gas. We can determine based on known CT attenuation values for xenon gas at 80 kVp (~2.25 HU⇧ per % xenon) that the maximum density enhancement from will be around 68 HU. Thus, if the intensity of a data point is enhanced greatly above this level then it is most likely an artifact and does not represent true ventilation. Additionally, *Wolfkiel7* was developed using the simplified formulation of the gamma variate model, rather than the traditional model, to allow for a more robust fitting procedure (188,189).

Figure 53 illustrates the improvements in the wash-in xenon-CT algorithm using the new parameter-constrained algorithm. Curve fit error is dramatically reduced (Figure 53, *bottom row*) and the values for wash-in magnitude (Figure 53, $2^{nd}$ *row*) and time constant (Figure 53, $4^{th}$ *row*) are more realistic. While the results in Figure 53 are an improvement, the combination of both image registration and algorithm improvements were necessary to consistently provide accurate functional results for our human wash-in xenon-CT subjects presented in Chapter 6.

### 5.3.2 Optimizing the xenon-CT Scanning Protocol

Transitioning the xenon-CT method from the laboratory to the clinic required protocol optimization in order to obtain the maximum information with the minimum amount of risk to the subject. Excess radiation and xenon exposure is a noteworthy concern when using the wash-in xenon-CT method with human subjects. Therefore we needed to be diligent to minimize the exposure to both. The level for acceptable radiation exposure set by our IRB permitted the acquisition of 20 time-points during a wash-in

xenon-CT study. Therefore we needed to determine how to best utilize 20 scans to accurately portray regional ventilation while at the same time determine if it was possible to use fewer than 20 scans. To tackle this issue we utilized an animal xenon-CT dataset comprised of 45 consecutive data points (10 unenhanced baseline scans while breathing room air and 35 during xenon gas wash-in) and manipulated the number of scans used to perform the exponential curve fitting (Figure 54).

We compared the curve fit results from: 1) all 45 time points; 2) 3 baseline and 17 wash-in consecutive time points; 3) 3 baseline, 3 during the rapid rise and 16 every other breath during wash-in; and 4) 3 during baseline and 4 randomly selected throughout the wash-in portion. From the strategies explored, it was clear that a minimum of 2-3 scans should be devoted to obtaining an accurate baseline value, and the rest should be distributed to cover the xenon wash-in. For high ventilating regions, a clustering of data points near the initial density rise is important to accurately capture the time constant. For slow ventilating regions, spreading out the remaining time points to cover as much time as possible helped to accurately represent the density level after equilibration.

Due to a 10-second time limit between scans on the Siemens Somatom 64, it was necessary to use the method incorporating 20 sequential breaths (3 room air baseline and 17 xenon wash-in). Unfortunately, this approach does not always allow for complete equilibration in slow ventilating areas possibly making their results less reliable. Picking 4 widely-spaced breaths during wash-in, a strategy implemented previously by some groups (190), cannot capture the true exponential nature of the xenon wash-in curve and yielded extremely flawed results (Table 8).

The ideal strategy, if equipment and subjects complied properly, would be to scan sequentially in the first few breaths of wash-in, and then every other to increase the time available to complete wash-in in slow ventilating regions. However, as discussed in Chapter 4, maintaining an adequate seal around a mouthpiece requires subjects to sustain proper focus on their breathing, a task that can be difficult for extended periods especially

with the slight anesthetic effects of xenon. Therefore based on real world testing in our human subjects we recommend eliminating some of the later time points that were often excluded because of subject non-compliance. We can reduce the number of baseline scans from 3 to 2 and reduce the wash-in phase from 17 scans to 12. This reduction in the number of scans will reduce the radiation dose to the subject by 30%.

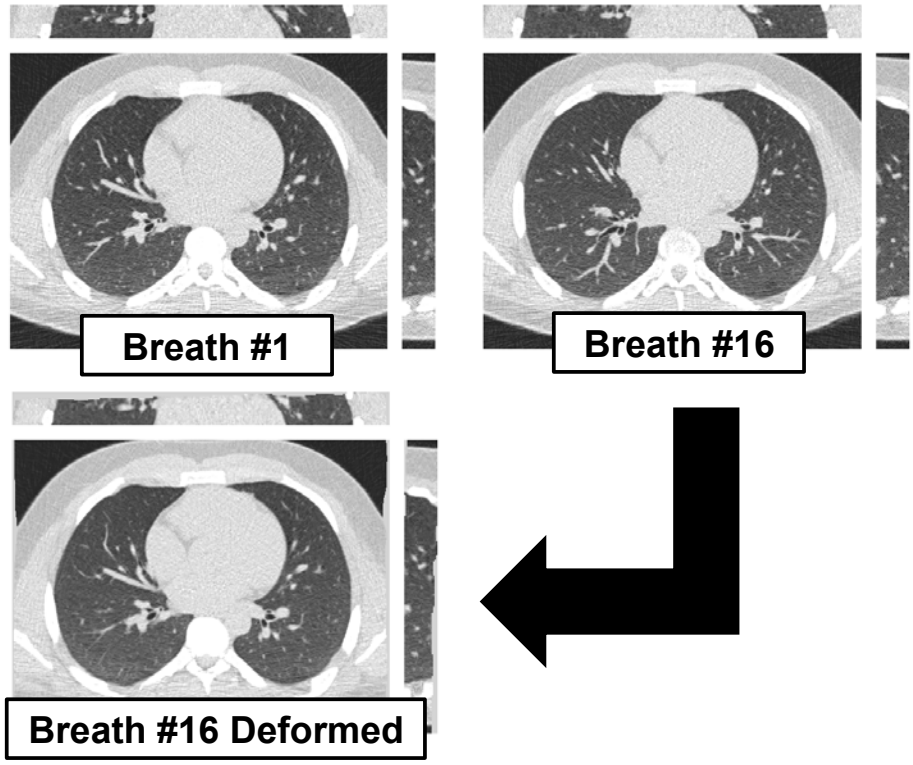


Figure 42. An example of the improvements in alignment by using the initial workflow designed to perform time-series image registration.

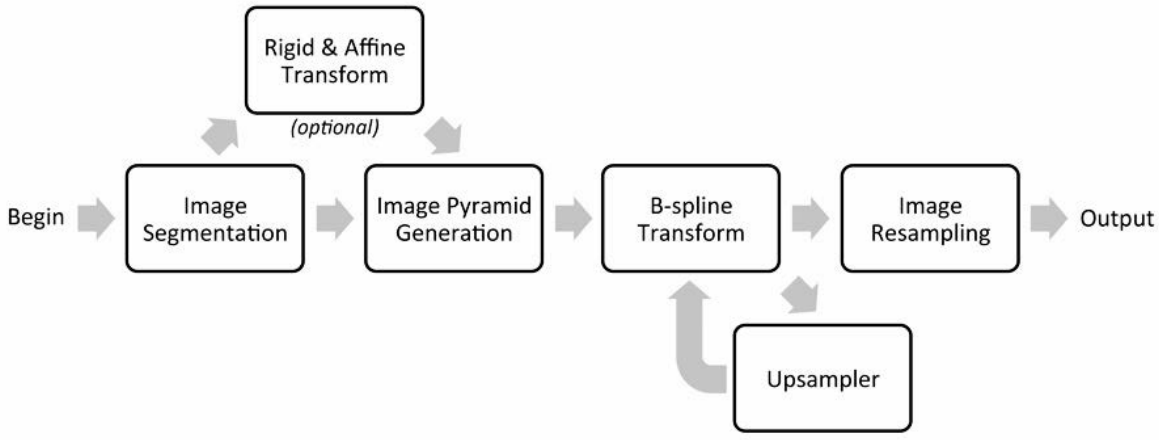


Figure 43. Schematic diagram of the final time-series image registration workflow that allows the use of a multi-resolution image pyramid and multi-level b-splines.

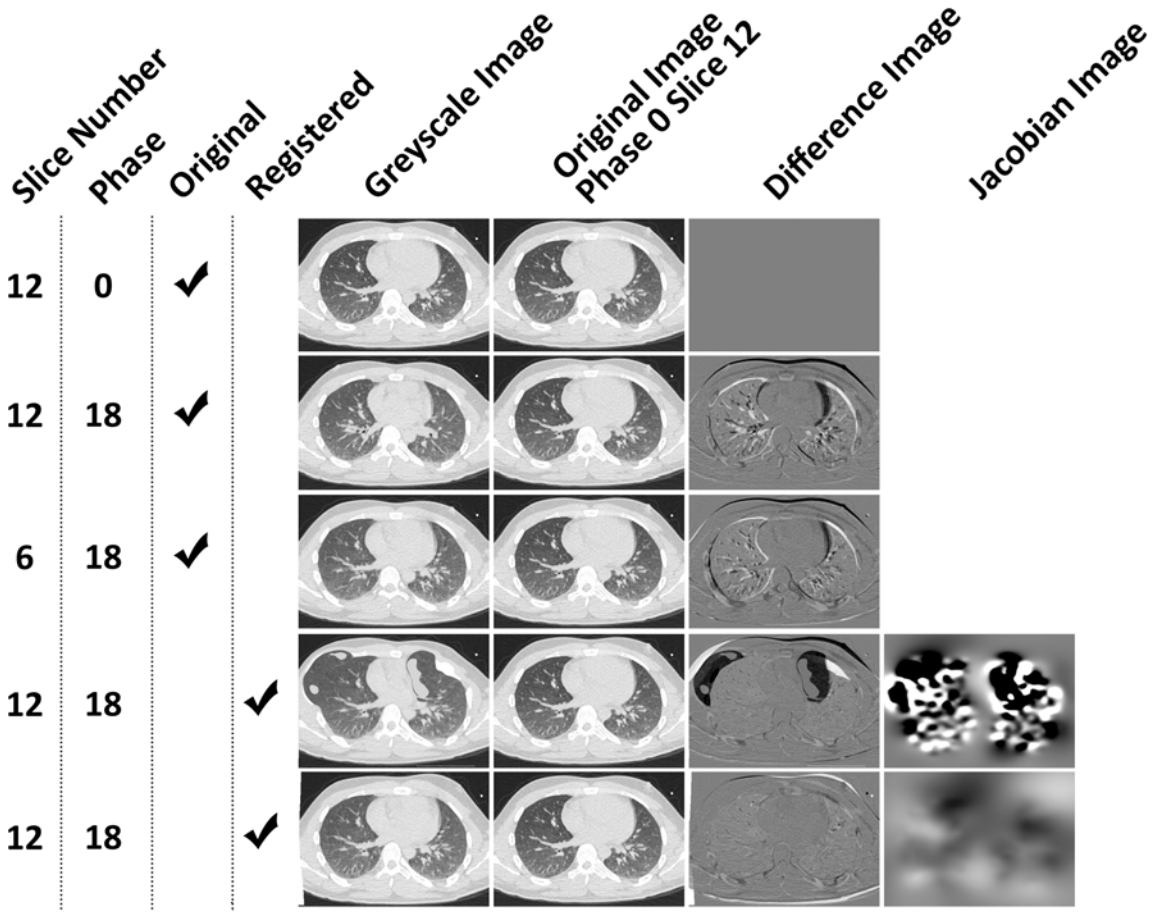


Figure 44. Image registration can produce unexpected results. The fixed image is shown in the *top row* and *2nd image column*. Calculated difference images from the fixed image are shown in the *3rd image column*. The *2nd row* contains the original moving image while the *3rd row* contains the slice most visually similar to fixed image within the phase of the moving image. Registration results in the *4th row* are extremely flawed. This case was forced to only use voxels within the segmentation mask resulting distortion at the lung boundaries (*4th row, 1st column*). This case did not incorporate b-spline node displacement constraints as seen by the extreme jacobian values (*4th row, 4th column*). The jacobian should be positive and reasonably constrained. In this image it ranged from -8 to 20. When the voxels are not limited to the segmentation mask but instead set to a single intensity and displacement constraints are added, the registration improves considerably (5th row, 1st column) with jacobian values ranging from 0.25 to 1.6.

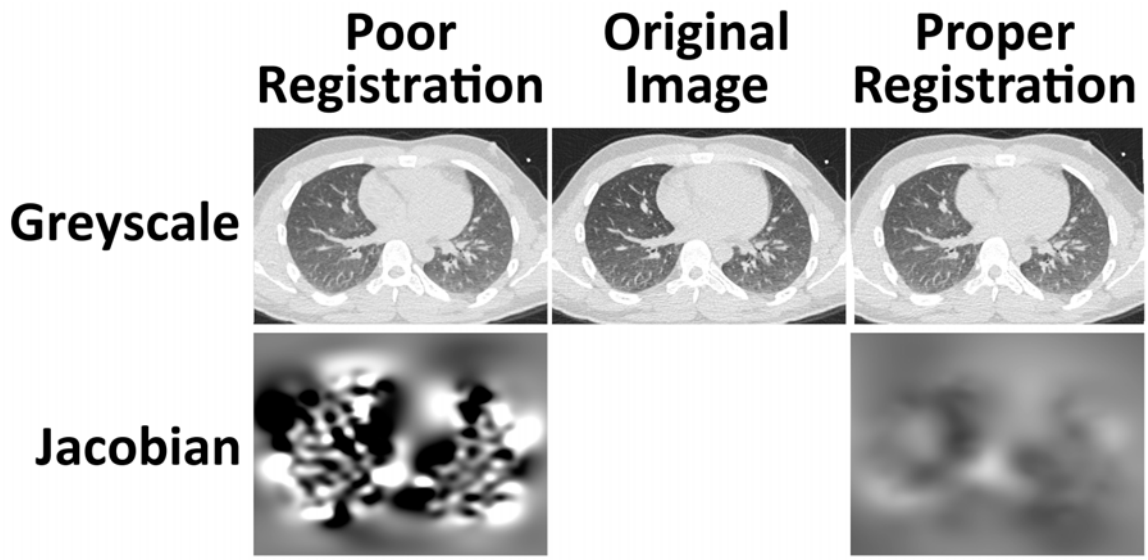


Figure 45. Noticing poor registration is often difficult. By examining the greyscale images in the *top row*, you would expect similar results between the scans. However, a closer look at the jacobian images shows a distinctly different story. When b-spline node displacement constraints are added along with spatial sampling not limited to only within the lung mask, the registration result improves dramatically (*bottom-right panel*).

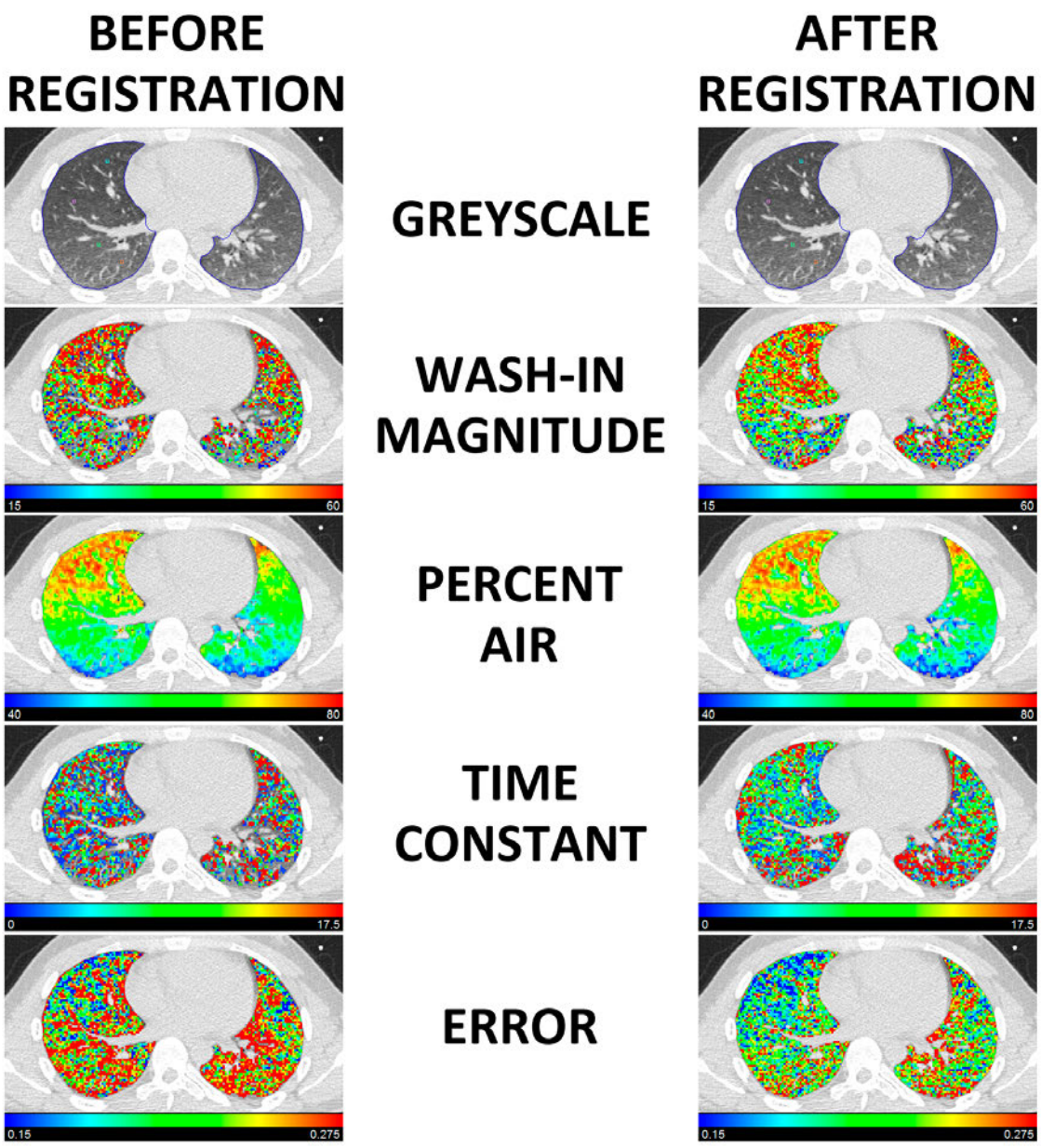


Figure 46. Image registration considerably improves the results of non-linear curve fitting of time-series MDCT datasets. Curve fit error is dramatically reduced (*bottom row*) when registration is utilized. Values of regional function also become more realistic when they are not contaminated by movement as seen in the colormaps for wash-in magnitude ($2^{nd}$ *row*) and time constant ($4^{th}$ *row*).

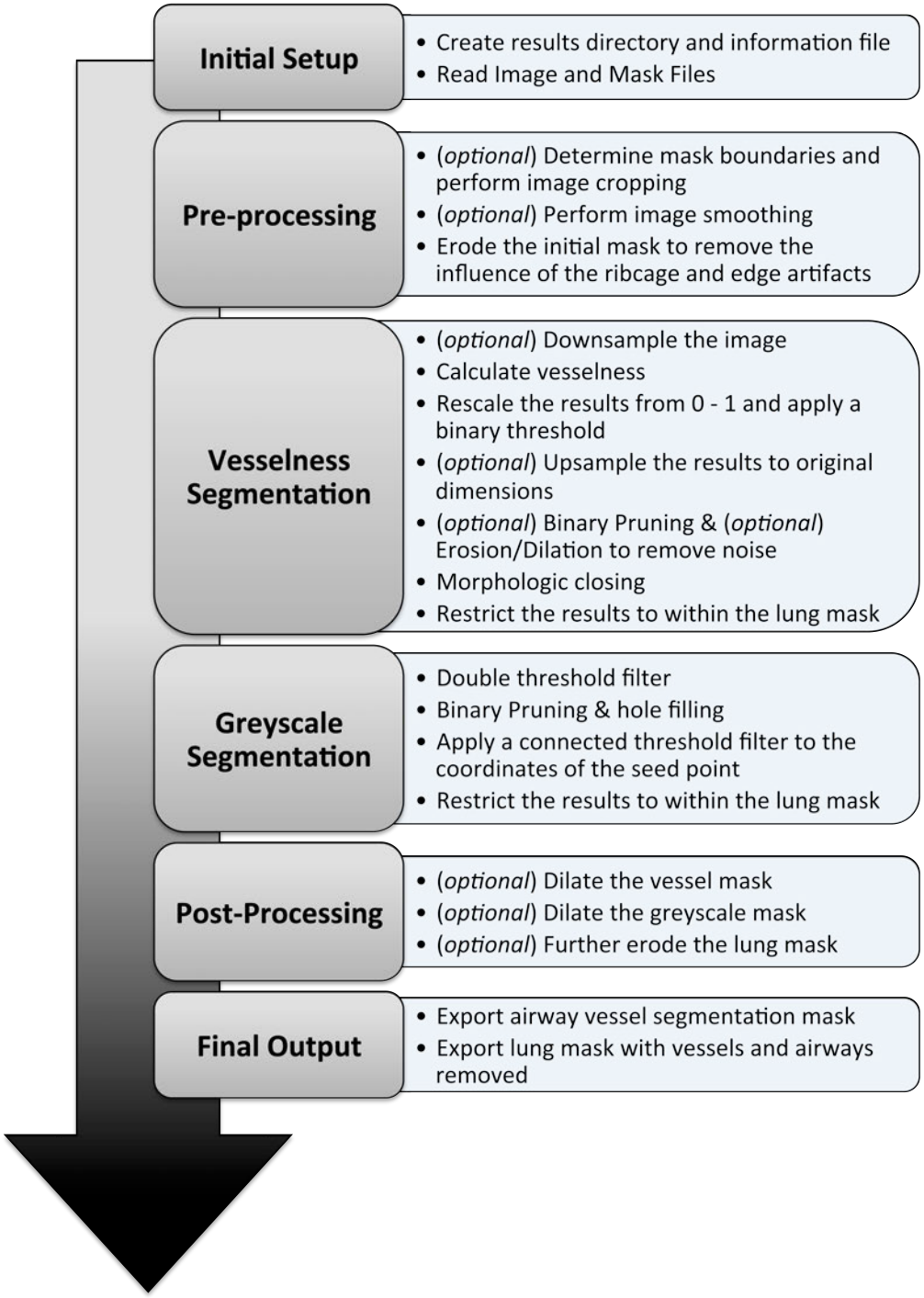


Figure 47. Workflow for the vesselness segmentation program.

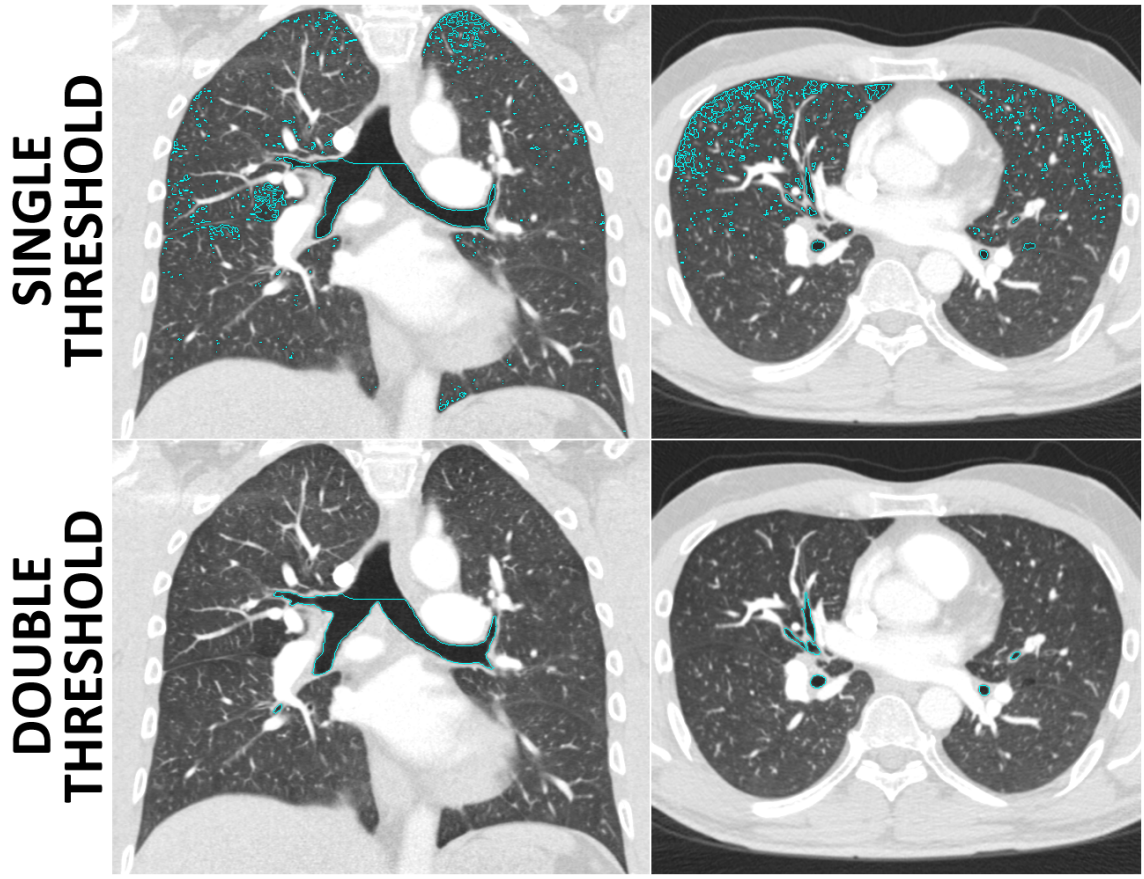


Figure 48. Double thresholding (*bottom row*) plus additional morphological operators considerably improves upon the results from a single threshold (*top row*) operation.

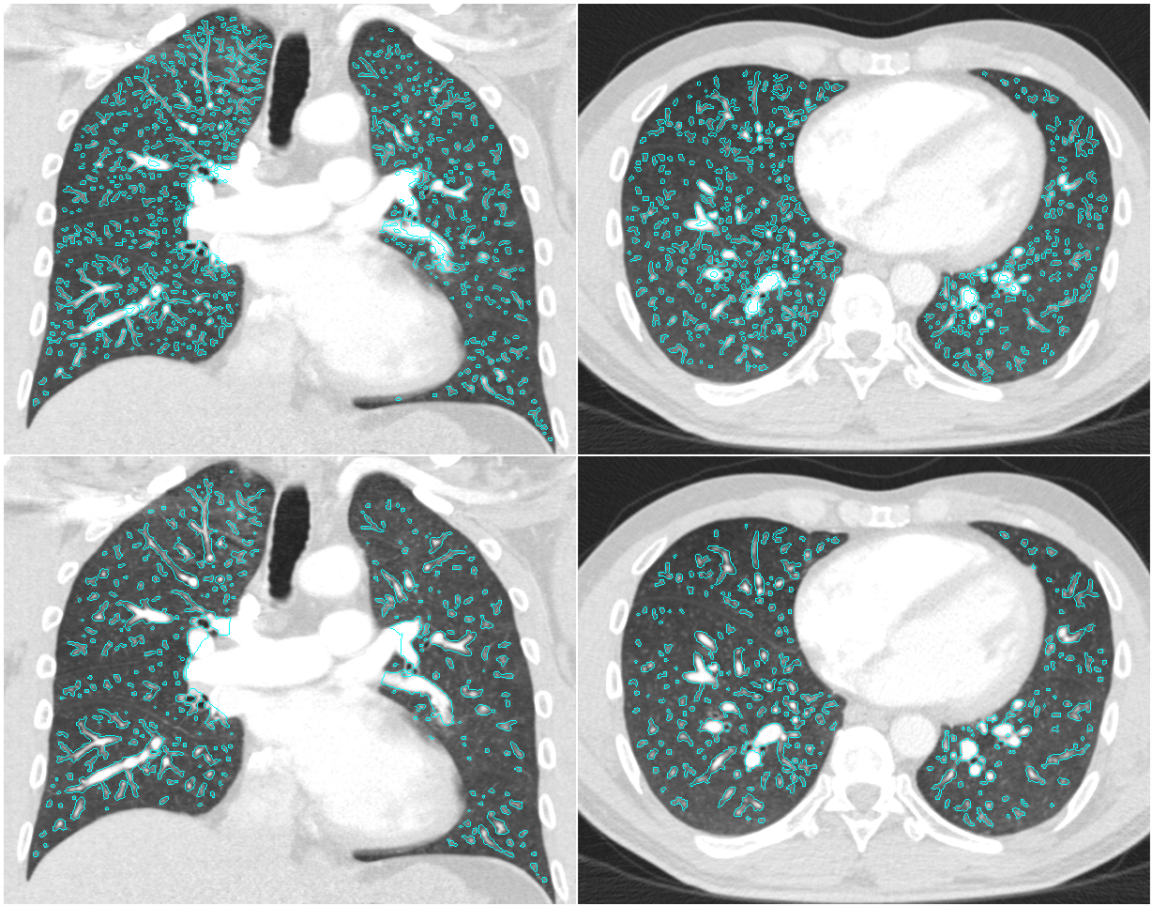

Figure 49. Results from the vesselness program when varying the value of sigma by changing the number of steps. Using 2 steps (*top row*) yields results with a higher density of small sized vessels, but also likely more errors from noise. Using 6 steps (*bottom row*) yields a cleaner vessel tree that is able to handle both small and large vessels. Vessels in the 6-step process are solid while vessels using 2 steps may contain gaps.

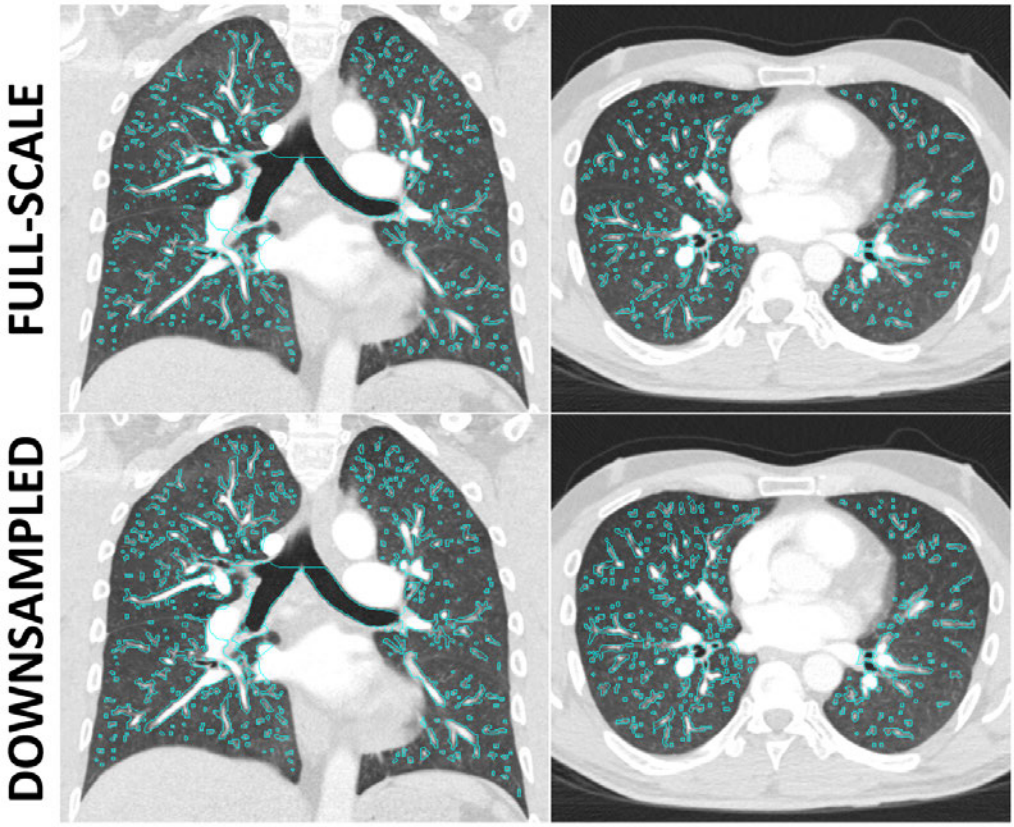


Figure 50. Depending on the size of a particular dataset, downsampling could be necessary to allow the vesselness program to complete using the amount of RAM available on a computer. The downside of downsampling is a loss of spatial resolution resulting in a staircase effect on the edges of vessel borders. Time for analysis: Downsampled = 3 min 40 sec, Full-scale = 6 min 30 sec for an 512 x 512 x 575 voxel image, with voxel dimensions 0.6 x 0.6 x 0.5 mm.

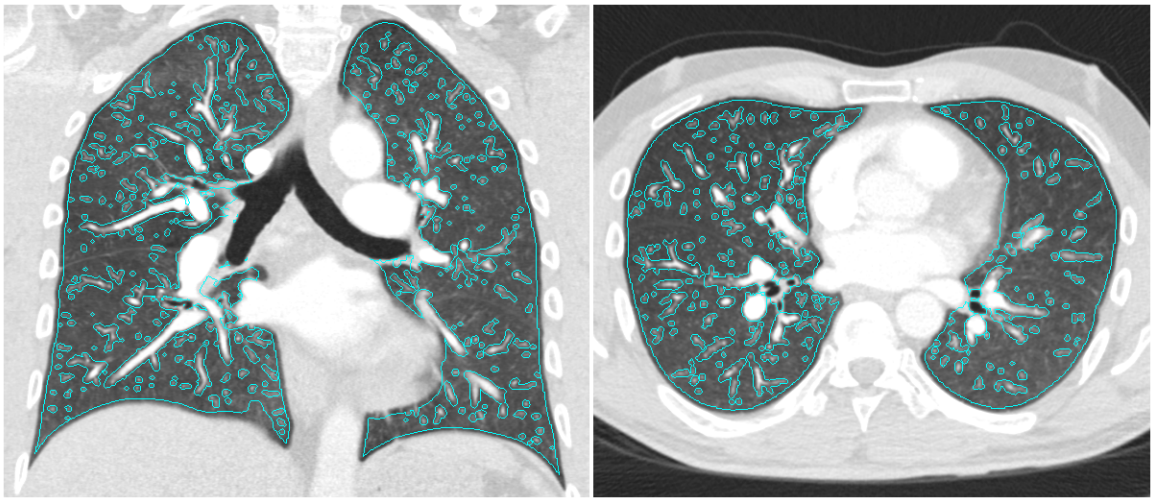

Figure 51. The final result of the *vesselness* program is a lung mask with the airways and vessels removed.

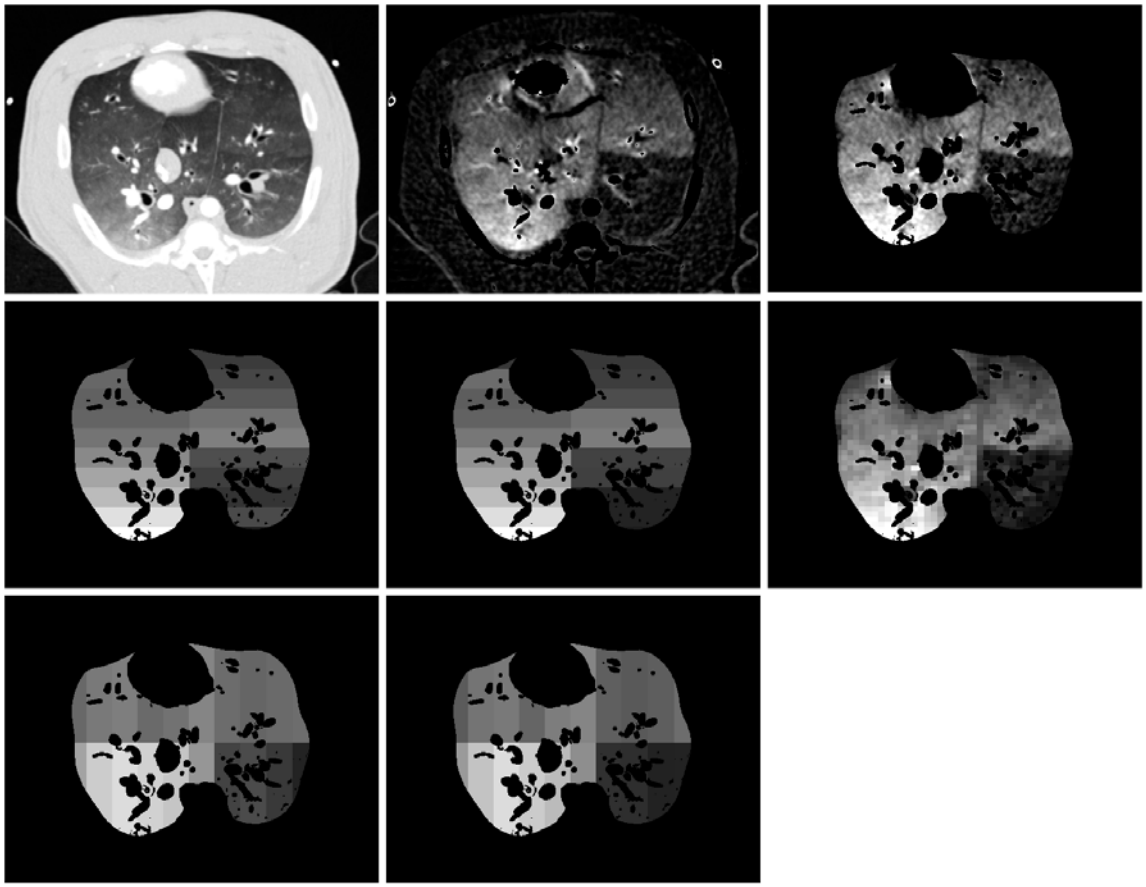

Figure 52. *QuickCompare* can be used to filter and analyze functional datasets. Choosing the size and location of regions can influence your interpretation of functional results. A number of example settings are shown from the results of an animal subject with a portion of the pulmonary vasculature occluded with a balloon. From left to right, top to bottom: Original greyscale image, original DECT functional CT-PBV image, normalized and filtered CT-PBV image, 2-X 10-Y 1-Z regions, 2-X 10-Y 5-Z regions, 40-X 40-Y 20-Z regions, 10-X 2-Y 1-Z regions, and 10-X 2-Y 5-Z regions.

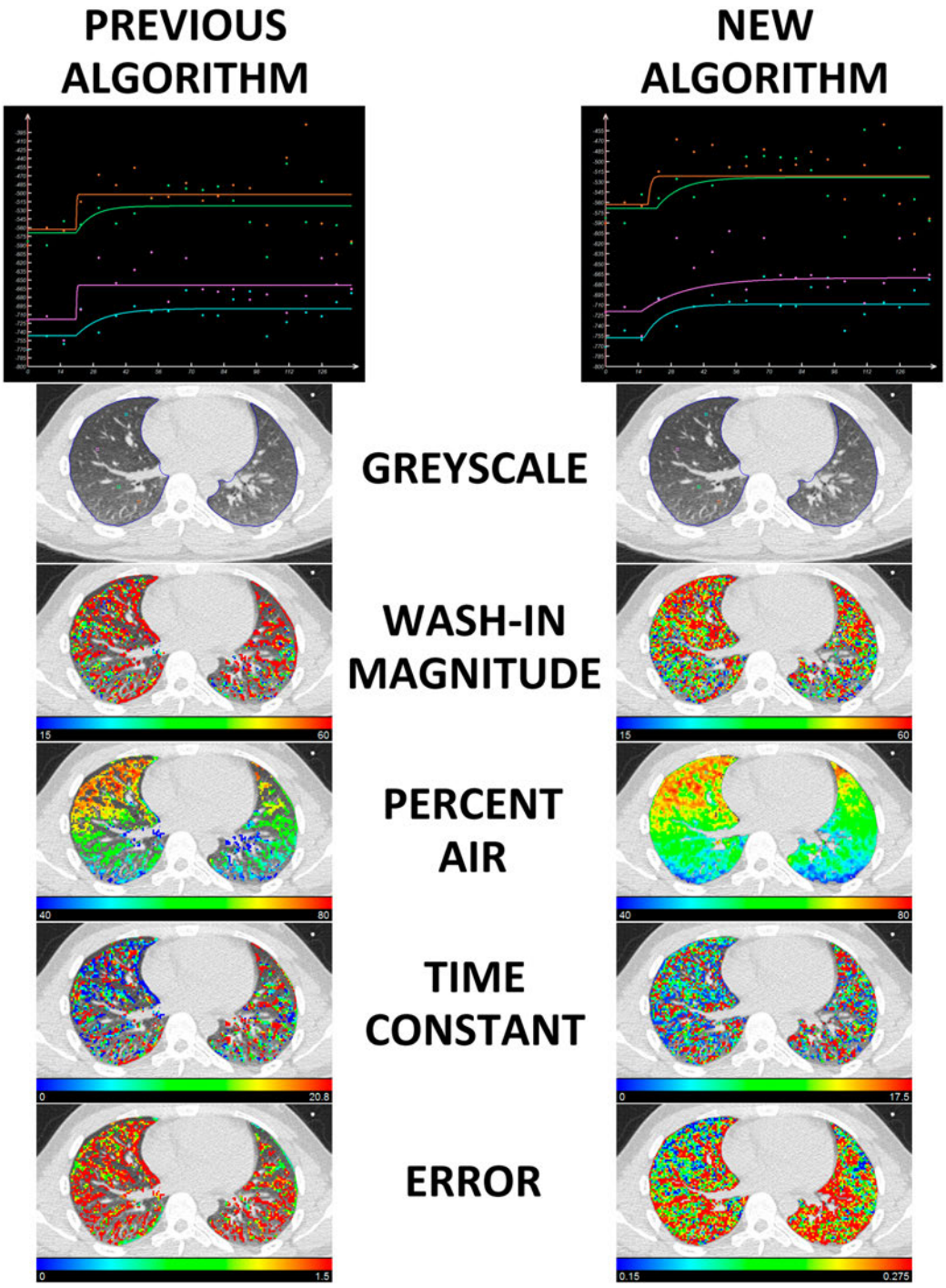


Figure 53. Colormaps illustrating wash-in xenon-CT results after algorithm improvements, specifically the addition of parameter constraints in the Levenberg-Marquardt optimization of the curve fitting parameters. These results are considerably improved even without image registration.

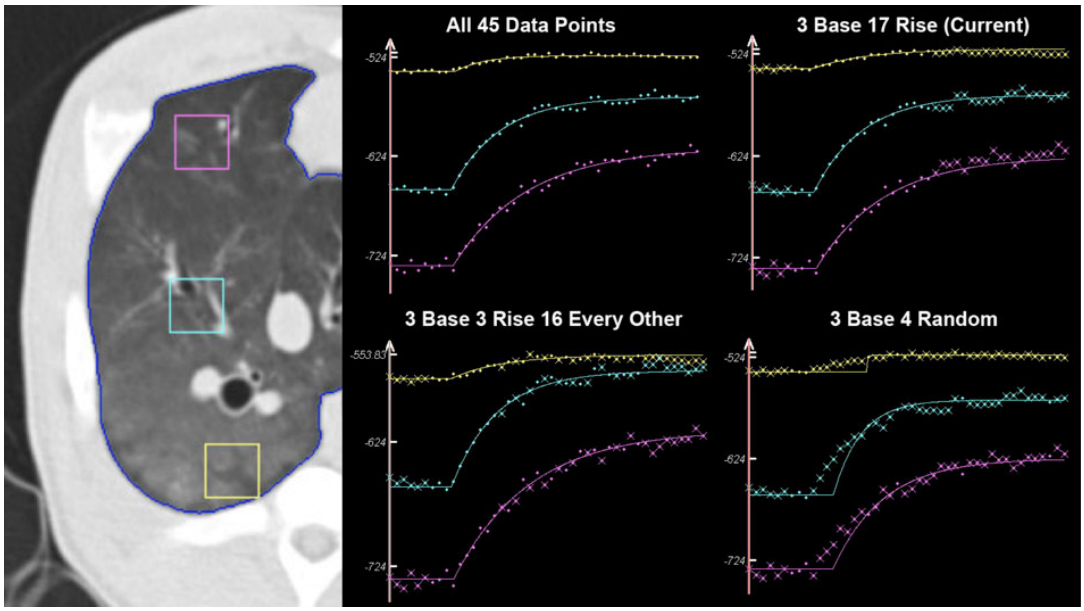


Figure 54. Time-intensity plots from three anatomical locations of a 45 scan (10 room air baseline, 35 xenon wash-in) wash-in xenon-CT dataset in an animal model. As the number of scans used and the distribution over time is varied, the resultant curve-fits fluctuates widely.

| FLAG | TYPE | FLAG | TYPE |
|---|---|---|---|
| Deformation Type | *Integer* | MI Use PDF Derivatives | *(FIXED)* |
| Intensity Truncation | *Bool* | MI Use B-Spline Weight Caching | *(FIXED)* |
| Intensity Truncation Value | *Integer* | Perform Rigid / Affine | *Bool* |
| Unsharp Masking | *Bool* | R/A Histogram Bins | *Integer* |
| Smoothing | *Bool* | R/A # of Iterations | *Integer* |
| Smoothing Time Step | *Float* | R/A Sampling Percent | *Float* |
| Smoothing # Of Iterations | *Integer* | R/A Precision | *(FIXED)* |
| Smoothing Filter Conductance | *Float* | Center of Mass | *(FIXED)* |
| Constrain Node Displacement | *Bool* | # Of Resolution Levels | *Integer* |
| Processing Cores | *Integer* | # Of B-Spline Levels | *Integer* |
| Save Results Incrementally | *Bool* | B-Spline X/Y Grid | *Integer* |
| Extra Label | *String* | B-Spline Z Grid | *Integer* |
| Perform Image Cropping | *Bool* | B-Spline Convergence Factor | *Float* |
| Crop Boundary Left | *Integer* | B-Spline Histogram Bins | *Integer* |
| Crop Boundary Right | *Integer* | B-Spline Resolution Level | *Integer* |
| Crop Boundary Top | *Integer* | B-Spline # of Iterations | *Integer* |
| Crop Boundary Bottom | *Integer* | B-Spline Use Mask | *Bool* |
| Remove Background | *Bool* | B-Spline Sampling Percent | *Float* |
| Output Interpolator | *Integer* | LBFGSB Evaluations | *Integer* |
| Optimizer | *(FIXED)* | LBFGSB Corrections | *Integer* |
| Metric | *(FIXED)* | | |

Table 5. Time Series Registration (*TSReg*) Input Parameters

| FLAG | TYPE | FLAG | TYPE |
|---|---|---|---|
| Perform Vesselness | *Bool* | Image Downsampling | *Bool* |
| Sigma Min | *Float* | Image Smoothing | *Bool* |
| Sigma Max | *Float* | Smoothing Time Step | *Float* |
| Sigma Steps | *Float* | Smoothing # of Iterations | *Integer* |
| Vesselness Lower Threshold | *Float* | Smoothing Filter Conductance | *Float* |
| Vesselness Upper Threshold | *Float* | Pruning Filter | *Bool* |
| Alpha 1 | *Float* | Closing Filter | *Bool* |
| Alpha 2 | *Float* | Erode Lung Mask | *Integer* |
| Greyscale Thresholding | *Bool* | Dilate Vessel Mask | *Integer* |
| GS Threshold Wide Min | *Integer* | Dilate Greyscale Mask | *Integer* |
| GS Threshold Narrow Min | *Integer* | | |
| GS Threshold Narrow Max | *Integer* | | |
| GS Threshold Wide Max | *Integer* | | |
| Seed Point X Coordinate | *Integer* | | |
| Seed Point Y Coordinate | *Integer* | | |
| Seed Point Z Coordinate | *Integer* | | |

Table 6. *Vesselness* Segmentation Input Parameters

| FLAG | TYPE | FLAG | TYPE |
|---|---|---|---|
| # Of Regions X | *Integer* | Image Directory | *Path* |
| # Of Regions Y | *Integer* | Mask Image | *Path* |
| # Of Regions Z | *Integer* | Parameter Filename | *String* |
| Output Image Results | *Bool* | Parameter Name | *String* |
| Perform Normalization | *Bool* | Parameter Min | *Float* |
| Normalization Type | *Integer* | Parameter Max | *Float* |
| Extra Label | *String* | Number of Filters | *Integer* |
| Grid Size | *Integer* | Filter Name | *String* |
| Edge Location Top | *Integer* | Filter Min | *Float* |
| Edge Location Bottom | *Integer* | Filter Max | *Float* |
| Edge Location Left | *Integer* | | |
| Edge Location Right | *Integer* | | |
| Edge Location Cranial | *Integer* | | |
| Edge Location Caudal | *Integer* | | |

Table 7. Regional Analysis Software (*QuickCompare*) Input Parameters

| ROI Location | All 45 Scans | 3 Baseline 17 Initial Wash-in | 3 Baseline 3 Initial Wash-in 16 Every Other Breath | 3 Baseline 4 Randomly chosen from wash-in |
|---|---|---|---|---|
| **Upper** | 16.66 | 30.61 | 17.47 | 0.57 |
| **Middle** | 27.70 | 27.14 | 26.90 | 15.18 |
| **Lower** | 42.15 | 37.89 | 40.37 | 27.81 |

Table 8. Values for the time constant of regional ventilation in three anatomical locations in an animal model derived from the nonlinear curve fitting of time-intensity curves acquired during wash-in xenon-CT. As the number of scans used and the distribution over time was varied, the resultant values from curve-fit process fluctuated widely.

# CHAPTER 6: REGIONAL VENTILATION DIFFERENCES BETWEEN NORMAL NEVER-SMOKERS, NORMAL SMOKERS & SMOKERS WITH COPD MEASURED WITH WASH-IN XENON-CT

It has recently been shown that there is an increase in the heterogeneity of regional perfusion in a sub population of smokers with normal pulmonary function tests (PFTs) but with early computed tomography-based evidence of small apical signs of centrilobular emphysema (14). This finding is supportive of the hypothesis that smoking-associated centrilobular emphysema, a disease characterized by regional alveolar destruction, is caused by an inability to attenuate hypoxic pulmonary vasoconstriction (HPV) when the hypoxia is associated with local parenchymal inflammation. Vascular constriction in the presence of inflammation is proposed to be integral to the process whereby inflammation goes unresolved and repair mechanisms are unable to correct tissue destruction (14,15). Central to this hypothesis is that smoking will cause heterogeneous inflammatory processes in all smokers with associated localized alveolar flooding. Thus in turn will be reflected in a heterogeneous pattern of ventilation in all smoking subjects. While the majority of subjects (~70%) will maintain flow to the inflamed hypoxic regions, a subset will not, leading to increased perfusion heterogeneity. Thus, the emphysema susceptible subjects are hypothesized to have matched increased ventilation and perfusion heterogeneity while emphysema resistant subjects will have a mismatched ventilation and perfusion heterogeneity (ventilation heterogeneity increased and perfusion heterogeneity remaining similar relative to normal never-smokers). The work of Alford et al. (14) has demonstrated the increased heterogeneity of perfusion in normal smokers susceptible to centrilobular emphysema, and our goal here is to demonstrate that this is not the result of differences in altered ventilation but rather an altered perfusion response to the presence of patchy ventilation deficits in all normal smokers. The work presented here establishes a methodology for translating our wash-in

xenon-CT methodologies from animals (established previously in comparison to inhaled fluorescent microspheres (Chapter 3)) to humans and to use this technology to explore regional ventilation ($r\dot{V}_A$) at the anatomic resolution of modern multi-detector row computed tomography (MDCT) in a normal population of smokers and never-smokers. Normal here is defined by the pulmonary function test results.

## 6.1 Methods

The Institutional Review Board approved this study, and written informed consent was obtained from all subjects before they entered the study.

The imaging and analysis protocols for the wash-in xenon-CT method are established in Chapters 3 - 5. We use the wash-in xenon-CT method in 44-subjects (23 Males / 21 Females, 34 Normal Never-smokers, 7 Normal Smokers, 3 COPD; Age (years): min=20, max=73, median=31.5; BMI: min=17.9, max=32.7, median=25.1). Study inclusion criteria were "never smokers" (with a total smoking history of less than 1 pack-year), smokers currently smoking one pack per day, and COPD subjects with no other lung disease. Exclusion criteria were known heart disease, kidney disease, diabetes, presence of metal in the lung field, pregnancy, an X-ray/CT scan in the past 12 months, and a body mass index over 32. Normal never smokers with clinically important pathology detected on MDCT were excluded, as were smokers with significant lung disease other than emphysema. The baseline dyspnea index was determined by the technique of Mahler et al. (177). Prebronchodilator spirometry including DLCO measurements were performed via a V6200 Body Box (Sensor Medics) or an OWL body plethysmograph (Ferraris Respiratory), verified for equivalency. Spirometry quality followed the American Thoracic Society and European Respiratory Society guidelines (178). Subjects were divided into 5 groups: normal never smokers (NS, N=34), normal smokers with no early signs of parenchymal destruction (SNI, N=4), normal smokers with early parenchymal destruction (SCE, N=3), smokers with COPD without

parenchymal destruction (COPD-NI, N=1), and smokers with COPD with parenchymal destruction (COPD-CE, N=2). A trained radiologist characterized the lung parenchyma for each subject by examining separate volume-controlled breath-held TLC volume scans from each subject (98). Volumetric MDCT scan times were less than 10 seconds with a z-coverage of 22–30 cm, adjusted to capture the full apical-basal extent of the lung. Voxels were near isotropic at 0.61 mm × 0.61 mm × 0.5 mm. The following imaging protocol was used: 100 mAs, 120 kV, 1 mm pitch, 512 × 512 matrix, and B35f reconstruction kernel, with the majority of subjects imaged on a 64-slice MDCT scanner (Siemens Somatom 64, Erlangen, Germany). Two subjects were scanned using the same imaging protocol but utilizing a Siemens Definition 128 Flash CT scanner.

Subjects received a dynamic volume-controlled axial lung scan consisting of 20 time points scanned during brief end-expiratory breath-holds at FRC using a custom dual-piston volume control system described in Chapter 4 (98). Scan times varied between 1 and 3 minutes, dependent on subject specific respiratory rates, with a z-coverage of approximately 3 cm positioned just above the diaphragm. Voxel sizes were around 0.61 mm × 0.61 mm × 1.2 mm depending on field of view. The imaging protocol used was: 150 mAs, 80 kV, 0.375 sec rotation time, 512 × 512 matrix, and B35f reconstruction kernel.

Semi-automated lung segmentation was performed for each time point using the Pulmonary Analysis Software Suite (PASS)(161). 4D greyscale images and lung segmentation masks were fed into a custom ITK-based (31) time-series image registration tool (*TSReg*) in order to more precisely align the lung between time points. The workflow for this program is fully described in Chapter 5. Following image registration, the initial phase of the time-series was extracted and used for vessel and airway segmentation using the *Vesselness* program described in Chapter 5. This mask was used when performing time-series image analysis within the Time Series Image Analysis (TSIA) module of PASS. The TSIA module characterizes the density change

over time in each lung parenchymal voxel by fitting the data to a single exponential model, the time constant of which is equal to the inverse of the voxel-specific ventilation, as previously described (179). Additional information on this module and enhancements necessary for human use are also described in Chapter 5. Finally, the results from fitting the time-series data to an exponential wash-in model in PASS were fed through the *QuickCompare* tool described in Chapter 5 to characterize the mean and coefficient of variation of the time constant, magnitude of wash-in, and percent air for each subject. Mean values for each parameter were determined for each subject group. SPSS was used to calculate values for independent-samples t-test between the parameters for each group.

## 6.2 Results

After recruitment, PFTs and MDCT scanning, some subjects were excluded for a variety of reasons including: scanner failure (N=1), significant beam hardening artifact associated with metal or calcifications (N=2), insufficient respiratory efforts associated with discomfort due to disorientation associated with xenon (N=5), subject motion during scan acquisition (N=6) and subject non-compliance with the volume controller largely associated with leak around the mouthpiece (N=11). After subject exclusion, 11 NS, 3 SNI, 3 SCE, 1 COPD-NI, and 1 COPD-CE were used for the analysis (10 Males / 9 Females; Age (years): min=20, max=70, median=30; BMI: min=17.9, max=32.0, median=23.4).

Full results including subject demographics, pulmonary function test results, and regional ventilation parameters are summarized in Table 9. NS and SNI subjects had very similar pulmonary function, whereas SCE had slightly lower values for % predicted FVC, FEV1, SVC, IC, and TLC, however all were still in the normal range. COPD-NI & COPD-CE had appropriately reduced values for % predicted FEV1, FEF25/75, DLCO, IC, TLC, and RV. Regional aeration (% air) was similar for the NS, SNI, SCE, and COPD-NI while higher for COPD-CE. Magnitude of xenon wash-in was similar for all

subjects, though perhaps mildly higher in the NS. There was increased heterogeneity of the magnitude of xenon wash-in in the SNI and COPD-NI subjects, though not statistically significant. Average time constants were statistically similar between NS, SNI and COPD-NI, but statistically significantly higher in SCE and even higher in COPD-CE. Heterogeneity of the time constants of $r\dot{V}_A$ were statistically significantly higher in SNI compared to NS. SCE and COPD-CE had similar heterogeneity statistically significantly lower than NS, SNI and COPD-NI. Due to the small sample size, the assumption of equal variances between subject groups was used. Using this assumption, all of the noted statistically significant comparisons had $p<0.05$. $r\dot{V}_A$ parameters are presented graphically in Figure 55 to better illustrate the differences between groups. Representative subjects from each group are presented Figure 56. NS, SNI, SCE, COPD-CE, and COPD-NI are shown in *Panel A*, *Panel B*, *Panel C*, *Panel D*, and *Panel E* respectively. The mean values for time constants, as depicted in Figure 56, were similar in the NS, SNI and COPD-NI while lengthened in the SCE and COPD-CE subjects (*bottom-right colormaps*). Gravitational gradients in aeration are evident in the NS, SNI, SCE, and COPD-NI subjects, however the COPD-CE subject has considerable tissue loss resulting in massive air spaces and an elimination of the gradient in aeration. Additionally, time constants are longer (slower ventilation) in the gravitationally non-dependent versus dependent lung regions in the NS and SNI subjects consistent with known physiology (*bottom-right colormaps*)(43).

## 6.3 Discussion

The wash-in xenon-CT method successfully measured $r\dot{V}_A$ in 19 human subjects and demonstrated differences between subject groups. It was necessary to exclude 25 subjects for a mixture of reasons, which prevented the wash-in xenon-CT method from adequately calculating $r\dot{V}_A$. The most common exclusionary factor was subject non-compliance that caused significant end-expiratory lung volume fluctuation. Once the

inhalation of xenon gas commenced, some subjects became disoriented and no longer maintained an adequate seal around the mouthpiece resulting in a loss of end-expiratory lung volume control. Variation in end-expiratory lung volume has a considerable effect on lung density thus making time-series density-based measurements unreliable, thus dictating a decision for exclusion. When subjects followed verbal instructions, proper procedures, and maintained an adequate seal around the mouthpiece the lung volume control system worked and repeatable end-expiratory lung volumes were achieved, thus enabling $r\dot{V}_A$ measurements.

$r\dot{V}_A$ parameters measured with wash-in xenon-CT differentiated between groups which appeared similar by PFTs. Our results demonstrated an increase in $r\dot{V}_A$ heterogeneity in smokers compared to never-smokers as previously hypothesized. Furthermore, the normal smoker population can be divide into two groups based on differences in $r\dot{V}_A$ time constant length: smokers that are susceptible to the development of emphysema, based on early CT findings of apical centrilobular emphysema, have increased time constants compared to smokers with no early signs of parenchymal destruction.

While we hypothesized that we would see an increased heterogeneity of ventilation in both the SNI and the SCE groups, demonstrating inflammation associated ventilation abnormalities, we found a different scenario but still supporting the notion that all smokers have alterations in ventilation likely associated with inflammation. We found that the SNI subjects have similar average time constants to the NS group but a statistically significant increased heterogeneity of the wash-in time constants indicating an increased heterogeneity of ventilation ($p<0.05$, assuming equal variance). Conversely, the SCE subjects showed a statistically significant increased average wash-in time constant indicating altered ventilation likely associated with inflammatory processes ($p<0.05$, assuming equal variance). However the SCE subjects showed statistically significant decreased heterogeneity because of larger scale regional changes similar to the

COPD-CE ($p<0.05$). Ventilation differences between never-smokers vs. both smoking groups suggest that both smoking groups likely have inflammatory processes present, supporting the notion that altered perfusion heterogeneity in the SCE group is due to an altered perfusion response in the presence of inflammation rather than the inflammation itself (14). In addition to these observations in the subjects with normal PFTs, the two subjects with COPD had distinctly different patterns of $r\dot{V}_A$. The COPD-NI subject exhibited $r\dot{V}_A$ time constants more consistent with NNS and heterogeneity of the magnitude of xenon wash-in with NS. These findings are more consistent with airway predominant disease further reinforced by a lack of parenchymal destruction. This suggests that the wash-in xenon-CT method may be suitable for distinguishing between airway-predominant and parenchymal-predominant COPD.

We recognize that the complexity of the wash-in xenon-CT method likely precludes it from routine clinical use. In fact, it proved difficult in a research setting. However, when performed properly it provides valuable information regarding dynamic regional ventilation that may not be detected by more recently developed dual-energy single volume acquisition xenon-CT methods (139-141,190-192). The strength of the method presented lies in the fact that it provides a dynamic protocol against which newer, more clinically feasible, single breath dual-energy xenon-CT methodologies can be compared.

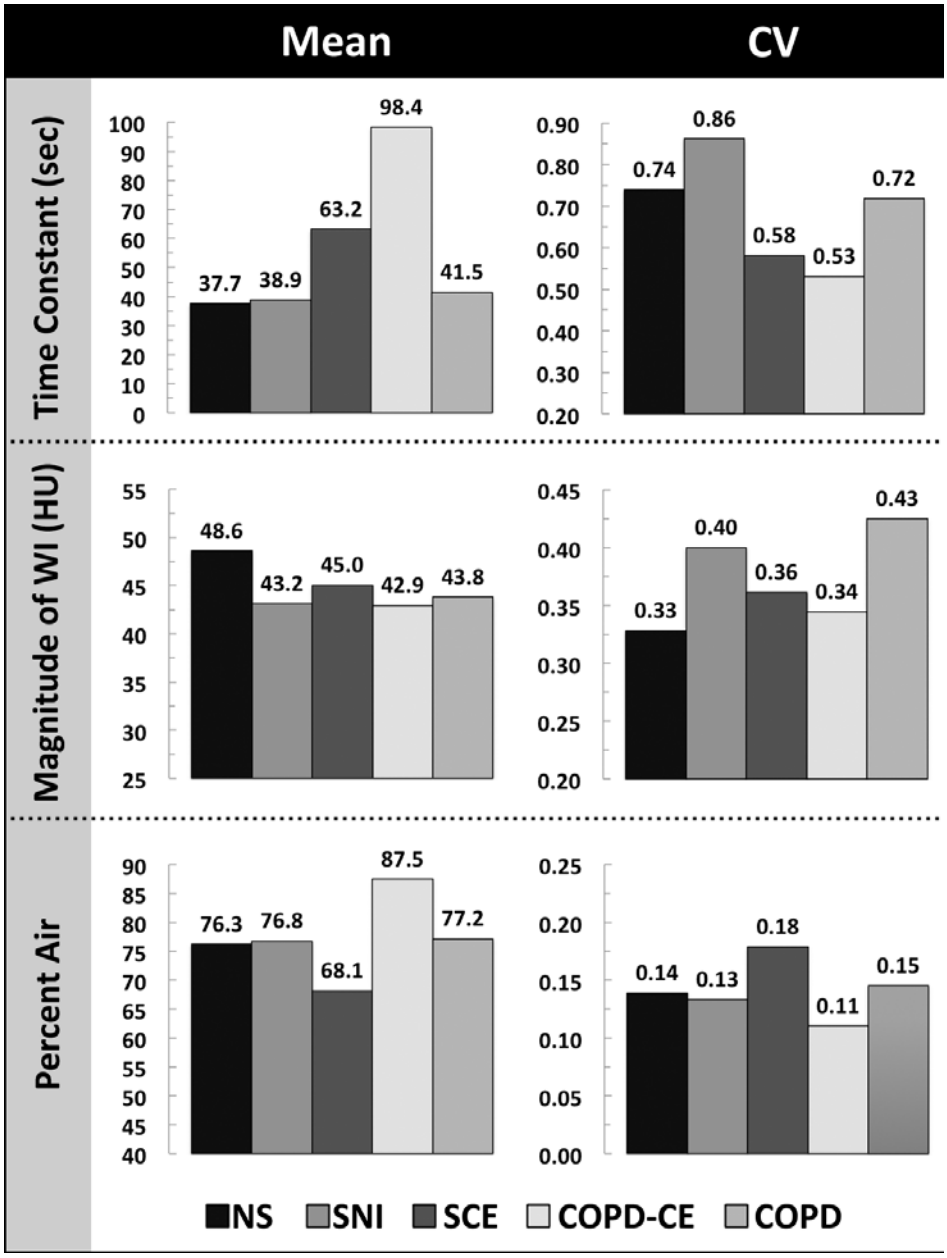


Figure 55. Average values of Mean and CV of the time constant (*top row*), magnitude of wash-in (*middle row*) and percent air (*bottom row*) from 11 normal never-smokers (NS), 3 normal smokers (SNI), 3 normal smokers with parenchymal destruction (SCE), 1 COPD subject with parenchymal destruction (COPD-CE), and 1 COPD subject without parenchymal destruction (COPD-CI).

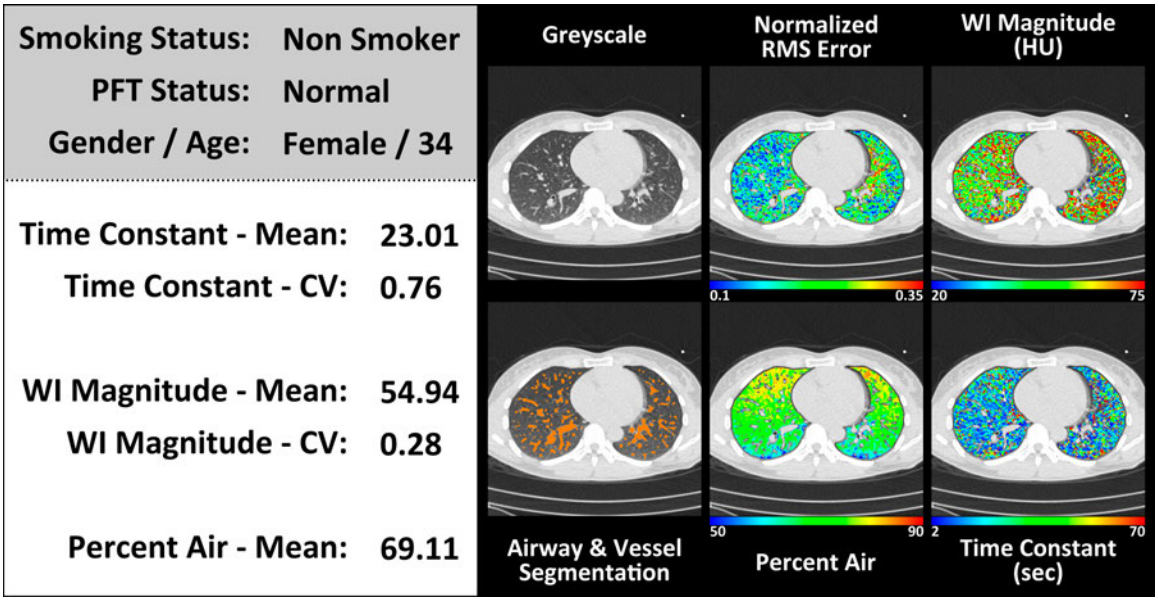


*(Panel A)*

Figure 56. Regional ventilation is clearly different between groups as shown in colormap results from the wash-in xenon-CT method in representative subjects: normal never-smoker (NS, *Panel A*), normal smoker (SNI, *Panel B*), normal smoker with parenchymal destruction (SCE, *Panel C*), COPD subject with parenchymal destruction (COPD-CE, *Panel D*), COPD subject without parenchymal destruction (COPD-CI, *Panel E*).

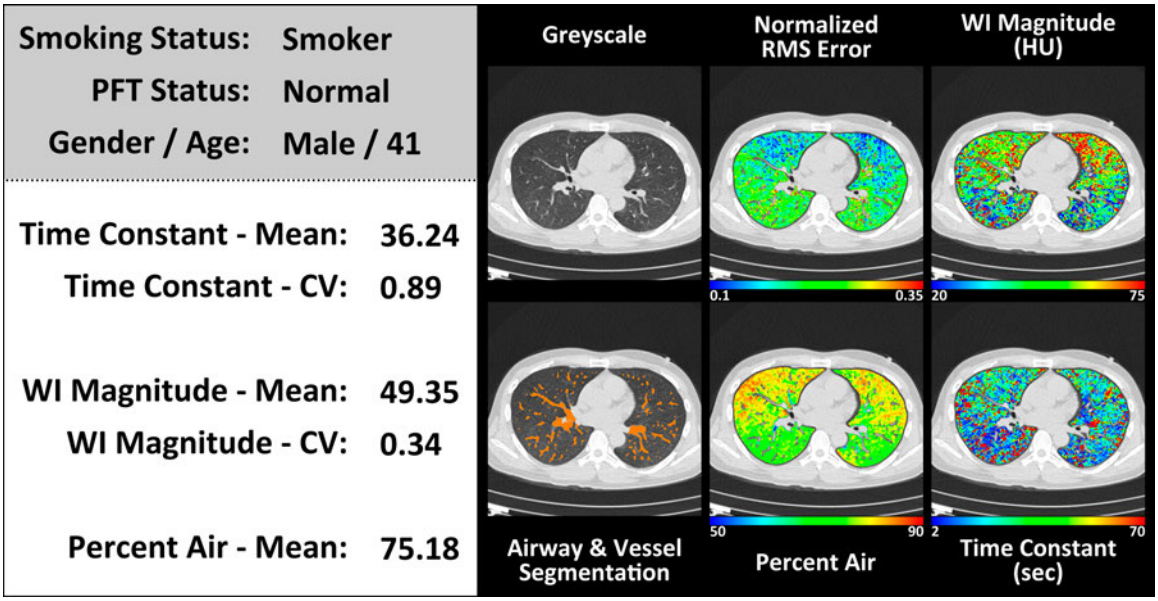


*(Panel B)*

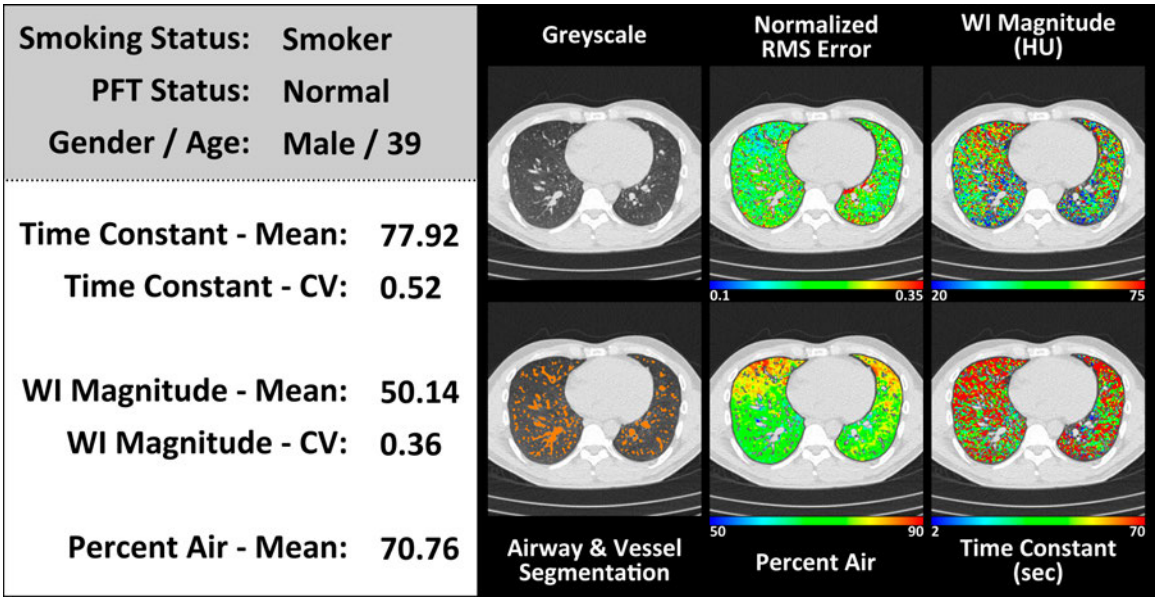


*(Panel C)*

Figure 56 (Continued)

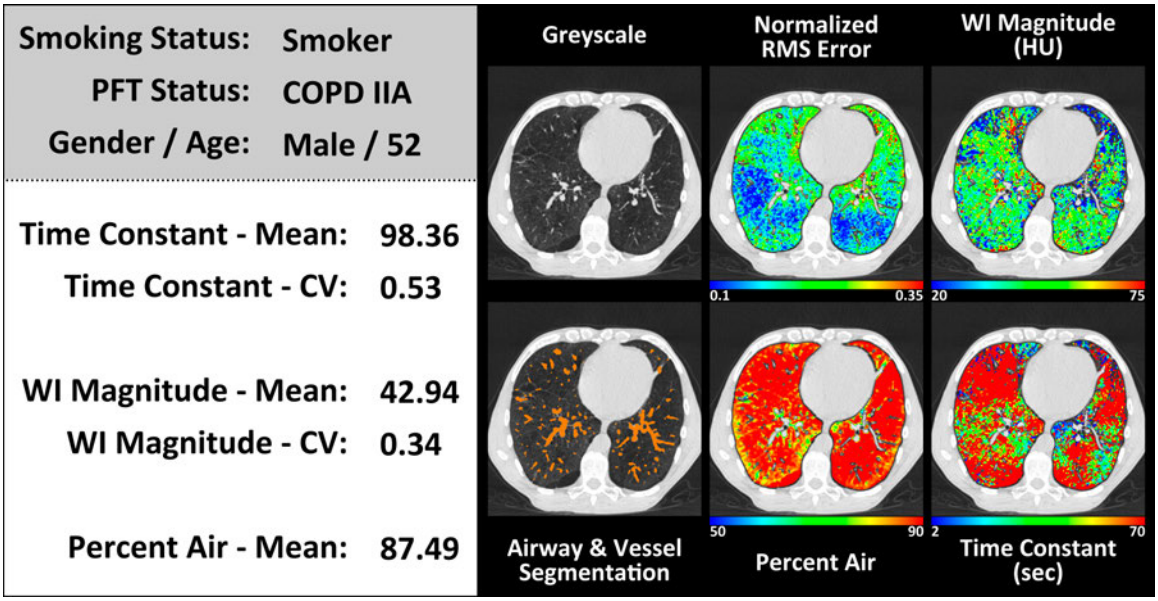


*(Panel D)*

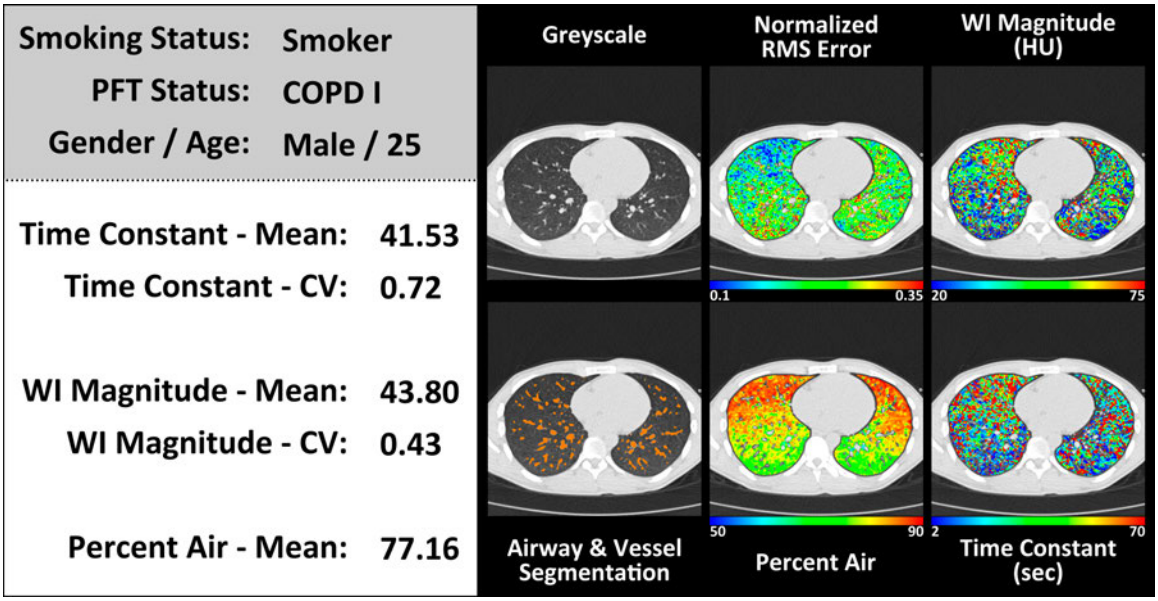


*(Panel E)*

Figure 56 (Continued)

| | Group | NS | SNI | SCE | COPD-CE | COPD-CI |
|---|---|---|---|---|---|---|
| Demographics | N | 11 | 3 | 3 | 1 | 1 |
| | Age | 35 ± 17 | 29 ± 10 | 34 ± 13 | 52 | 25 |
| | Height | 1.71 ± 0.11 | 1.73 ± 0.16 | 1.76 ± 0.08 | 1.79 | 1.79 |
| | Weight | 74.2 ± 14.0 | 66.0 ± 16.8 | 77.6 ± 10.9 | 57.5 | 63.5 |
| | BMI | 25.3 ± 3.9 | 21.7 ± 3.0 | 24.9 ± 2.0 | 17.9 | 19.9 |
| Pulmonary Function | PEF | 8.3 ± 2.0 | 10.3 ± 3.5 | 7.6 ± 2.3 | 5.9 | 8.2 |
| | $V_A$ | 7.0 ± 1.7 | 7.8 ± 1.9 | 8.5 ± 2.2 | 7.5 | 7.6 |
| | FVC %pred | 107.0 ± 13.9 | 110.2 ± 8.3 | 95.5 ± 12.4 | 100.6 | 102.2 |
| | FEV1 %pred | 111.8 ± 12.8 | 115.9 ± 8.1 | 99.2 ± 13.4 | 59.0 | 88.7 |
| | FEF25/75 %pred | 106.3 ± 25.2 | 105.6 ± 22.4 | 103.8 ± 28.3 | 26.6 | 62.3 |
| | SVC %pred | 100.7 ± 16.9 | 106.6 ± 11.1 | 93.4 ± 15.6 | 103.1 | 102.2 |
| | DLCO %pred | 131.8 ± 20.2 | 122.8 ± 40.0 | 125.6 ± 52.2 | 46.7 | 87.4 |
| | IC %pred | 128.6 ± 31.5 | 121.9 ± 24.7 | 107.2 ± 5.0 | 92.7 | 100.0 |
| | TLC %pred | 103.9 ± 16.7 | 106.8 ± 10.2 | 95.4 ± 7.1 | 94.4 | 94.4 |
| | FRC %pred | 89.5 ± 18.1 | 95.7 ± 11.5 | 86.0 ± 8.9 | 95.8 | 93.0 |
| | RV %pred | 116.3 ± 35.3 | 109.9 ± 24.6 | 103.9 ± 25.5 | 75.8 | 89.4 |
| | VC SVC | 3.96 ± 0.82 | 4.42 ± 1.26 | 3.75 ± 1.19 | 4.57 | 4.58 |
| Regional Ventilation | Tau (Mean) | 37.7 ± 7.1 | 38.9 ± 9.3 | 63.2 ± 12.8 | 98.4 | 41.5 |
| | Tau (CV) | 0.74 ± 0.06 | 0.86 ± 0.12 | 0.58 ± 0.07 | 0.53 | 0.72 |
| | MAG (Mean) | 48.6 ± 8.6 | 43.2 ± 7.8 | 45.0 ± 10.6 | 42.9 | 43.8 |
| | MAG (CV) | 0.33 ± 0.07 | 0.40 ± 0.06 | 0.36 ± 0.04 | 0.34 | 0.43 |
| | AIR (Mean) | 76.3 ± 3.4 | 76.8 ± 1.4 | 68.1 ± 4.2 | 87.5 | 77.2 |
| | AIR (CV) | 0.14 ± 0.02 | 0.13 ± 0.01 | 0.18 ± 0.03 | 0.11 | 0.15 |

Table 9. Demographic information, pulmonary function test results and regional ventilation parameters are presented as mean ± standard deviation for normal never-smokers (NS), normal smokers (SNI), normal smokers with parenchymal destruction (SCE), and COPD subjects with (COPD-CE) and without parenchymal destruction (COPD-CI). Values for pulmonary function are similar between NS, SNI, and SCE however there are significant differences in their regional ventilation parameters.

# CHAPTER 7: DEVELOP A METHOD USING DUAL-ENERGY IMAGING TO REPLACE STANDARD WASH-IN XENON-CT IMAGING

The earliest report of xenon gas as a radiopaque contrast agent used in conjunction with computed tomography (CT) imaging of the airways and pulmonary airspaces was presented 1978 (96), very early in relation to the development of computed tomography itself. Since that early observation there have been numerous reports of xenon-CT in the literature (25,27,95,98,104,105,107,108,112,139,142,147,192-196). Quantitative xenon-CT methods used to evaluate regional ventilation have employed wash-in and/or wash-out kinetic measurements (25,27,95,98,104,107,108,112,142,192-196) of the gas by imaging serially acquired axial stacks of images in conjunction with multi-detector row computed tomography (MDCT). This axial mode of scanning limits the z-axis coverage of the lung yet interrogates regional ventilation during, a ventilatory maneuver, thus providing a gold standard for regional ventilation. The procedures for dynamically following wash-in kinetics of xenon gas requires complex CT scanning methodologies that are difficult to transfer to clinical settings (98). The development of dual-energy CT (DECT) (190) has offered the possibility of imaging regional ventilation throughout the whole lung, albeit via a breath hold technique (139,140,190). Because little has been done to explore the quantitative measures obtained via the emerging static dual-energy CT methods of imaging the lung with xenon gas and because little has been done to evaluate optimal dual-energy xenon-CT imaging protocols to minimize the gravitational effects of the very dense xenon gas, we have undertaken, here, to explore xenon-CT imaging of regional ventilation by comparing and optimizing methodological approaches.

In developing xenon-CT, it is important to take into consideration the effect xenon itself has on the dynamics of gas distribution. When using xenon gas to image

regional ventilation via radio-nuclear methods (9,43,46,47,157,158,197-199) one uses a very small amount of radioactive $^{133}$Xe gas. When xenon is used as a contrast agent for computed tomography, gas mixtures are on the order of 30-40% xenon for dynamic studies or higher in single breath studies. At this concentration of xenon, the inhaled gas mixtures will have considerably different physical properties than typical room air. For example, xenon gas (5.86 kg/m$^3$) is much heavier than typical room air (1.293 kg/m$^3$), thus gravity (along with altered viscosity) is modeled (200) to have a significant impact on its distribution during inhalation and will likely result in turbulent rather than laminar flow (113). Thus, as part of our efforts to understand and optimize xenon-CT methodologies, we here evaluate the hydraulic nature of the gas mixture through use of an airway phantom coupled with inclusion of helium gas to the xenon/oxygen mixture.

## 7.1 Methods

A series of test-objects were used to: 1) establish a density calibration curve associated with incrementally decreasing concentrations of xenon gas, 2) evaluate the use of resultant calibration curves to assess known volumes of xenon gas within balloons placed inside objects designed to simulate thoracic densities and 3) evaluate the role of gas density (He, Xe and $O_2$ mixtures) and flow rates on the distribution of the gas in a rapid prototyped central airway tree. Animal studies were carried out to then evaluate the role of pitch, collimation and kVp pairs in dual-energy imaging to maximize signal and minimize artifacts.

*DECT Technique:* All imaging was performed on a second-generation DECT scanner (Somatom Definition Flash: Siemens Medical Systems, Erlangen, Germany). Scan protocols varied according the particular question being asked as presented below.

*Three-material decomposition:* The issue in using dual-energy CT and xenon gas for assessing regional ventilation is that there are three unknown independent variables per voxel (air, soft tissue/blood, and xenon and only two measured linear attenuation

coefficients per voxel. We solve this using a generalized three-material mass fraction decomposition technique discussed elsewhere (134).

### 7.1.1 Test Object Experiments

*Syringes:* Plastic 60cc syringes filled with a range of xenon concentrations (0, 20, 25, 33, 50, 66, 100%; balance oxygen) were positioned in groups of three suspended in open air and inside an "Alderson RS-320 Lung/Chest Phantom" (Radiology Support Devices, Long Beach, CA) as depicted in Figure 57. This syringe-based test-object was scanned using the standard dual-energy kVp pairs, 80/140Sn (tin filtered) kVp and 100/140Sn kVp with a 0.75 mm slice thickness, a 0.5 mm increment, and a 0.55 pitch, to establish scales for radiodensity enhancement as a function of photon energy. Empty space inside the phantom was filled with potato flakes, roughly simulating the density of lung parenchyma (54).

*Balloon*: Settings determined from the syringe calibrations were tested using a 3-L anesthesia-breathing bag (Vital Signs, Inc.; Totowa, NJ) positioned in open air as well as inside the chest phantom. The balloon was scanned after being initially filled with a known amount of xenon gas and room air. Small amounts of room air were sequentially added to increase the volume of gas in the balloon while keeping the total xenon content the same; the balloon was rescanned after each increase in volume. Scanning used the dual-energy kVp pairs of 80/140Sn (tin filtered) kVp with a 0.75 mm slice thickness, a 0.5 mm increment, and a 0.55 pitch. These scans were processed with the default three-material decomposition parameters provided by the scanner associated software as well as those derived from the syringe-based test-object. These image data sets were used to determine accuracy of xenon concentration metrics derived from the two calibration sets as a function of per voxel xenon concentration. Xenon volumes were assessed based upon per-voxel xenon concentration multiplied by the voxel volume and summed over the total number of voxels.

*Rapid Prototyped Airway Tree*: To examine the relationship between delivery rate, gas composition, and gas distribution during simulated inhalation, an experiment was performed in which various xenon gas mixtures were delivered via a syringe manifold (Figure 58) into a transparent plastic airway test-object. With the airway test-object positioned parallel to the detector plane of the scanner, axial (4-cm z-axis extent) time-series images (80 kVp, 150 mAs, 0.75 mm slice thickness, 0.5 mm increment, 0.28 sec rotation time, 60 time-points) were acquired during the delivery of the various xenon gas mixtures at two flow-rates (80%Xe/20%$O_2$, 4.9738 kg/$m^3$; 40%Xe/60%$O_2$, 3.2014 kg/$m^3$; 40%Xe/40%He/20%$O_2$, 2.7012 kg/$m^3$; composition and density respectively). The test-object was derived from a high resolution MDCT scan of a normal never-smoking male acquired previously on a Siemens Somatom 64 scanner (Siemens, Erlangen, Germany), at 95% vital capacity (98). Automatic segmentation and generation of the lung (201,202) and airway (203-205) masks were carried out through the use of Pulmonary Workstation (PW2, Vida Diagnostics, Coralville, IA). Based on the airway geometries, a rapid prototype of the segmented airways was generated through the use of a polycarbonate material, to ensure strength and durability. For each scan, time-versus-density profiles were created for regions of interest (ROI) placed in gravitationally dependent (*right-main bronchus*) and non-dependent (*left-main bronchus*) airways (Figure 62, *top-row 2nd column*). The maximal increase in density for each time-series was compared to its expected level, $HU_E = HU_i + 2.25 * Xe_{Conc}$ $HU_E = HU_i + 2.25*Xe_{Conc}$ ($HU_E$ $HU_E$ *: ROI expected density;* $HU_i$ $HU_i$ *: ROI baseline density;* $Xe_{Conc}$ $Xe_{Conc}$*: concentration of xenon*). Additionally, syringes filled with 40% xenon and a range of helium concentrations (20, 40, 60%; balance oxygen) were also scanned to determine the effect of the carrier gas used on radiodensity; seeking to verify that the decreased gas density caused by the use of helium gas does not affect material decomposition methods used in association with DECT measures.

### 7.1.2 Animal Experiments

To further develop the optimum DECT imaging protocol scans from animal studies in which kVp pair, pitch, and collimation were varied following xenon inhalation were analyzed.

*Animal Preparation.* The Institutional Animal Care and Use Committee approved all animal studies reported here. Five farm-bred ovine (40 kg ± 2.5; 3 males) and one farm-bred swine (60 kg; female) were premedicated with Ketamine (20 mg/kg) and Xylazine (2 mg/kg) intramuscularly, and anesthetized with 3–5% isoflurane in oxygen by nose cone inhalation. Once surgical depth of anesthesia was achieved, an 8.0-mm inner diameter cuffed endotracheal tube was placed through a tracheostomy and the animal was mechanically ventilated with 100% oxygen, tidal volume of 10-14 mL/kg, rate of 10-20 breaths/min adjusted to achieve an end-tidal $PCO_2$ of 30–40 mm Hg. Carotid arterial and external jugular venous introducers were placed. Surgical plane of anesthesia was maintained with inhaled isoflurane (1–5% in oxygen), neuromuscular blockade was achieved with pancuronium (0.1 mg/kg IV initial dose and 0.5–1 mg/kg hourly as needed). Arterial pressure, oxygen saturation, and airway pressures were continuously monitored and recorded. Animals were placed in the supine position and held with gentle forelimb traction. Three ovine were used for protocol development. Two subsequent ovine were used to evaluate kVp combinations for use with dual-energy scanning and the final (sixth) animal was used to evaluate the role played by an addition of helium to a xenon/oxygen mixture to ameliorate the effects of density and viscosity of xenon on gas distribution patterns. For our sixth study we utilized a 60kg (male) swine, selected to better represent the size and shape of a standard adult male human thorax.

In the fourth and fifth animals (ovine), volumes of gas sufficient to raise mouth-pressure from 0 to 25 $cmH_20$ were rapidly delivered via 3-L calibration syringe to the anesthetized supine animal and then scanned. The delivered gas mixtures were sequentially varied to include a higher proportion of xenon gas (0, 20, 40, 60, 80, 100%

Xe; balance $O_2$) in each subsequent scan. Scans were acquired at both 80/140Sn and 100/140Sn during the same breath-hold. Whole lung and central airway segmentations were performed on the linear mixed images from each scan using Apollo (Vida Diagnostics, Coralville, IA). The mean and coefficient of variation of the xenon concentration in the lung parenchyma and central airways were then compared between the 80/140Sn and 100/140Sn scans.

The use of 80kVp versus 100kVp provides for a greater density separation between low and high kVp images critical for the accurate discrimination of low xenon concentrations (112). However, the use of lower photon energies increases the likelihood for signal artifacts (cupping etc.) caused by poor photon penetration especially in larger subjects. To verify that the 60kg swine reasonably represented what might be expected in regards to thoracic density and density distributions in humans, we utilized image data acquired from two human subjects (BMI of 25 and 33) associated with another ongoing study protocol approved by the institutional review board and radiation protection committees. The anterior-posterior and lateral cumulative tissue densities through mid thorax of the humans and swine were compared along line profiles as shown in the right panel of Figure 59. Example thoracic cross sections for both humans and the swine are shown in the left three panels of Figure 59.

A volume of 40% xenon, sufficient to raise mouth-pressure from 0 to 25 $cmH_20$, was rapidly delivered via 3-L calibration syringe (Model 5530: Hans Rudolf, Kansas City, MO) to an anesthetized supine swine and then scanned. In addition to scanning at both 80/140Sn and 100/140Sn, various combinations of pitch and collimation were also acquired. These scans were qualitatively and quantitatively examined for artifacts by placing small circular ROIs along the x-axis of the same transverse slice from each scan. The mean and standard deviation of xenon concentration were calculated for each ROI and compared.

## 7.2 Results

### 7.2.1 Test-Object Results

Using the scans of the xenon-filled syringes at 80,100, and 140Sn kVp, density enhancements as a function of xenon concentration were determined. Plots of mean density versus xenon concentration for the syringes in open air and within the Alderson RS-320 Chest Phantom are shown in Figure 60. Within the Chest Phantom, HU enhancement per percent xenon was 2.25 at 80kVp, 1.7 at 100 kVp, and 0.76 at 140 kVp (with tin filter). Similarly, in open air, HU enhancement per percent xenon was 2.5 at 80kVp, 1.95 at 100 kVp, and 0.81 at 140 kVp (with tin filter). These syringe tests provide two new sets of numbers to use in the scanner-based xenon three-material decomposition module. Our "within test-object" settings for 80 and 140 kVp respectively are: air; -993 and -1000 and xenon; -771 and -925. Similar "in-air" settings are air: -999 and -999 and xenon: -751 and -917. For reference, the default Siemens settings are air: -1000 and -1000 and xenon: -796 and -928 for 80 and 140 kVp respectively.

The comparisons between the Siemens' default three-material decomposition calibration parameters and those derived from our syringe calibrations demonstrate noteworthy differences between the balloon inside the phantom and in open air (Figure 61, Table 10). The Siemens' calibration over estimates the xenon content of each included voxel. Thus, as the number of included voxels increases with balloon volume, the estimation of overall xenon content increasingly diverges from the actual value (dotted line in graphs displayed in Figure 61). This effect is accentuated with the balloon placed inside the chest phantom (Figure 61, *middle-left panel*). The results from the new syringe-based calibrations are offset from the manufacturer's default calibrations and resulted in lower than expected calculated xenon content at the smallest balloon volumes, representing the highest per-voxel xenon concentrations. However, the estimation of

total xenon content within the balloon showed much less deviation with increasing balloon volumes and in fact matched more closely with the expected xenon volume as the balloon volume increased. Volume renderings of the step-wise inflated balloon are shown in the *top panel* of Figure 61, and sagittal images of the balloon positioned within the phantom and in open air are shown in the *lower panel* of Figure 61.

Time-series analysis of the 80%Xe/20%$O_2$ and 40%Xe/60%$O_2$ gas mixtures delivery to the hollow airway phantom indicates a flow-rate dependent profile. While gravitationally dependent airways achieved their expected maximal luminal density regardless of delivery speed (velocity) (Figure 62, *right column*), gravitationally non-dependent airways only achieved their expected maximal luminal density during high-speed delivery of xenon gas (Figure 62, *middle column*). However, when the gas density was lowered using a mixture containing helium (40%Xe/40%He/20%$O_2$) the gravitational effects were attenuated, thus allowing both dependent and non-dependent airway pathways to achieve their expected luminal density at both delivered speeds (Figure 62, *rows 3 and 6*).

To test the effect that helium vs. oxygen carrier gases had on the three-material decomposition-based assessment of xenon in a 40% xenon mixture, we replaced a portion of the oxygen with increasing amounts of helium within a set of 4 syringes. The syringes were placed in the Alderson Chest Phantom, and our developed xenon calibration shown in Figure 60 was used to assess xenon concentration in the 4 syringes. As demonstrated in Figure 63, the helium did not affect the calculated xenon percentage.

### 7.2.2 Animal Experiment Results.

Deviations from the suggested default values for pitch and collimation from Siemens (0.55, 64 channels) yielded images suffering from considerable visual artifacts. Changing the pitch from 0.55 to 1.00, increasing the number of channels from 64 to 128, or doing both increased artifacts (Figure 64, *left panel*). The mean xenon value (Figure

64, *upper-right panel*) stays relatively consistent when the number of channels is changed from 64 to 128, however, the standard deviation (Figure 64, *lower-right panel*) increases in many of the ROIs. Changing the pitch from 0.55 to 1.00 causes variations in the mean xenon value and considerable increases in standard deviation.

Scanning with 80/140Sn kVp yielded better overall dual-energy xenon-CT image quality compared to 100/140Sn kVp. Though a single-energy 100kVp scan has less image noise than an 80kVp scan (133), the lower HU enhancement of xenon at 100kVp produces inferior material separation and consequently inferior three-material decomposition. This difference is clear in the transverse (*left column*), sagittal (*middle column*), and coronal (*right column*) views from scans of a swine following a large single breath inhalation of 40%Xe/40%He/20%$O_2$ gas mixture seen in Figure 65. While the mean xenon concentrations for the entire lung are similar (80/140Sn, 22.7%; 100/140Sn, 21.8%) the coefficient of variation of xenon concentration is higher in the 100/140Sn scan (80/140Sn, 0.349; 100/140Sn, 0.380). Even more telling are the airways. For the same delivered xenon gas mixture, the airways are brighter the 80/140 kVp scan (80/140Sn, 31.6%; 100/140Sn, 25.1%) with considerably lower noise (80/140Sn, CV of 0.140; 100/140Sn, CV of 0.216). Thus the SNR (signal-to-noise ratio; SNR = 1/CV) for the 80/140 kVp pair is 7.1. For the 100/140 kVp pair SNR = 4.6. The SNR for the 80/140 kVp pair is greater than the Rose Criterion (SNR > 5) (206) while the 100/140 kVp pair is not. As shown in Figure 66, when a 40Xe/40He/20$O_2$ gas mixture was used in conjunction with 80/140kVp DECT, good xenon delivery is achieved in both the dependent and non-dependent airway structures. Shown here is a volume rendering of the high xenon concentration regions of the xenon image represented by the lower panel of Figure 65.

The comparison between the 80/140Sn and the 100/140Sn kVp pairs in two animals (*animals 4 & 5*) scanned over a range of xenon concentrations (0, 20, 40, 60, 80, 100% Xe) using a paired samples t-test shows statistically significant differences to the

$p<0.05$ level between the mean of the measured xenon concentration in the lung parenchyma ($p<0.001$) and in the mean ($p<0.001$) and CV ($p<0.001$) of the measured xenon concentration in the central airway tree.

The body size comparison, using integrated radial density profiles, showed that the 60kg swine had a relative density of 138% of the 25 BMI and 89% of the 33 BMI human subjects respectively.

## 7.3 Discussion

An improved understanding of the technique and proper calibrations are necessary in order to accurately interpret physiological information from imaging studies. To that end, we have determined an optimized protocol to be used when performing a xenon-DECT scan. The protocol includes: a gas mixture containing 35-40% xenon while using a helium/oxygen mixture as the carrier gas, fast delivery speeds to adequately distribute to both gravitationally dependent and non-dependent lung regions, scanning with the 80/140Sn kVp pair for greater xenon contrast, while using 64 detector rows and the manufacturers recommended pitch setting of 0.55 to help limit imaging related artifacts. DECT reconstruction kernels were also used as directed by the manufacturer. In addition, identifying the proper calibration parameters for the three-material decomposition technique in each subject is essential to adapt for variations in beam hardening and scatter. While neither calibration in this study yielded the expected xenon content (400 mL) at every inflation level in the balloon test-object studies, the more consistent results from our calibrations would likely allow for improved comparisons between regions.

Previous work using wash-in and wash-out xenon-CT techniques (112) have indicated that a 40% xenon gas concentration was minimal to achieve an SNR which allowed for curve fitting. To study a single breath hold DECT xenon gas protocol to evaluate regional ventilation, we have explored xenon gas concentrations of 25%, 40%,

60% and 80%. We considered that the administration of a gas mixture that is heavier than room air might have flow-dependent gravitational effects. The greater the gas density and the slower the gas flow the more likely opacification of only dependent airways would occur. This has been verified by use of computational fluid dynamics (CFD) modeling (113). To explore whether or not these hydraulic properties of xenon gas might be brought more in line with room air by mixing xenon gas with helium we first sought to understand the effect of the presence of helium on the three-material decomposition methodologies. Initially we used cylindrical test-objects filled with different xenon and oxygen gas mixtures guide us to the minimal xenon gas concentration that provides adequate opacification of the airways. 40% xenon worked best and is tolerated by the patient. Honda et al. have used 35% xenon in conjunction with dual-energy imaging (139). The mean alveolar concentration whereby 50% of patients will respond to a verbal command (MAC awake) is 33% (30). This represents a concentration of xenon gas being delivered continuously. To prevent gravitational effects we used 40% helium gas along with the requisite 20% oxygen gas. At higher flow rates this provided good airway opacification of both dependent and non-dependent airways. These techniques were then performed in an anesthetized swine and confirmed that our technique was successful in imaging all of the swine's central airways and peripheral airways out to those with an approximately 2 mm diameter as shown in Figure 66. The rapid prototyped airway tree test-object that we used was derived from a CT scan of an adult human. It has been shown that the bipodial airway branching pattern of a human results in different airflow patterns than animals with a monopodial branching pattern (207). The ability of the xenon/helium/oxygen mixture to overcome the gravity dependent effects in an animal with a monopodial branching pattern where gravity effects on flow properties are more extreme than in humans provides a maximum challenge for such a methodology.

Xenon performs well as a contrast agent for DECT studies. However it is limited by it's high density and anesthetic properties (28). Xenon is not the only radiodense gas.

Recent work utilizing krypton (3.28 kg/m$^3$) alone in conjunction with DECT has shown that a signal can be detected using three-material decomposition (135) whereby a maximum signal of 18 HU at an 80% concentration was observed and mean HU in emphysematous vs. normal appearing lung was 7.58 ± 4.05 and 12.36 ± 3.75 respectively. This is too low for assessment of regional ventilation heterogeneities other than large-scale pathologies. The lower signal enhancement from krypton yields data that is highly susceptible to image artifacts. It may be possible to use krypton alone in the future with advancements in reconstruction algorithms and detector design or as a supplement to xenon. The advantage of krypton is that it shows no anesthetic effect. Krypton gas has been shown to be useful as a supplementation to 40% xenon so as to increase signal-to-noise while avoiding the anesthetic effects of higher concentrations of xenon (112).

Three-material decomposition techniques for DECT have used paired X-ray tube peak energies of 100/140 kVp and 80/140 kVp. The demonstration that our swine studies provide a similar density load to the reconstructed images as would be expected from human scanning of subjects with a BMI between 25 and 33. Thus, our observations, highlighted in Figure 65, suggest that the use of 80/140 kVp would be appropriate for the majority of subjects up to a BMI of at approximately 33. A future and larger study would be needed to more specifically define a BMI cutoff for the use of 80/140 kVp for dual-energy xenon-CT in high BMI subjects. The observation that 80 kVp provides better contrast to noise in our xenon study compared with 100 kVp is in agreement with previous reports (139). Use of newly emerging iterative reconstruction techniques (208) along with more sensitive DECT detectors (209,210) are expected to provide further improvements in contrast resolution.

In summary, we demonstrate that with appropriate calibration, three-material decomposition methodologies used in conjunction with dual-energy computed tomography provides accurate measures of xenon gas volumes within a realistic thoracic

phantom, and use of helium within a xenon/oxygen/helium gas mixture can overcome gravitational effects associated with the high density of xenon gas without effecting quantitative measurements.

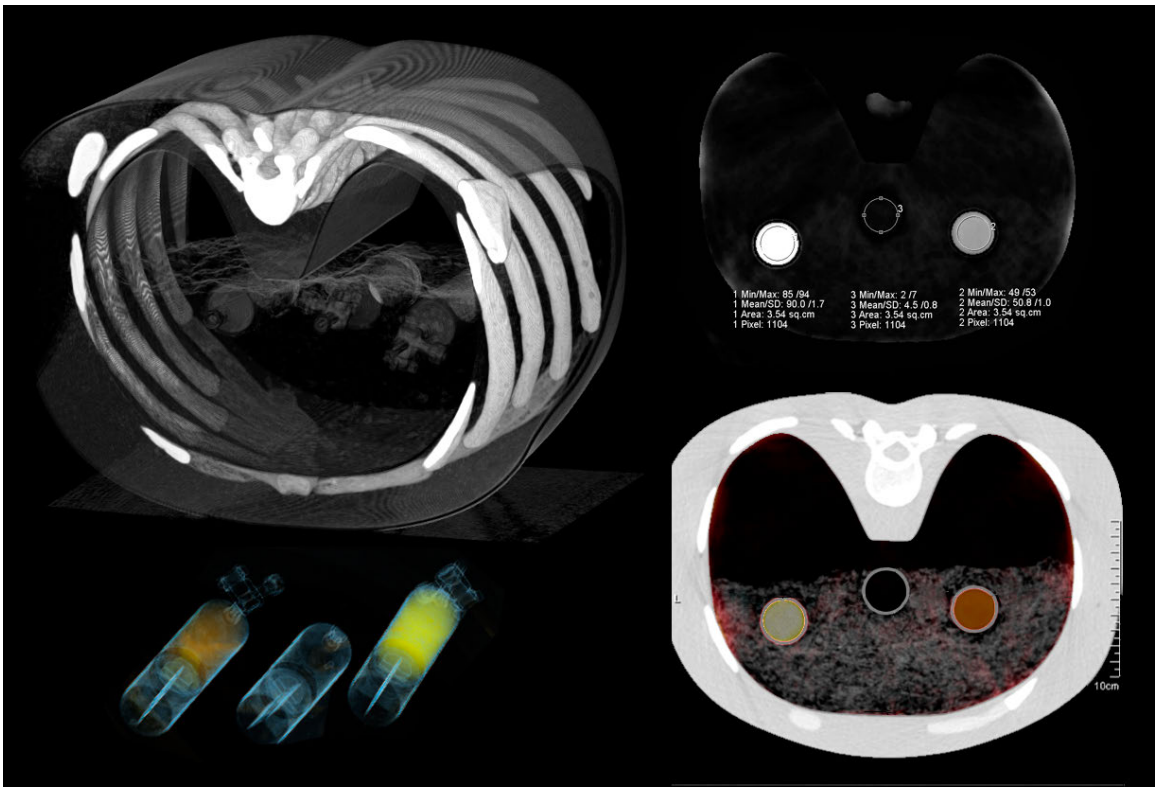


Figure 57. Groups of three 60cc plastic syringes were sequentially placed inside an Alderson RS-320 Lung/Chest Phantom (Radiology Support Devices, Long Beach, CA) to establish radiodensity enhancement scales for xenon gas at different photon energies (80, 100, 140 kV). A volume rendering of the setup is show in the *upper-left panel*. A resultant xenon intensity image from dual-energy three-material decomposition is shown in the *upper-right panel* using the established scales. This result is also presented as an image fusion with the greyscale CT image, seen in the *bottom-right panel*, and rendered in 3D in the *bottom-left panel*.

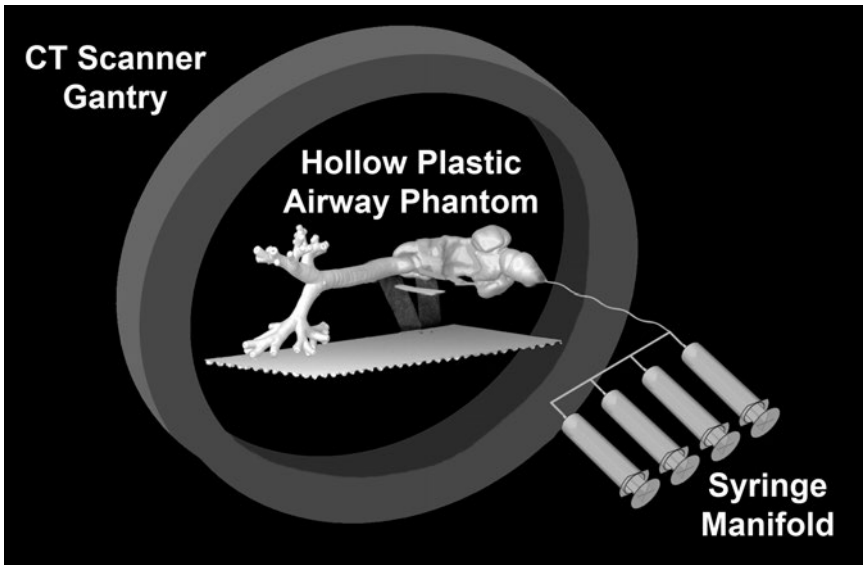


Figure 58. A hollow plastic airway phantom positioned along the imaging plane of the CT scanner is used to characterize inspired gas distribution to the central airways. The syringe manifold consisted of four 60cc syringes linked together to allow controlled delivery of gas to the phantom.

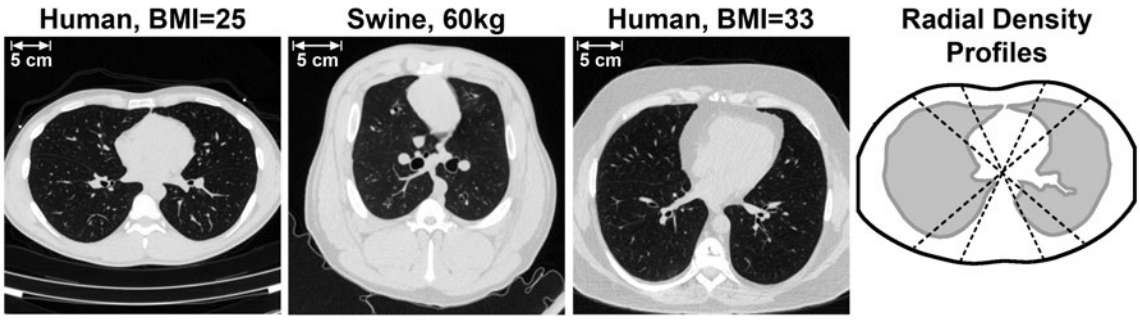


Figure 59. To explore the relationship between body size and dual-energy xenon-CT measurements, integrated radial density profiles from a 60 kg swine were compared against two human subjects. The first three panels show transverse images from an average size human (BMI of 25), a swine (60 kg) and larger size human (BMI 33) respectively. The fourth panel is a diagram illustrating the location of the examined density profiles. The 60 kg swine had a relative density of 138% of the 25 BMI and 89% of the 33 BMI human subjects respectively. The field of view varies between subjects, a 5cm length reference is provided.

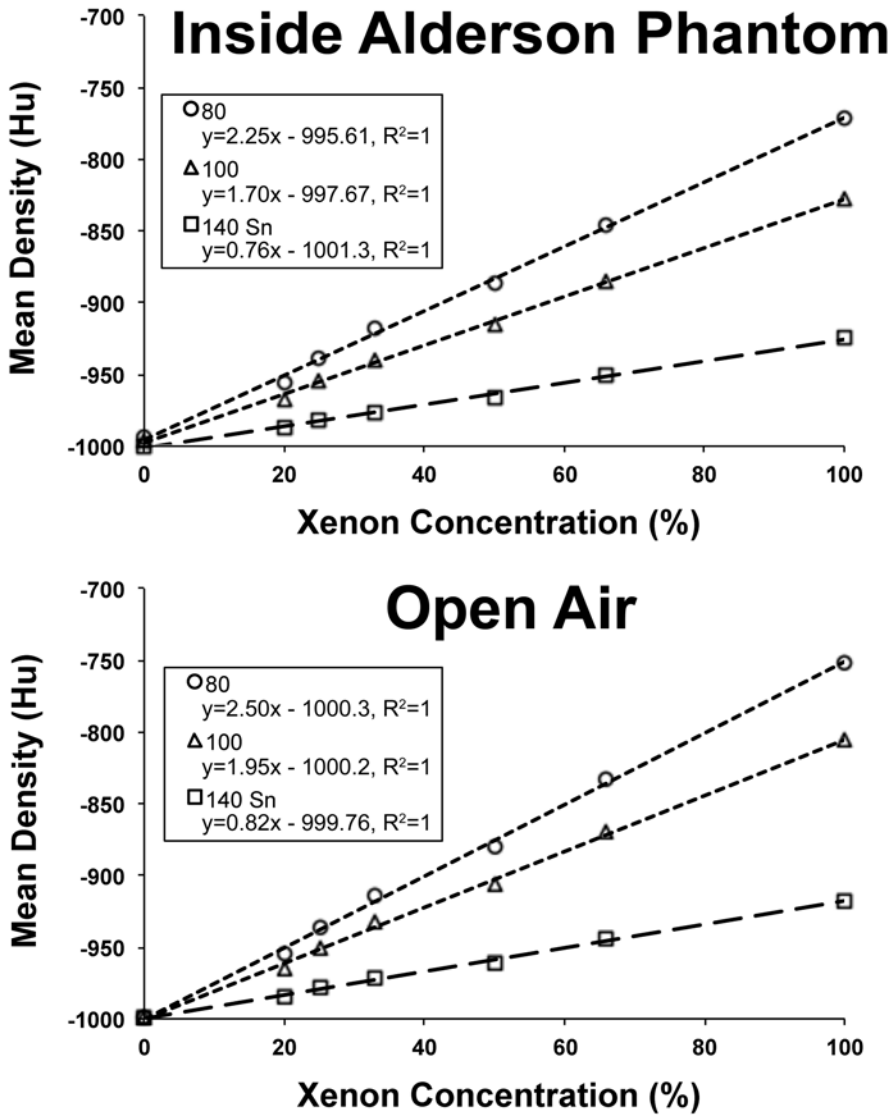


Figure 60. Mean Hu measurements from the syringe studies, inside the Alderson RS-320 Lung/Chest Phantom and in open air, plotted as a function of xenon concentration.

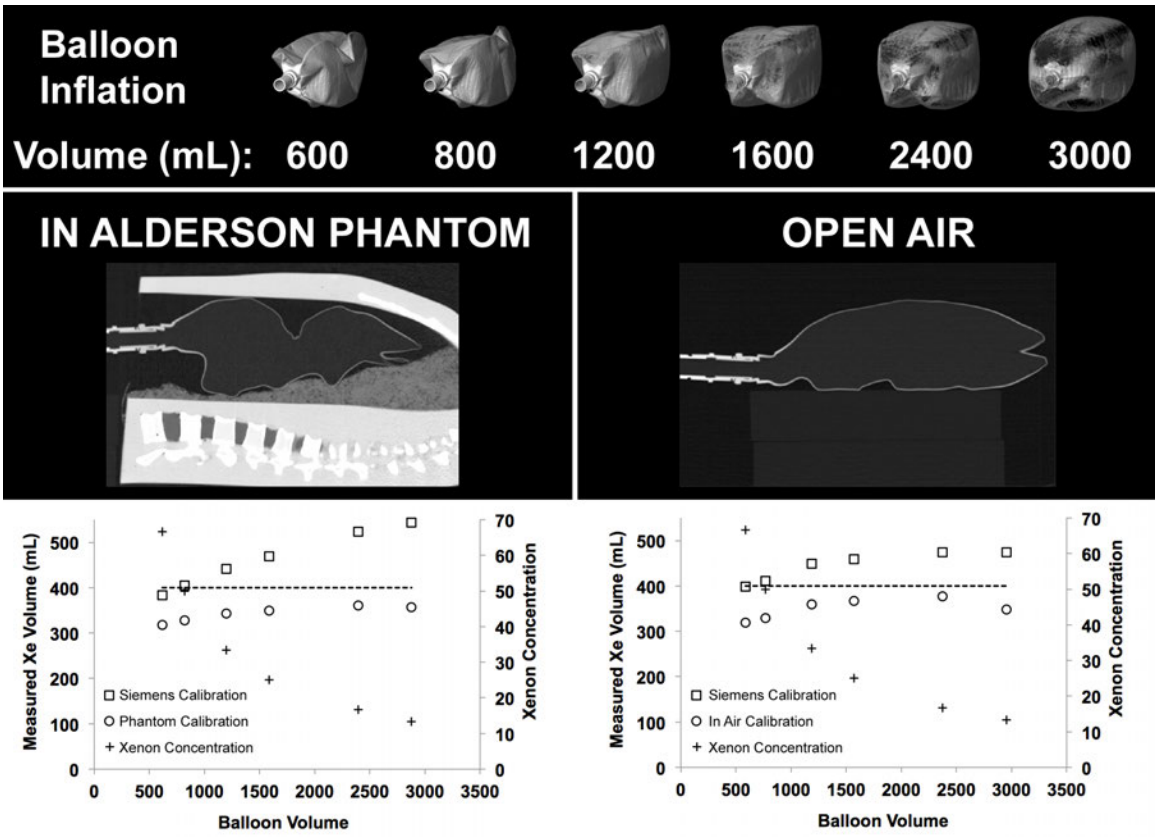


Figure 61. A 3-L respiratory balloon, place inside the Alderson chest phantom (*middle-left panel*) and in open air (*middle-right panel*), was filled with an initial amount of xenon gas and scanned via DECT. Small amounts of room air were then sequentially added to increase the volume of gas in the balloon while keeping the xenon content the same. The balloon was rescanned (*bottom-row*) after each increase in volume. The goal was to determine the quantitative accuracy of the assessment of total xenon content within the balloon as the concentration of xenon gas decreased while the xenon gas volume remained constant. Plots of xenon volume inside the phantom (*top-left panel*) and in open air (*top-right panel*) compare the default calibration with a custom calibration based on previous syringe tests.

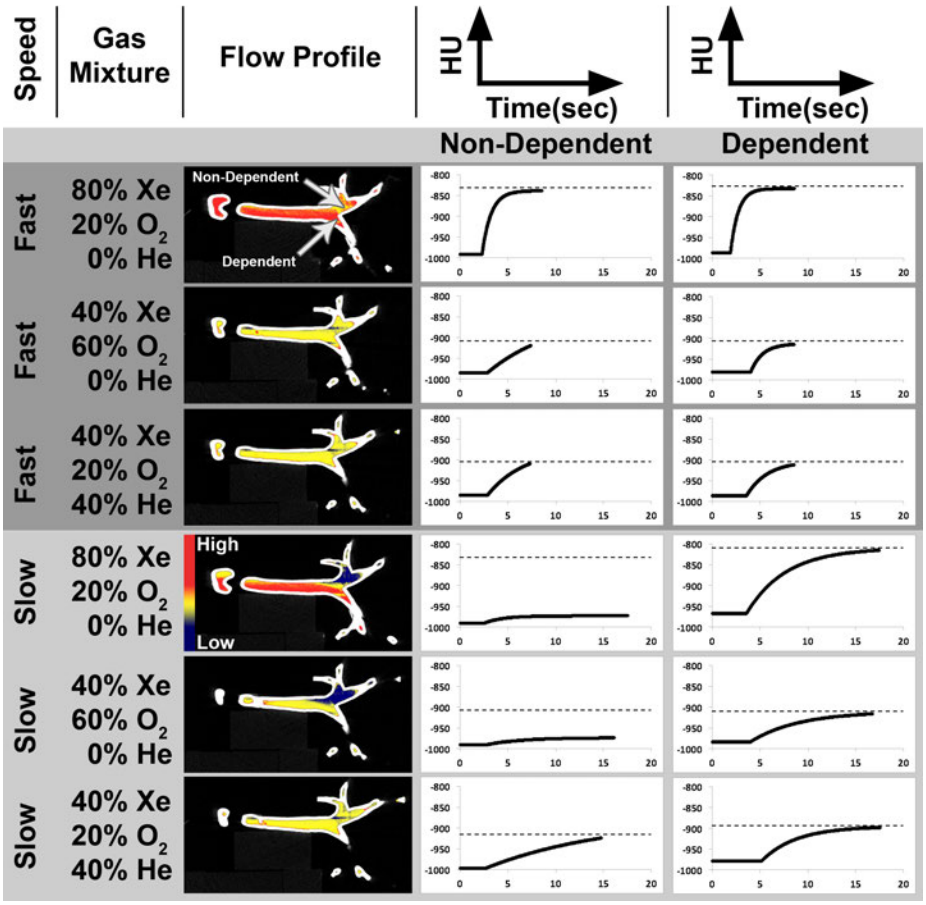


Figure 62. Three xenon gas mixtures (80%Xe/20%$O_2$; 40%Xe/60%$O_2$; 40%Xe/20%$O_2$/40%He) were delivered during time-series MDCT axial image acquisition, at fast and slow flow rates, to a hollow plastic airway phantom positioned along the imaging plane of the CT scanner *(Figure 2)*. Gravitationally non-dependent and dependent ROIs were placed as shown in the flow profile column, row 1. Intensity vs. time plots for both ROIs are shown in the middle and right columns respectively, with dashed lines on each plot indicating the expected level of density enhancement from baseline for each gas mixture. With a fast delivery, density measurements for non-dependent and dependent ROIs reach their expected levels in all cases. However, when delivered slowly, gravity plays a larger role in the gas distribution. Thus, all of the dependent ROI reach expected levels; while the only non-dependent ROI to reach it's expected level is the one that includes helium.

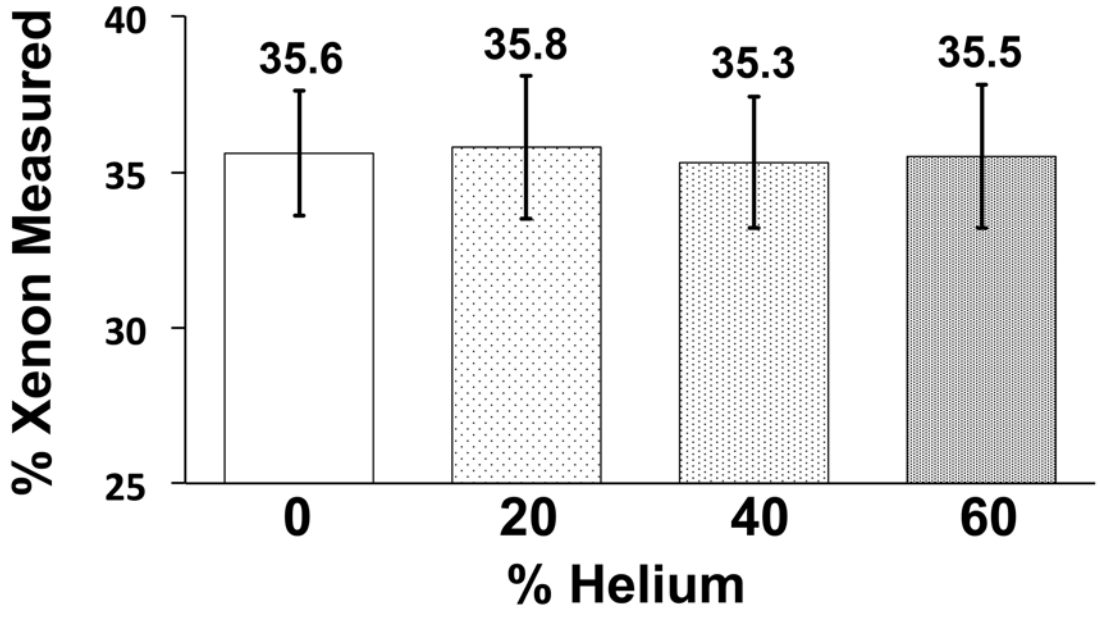


Figure 63. Helium gas does not affect the radiodensity of xenon gas. Columns represent the calculated dual-energy xenon signal from plastic syringes placed inside an artificial chest phantom (see Figure 57) filled with 40% xenon gas and various percentages of helium gas, balance oxygen. The xenon signal is the output of the three-material decomposition algorithm within Siemen's "xenon" module. (Error bars reflect ± standard deviation)

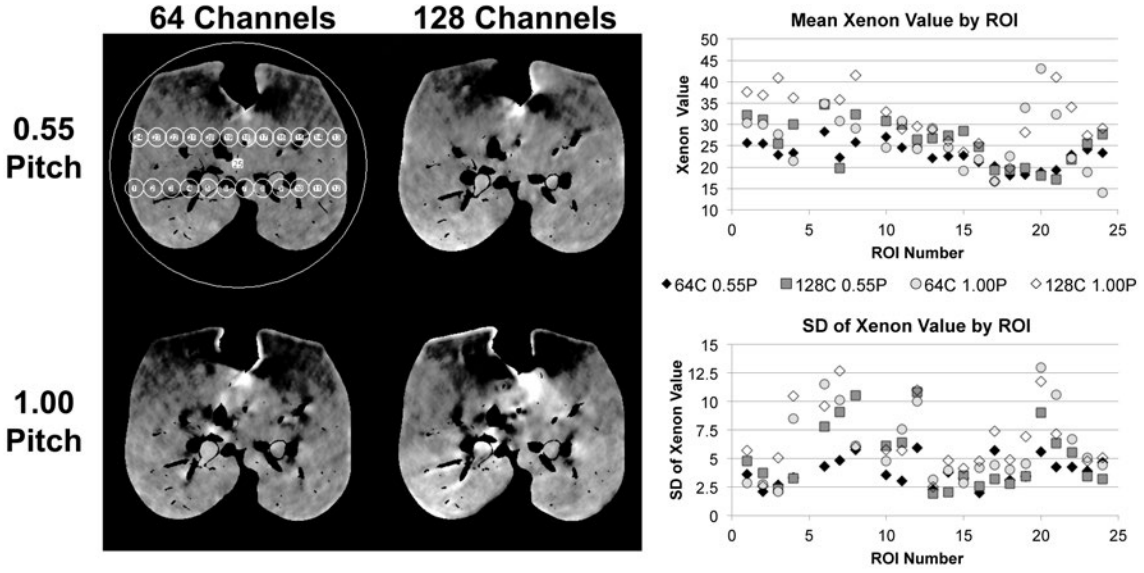


Figure 64. Deviations from the suggested default values by raising the pitch from 0.55 to 1.00, increasing the number of channels from 64 to 128, or doing both yielded considerable visual artifacts (*left panel*). The mean xenon value (*upper-right panel*) stays relatively consistent when the number of channels is changed from 64 to 128, however, the standard deviation (*lower-right panel*) increases in many of the ROIs. Changing the pitch from 0.55 to 1.00 causes variations in the mean xenon value and considerable increases in standard deviation.

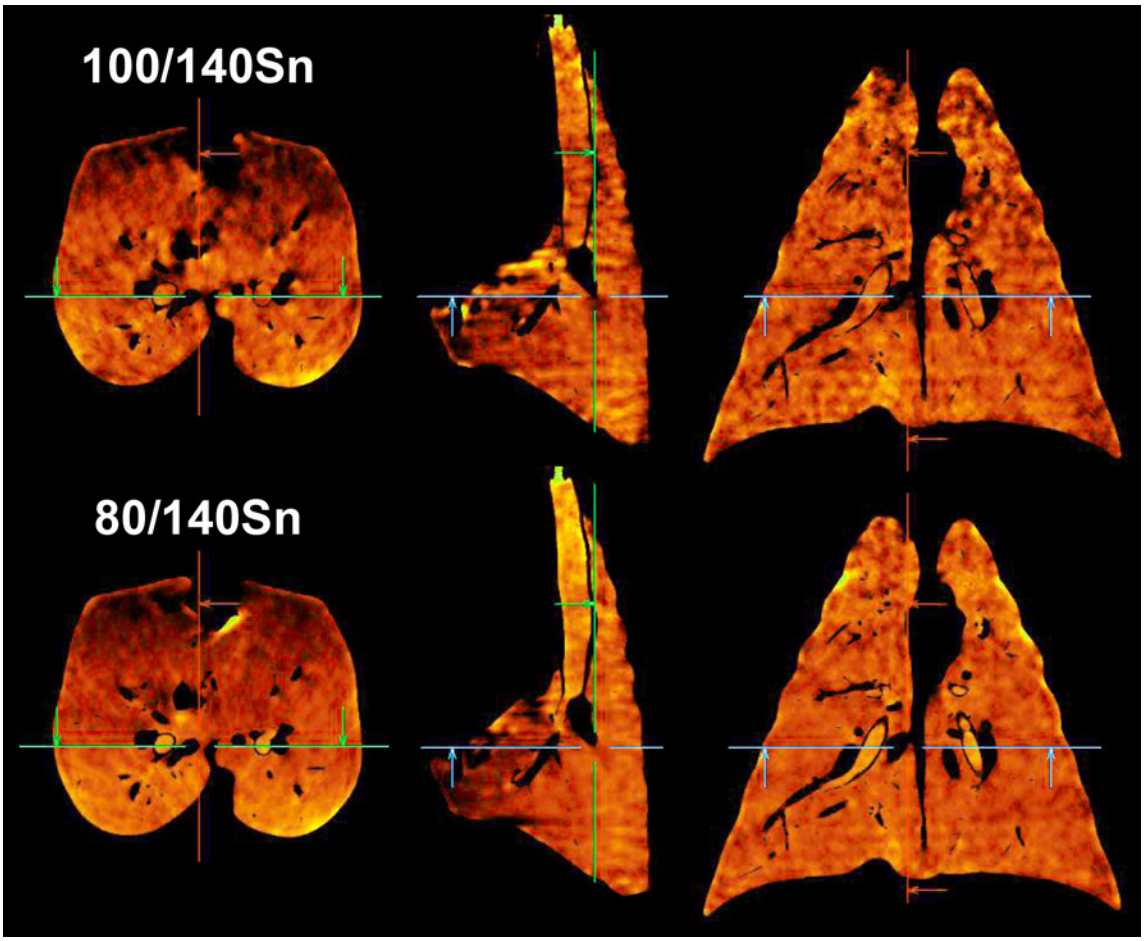


Figure 65. Scanning with 80/140Sn kVp yields more accurate dual-energy xenon-CT images compared to those using 100/140Sn kVp. Transverse (*left column*), sagittal (*middle column*), and coronal (*right column*) views are shown from scans of a swine following a large single breath inhalation of 40%Xe/40%He/20%$O_2$ gas mixture. The increased density separation between 80 and 140 kVp (*bottom row*) over 100 and 140 kVp (*top row*) allows for better calculation of xenon content. Airways are clearer and brighter in the 80/140 kVp results in addition to an overall smoother image.

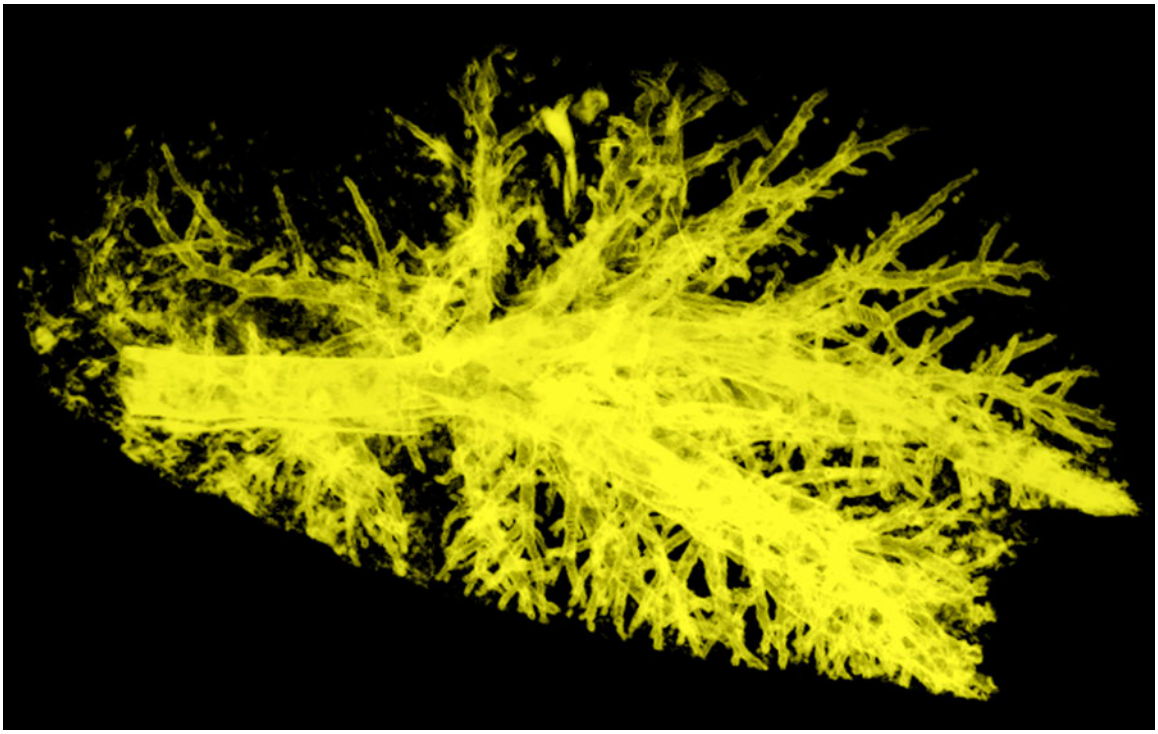

Figure 66. Volume rendered image of the three-material decomposition derived xenon imaged of a swine. Xenon-DECT using a 40%Xe/40%He/20%$O_2$ gas mixture was successful in imaging all of the swine's central airways and peripheral airways out to those with an approximately 2-mm diameter.

| | Instilled Volume | | | | Measured Volume | | |
|---|---|---|---|---|---|---|---|
| | Xe | Air | Total | % Xe | Mask Volume | Siemens Calibration | Phantom Calibration |
| Inside Alderson Chest Phantom Tests | 400 | 200 | 600 | 67 | 616 | 383 | 318 |
| | 400 | 400 | 800 | 50 | 821 | 405 | 328 |
| | 400 | 800 | 1200 | 33 | 1198 | 442 | 343 |
| | 400 | 1200 | 1600 | 25 | 1588 | 469 | 350 |
| | 400 | 2000 | 2400 | 17 | 2395 | 523 | 360 |
| | 400 | 2600 | 3000 | 13 | 2879 | 544 | 357 |

| | Instilled Volume | | | | Measured Volume | | |
|---|---|---|---|---|---|---|---|
| | Xe | Air | Total | % Xe | Mask Volume | Siemens Calibration | Open Air Calibration |
| Open Air Tests | 400 | 200 | 600 | 67 | 588 | 398 | 319 |
| | 400 | 400 | 800 | 50 | 767 | 411 | 329 |
| | 400 | 800 | 1200 | 33 | 1189 | 449 | 359 |
| | 400 | 1200 | 1600 | 25 | 1573 | 459 | 367 |
| | 400 | 2000 | 2400 | 17 | 2374 | 474 | 377 |
| | 400 | 2600 | 3000 | 13 | 2953 | 475 | 348 |

Table 10. Xe-DECT three-material decomposition calibration test results comparing the default values suggested by Siemens with those obtained via our syringe calibrations in open air and inside the Alderson RS-230 Lung/Chest Phantom.

# CHAPTER 8: DUAL-ENERGY PULMONARY PERFUSED BLOOD VOLUME AS SURROGATE FOR DYNAMIC PULMONARY PERFUSION ASSESSED BY MDCT

Despite considerable successes with quantitative computed tomography, and its adoption into numerous multi-center pharmaceutical and device trials, the assessment of the presence and distribution of emphysema and airway wall remodeling in chronic obstructive pulmonary disease (COPD) may be missing critical underlying differences more closely aligned with disease pathophysiology (14,15). It has recently been demonstrated (14) that a subset of smokers with very early CT-based evidence of susceptibility to centrilobular emphysema and normal spirometry have increased regional heterogeneity of pulmonary blood flow (PBF) and mean transit time (MTT). These findings are consistent with the hypothesis that patchy, inflammation-based hypoxic pulmonary vasoconstriction (HPV) is occurring in smokers susceptible to centrilobular emphysema while the normal response to inflammation associated hypoxia (local alveolar flooding) is to maintain regional perfusion(115,211). We strongly believe that an assessment of functional phenotypes such as PBF and MTT are critical in the advancement of the understanding of the etiology of the disease and are critical to the development of new, targeted therapies.

Implementation of the CT-PBF method, requiring placement of a central line for rapid high-pressure injection of X-ray contrast agent during sequential cardiac-gated axial CT scans during a breath-hold, is impractical for wide spread implementation in multi-center studies. Recent developments in dual-source dual-energy CT offer the ability to image regional pulmonary perfused blood volume (CT-PBV) utilizing a peripheral venous line and slow infusion of contrast agent while spirally imaging the entire lung in a single, short breath-hold; a protocol similar to that used for assessment of pulmonary emboli (147,149,212-216).

The lung has a large capacity for dilation and recruitment of capillary beds as the entire blood volume passes through the pulmonary vascular bed while maintaining very low pressures relative to the systemic circulation (217). There is a close relationship between pulmonary perfusion and capillary recruitment (218). Thus, one would expect that there is a correlation between CT measures of regional perfused blood volume (PBV) and CT measures of pulmonary perfusion. As perfusion to a region increases, capillary beds would be expected to both expand and new portions of the capillary bed may be recruited. Thus, simpler measures of pulmonary PBV, requiring only a single volume scan using dual-energy CT (19) to quantitate regional iodine concentrations can serve as a surrogate for the dynamic imaging methods that have been used to date (14,122). In this study, we utilize two pig models whereby interventions are employed to modify regional patterns of pulmonary parenchymal perfusion so that our measures of regional PBV and PBF can be compared.

## 8.1 Materials and Methods

### 8.1.1 Animal Preparation.

The Institutional Animal Care and Use Committee approved all animal studies reported here. Four farm-bred swine (32.7 ± 5.6 kg; 2 males) were premedicated with Ketamine (20 mg/kg) and Xylazine (2 mg/kg) intramuscularly, and anesthetized with 3–5% isoflurane in oxygen by nose cone inhalation. Once surgical depth of anesthesia was achieved, an 8.0-mm inner diameter cuffed endotracheal tube was placed through a tracheostomy and the animal was mechanically ventilated with 100% oxygen, tidal volume of 10-14 mL/kg, rate of 10-20/min adjusted to achieve an end-tidal $PCO_2$ of 30–40 mm Hg. Femoral arterial, femoral venous, and external jugular venous introducers were placed. A 7-French pigtail catheter was advanced into the right ventricle under hemodynamic and fluoroscopic control. Surgical plane of anesthesia was maintained with inhaled isoflurane (1–5% in oxygen), neuromuscular blockade was achieved with

pancuronium (0.1 mg/kg IV initial dose and 0.5–1 mg/kg hourly as needed). Arterial pressure, oxygen saturation, and airway pressures were continuously monitored and recorded. Thermodilution cardiac output was performed.

### 8.1.2 CT Imaging

All imaging was performed on a second-generation dual-source CT scanner (Somatom Definition Flash: Siemens Medical Systems, Erlangen, Germany). Axial (4 cm z-axis extent) ECG-gated dynamic CT-PBF scans (80 kV, 150 mAs, 0.75 mm slice thickness, 0.5 mm increment, 0.28 sec rotation time, 25 time-points, ~4.2 mSv) were acquired during continuous airway pressure breath-holds with right ventricular injection of iodinated contrast (0.5 cc/kg over 2 sec, Isovue: 370mgI/mL, Bracco Diagnostics Inc., Princeton NJ), as previously described (14,119,122). Spiral dual-energy CT-PBV scans (either 80/140 or 100/140 kV, 0.75 mm slice thickness, 0.5 mm increment, 0.55 pitch, ~3.5 mSv) were acquired during continuous airway pressure ($P_{awy}$) breath-holds with an infusion of Isovue (4 cc/sec). A delay adequate for Isovue equilibration, approximately 15 seconds, was included before the initiation of the dual-energy scan in accordance with the standard pulmonary embolism scanning protocol (219).

The issue in using dual-energy CT and iodinated intravenous contrast material for assessing PBV is that there are three unknown independent variables per voxel (air, soft tissue/blood, and iodine and only two measured linear attenuation coefficients per voxel. We solve this using a generalized three-material mass fraction decomposition technique discussed elsewhere (134).

### 8.1.3 Perfusion Heterogeneity

Pulmonary perfusion was altered using two methods chosen to facilitate the comparison of the two techniques over a variety of PBF values and induce a range of PBF heterogeneities. Two of the animals (animal 1 & 2) were examined following sequential occlusion with a balloon catheter placed in a pulmonary artery, such that blood

flow to progressively larger portions of lung parenchyma was occluded. In the other two animals (animals 3 & 4), the continuous airway inflation pressures were increased by 5 $cmH_20$ increments, from 5 to 25 $cmH_20$ $P_{awy}$, to obtain five different lung inflation levels for comparison. The acquisition of CT-PBF and CT-PBV datasets was done as a coupled pair performed sequentially at each state with a minimal delay between scans necessary for animal recovery and contrast washout. Thus, at each state, animals received two CT scans, one for PBF and one for PBV. The balloon model incorporated 4 states (baseline, balloon 1, balloon 2, & balloon 3) resulting in 8 scans, while the lung inflation model incorporated 5 states (5, 10, 15, 20, & 25 $cmH_20$) resulting in 10 scans.

### 8.1.4 Image Analysis

Quantitative regional CT-PBF was determined by the application of indicator dilution theory and first-pass kinetics to the 4-D ECG-gated axial CT perfusion images (119,122). CT-PBF was calculated using the ratio of peak parenchymal density enhancement to the area under the time-density curve of a reference pulmonary artery using the Time-Series Image Analysis (TSIA) module of the Pulmonary Analysis Software Suite (PASS) (Figure 67) (161). Voxels for the CT-PBF imaging were 0.46 x 0.46 x 0.5 mm. The software performs a curve fitting process on the mean intensity of a ROI over time. To reduce noise, a neighborhood-averaging filter is applied on each ROI such that the mean value from a 7x7-voxel region surrounding a voxel was used to represent the intensity of the voxel for that time-point. Regional perfusion ($PBF_{roi}$) values (milliliters per minute per ROI) were normalized by total blood flow in the 4-cm slice stack and presented as a percentage to allow for comparisons between conditions. CT-PBV was calculated using scanner associated (Somatom Definition Flash: Siemens Medical Systems, Erlangen, Germany) three-material decomposition software (Figure 68) that extracts the iodine signal and creates and image for the entire lung representing blood volume as discussed above. Voxels for the CT-PBV imaging were 0.46 x 0.46 x 0.5 mm.

Similarly to CT-PBF, noise reduction for CT-PBV, performed by the scanner associated software, is accomplished by calculating values using a 7x7 neighborhood average to represent the intensity of each voxel. Corresponding regions from the full lung CT-PBV scan were isolated and extracted to match the axial 4-cm slice stack obtained in during the CT-PBF scans. Thresholding was used to exclude voxels outside of the -910 HU to -50HU range. CT-PBF was thresholded using a range of 0 to 0.25 ml/min, and CT-PBV was thresholded using a range of 0 to 375. Simple thresholding is confounded by potential difference in contrast distribution between CT-PBF and CT-PBV scans. CT-PBF utilizes the distribution over time of a short bolus of iodinated contrast while CT-PBV utilizes a continuous infusion until a plateau is reached. Scans acquired during CT-PBF will have a variety of iodine profiles as the distribution of contrast will vary with mean transit times for each location. Therefore in addition to simple thresholding, a combination of semi-automated lung and vessel segmentations were used to restrict the areas of comparison to the lung parenchyma. Manual removal of areas affected by partial volume artifacts (e.g. near cardiac and diaphragmatic borders) as well as regions with artifacts caused by contrast filled catheters placed in the right ventricle of the heart necessary for CT-PBF. The lung boundaries were also eroded to further reduce edge artifacts. CT-PBV values were also normalized to represent a percent of total signal in the 4-cm slice stack. CT-PBF and CT-PBV were compared on a regional basis by dividing the matching 4-cm slice stacks into a 10x10x3 (X, Y, Z) grid of blocks. The volume of each block contained between 100 and 25000 CT-PBF or CT-PBV ROI. Blocks that had a difference in ROI count between CT-PBF and CT-PBV greater that 40% were also excluded. Normalized mean CT-PBF and CT-PBV values as well as the coefficient of variation (CV) of Normalized CT-PBF and CT-PBV values were compared using the sectioned data. Pearson's R and linear correlation coefficients were calculated for both comparisons. The analysis process is depicted in Figure 69.

## 8.2 Results

Normalized CT-PBF values and CV of CT-PBF were highly correlated with normalized CT-PBV values and CV of the CT-PBV, respectively. Normalized colormaps for CT-PBF and CT-PBV are shown in Figure 70 and Figure 71 for the balloon occlusion and lung inflation models respectively. CT-PBF and CT-PBV colormaps for both paradigms are strikingly similar. Representing an example data set from the balloon occlusion model, Figure 70 demonstrates the decreased CT-PBF (*bottom row*) in the occluded region of the left lung and the increased area of this region when the balloon is repositioned to a more proximal location. As seen in the middle row, CT-PBV tracks closely with CT-PBF maps. In Figure 71, note the increasing extent of the non-dependent low perfusion regions (*lower row*) associated with lung inflation. The increased non-dependent area of low perfusion associated with lung inflation is mirrored in the CT-PBV maps (*middle row*).

As shown in Table 11 for the balloon occlusion model, Pearson's R ranged from 0.91 to 0.99 comparing normalized mean CT-PBF with normalized mean CT-PBV and 0.78 to 0.98 for CV of normalized mean CT-PBF with CV of normalized mean CT-PBV with all correlations being statistical significant ($P < 0.01$). $R^2$ values for the linear correlation of normalized mean CT-PBF and normalized mean CT-PBV in Animal 1 were equal to 0.83 for the combined data (0.91 Baseline, 0.87 Balloon 1, 0.86 Balloon 2 and 0.91 Balloon 3) (Figure 72A) and equal to 0.96 for the combined data in Animal 2 (0.96 Baseline, 0.97 Balloon 1, 0.96 Balloon 2 and 0.97 Balloon 3) (Figure 72C). $R^2$ values for the linear correlation of CV of normalized mean CT-PBF and CV of normalized mean CT-PBV in Animal 1 were equal to 0.53 for the combined data (0.59 Baseline, 0.26 Balloon 1, 0.55 Balloon 2 and 0.60 Balloon 3) (Figure 72B) and equal to 0.76 for the combined data in Animal 2 (0.57 Baseline, 0.52 Balloon 1, 0.86 Balloon 2 and 0.68 Balloon 3) (Figure 72D). Table 11 also demonstrates that, for the lung inflation model Pearson's R ranged from 0.94 to 0.97 comparing normalized mean CT-PBF with

normalized mean CT-PBV, and 0.64 to 0.84 for CV of normalized mean CT-PBF with CV of normalized mean CT-PBV with all correlations being statistically significant ($P < 0.01$). $R^2$ values for the linear correlation of normalized mean CT-PBF and normalized mean CT-PBV in Animal 3 were equal to 0.88 for the combined data (0.93 PEEP=5, 0.93 PEEP=10, 0.89 PEEP=15, 0.90 PEEP=20 and 0.89 PEEP=25) (Figure 73A) and equal to 0.88 for the combined data in Animal 4 (0.90 PEEP=5, 0.93 PEEP=10, 0.93 PEEP=15, 0.92 PEEP=20 and 0.94 PEEP=25) (Figure 73C). $R^2$ values for the linear correlation of CV of normalized mean CT-PBF and CV of normalized mean CT-PBV in Animal 3 were equal to 0.54 for the combined data (0.41 PEEP=5, 0.58 PEEP=10, 0.71 PEEP=15, 0.56 PEEP=20 and 0.60 PEEP=25) (Figure 73B) and equal to 0.51 for the combined data in Animal 4 (0.41 PEEP=5, 0.57 PEEP=10, 0.62 PEEP=15, 0.58 PEEP=20 and 0.46 PEEP=25) (Figure 73D).

To address the possibility that the correlation between CT-PBF and CT-PBV might simply reflect a persistent association in the regions studied we performed additional statistical evaluations for the lung inflation model. This was not possible for the balloon occlusion model for several reasons: 1) Animal 1 had the left lung occluded while animal 2 the right and 2) the balloon was placed along whatever peripheral path the catheter took at the time of insertion with the goal of occluding a sublobar segment when the balloon was resting at its most distal location. The lung inflation model had no localized intervention effects and was simply associated with lung geometry. Therefore we chose to use the inflation model for the test of region-based effects.

For each block within the 4-cm slice stack, the mean value between both animals for the normalized means and CV were calculated and then subtracted from animal 4. A second Pearson correlation analysis was then performed on the mean-corrected animal 4 data. For the normalized means, prior to correction, the Pearson's R was 0.93 using

1,011 regions. After correction, Pearson's R was 0.75 and remained statistically significant well below the $p<0.001$ level. This correction suggests approximately a 31% region level effect. While not small, the 31% region level effect yields an $R^2$ (after adjustment) of 0.56, a value well above a standard error of 0.06 for a measurement containing 1,011 regions. Following a similar correction for the CV, the Pearson's R was 0.54 also statistically significant well below the $p<0.001$ level. The CV correction suggests approximately a 25% region level effect. While not small, the 25% region level effect yields an $R^2$ (after adjustment) of 0.29, a value well above a standard error of 0.06 for a measurement containing 1,011 regions.

## 8.3 Discussion

CT-PBV has been shown here to be a good surrogate for CT-PBF heterogeneity, providing an alternative protocol that is considerably more suited for implementation in a clinical setting and in association with multi-center studies. A prerequisite for the CT-PBV method is the requirement of a dual-energy CT scanner. Dual-energy scanners are available from two of the major manufacturers, and will likely be more widely available in the near future. An assumption of the CT-PBV method is that the pulmonary blood volume is uniformly enhanced. In this paper we used normal pigs of similar age and weight and utilized an injection and scanning protocol that had previously proven to assure good, uniform blood pool enhancement. To implement this study in a clinical setting, a protocol should incorporate a test injection to assure that the timing and rate of infusion is adequate for blood volume enhancement. With experience, protocols may emerge which limit the need for such test injections.

The visual assessment of the CT-PBF and CT-PBV color maps in Figure 70 shows that a strong relationship exists between these two methods for assessing regional pulmonary parenchymal perfusion. With progressive obstruction of pulmonary parenchymal perfusion, equivalent lobar boundaries become visible in both of the

functional maps. Comparing the CV of the two techniques shows a strong correlation, as seen by direct comparison (Figure 72,

Figure 73) and by examining the bivariate Pearson's correlation (Table 11). From this we can conclude that CV of CT-PBV is a suitable surrogate for CV of CT-PBF.

The main goal of this study was to determine whether CT-PBF and CT-PBV correlate with each other in general, which we believe has been clearly demonstrated in our results. That being said, CT-PBF and CT-PBV are not 100% the same due to differences in methodological artifacts unique to each method. The major artifacts in both methods relate to measurement proximity to the heart being either partial volume effects from cardiogenic motion or beam hardening streaks related to high concentration of contrast and the presence of catheters in the heart. Ideally, we would simply avoid regions containing the heart, however the CT-PBF method requires a reference ROI placed in a main pulmonary artery in order to perform properly and with the axial sections acquired being only 4-cm long in the z-axis, the heart could not be avoided in this study.

In Figure 72A and Figure 72C as well as

Figure 73A and

Figure 73C, we observe that the shape of the plots comparing the normalized means indicate that the steepness of the slope correlating CT-PBF and CT-PBV increases at a certain level of CT-PBF. We believe that flow through the vessel can increase to a point beyond which there is no further room for capillary recruitment or vessel expansion. Thus, at the higher flow rates, CT-PBF is seen to increase while CT-PBV increases more slowly. When the two parts are combined it yields an overall slope greater than 1. Linear regression plots for CV on the other hand have a slope very close to 1 indicating that the measurement error for each technique is likely unaffected by the flow limitation and clearly illustrates that the CV is not a duplication of mean PBF with a constant standard deviation but offers added information.

CT-PBV, in addition to providing a simpler protocol, reduces radiation exposure compared with CT-PBF protocols and provides for an assessment of the whole lung. Because the Siemens 128-slice Flash CT scanner splits energy spectra between the two X-ray guns such that there is minimal over-lap, dual-energy imaging is achieved with no additional radiation dose compared to single X-ray gun scanners (220). The CT-PBV method also eliminates the need for central line placement because of the elimination of a high-pressure injection. In principle, dual-energy imaging allows the removal of the iodine signal from the images, creating a "virtual" unenhanced image data set that can provide the more traditional quantitative measures of the lung parenchyma and airway structure.

In summary, this study supports the notion that CT-PBV is a suitable surrogate for CT-PBF, providing a functional measure that may lead to new insights into disease processes not achievable by simply mapping the aftermath (parenchymal destruction and airway remodeling) of the pathologic process.

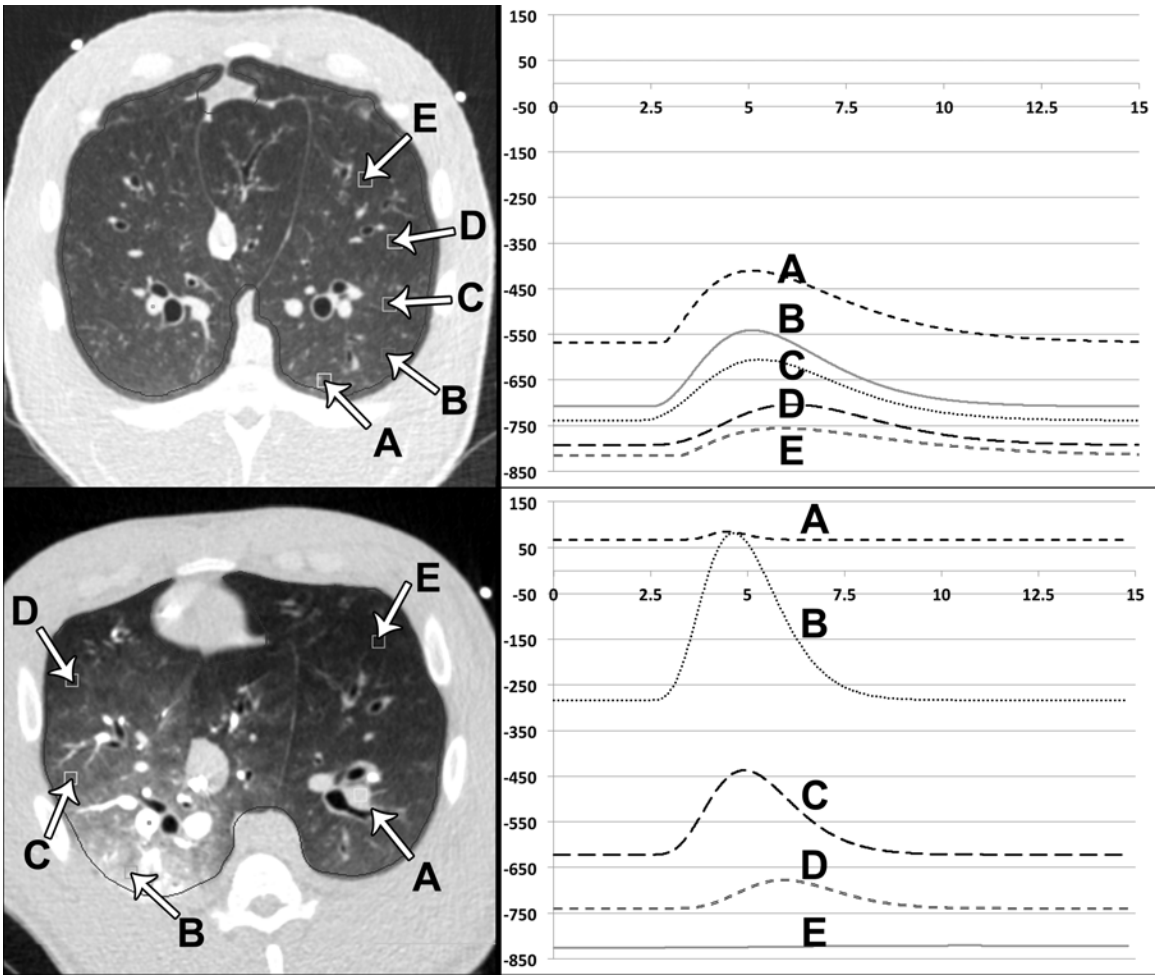


Figure 67. Example CT images and time-intensity curves from the lung inflation model (*top*) and balloon occlusion model (*bottom*). A gravitational gradient in CT-PBV is clearly evident in the lung inflation model. The placement of the occlusion balloon has severely reduced CT-PBF in the left lung (*bottom, curves A and E*). In addition to the time-intensity curves shown here an arterial input curve (*not shown*) from an ROI placed in a main pulmonary artery is utilized to calculate CT-PBF.

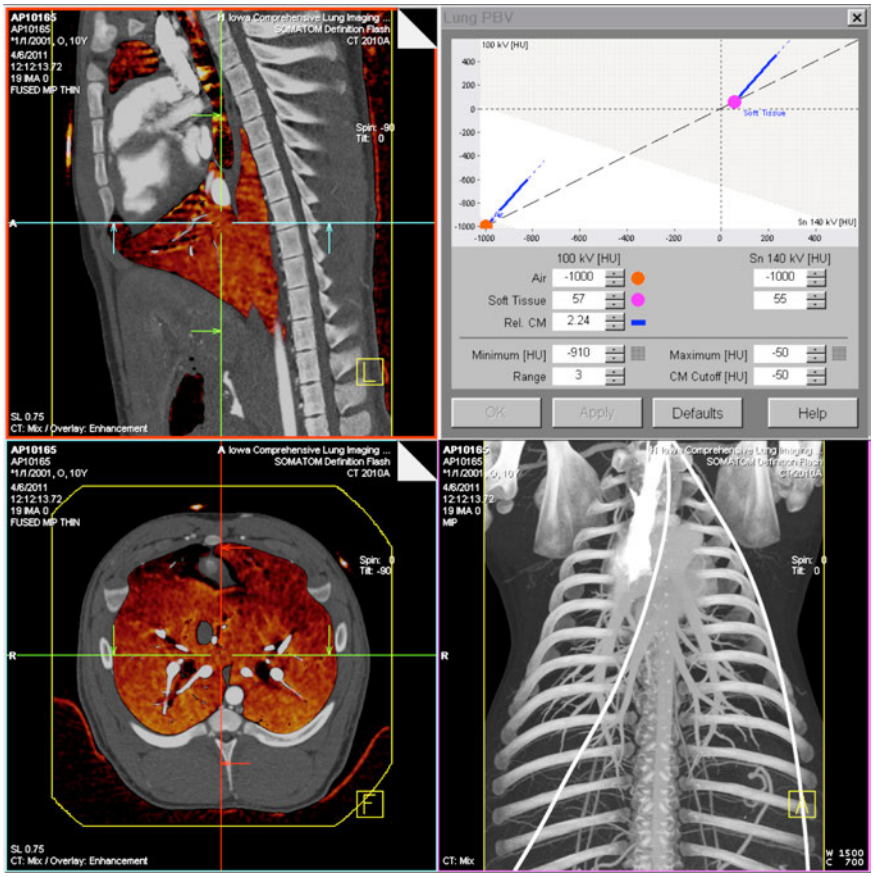


Figure 68. Screenshot of the dual-energy application used to calculate CT-PBV. Sagittal and transverse views of the lung in greyscale with a color overlay of CT-PBV values are seen in the *left* panels. The *upper-right* panel is the parameters box used to input the energy-dependent three-material decomposition attenuation properties used to calculate CT-PBV. A 3D visualization of the pulmonary vasculature is visible in the *bottom-right* panel.

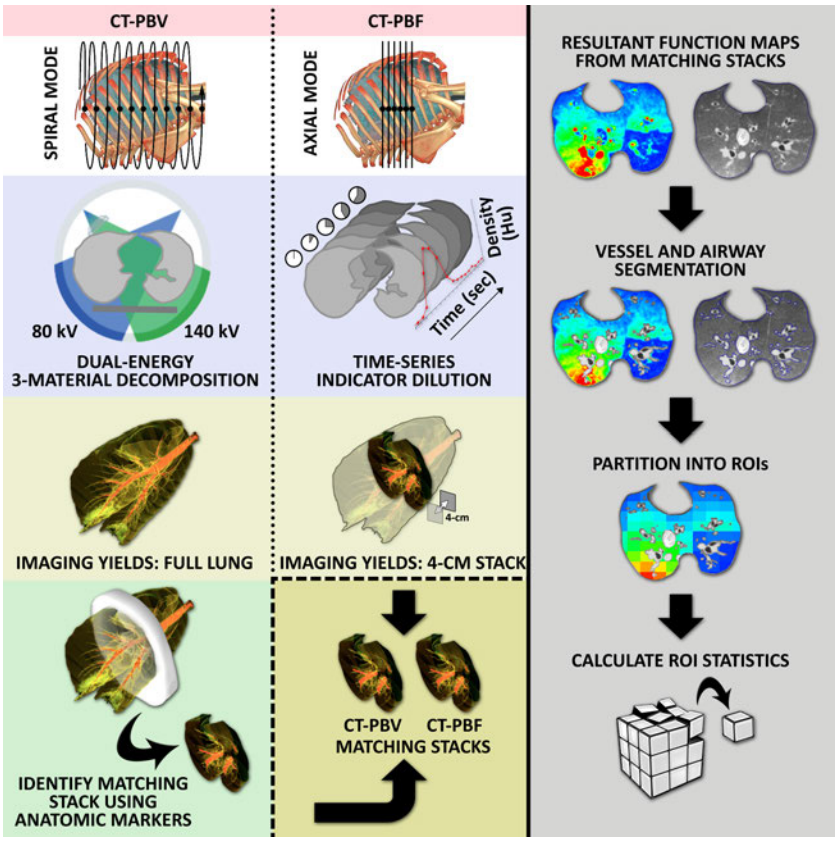


Figure 69. Flowchart of the image acquisition and analysis process. The CT-PBV method (*left-column*) employs dual-energy imaging in spiral scanning mode (*left-column, 1st row*) with a three-material decomposition process (*left-column, 2nd row*) to extract the iodine signal for the full lung (*left-column, 3rd row*). The CT-PBF method (*middle-column*) employs an axial scanning mode (*middle-column, 1st row*) to perform time-series indicator dilution (*middle-column, 2nd row*) resulting in a blood flow map for a 4-cm slice stack of the lung near the heart (*middle-column, 3rd row*). To compare CT-PBF with CT-PBV a matching 4-cm slice stack is identified and extracted from the full-lung CT-PBV scan (*left & middle-columns, 4th row*). Semi-automated lung segmentation along with vessel and airway segmentation is used to limit the analysis region to the lung parenchyma (*right-column, 2nd row*). 4-cm slice stacks are then divided into a 10x10x3 grid of blocks (*middle-column, 3rd row*) and the mean and coefficient of variation within each block is calculated (*middle-column, 4th row*).

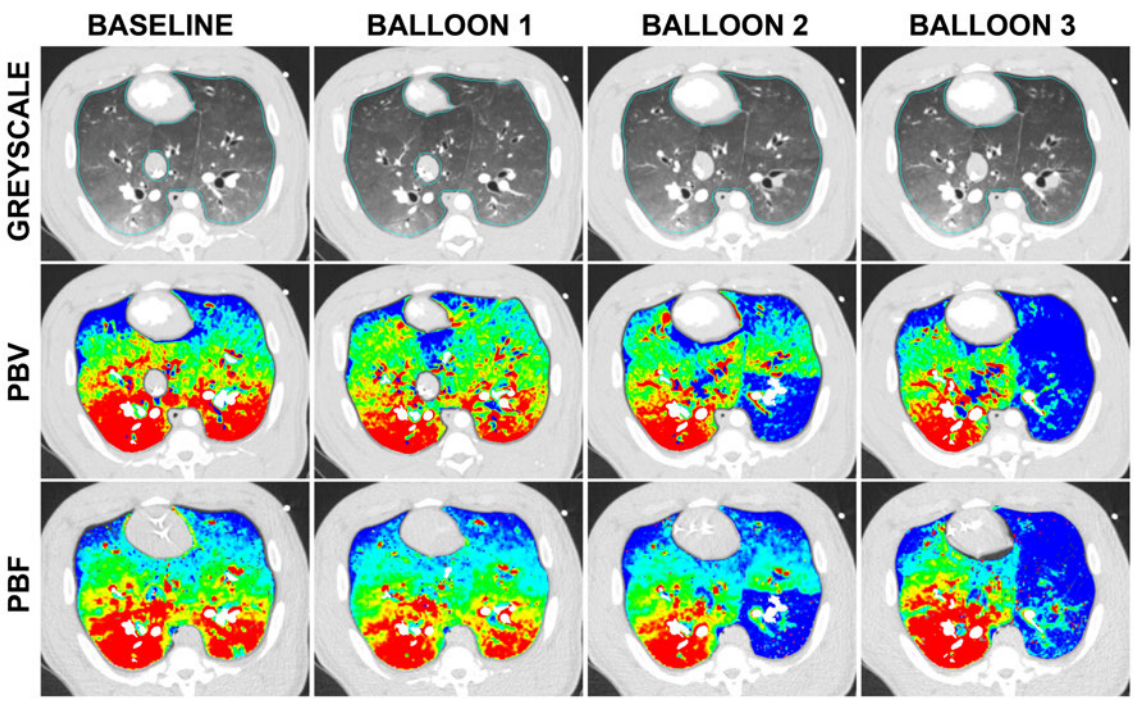


Figure 70. Greyscale (*top*), CT-PBV (*middle*), and CT-PBF (*bottom*). Color map comparison of CT-PBF and CT-PBV from an example pig studied in the balloon occlusion model. For each condition color-coding is the same with low to high values represented by from blue to red colors respectively for both CT-PBV and CT-PBF.

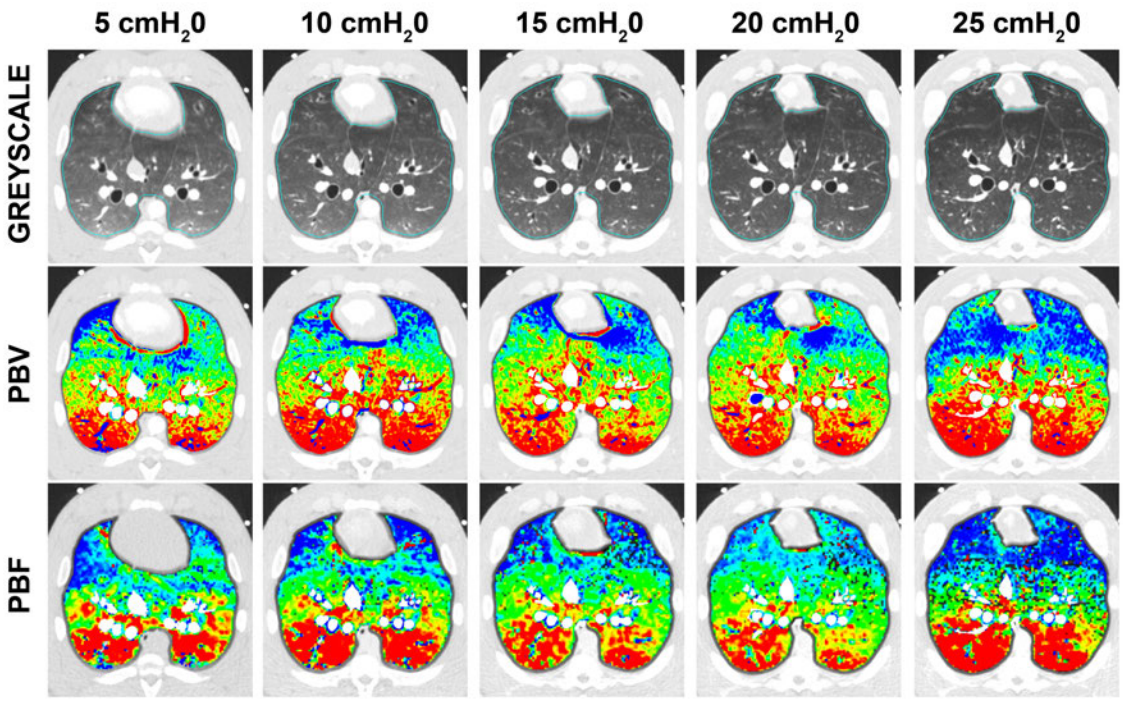


Figure 71. Greyscale (*top*), CT-PBV (*middle*), and CT-PBF (*bottom*). Color map comparison of CT-PBF and CT-PBV from an example pig studied over five different lung volumes, used to achieve a range of pulmonary perfusion values. For each condition color-coding is the same with low to high values represented by from blue to red colors respectively for both CT-PBV and CT-PBF.

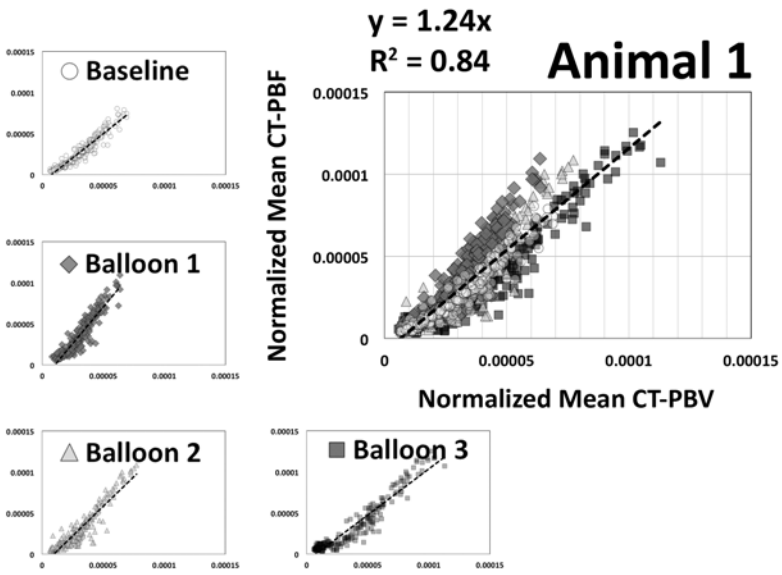


*(Panel A)*

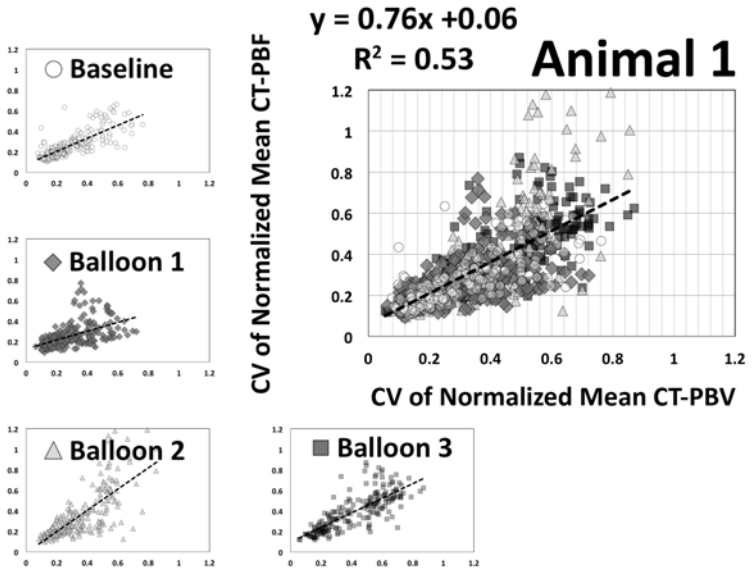


*(Panel B)*

Figure 72. Comparison of normalized mean and coefficient of variation of CT-PBF vs. CT-PBV. Data are from two animals studied using the balloon occlusion model, used to achieve a range of pulmonary perfusion values and heterogeneities. The comparison of normalized mean values for animals 1 and 2 are in panels A and C respectively with the comparison of CV of normalized values in panels B and D.

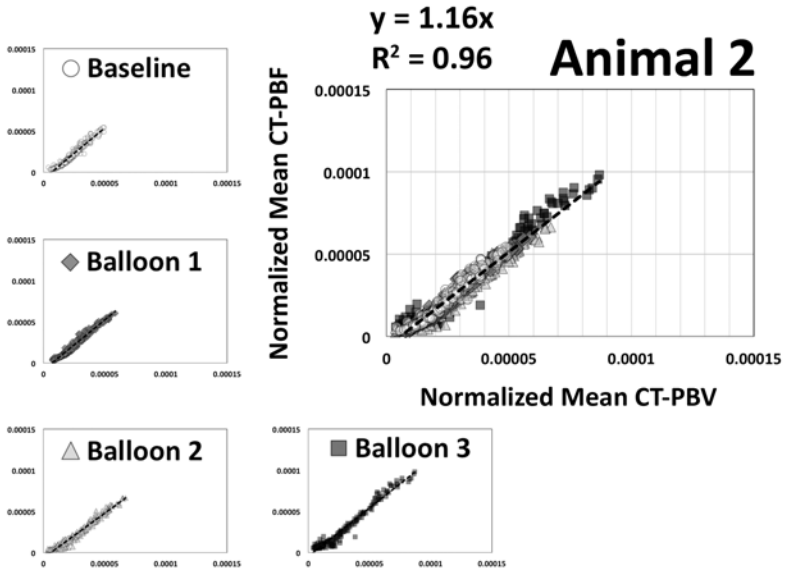


*(Panel C)*

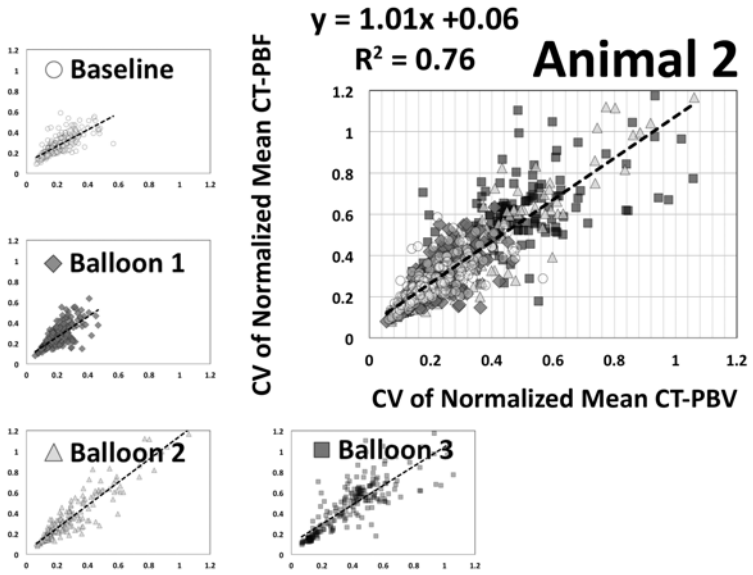


*(Panel D)*

Figure 72 (Continued)

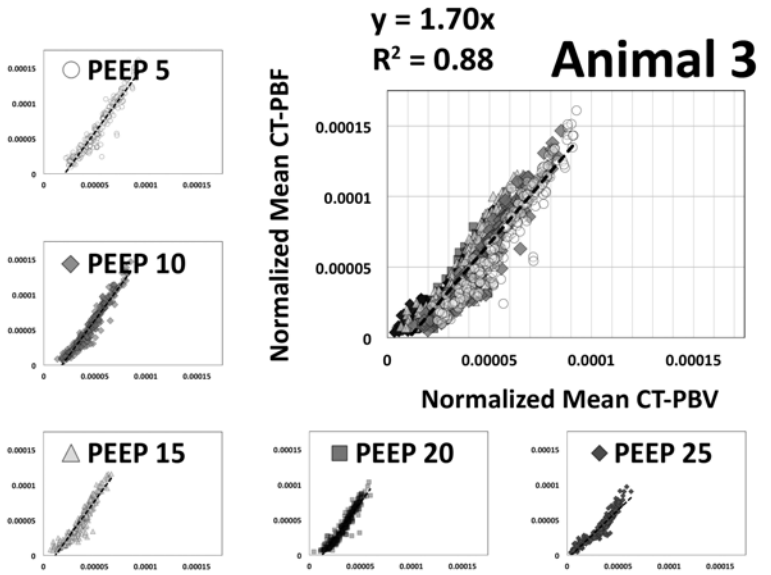


*(Panel A)*

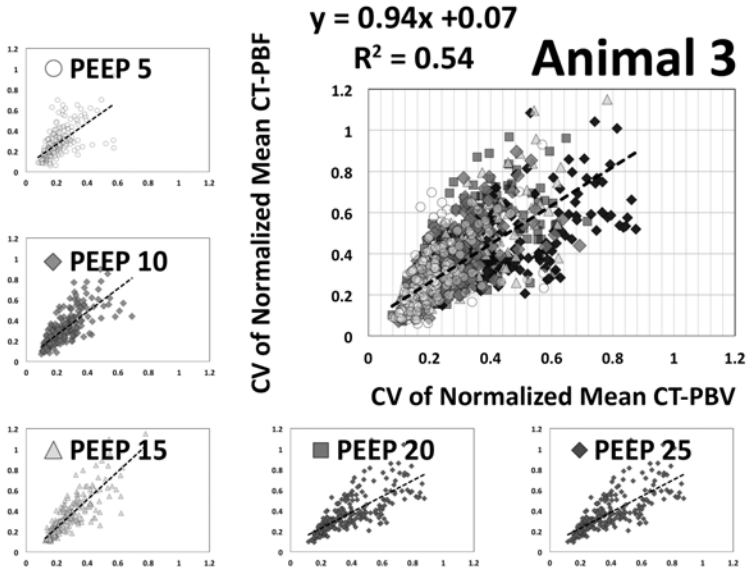


*(Panel B)*

Figure 73. Comparison of normalized mean and coefficient of variation of CT-PBF vs. CT-PBV. Data is from two animals studied over five different lung volumes, used to achieve a range of pulmonary perfusion values and heterogeneities. The comparison of normalized mean values for animals 3 and 4 are in panels A and C respectively with the comparison of CV of normalized values in panels B and D.

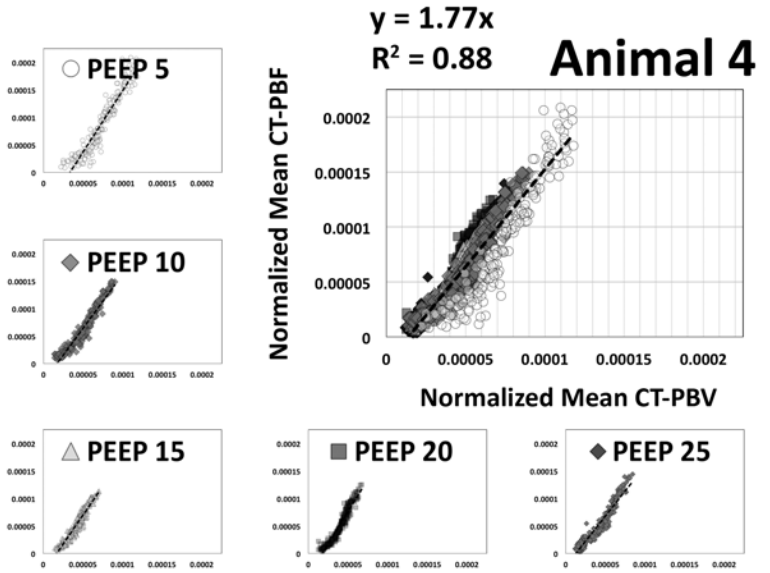


*(Panel C)*

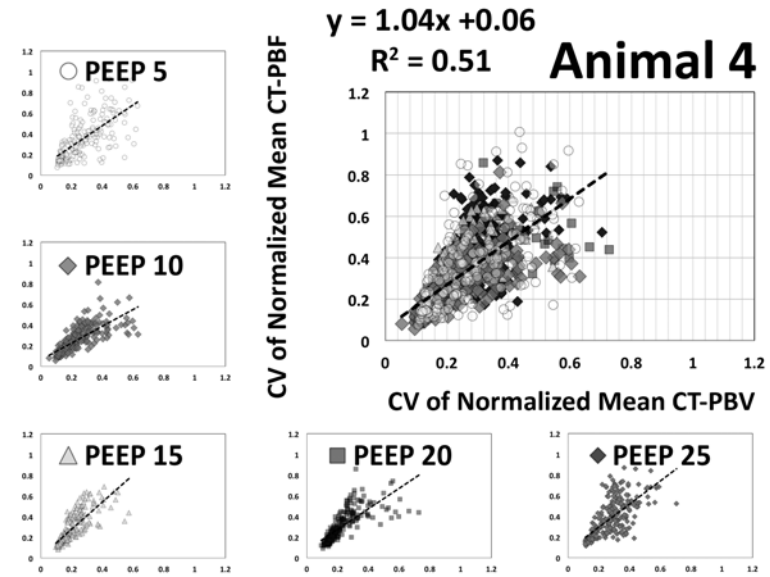


*(Panel D)*

Figure 73 (Continued)

| *Balloon Occlusion Model* | | | | | *Lung Inflation Model* | | | | |
|---|---|---|---|---|---|---|---|---|---|
| **State** | **Animal 1** | | **Animal 2** | | **Animal 3** | | **Animal 4** | | **Inflation Level** |
| | CT-PBF vs. CT-PBV | CV of CT-PBF vs. CV of CT-PBV | CT-PBF vs. CT-PBV | CV of CT-PBF vs. CV of CT-PBV | CT-PBF vs. CT-PBV | CV of CT-PBF vs. CV of CT-PBV | CT-PBF vs. CT-PBV | CV of CT-PBF vs. CV of CT-PBV | |
| ***Baseline*** | 0.96 | 0.77 | 0.98 | 0.75 | 0.96 | 0.64 | 0.95 | 0.64 | ***5 cm $H_20$*** |
| ***Balloon 1*** | 0.93 | 0.51 | 0.99 | 0.72 | 0.97 | 0.76 | 0.97 | 0.69 | ***10 cm $H_20$*** |
| ***Balloon 2*** | 0.93 | 0.74 | 0.98 | 0.93 | 0.94 | 0.84 | 0.96 | 0.79 | ***15 cm $H_20$*** |
| ***Balloon 3*** | 0.96 | 0.78 | 0.98 | 0.83 | 0.95 | 0.75 | 0.96 | 0.76 | ***20 cm $H_20$*** |
| **-** | - | - | - | - | 0.95 | 0.77 | 0.97 | 0.68 | ***25 cm $H_20$*** |
| ***Combined*** | 0.91 | 0.73 | 0.98 | 0.87 | 0.94 | 0.74 | 0.94 | 0.69 | ***Combined*** |

Table 11. Pearson R values from the comparison between normalized values of CT-PBF and CT-PBV and from the coefficient of variation (CV) of normalized values of CT-PBF and CT-PBV. Data are from all animals using either method to create range of pulmonary perfusion values and heterogeneities. All values are statistically significant to the 0.01 level.

# CHAPTER 9: CONCLUSION & FUTURE CONSIDERATIONS

Pulmonary diseases such as emphysema and COPD are characterized by both small-scale and large-scale alterations in structure and function of the lung. It is therefore critical to accurately measure structure and function on both large and small-scales. In recent years, MDCT has emerged as a powerful tool for the quantitative assessment of parenchymal destruction, air trapping (density metrics) and airway remodeling (metrics relating airway wall and lumen geometry) in COPD and asthma (16-23). With the latest advances in MDCT and DECT, along with novel imaging techniques and contrast agents, the ability to measure regional function in addition to structure has finally become a clinical reality. In this thesis we focused on developing and evaluating MDCT-based tools for measuring regional lung function. We did initial development and testing in animal models and then transitioned these methods so that they were also suitable for studying human subjects.

We begin by validating regional ventilation measurements from the wash-in xenon-CT method by performing a comparison with inhaled fluorescent microspheres, a highly invasive but recognized gold standard for measuring regional ventilation. Wash-in xenon-CT correlated well with FMS and demonstrated similar vertical gradients in the prone and supine postures. Small-scale measurements of regional ventilation with wash-in xenon-CT seem to be less susceptible to partial volume errors and resulted in reduced scatter in regional ventilation measurements.

Once validated with FMS, we began the process of transitioning the wash-in xenon-CT method from animals to humans by systematically developing the tools necessary to adequately control the conditions under which subjects were scanned. Our goal was to acquire measures of regional structure and function on awake-free-breathing humans. Since a critical factor of the accuracy and interpretability of MDCT-derived metrics is the assurance that the lungs are scanned during at a standardized volume, we

realized it was necessary to develop and validate systems appropriate for lung volume standardization during static and dynamic breathing.

The next step in the transition process was the development of a 4D image registration program to properly align time-series datasets and make them robust in the face of variability caused when scanning awake-free-breathing subjects. After alignment, airway and vessel segmentation was used to prepare xenon-CT datasets for analysis. Due to the anesthetic effects of xenon gas on awake-human subjects, it was necessary to use 30% rather than 55% xenon concentration used previously in animal models. By lowering the xenon gas concentration, the available signal enhancement diminished resulting in a lower signal-to-noise ratio. A lower signal-to-noise ratio made it more difficult to fit time-series data to the single exponential curve-fit algorithm available and required improvements to increase its accuracy in order to bolster our confidence in regional ventilation measurements from human subjects.

We were then able to use these tools to compare regional ventilation between normal never-smokers (NS), normal smokers (SNI), normal smokers with early signs of centrilobular emphysema not evident by PFTs (SCE) and smokers with COPD. In this study we showed an increase in regional ventilation heterogeneity in SNI compared to NS along with lengthened time constants in COPD and SCE. We also showed that smokers with normal PFTs could be split into two groups based on their regional ventilation parameters, those susceptible and demonstrating early signs of emphysema not evident by PFTs (SCE) and those with normal lung parenchyma (SNI). These findings are consistent with our hypothesis that, while patchy inflammation will occur in all smoking subjects, there is a subset of the population in which perfusion will be decreased because of a failure to block HPV creating a susceptibility to emphysema.

In order to make studying regional lung function possible in a clinical enviornment, simpler-to-perform dual-energy-CT measures of regional ventilation and perfusion were devised and evaluated to replace time-series laboratory-centered

techniques. DECT ventilation measures using xenon gas were optimized through a series of phantom and animal studies designed to determine the proper three-material decomposition calibrations, the best set of imaging parameters, and the proper gas mixture and delivery protocol. These studies showed that the greater contrast provided by using the 80/140 kVp pair was superior to the 100/140 kVp pair and reduced measurement noise. Furthermore, by replacing a portion of the oxygen with helium in the xenon / oxygen gas mixture we were able to decrease gas density improving the distribution of gas to gravitationally non-dependent airways while not affecting radiodensity. DE CT-PBV was then validated as a surrogate for CT-PBF in a series of animal studies in which blood flow patterns were altered either by increasing lung inflation or by occluding a portion of the vascular bed with a balloon catheter. The value of CT-PBV and the CV of CT-PBV correlated well with the value of CT-PBF and the CV of CT-PBF in both models of blood flow alteration thus demonstrating the suitability of DE CT-PBV as a simpler-to-perform surrogate for CT-PBF.

In summary, we have validated a dynamic xenon wash-in methodology for assessing regional ventilation by MDCT; we have established the lung volume control system used to translate this wash-in methodology to humans. In a series of human studies comparing smokers with never-smokers, we have provided evidence that smokers, with and without evidence of emphysema susceptibility, show ventilation-based signs consistent with the presence of inflammatory processes serving to interfere with regional ventilation, consistent with our notion that all smokers have inflammatory processes present but only a portion of those smokers show an aberrant perfusion response to inflammation whereby HPV is not attenuated in the regions of inflammation. To allow for the extension of our ventilation studies to a broader set of clinical centers, we have established dual-energy methods for assessing regional ventilation heterogeneity and we have established that similar technology can be used to assess regional perfused blood volume as a surrogate for parenchymal perfusion. To aid in the analysis of the

resultant images from the above work, we have established a series of software tools for time series analysis of ventilation and perfusion-based images and have established methods to register images within a time series study, required for use in human data sets where temporal stability of gated time series are less reliable than when an animal is studied on a ventilator.

The key element necessary to examine the complexity of lung function and provide greater insight into the effects of the disease processes and their etiology is the ability the describe the parameters of gas-exchange not only globally but on a small-scale as well. Novel MDCT-based techniques provide the spatial resolution necessary to examine ventilation and perfusion on a small-scale offering an avenue to identify novel phenotypes that may not only yield insights into disease processes but also may provide tools leading to drug and device developments, outcomes assessment and ultimately to the selection of subpopulations suitable for a particular intervention.

REFERENCES:


1. Weibel ER. Morphometry of the human lung. Book. Springer Verlag; 1963.

2. Weibel ER, Gomez DM. Architecture of the Human Lung: Use of quantitative methods establishes fundamental relations between size and number of lung structures. Science. 1962 Aug. 24;137(3530):577–85.

3. West J, Fowler K, Hugh-Jones P, O'Donnell T. Measurement of the ventilation-perfusion ratio inequality in the lung by the analysis of a single expirate. Clin Sci (Lond). 1957.

4. Beck KC, Vettermann J, Rehder K. Gas exchange in dogs in the prone and supine positions. J Appl Physiol. 1992 Jun.;72(6):2292–7.

5. Hlastala MP, Standaert TA, Pierson DJ, Luchtel DL. The matching of ventilation and perfusion in the lung of the Tegu lizard, Tupinambis nigropunctatus. Respir Physiol. 1985 Jun.;60(3):277–94.

6. West J. Ventilation-perfusion inequality and overall gas exchange in computer models of the lung. Respir Physiol. 1969 Jun.;1:88–110.

7. Wagner PD. Calculating the distribution of ventilation-perfusion ratios from inert gas elimination data. Fed Proc. 1982 Jan.;41(1):136–9.

8. Powell FL, Wagner PD. Measurement of continuous distributions of ventilation-perfusion in non-alveolar lungs. Respir Physiol. 1982 May;48(2):219–32.

9. Wagner PD, Saltzman HA, West JB. Measurement of continuous distributions of ventilation-perfusion ratios: theory. Journal of Applied Physiology. 1974 May;36(5):588–99.

10. Robertson HT, Hlastala MP. Microsphere maps of regional blood flow and regional ventilation. J Appl Physiol. 2007 Mar.;102(3):1265–72.

11. Beck KC. Regional trapping of microspheres in the lung compares well with regional blood flow. J Appl Physiol. 1987 Aug.;63(2):883–9.

12. Glenny RW, Bernard S, Brinkley M. Validation of fluorescent-labeled microspheres for measurement of regional organ perfusion. J Appl Physiol. 1993 May;74(5):2585–97.

13. Robertson HT, Kreck T, Krueger M. The spatial and temporal heterogeneity of regional ventilation: comparison of measurements by two high-resolution methods. Respir Physiol Neurobiol. 2005 Aug. 25;148(1-2):85–95.

14. Alford SK, van Beek EJ, McLennan G, Hoffman EA. Heterogeneity of pulmonary perfusion as a mechanistic image-based phenotype in emphysema susceptible smokers. Proceedings of the National Academy of Sciences of the United States of America. 2010 Apr. 20;107(16):7485–90.

15. Hoffman EA, Simon BA, McLennan G. State of the Art. A structural and functional assessment of the lung via multidetector-row computed tomography: phenotyping chronic obstructive pulmonary disease. Proceedings of the American Thoracic Society. 2006 Aug. 1;3(6):519–32.

16. Lynch DA, Newell JD. Quantitative imaging of COPD. J Thorac Imaging. 2009 Aug.;24(3):189–94.

17. National Lung Screening Trial Research Team, Aberle DR, Berg CD, Black WC, Church TR, Fagerstrom RM, et al. The National Lung Screening Trial: overview and study design. Radiology. 2011 Jan.;258(1):243–53.

18. Kim WJ, Hoffman EA, Reilly J, Hersh C, Demeo D, Washko G, et al. Association of COPD candidate genes with computed tomography emphysema and airway phenotypes in severe COPD. Eur. Respir. J. 2011 Jan.;37(1):39–43.

19. Brown M, Abtin F, Kim HJ, McNitt-Gray M, Goldin JG. Imaging biomarkers for patient selection and treatment planning in emphysema. Imaging in Medicine. 2010 Oct.;2(5):565–73.

20. Buckler AJ, Mozley PD, Schwartz L, Petrick N, McNitt-Gray M, Fenimore C, et al. Volumetric CT in lung cancer: an example for the qualification of imaging as a biomarker. Academic Radiology. 2010 Jan. p. 107–15.

21. Bafadhel M, Umar I, Gupta S, Raj JV, Vara DD, Entwisle JJ, et al. The Role of CT Scanning in Multidimensional Phenotyping of COPD. Chest. 2011 Sep. 5;140(3):634–42.

22. Goldin JG. Imaging the lungs in patients with pulmonary emphysema. J Thorac Imaging. 2009 Aug.;24(3):163–70.

23. Newell JD. Quantitative computed tomography of lung parenchyma in chronic obstructive pulmonary disease: an overview. Proceedings of the American Thoracic Society. 2008 Dec. 15;5(9):915–8.

24. Hoffman EA, Chon D. Computed tomography studies of lung ventilation and perfusion. Proceedings of the American Thoracic Society. 2005;2(6):492–8, 506.

25. Chon D, Simon BA, Beck KC, Shikata H, Saba OI, Won C, et al. Differences in regional wash-in and wash-out time constants for xenon-CT ventilation studies. Respiratory Physiology & Neurobiology. 2005 Aug. 25;148(1-2):65–83.

26. Fuld M, Easley RB, Saba OI, Chon D, Reinhardt JM, Hoffman EA, et al. CT-measured regional specific volume change reflects regional ventilation in supine sheep. J Appl Physiol. 2008 Apr.;104(4):1177–84.

27. Tajik JK, Chon D, Won C, Tran BQ, Hoffman EA. Subsecond multisection CT of regional pulmonary ventilation. Academic Radiology. 2002 Feb.;9(2):130–46.

28. Cullen S, Gross E. The anesthetic properties of xenon in animals and human beings, with additional observations on krypton. Science (New York. 1951.

29. Lachmann B, Armbruster S, Schairer W, Landstra M, Trouwborst A, Van Daal GJ, et al. Safety and efficacy of xenon in routine use as an inhalational anaesthetic. Lancet. 1990 Jun. 16;335(8703):1413–5.

30. Jordan BD, Wright EL. Xenon as an anesthetic agent. AANA J. 2010 Oct.;78(5):387–92.

31. Yoo TS, Metaxas DN. Open science--combining open data and open source software: medical image analysis with the Insight Toolkit. Medical Image Analysis. 2005 Dec.;9(6):503–6.

32. West JB. Respiratory Physiology - The Essentials. Book. 2005.

33. Guisan M, Tisi GM, Ashburn WL, Moser KM. Washout of 133xenon gas from the lungs: Comparison with nitrogen washout. Chest. American College of Chest Physicians; 1972;62(2):146–51.

34. Whiteley JP, Gavaghan DJ, Hahn CE. A mathematical evaluation of the multiple breath nitrogen washout (MBNW) technique and the multiple inert gas elimination technique (MIGET). J. Theor. Biol. 1998 Oct. 21;194(4):517–39.

35. Paiva M, Yernault JC, Martins D, Englert M. [A new interpretation of nitrogen wash-out curves (author's transl)]. Bull Physiopathol Respir (Nancy). 1974 Nov.;10(6):831–44.

36. Verbanck S. Noninvasive Assessment of Airway Alterations in Smokers: The Small Airways Revisited. Am J Respir Crit Care Med. 2004 Aug. 15;170(4):414–9.

37. Hlastala MP, Robertson HT. Inert gas elimination characteristics of the normal and abnormal lung. Journal of applied physiology: respiratory, environmental and exercise physiology. 1978 Feb.;44(2):258–66.

38. Evans JW, Wagner PD. Limits on VA/Q distributions from analysis of experimental inert gas elimination. Journal of applied physiology: respiratory, environmental and exercise physiology. 1977 Jun.;42(6):889–98.

39. Wagner PD. Ventilation-perfusion relationships. Annu. Rev. Physiol. 1980;42:235–47.

40. Hlastala MP. Multiple inert gas elimination technique. Journal of applied physiology: respiratory, environmental and exercise physiology. 1984 Jan.;56(1):1–7.

41. Hopkins SR, Johnson EC, Richardson RS, WAGNER H, DE ROSA M, Wagner PD. Effects of inhaled nitric oxide on gas exchange in lungs with shunt or poorly ventilated areas. Am J Respir Crit Care Med. 1997 Aug.;156(2 Pt 1):484–91.

42. West JB, Wagner PD, Derks CM. Gas exchange in distributions of VA-Q ratios: partial pressure-solubility diagram. Journal of Applied Physiology. 1974 Oct.;37(4):533–40.

43. Milic-Emili J, Henderson JA, Dolovich MB, Trop D, Kaneko K. Regional distribution of inspired gas in the lung. Journal of Applied Physiology. 1966 May 1;21(3):749–59.

44. Bunow B, Line BR, Horton MR, Weiss GH. Regional ventilatory clearance by xenon scintigraphy: a critical evaluation of two estimation procedures. J Nucl Med. 1979 Jul. 1;20(7):703–10.

45. Anthonisen NR, Milic-Emili J. Distribution of pulmonary perfusion in erect man. Journal of Applied Physiology. 1966 May;21(3):760–6.

46. Kaneko K, Milic-Emili J, Dolovich MB, Dawson A, Bates D. Regional distribution of ventilation and perfusion as a function of body position. Journal of Applied Physiology. 1966 May;21(3):767–77.

47. West JB. Pulmonary Function Studies with Radio-Active Gases. Annual Review of Medicine. Annual Reviews 4139 El Camino Way, PO Box 10139, Palo Alto, CA 94303-0139, USA; 1967;18(1):459–70.

48. Cinotti L, Bazin J, Meignan M, Aubry F, Paola R. Factor analysis of 81m Kr lung ventilation studies. European Journal of Nuclear Medicine and Molecular Imaging. Springer; 1985;10(11):511–8.

49. Suga K, Nishigauchi K, Kume N, Koike S, Takano K, Tokuda O, et al. Dynamic pulmonary SPECT of xenon-133 gas washout. J Nucl Med. 1996 May;37(5):807–14.

50. Petersson J, Sánchez-Crespo A, Rohdin M, Montmerle S, Nyrén S, Jacobsson H, et al. Physiological evaluation of a new quantitative SPECT method measuring regional ventilation and perfusion. J Appl Physiol. 2004 Mar.;96(3):1127–36.

51. Stavngaard T, Søgaard LV, Mortensen J, Hanson LG, Schmiedeskamp J, Berthelsen AK, et al. Hyperpolarized 3He MRI and 81mKr SPECT in chronic obstructive pulmonary disease. European Journal of Nuclear Medicine and Molecular Imaging. 2005 Apr. 1;32(4):448–57.

52. Treppo S, Mijailovich SM, Venegas JG. Contributions of pulmonary perfusion and ventilation to heterogeneity in V(A)/Q measured by PET. J Appl Physiol. 1997 Apr.;82(4):1163–76.

53. Galletti GG, Venegas JG. Tracer kinetic model of regional pulmonary function using positron emission tomography. J Appl Physiol. 2002 Sep.;93(3):1104–14.

54. Hoffman EA. Effect of body orientation on regional lung expansion: a computed tomographic approach. J Appl Physiol. 1985 Aug.;59(2):468–80.

55. Hoffman EA, Ritman EL. Heart-lung interaction: effect on regional lung air content and total heart volume. Annals of Biomedical Engineering. 1987;15(3-4):241–57.

56. Robb RA, Sinak LJ, Hoffman EA, Kinsey JH, Harris LD, Ritman EL. Dynamic volume imaging of moving organs. Journal of Medical Systems. 1982 Dec.;6(6):539–54.

57. West J. State of the art: ventilation-perfusion relationships. Am Rev Respir Dis. 1977 Nov.;116(5):919–43.

58. Lenfant C. Measurement of Ventilation/Perfusion Distribution with Alveolar-Arterial Differences. Journal of Applied Physiology. 1963 Nov.;18:1090–4.

59. West JB, Dollery CT. Distribution of blood flow and ventilation-perfusion ratio in the lung, measured with radioactive carbon dioxide. Journal of Applied Physiology. 1960 May;15:405–10.

60. West JB. Distribution of blood and gas in lungs. Physics in Medicine and Biology. 1966 Jul.;11(3):357–70.

61. West JB. Distortion of the lung within the chest. Fed Proc. 1979;38(1):11–6.

62. West J, Dollery C, Naimark A. Distribution of blood flow in isolated lung; relation to vascular and alveolar pressures. J Appl Physiol. Am Physiological Soc; 1964;19(4):713.

63. Howell JB, Permutt S, Proctor DF, Riley RL. Effect of inflation of the lung on different parts of pulmonary vascular bed. Journal of Applied Physiology. 1961 Jan.;16:71–6.

64. Permutt S, Howell JB, Proctor DF, Riley RL. Effect of lung inflation on static pressure-volume characteristics of pulmonary vessels. Journal of Applied Physiology. 1961 Jan.;16:64–70.

65. Permutt S, Bromberger-Barnea B, BANE HN. Alveolar pressure, pulmonary venous pressure, and the vascular waterfall. Med Thorac. 1962;19:239–60.

66. West J. Distribution of ventilation/perfusion ratios. Rev Fr Mal Respir. 1980.

67. Fazio F, Lavender JP, Steiner RE. 81mKr ventilation and 99mTc perfusion scans in chest disease: comparison with standard radiographs. AJR American journal of roentgenology. 1978 Mar. 1;130(3):421–8.

68. West J. A Century of Pulmonary Gas Exchange. Am J Respir Crit Care Med. 2004.

69. Hasegawa BH, Iwata K, Wong KH, Wu MC, Da Silva AJ, Tang HR, et al. Dual-modality imaging of function and physiology. Academic Radiology. Elsevier; 2002;9(11):1305–21.

70. Kauczor H-U. Hyperpolarized helium-3 gas magnetic resonance imaging of the lung. Top Magn Reson Imaging. 2003 Jun.;14(3):223–30.

71. Salerno M, Altes TA, Brookeman JR, de Lange EE, Mugler JP. Dynamic spiral MRI of pulmonary gas flow using hyperpolarized (3)He: preliminary studies in healthy and diseased lungs. Magnetic resonance in medicine : official journal of the Society of Magnetic Resonance in Medicine / Society of Magnetic Resonance in Medicine. 2001 Oct.;46(4):667–77.

72. Fichele S, Woodhouse N, Swift AJ, Said Z, Paley MNJ, Kasuboski L, et al. MRI of helium-3 gas in healthy lungs: posture related variations of alveolar size. J Magn Reson Imaging. 2004 Aug.;20(2):331–5.

73. Kirby M, Mathew L, Wheatley A, Santyr GE, McCormack DG, Parraga G. Chronic obstructive pulmonary disease: longitudinal hyperpolarized (3)He MR imaging. Radiology. 2010 Jul.;256(1):280–9.

74. Dregely I, Mugler JP, Ruset IC, Altes TA, Mata JF, Miller GW, et al. Hyperpolarized Xenon-129 gas-exchange imaging of lung microstructure: first case studies in subjects with obstructive lung disease. J Magn Reson Imaging. 2011 May;33(5):1052–62.

75. van Beek EJ, Wild JM, Kauczor H-U, Schreiber W, Mugler JP, de Lange EE. Functional MRI of the lung using hyperpolarized 3-helium gas. J Magn Reson Imaging. 2004 Oct.;20(4):540–54.

76. Stolk J, Dirksen A, Van Der Lugt A, Hutsebaut J, Mathieu J, D e REE J, et al. Repeatability of Lung Density Measurements with Low-Dose Computed Tomography in Subjects with [alpha]-1-Antitrypsin Deficiency-Associated Emphysema. Investigative Radiology. 2001;36(11):648.

77. Röntgen WC. On a new kind of rays. Science. American Association for the Advancement of Science; 1896;3(59):227.

78. Oldendorf WH. Isolated Flying Spot Detection of Radiodensity Dis-Continuities-Displaying the Internal Structural Pattern of a Complex Object. IRE Trans. Bio-med. Electron. 1961;8(1):68–72.

79. Cormack AM. Representation of a Function by Its Line Integrals, with Some Radiological Applications. Journal of Applied Physics. 1963;34(9):2722.

80. Hounsfield GN. Computerized transverse axial scanning (tomography): Part 1. Description of system. The British journal of radiology. 1973 Dec. 1;46(552):1016–22.

81. Kalender WA, Seissler W, Klotz E, Vock P. Spiral volumetric CT with single-breath-hold technique, continuous transport, and continuous scanner rotation. Radiology. 1990 Jul.;176(1):181–3.

82. Vock P, Soucek M, Daepp M, Kalender WA. Lung: spiral volumetric CT with single-breath-hold technique. Radiology. 1990 Sep.;176(3):864–7.

83. Robb R, Hoffman EA, Sinak L, Harris L. High-speed three-dimensional X-ray computed tomography: The dynamic spatial reconstructor. Proceedings of the IEEE. 1983.

84. Ritman EL, Kinsey JH, Robb RA, Gilbert BK, Harris LD, Wood EH. Three-dimensional imaging of heart, lungs, and circulation. Science. 1980 Oct. 17;210(4467):273–80.

85. Robb R, Lent A, Gilbert B, Chu A. The dynamic spatial reconstructor. Journal of Medical Systems. 1980.

86. Brooks RA. A Quantitative Theory of the Hounsfield Unit and Its Application to Dual Energy Scanning. J Comput Assist Tomogr [Internet]. 1977 Oct. 1;1(4):487. Available from: http://journals.lww.com/jcat/Fulltext/1977/10000/A_Quantitative_Theory_of_the_Hounsfield_Unit_and.16.aspx

87. Kauczor H-U, Hanke A, van Beek EJ. Assessment of lung ventilation by MR imaging: current status and future perspectives. European Radiology. 2002 Aug.;12(8):1962–70.

88. van Beek EJ, Hoffman EA. Functional imaging: CT and MRI. Clin Chest Med. 2008 Mar.;29(1):195–216, vii.

89. Dollery C, Gillam P. The distribution of blood and gas within the lungs measured by scanning after administration of 133Xe. Thorax. BMJ Publishing Group Ltd and British Thoracic Society; 1963;18(4):316.

90. West JB. Regional differences in gas exchange in the lung of erect man. Journal of Applied Physiology. 1962 Nov.;17:893–8.

91. Ball W Jr, Stewart P, Newsham L, Bates D. Regional pulmonary function studied with xenon 133. J Clin Invest. 1962 Mar.;41(3):519–31.

92. Dollery C, Hugh-Jones P, Matthews C. Use of radioactive xenon for studies of regional lung function: a comparison with oxygen-15. The British Medical Journal. JSTOR; 1962;2(5311):1006–16.

93. KETY SS. The theory and applications of the exchange of inert gas at the lungs and tissues. Pharmacol Rev. 1951 Mar. 1;3(1):1–41.

94. Gur D, Yonas H, Wolfson SK, Herbert D, Kennedy WH, Drayer BP, et al. Xenon and iodine enhanced cerebral CT: A closer look. Stroke. 1981 Aug.;12(5):573–8.

95. Gur D, Drayer BP, Borovetz HS, Griffith BP, Hardesty RL, Wolfson SK. Dynamic computed tomography of the lung: regional ventilation measurements. J Comput Assist Tomogr. 1979 Dec.;3(6):749–53.

96. Foley WD, Haughton VM, Schmidt J, Wilson CR. Xenon contrast enhancement in computed body tomography. Radiology. 1978 Oct.;129(1):219–20.

97. Marcucci C, Nyhan D, Simon BA. Distribution of pulmonary ventilation using Xe-enhanced computed tomography in prone and supine dogs. J Appl Physiol. 2001 Feb.;90(2):421–30.

98. Fuld M, Grout RW, Guo J, Morgan JH, Hoffman EA. Systems for Lung Volume Standardization during Static and Dynamic MDCT-based Quantitative Assessment of Pulmonary Structure and Function. Academic Radiology. 2012 May 1;In Press.

99. Saba OI, Chon D, Beck KC, McLennan G, Sieren J, Reinhardt JM, et al. Static versus prospective gated non-breath hold volumetric MDCT imaging of the lungs. Academic Radiology. 2005 Nov. 1;12(11):1371–84.

100. Lu W, Parikh PJ, Hubenschmidt JP, Politte DG, Whiting BR, Bradley JD, et al. Reduction of motion blurring artifacts using respiratory gated CT in sinogram space: A quantitative evaluation. Med. Phys. American Association of Physicists in Medicine; 2005;32(11):3295.

101. Gierada DS, Yusen RD, Pilgram TK, Crouch L, Slone RM, Bae KT, et al. Repeatability of quantitative CT indexes of emphysema in patients evaluated for lung volume reduction surgery. Radiology. 2001 Aug.;220(2):448–54.

102. Lamers R, Kemerink G, Drent M, Van Engelshoven J. Reproducibility of spirometrically controlled CT lung densitometry in a clinical setting. Eur. Respir. J. Eur Respiratory Soc; 1998;11(4):942–5.

103. Kalender WA, Rienmüller R, Seissler W, Behr J, Welke M, Fichte H. Measurement of pulmonary parenchymal attenuation: use of spirometric gating with quantitative CT. Radiology. 1990 Apr.;175(1):265–8.

104. Herbert D, Gur D, Shabason L, Good W, Rinaldo J. Mapping of human local pulmonary ventilation by xenon enhanced computed tomography. J Comput Assist Tomogr. 1982.

105. Hoag JB, Fuld M, Brown RH, Simon BA. Recirculation of inhaled xenon does not alter lung CT density. Academic Radiology. 2007 Jan.;14(1):81–4.

106. Uppaluri R, McLennan G, Enright P, Standen J, Boyer-Pfersdorf P, Hoffman EA. Adaptive Multiple Feature Method (AMFM) for the early detection of parenchymal pathology in smoking population. SPIE Med Imaging Physiol Function. 1998;3337:8–13.

107. Tajik JK, Tran BQ, Hoffman EA. Xenon-enhanced CT imaging of local pulmonary ventilation. Proceedings of SPIE. 1996;2709:40.

108. Simon BA, Marcucci C, Fung M, Lele SR. Parameter estimation and confidence intervals for Xe-CT ventilation studies: a Monte Carlo approach. J Appl Physiol. 1998 Feb.;84(2):709–16.

109. Chon D, Beck KC, Simon BA, Shikata H, Saba OI, Hoffman EA. Effect of low-xenon and krypton supplementation on signal/noise of regional CT-based ventilation measurements. J Appl Physiol. 2007 Apr. 1;102(4):1535–44.

110. Chon D, Beck KC, Shikata H, Saba OI, Simon BA, Won C, et al. Xenon gas flow patterns evaluated by high speed multi-row detector CT. Progr Biomed Opt Imaging. 2004;5:89–101.

111. Kreck TC, Krueger MA, Altemeier WA, Sinclair SE, Robertson HT, Shade ED, et al. Determination of regional ventilation and perfusion in the lung using xenon and computed tomography. J Appl Physiol. 2001 Oct.;91(4):1741–9.

112. Chon D, Beck KC, Simon BA, Shikata H, Saba OI, Hoffman EA. Effect of low-xenon and krypton supplementation on signal/noise of regional CT-based ventilation measurements. J Appl Physiol. 2007 Apr.;102(4):1535–44.

113. Miyawaki S, Tawhai MH, Hoffman EA, Lin C-L. Effect of Carrier Gas Properties on Aerosol Distribution in a CT-based Human Airway Numerical Model. Annals of Biomedical Engineering. 2012 Jan. 14.

114. Koblin DD, Fang Z, Eger E, Laster MJ, Gong D, Ionescu P, et al. Minimum Alveolar Concentrations of Noble Gases, Nitrogen, and Sulfur Hexafluoride in Rats: Helium and Neon as Nonimmobilizers (Nonanesthetics). Anesthesia & Analgesia. IARS; 1998;87(2):419.

115. Easley RB, Fuld M, Fernandez-Bustamante A, Hoffman EA, Simon BA. Mechanism of hypoxemia in acute lung injury evaluated by multidetector-row CT. Academic Radiology. 2006 Jul.;13(7):916–21.

116. Clough AV, Linehan JH, Dawson CA. Regional perfusion parameters from pulmonary microfocal angiograms. The American journal of physiology. 1997 Mar.;272(3 Pt 2):H1537–48.

117. Clough AV, Haworth ST, Hanger CC, Wang J, Roerig DL, Linehan JH, et al. Transit time dispersion in the pulmonary arterial tree. J Appl Physiol. 1998 Aug.;85(2):565–74.

118. Wolfkiel CJ, Ferguson JL, Chomka EV, Law WR, Labin IN, Tenzer ML, et al. Measurement of myocardial blood flow by ultrafast computed tomography. Circulation. 1987 Dec.;76(6):1262–73.

119. Chon D, Beck KC, Larsen RL, Shikata H, Hoffman EA. Regional pulmonary blood flow in dogs by 4D-X-ray CT. J Appl Physiol. 2006 Nov.;101(5):1451–65.

120. Hoffman EA, Tajik JK, Kugelmass SD. Matching pulmonary structure and perfusion via combined dynamic multislice CT and thin-slice high-resolution CT. Comput Med Imaging Graph. 1995;19(1):101–12.

121. Tajik JK, Tran BQ, Hoffman EA. New technique to quantitate regional pulmonary microvascular transit times from dynamic X-ray CT images. Medical Imaging. 1998.

122. Won C, Chon D, Tajik J, Tran BQ, Robinswood GB, Beck KC, et al. CT-based assessment of regional pulmonary microvascular blood flow parameters. J Appl Physiol. 2003 Jun.;94(6):2483–93.

123. Dakin JH, Evans TW, Hansell DM, Hoffman EA. Regional pulmonary blood flow in humans and dogs by 4D computed tomography. Academic Radiology. 2008 Jul.;15(7):844–52.

124. Hoffman EA. Advances in physiologic lung assessment via electron beam computed tomography (EBCT). Proceedings of SPIE. 1999;3772:2.

125. Flohr TG, McCollough CH, Bruder H, Petersilka M, Gruber K, Süss C, et al. First performance evaluation of a dual-source CT (DSCT) system. European Radiology. 2006 Feb.;16(2):256–68.

126. Johnson TRC. Dual-Energy CT–Technical Background. Multislice CT. Springer; 2009;:65–73.

127. Johnson TRC, Krauss B, Sedlmair M, Grasruck M, Bruder H, Morhard D, et al. Material differentiation by dual energy CT: initial experience. European Radiology. 2007 Jun.;17(6):1510–7.

128. Petersilka M, Bruder H, Krauss B, Stierstorfer K, Flohr TG. Technical principles of dual source CT. Eur J Radiol. 2008 Dec.;68(3):362–8.

129. Fornaro J, Leschka S, Hibbeln D, Butler A, Anderson N, Pache G, et al. Dual- and multi-energy CT: approach to functional imaging. Insights into Imaging. Springer; 2011;:1–11.

130. Avrin DE, Macovski A, Zatz LE. Clinical application of Compton and photo-electric reconstruction in computed tomography: preliminary results. Investigative Radiology. 1978 May;13(3):217–22.

131. Boroto K, Remy-Jardin M, Flohr T, Faivre J-B, Pansini V, Tacelli N, et al. Thoracic applications of dual-source CT technology. Eur J Radiol. 2008 Dec.;68(3):375–84.

132. Petersilka M, Bruder H, Krauss B, Stierstorfer K, Flohr TG. Technical principles of dual source CT. Eur J Radiol. 2008 Dec.;68(3):362–8.

133. Primak AN, Giraldo JCR, Eusemann CD, Schmidt B, Kantor B, Fletcher JG, et al. Dual-Source Dual-Energy CT With Additional Tin Filtration: Dose and Image Quality Evaluation in Phantoms and In Vivo. American Journal of Roentgenology. 2010 Nov. 1;195(5):1164–74.

134. Liu X, Yu L, Primak AN, McCollough CH. Quantitative imaging of element composition and mass fraction using dual-energy CT: three-material decomposition. Med. Phys. 2009 May;36(5):1602–9.

135. Hachulla A-L, Pontana F, Wemeau-Stervinou L, Khung S, Faivre J-B, Wallaert B, et al. Krypton ventilation imaging using dual-energy CT in chronic obstructive pulmonary disease patients: initial experience. Radiology. 2012 Apr.;263(1):253–9.

136. Winkler SS, Holden JE, Sackett JF, Flemming DC, Alexander SC. Xenon and krypton as radiographic inhalation contrast media with computerized tomography: preliminary note. Investigative Radiology. 1977;12(1):19–20.

137. Fuld M, Sieren J, Hoffman EA. Dual Source/Dual Energy Xe-MDCT For Automated Quantitative Assessment Of The Central Airway Tree. Am J Respir Crit Care Med. 2010;181:A6622.

138. Fuld M, Hudson M, Halaweish A. Quantification Of Regional Ventilation Via Dual Energy Xenon MDCT. Am J Respir Crit Care Med. 2010;181:A5525.

139. Honda N, Osada H, Watanabe W, Nakayama M, Nishimura K, Krauss B, et al. Imaging of ventilation with dual-energy CT during breath hold after single vital-capacity inspiration of stable xenon. Radiology. 2012 Jan.;262(1):262–8.

140. Goo HW, Yang DH, Hong S-J, Yu J, Kim B-J, Seo JB, et al. Xenon ventilation CT using dual-source and dual-energy technique in children with bronchiolitis obliterans: correlation of xenon and CT density values with pulmonary function test results. Pediatr Radiol. 2010 Sep.;40(9):1490–7.

141. Chae EJ, Seo JB, Lee J, Goo HW, Lee HJ, Lee CW, et al. Xenon ventilation imaging using dual-energy computed tomography in asthmatics: initial experience. Invest Radiol. 2010th ed. 2010 Jun.;45(6):354–61.

142. Chae EJ, Seo JB, Kim N, Song K-S, Shin JH, Kim T-H, et al. Collateral Ventilation in a Canine Model with Bronchial Obstruction: Assessment with Xenon-enhanced Dual-Energy CT. Radiology. 2010 Jun. 1;255(3):790–8.

143. Bauer RW, Kerl JM, Weber E, Weisser P, Korkusuz H, Lehnert T, et al. Lung perfusion analysis with dual energy CT in patients with suspected pulmonary embolism--influence of window settings on the diagnosis of underlying pathologies of perfusion defects. Eur J Radiol. 2011 Dec.;80(3):e476–82.

144. Chandarana H, Megibow AJ, Cohen BA, Srinivasan R, Kim D, Leidecker C, et al. Iodine Quantification With Dual-Energy CT: Phantom Study and Preliminary Experience With Renal Masses. American Journal of Roentgenology. 2011 Jun. 1;196(6):693–700.

145. Van Abbema JK, Van der Schaaf A, Kristanto W, Groen JM, Greuter MJW. Feasibility and accuracy of tissue characterization with dual source computed tomography. Physica Medica. 2011 Feb. 18;:1–8.

146. Ferda J, Ferdová E, Mírka H, Baxa J, Bednářová A, Flohr T, et al. Pulmonary imaging using dual-energy CT, a role of the assessment of iodine and air distribution. Eur J Radiol. 2011 Feb.;77(2):287–93.

147. Thieme SF, Hoegl S, Nikolaou K, Fisahn J, Irlbeck M, Maxien D, et al. Pulmonary ventilation and perfusion imaging with dual-energy CT. European Radiology. 2010 Dec.;20(12):2882–9.

148. Thieme SF, Graute V, Nikolaou K, Maxien D, Reiser MF, Hacker M, et al. Dual Energy CT lung perfusion imaging-Correlation with SPECT/CT. Eur J Radiol. 2010 Dec. 22.

149. Thieme SF, Johnson TRC, Reiser MF, Nikolaou K. Dual-energy lung perfusion computed tomography: a novel pulmonary functional imaging method. Semin. Ultrasound CT MR. 2010 Aug.;31(4):301–8.

150. Pontana F, Remy-Jardin M, Duhamel A, Faivre J-B, Wallaert B, Remy J. Lung perfusion with dual-energy multi-detector row CT: can it help recognize ground glass opacities of vascular origin? Academic Radiology. 2010 May;17(5):587–94.

151. Brower R, Wise RA, Hassapoyannes C, Bromberger-Barnea B, Permutt S. Effect of lung inflation on lung blood volume and pulmonary venous flow. J Appl Physiol. 1985;58(3):954–63.

152. Lopez-Muniz R, Stephens NL, Bromberger-Barnea B, Permutt S, Riley RL. Critical closure of pulmonary vessels analyzed in terms of Starling resistor model. Journal of Applied Physiology. 1968 May;24(5):625–35.

153. Fowler K. Vertical gradient of perfusion in the erect human lung. J Appl Physiol. Am Physiological Soc; 1965;20(6):1163–72.

154. Altemeier WA, Robertson HT, Glenny RW. Pulmonary gas-exchange analysis by using simultaneous deposition of aerosolized and injected microspheres. J Appl Physiol. 1998 Dec.;85(6):2344–51.

155. Robertson HT, Glenny RW, Stanford D, McInnes LM, Luchtel DL, Covert D. High-resolution maps of regional ventilation utilizing inhaled fluorescent microspheres. J Appl Physiol. 1997 Mar.;82(3):943–53.

156. Anthonisen NR, Milic-Emili J. Distribution of pulmonary perfusion in erect man. Journal of Applied Physiology. 1966 May 1;21(3):760–6.

157. Bryan A, Milic-Emili J, Pengelly D. Effect of gravity on the distribution of pulmonary ventilation. Journal of Applied Physiology. 1966 May;21(3):778–84.

158. Holley HS, Milic-Emili J, Becklake MR, BATES DV. Regional distribution of pulmonary ventilation and perfusion in obesity. J Clin Invest. 1967 Apr.;46(4):475–81.

159. Hübler M, Souders JE, Shade ED, Hlastala MP, Polissar NL, Glenny RW. Validation of fluorescent-labeled microspheres for measurement of relative blood flow in severely injured lungs. J Appl Physiol. 1999 Dec.;87(6):2381–5.

160. Schimmel C, Frazer D, Glenny RW. Extending fluorescent microsphere methods for regional organ blood flow to 13 simultaneous colors. Am. J. Physiol. Heart Circ. Physiol. 2001 Jun.;280(6):H2496–506.

161. Guo J, Fuld M, Alford SK, Reinhardt JM, Hoffman EA. Pulmonary Analysis Software Suite 9.0 Integrating quantitative measures of function with structural analyses. 2008. p. 283–92.

162. Christensen GE, Johnson HJ. Consistent image registration. IEEE Transactions on Medical Imaging. 2001 Jul.;20(7):568–82.

163. Robertson HT, Kreck TC, Krueger MA. The spatial and temporal heterogeneity of regional ventilation: comparison of measurements by two high-resolution methods. Respiratory Physiology & Neurobiology. 2005 Aug. 25;148(1-2):85–95.

164. West JB, Glenny RW, Hlastala MP, Robertson HT. Importance of gravity in determining the distribution of pulmonary blood flow. J Appl Physiol. Am Physiological Soc; 2002;93(5):1888–91.

165. Glenny RW, Polissar L, Robertson HT. Relative contribution of gravity to pulmonary perfusion heterogeneity. J Appl Physiol. 1991 Dec.;71(6):2449–52.

166. Hlastala MP, Chornuk MA, Self DA, Kallas HJ, Burns JW, Bernard S, et al. Pulmonary blood flow redistribution by increased gravitational force. J Appl Physiol. 1998 Apr.;84(4):1278–88.

167. Altemeier WA, McKinney S, Glenny RW. Fractal nature of regional ventilation distribution. J Appl Physiol. 2000 May;88(5):1551–7.

168. Madani A, Van Muylem A, Gevenois PA. Pulmonary Emphysema: Effect of Lung Volume on Objective Quantification at Thin-Section CT. Radiology. 2010 Sep. 17;257(1):260–8.

169. Shaker S, Dirksen A, Laursen LC, Skovgaard L, Holstein Rathlou NH. Volume adjustment of lung density by computed tomography scans in patients with emphysema. Acta Radiologica. Royal Society of Medicine; 2004;45(4):417–23.

170. Stoel BC, Putter H, Bakker ME, Dirksen A, Stockley RA, Piitulainen E, et al. Volume correction in computed tomography densitometry for follow-up studies on pulmonary emphysema. Proceedings of the American Thoracic Society. 2008 Dec. 15;5(9):919–24.

171. Orlandi I, Moroni C, Camiciottoli G, Bartolucci M, Pistolesi M, Villari N, et al. Chronic obstructive pulmonary disease: thin-section CT measurement of airway wall thickness and lung attenuation. Radiology. 2005 Feb.;234(2):604–10.

172. Dirksen A, Piitulainen E, Parr DG, Deng C, Wencker M, Shaker SB, et al. Exploring the role of CT densitometry: a randomised study of augmentation therapy in alpha1-antitrypsin deficiency. Eur. Respir. J. 2009 Jun.;33(6):1345–53.

173. Camiciottoli G, Bartolucci M, Maluccio NM, Moroni C, Mascalchi M, Giuntini C, et al. Spirometrically gated high-resolution CT findings in COPD: lung attenuation vs lung function and dyspnea severity. Chest. 2006 Mar.;129(3):558–64.

174. Martinot-Lagarde P, Sartene R, Mathieu M, Durand G. What does inductance plethysmography really measure? J Appl Physiol. 1988 Apr.;64(4):1749–56.

175. Konno K, Mead J. Measurement of the separate volume changes of rib cage and abdomen during breathing. Journal of Applied Physiology. 1967 Mar.;22(3):407–22.

176. Hager DN, Fuld M, Kaczka DW, Fessler HE, Brower RG, Simon BA. Four methods of measuring tidal volume during high-frequency oscillatory ventilation. Crit Care Med. 2006 Mar. 1;34(3):751–7.

177. Mahler D, Weinberg D, Wells C, Feinstein A. The measurement of dyspnea. Contents, interobserver agreement, and physiologic correlates of two new clinical indexes. Chest. 1984 Jun. 1;85(6):751–8.

178. Miller MR, Hankinson J, Brusasco V, Burgos F, Casaburi R, Coates A, et al. Standardisation of spirometry. Eur. Respir. J. 2005. p. 319–38.

179. Simon BA, Marcucci C, Fung M, Lele SR. Parameter estimation and confidence intervals for Xe-CT ventilation studies: a Monte Carlo approach. J Appl Physiol. 1998 Feb.;84(2):709–16.

180. Lamers RJ, Thelissen GR, Kessels AG, Wouters EF, van Engelshoven JM. Chronic obstructive pulmonary disease: evaluation with spirometrically controlled CT lung densitometry. Radiology. 1994 Oct.;193(1):109–13.

181. Robinson PJ, Kreel L. Pulmonary tissue attenuation with computed tomography: comparison of inspiration and expiration scans. J Comput Assist Tomogr. 1979 Dec.;3(6):740–8.

182. Kohz P, Stäbler A, Beinert T, Behr J, Egge T, Heuck A, et al. Reproducibility of quantitative, spirometrically controlled CT. Radiology. 1995 Nov.;197(2):539–42.

183. Crum WR, Hartkens T, Hill DLG. Non-rigid image registration: theory and practice. The British journal of radiology. 2004;77 Spec No 2:S140–53.

184. Hill DL, Batchelor PG, Holden M, Hawkes DJ. Medical image registration. Physics in Medicine and Biology. 2001 Mar.;46(3):R1–45.

185. Schroeder W, Ng L. The ITK Software Guide Second Edition Updated for ITK version 2.4. 2005.

186. Yin Y, Hoffman EA, Lin C-L. Mass preserving nonrigid registration of CT lung images using cubic B-spline. Med. Phys. 2009;36:4213.

187. Press WH. Numerical Recipes. 2007.

188. Madsen MT. A simplified formulation of the gamma variate function. Phys Med Biol. 1992;37(7):1597–600.

189. Thompson HK, Starmer CF, Whalen RE, Mcintosh HD. INDICATOR TRANSIT TIME CONSIDERED AS A GAMMA VARIATE. Circulation Research. 1964 Jun.;14:502–15.

190. Chae EJ, Seo JB, Goo HW, Kim N, Song K-S, Lee SD, et al. Xenon ventilation CT with a dual-energy technique of dual-source CT: initial experience. Radiology. 2008 Aug.;248(2):615–24.

191. Goo HW, Chae EJ, Seo JB, Hong S-J. Xenon ventilation CT using a dual-source dual-energy technique: dynamic ventilation abnormality in a child with bronchial atresia. Pediatr Radiol. 2008 Oct.;38(10):1113–6.

192. Park E-A, Goo JM, Park SJ, Lee HJ, Lee CH, Park CM, et al. Chronic Obstructive Pulmonary Disease: Quantitative and Visual Ventilation Pattern Analysis at Xenon Ventilation CT Performed by Using a Dual-Energy Technique. Radiology. 2010 Sep. 1;256(3):985–97.

193. Simon BA. Regional ventilation and lung mechanics using X-Ray CT. Academic Radiology. 2005 Nov.;12(11):1414–22.

194. Tomiyama N, Takeuchi N, Imanaka H, Matsuura N, Morimoto S, Ikezoe J, et al. Mechanism of Gravity-Dependent Atelectasis: Analysis by Nonradioactive Xenon-Enhanced Dynamic Computed Tomography. Investigative Radiology. 1993 Jul.;28(7):633–8.

195. Snyder JV, Pennock B, Herbert D, Rinaldo JE, Culpepper J, Good WF, et al. Local lung ventilation in critically ill patients using nonradioactive xenon-enhanced transmission computed tomography. Crit Care Med. 1984 Jan.;12(1):46–51.

196. Ding K, Cao K, Fuld M, Du K, Christensen GE, Hoffman EA, et al. Comparison of Image Registration Based Measures of Regional Lung Ventilation from Dynamic Spiral CT with Xe-CT. Med. Phys. 2012 Jan. 28;(In Press.).

197. Salanitri J, Kalff V, Kelly M, Holsworth L, Williams T, Snell G. 133Xenon ventilation scintigraphy applied to bronchoscopic lung volume reduction techniques for emphysema: relevance of interlobar collaterals. Intern Med J. 2005 Feb.;35(2):97–103.

198. Bake B, Wood L, Murphy B, Macklem PT, Milic-Emili J. Effect of inspiratory flow rate on regional distribution of inspired gas. Journal of Applied Physiology. 1974 Jul.;37(1):8–17.

199. Glazier JB, Hughes JM, Maloney JE, West JB. Vertical gradient of alveolar size in lungs of dogs frozen intact. Journal of Applied Physiology. 1967 Nov.;23(5):694–705.

200. Lin C-L, Hoffman EA. A numerical study of gas transport in human lung models. Proceedings of SPIE. 2005;5746:92.

201. Hu S, Hoffman EA, Reinhardt JM. Automatic lung segmentation for accurate quantitation of volumetric X-ray CT images. IEEE Transactions on Medical Imaging. 2001 Jun.;20(6):490–8.

202. Zhang L, Hoffman EA, Reinhardt JM. Lung lobe segmentation by graph search with 3D shape constraints. Proceedings of SPIE. 2001;4321:204.

203. Aykac D, Hoffman EA, McLennan G, Reinhardt JM. Segmentation and analysis of the human airway tree from three-dimensional X-ray CT images. IEEE Transactions on Medical Imaging. IEEE; 2003;22(8):940–50.

204. Tschirren J, Palagyi K, Reinhardt J, Hoffman EA, Sonka M. Segmentation, skeletonization, and branchpoint matching—a fully automated quantitative evaluation of human intrathoracic airway trees. Medical Image Computing and Computer-Assisted Intervention—MICCAI 2002. Springer; 2002;:12–9.

205. Tschirren J, Hoffman EA, McLennan G, Sonka M. Intrathoracic airway trees: segmentation and airway morphology analysis from low-dose CT scans. Medical Imaging, IEEE Transactions on. 2005;24(12):1529–39.

206. ROSE A. Vision- Human and electronic(Book). New York. 1973.

207. Kabilan S, Lin C-L, Hoffman EA. Characteristics of airflow in a CT-based ovine lung: a numerical study. J Appl Physiol. 2007 Apr.;102(4):1469–82.

208. Baumueller S, Winklehner A, Karlo C, Goetti R, Flohr T, Russi EW, et al. Low-dose CT of the lung: potential value of iterative reconstructions. European Radiology. 2012 Jun. 15.

209. Zhang D, Li X, Liu B. Objective characterization of GE discovery CT750 HD scanner: gemstone spectral imaging mode. Med. Phys. 2011 Mar.;38(3):1178–88.

210. Fuchs T, Kachelriess M, Kalender WA. Direct comparison of a xenon and a solid-state CT detector system: measurements under working conditions. IEEE Transactions on Medical Imaging. 2000 Sep.;19(9):941–8.

211. Hoffman EA, Simon BA, McLennan G. State of the Art. A structural and functional assessment of the lung via multidetector-row computed tomography: phenotyping chronic obstructive pulmonary disease. Proceedings of the American Thoracic Society. 2006 Aug.;3(6):519–32.

212. Yuan R, Shuman WP, Earls JP, Hague CJ, Mumtaz HA, Scott-Moncrieff A, et al. Reduced iodine load at CT pulmonary angiography with dual-energy monochromatic imaging: comparison with standard CT pulmonary angiography--a prospective randomized trial. Radiology. 2012 Jan.;262(1):290–7.

213. Lee CW, Seo JB, Song J-W, Kim M-Y, Lee HY, Park YS, et al. Evaluation of computer-aided detection and dual energy software in detection of peripheral pulmonary embolism on dual-energy pulmonary CT angiography. European Radiology. 2011 Jan.;21(1):54–62.

214. Remy-Jardin M, Faivre J-B, Pontana F, Hachulla A-L, Tacelli N, Santangelo T, et al. Thoracic applications of dual energy. Radiologic Clinics of North America. 2010 Jan.;48(1):193–205.

215. Ferda J, Ferdová E, Mírka H, Baxa J, Bednářová A, Flohr T, et al. Pulmonary imaging using dual-energy CT, a role of the assessment of iodine and air distribution. Eur J Radiol. 2011 Feb.;77(2):287–93.

216. Pontana F, Faivre J-B, Remy-Jardin M, Flohr T, Schmidt B, Tacelli N, et al. Lung perfusion with dual-energy multidetector-row CT (MDCT): feasibility for the evaluation of acute pulmonary embolism in 117 consecutive patients. Academic Radiology. 2008 Dec.;15(12):1494–504.

217. Cournand A, Riley RL. Pulmonary circulation and alveolar ventilation perfusion relationships after pneumonectomy. J Thorac Surg. 1950 Jan.;19(1):80–116.

218. Presson RG, Hanger CC, Godbey PS, Graham JA, Lloyd TC, Wagner WW. Effect of increasing flow on distribution of pulmonary capillary transit times. J Appl Physiol. 1994 Apr.;76(4):1701–11.

219. Henzler T, Meyer M, Reichert M, Krissak R, Nance JW, Haneder S, et al. Dual-energy CT angiography of the lungs: Comparison of test bolus and bolus tracking techniques for the determination of scan delay. Eur J Radiol. 2012 Jan.;81(1):132–8.

220. Schenzle JC, Sommer WH, Neumaier K, Michalski G, Lechel U, Nikolaou K, et al. Dual energy CT of the chest: how about the dose? Invest Radiol. 2010 Jun.;45(6):347–53.